On The Inverse Design of Marine Ducted Propulsor Blading

by

Mark Edward Roddis

A thesis submitted for the degree of Doctor of Philosophy
in the Faculty of Engineering, University of London.

Department of Mechanical Engineering
University College London

June 1994

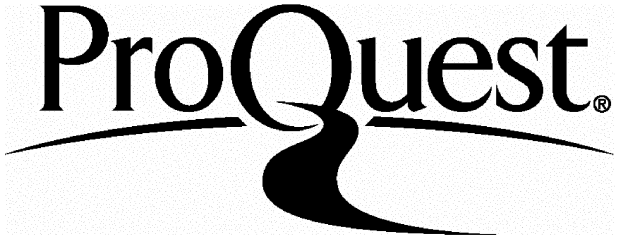

To my parents

ACKNOWLEDGEMENTS

I would like to thank my supervisors during the course of my research, Dr. Mehrdad Zangeneh and Professor Roy Burcher; without their support, encouragement and advice this work would not have been possible. Further thanks are due to Dr. Zangeneh for detailed advice regarding many of the mathematical and numerical techniques employed in this thesis. Additionally, I would like to express my gratitude to Vickers Shipbuilding and Engineering Limited (VSEL), Barrow-in-Furness, who not only financed my research at UCL, but also sponsored my undergraduate studies at the University of Newcastle-upon-Tyne, and provided invaluable secretarial support in the preparation of this thesis. I am also indebted to the workshop staff at UCL under Mr. Fred Arthur; without their enthusiasm, advice and hard work the experimental work could not have been conducted. Finally, I would like to thank numerous other members of UCL staff such as Dr. Alvin Blackie who offered advice and guidance regarding my work.

ABSTRACT

A three-dimensional computational design method is presented for multi-component marine ducted propulsors operating in axisymmetric shear flow.

An inverse design approach is adopted whereby the blade shapes at the specified design point are determined from a given blade circulation distribution and a condition of zero blade incidence. The corresponding three-dimensional propulsor flow field is also obtained, enabling the design-point performance of the synthesised design to be assessed.

Although based on an existing inviscid turbomachinery design technique, the method incorporates numerous modifications, firstly to enable propulsor mass flow to be determined, and secondly to model the shear flows that are encountered by propulsors operating within the boundary layers of ships.

Employing an assumption of inviscid flow and using the Clebsch representation of vorticity, both the propulsor through flow and bypass flow are described by simultaneous partial differential equations which are solved using finite difference and Fourier techniques.

The development of circumferential variations in both velocity and vorticity within the blade passages are included, as are the effects of spanwise variations of blade circulation. Moreover, by assuming that the duct wake remains axisymmetric slipstream contraction is accounted for.

In addition to the above formulation, a simplified three-dimensional formulation which neglects the development of circumferential variations in stagnation pressure is described, as is an "actuator duct" approach which neglects the circumferential variations of all flow quantities.

Computational results for practical ducted propulsors show the development of circumferential variations in flow quantities to have relatively little effect on either blades shape or overall propulsor performance predictions.

Finally, the experimental verification of the design method using a low speed wind tunnel is outlined. Velocity measurements conducted with a three-hole pitot probe show reasonable agreement with the predictions of the design method, whilst measurements of shaft power and mass flow show much closer agreement.

CONTENTS

LIST OF FIGURES

LIST OF TABLES

NOMENCLATURE

B_t	mean tangential blockage factor
D	duct diameter
$\hat{\mathbf{e}}_r^n$	unit normal to r = constant
$\hat{\mathbf{e}}_\theta^n$	unit normal to θ = constant
$\hat{\mathbf{e}}_z^n$	unit normal to z= constant
$\hat{\mathbf{e}}_\xi^n$	unit normal to ξ = constant
$\hat{\mathbf{e}}_\eta^n$	unit normal to η = constant
f	blade wrap angle (angular offset of blade camber line relative to meridional plane)
F	blade body force
H	rothalpy (= p_o^* / ρ)
i	$\sqrt{-1}$
L	duct length
M	Mach number
N	the number of Fourier harmonics taken
N_b	number of blades on a given blade row
p_0	absolute stagnation pressure
p_o^*	rotary stagnation pressure
Q	Shaft torque
r	radius
R_n	Reynolds number
$S(\alpha)$	Sawtooth function
T_n	blade thickness normal to mean camber line
T_t	tangential blade thickness
V	absolute velocity
W	velocity relative to blade surface
(r,θ,z)	the cylindrical polar co-ordinate system
α	Chapter 7: yaw angle of the Cobra Probe elsewhere: angular offset of a point relative to the key blade
$\delta_p(\alpha)$	Periodic Delta Function
ρ	fluid density
τ	drift function
ψ	Stokes stream function
ω	shaft angular speed
Γ	circulation

Φ	potential function
(ξ,θ,η)	the body-fitted co-ordinate system (mesh quasi-streamlines defined by η=constant, mesh quasi-orthogonals by ξ=constant)
Ω	absolute vorticity

Subscripts

r	radial component
θ	tangential component
z	axial component
ξ	derivative with respect to ξ
η	derivative with respect to η
1	refers to the upstream blade row
2	refers to the downstream blade row
bl	value on the blade surface/blade wake
le	value at the blade leading edge
te	value at the blade trailing edge
hub	value at the hub
tip	value at the blade tip
b	value in the propulsor bypass flow
c	value in the propulsor core (through) flow

Superscripts

+	value on the blade pressure surface
–	value on the blade suction surface
q,p,n,0	q^{th}, p^{th}, n^{th}, zeroth (mean) component of an IDFT

Overbars

–	circumferential average
~	periodic component ($\tilde{F} = F - \overline{F}$)

Miscellaneous

$\frac{\partial}{\partial n}$ partial derivative taken normal to the endwall

$\frac{\partial}{\partial s}$ partial derivative taken along the endwall in the plane θ = constant

CHAPTER 1 INTRODUCTION

Since its widespread adoption during the Nineteenth Century [1], a number of means have been proposed for improving the performance of the marine screw propeller (such as those outlined in [2], [3] and [4]). Of these "alternative" propulsion devices, perhaps none has found such widespread application as the ducted propulsor.

This type of device includes not only simple ducted propellers, which consist of a propeller enshrouded within an annular aerofoil (Figure 1.1), but also more elaborate configurations such as pumpjets ([5], [6]) where a second blade row is mounted immediately behind the first.

The development of the marine ducted propulsor as an alternative to conventional open propellers is directly attributable to experimental work earlier this Century by Stipa [7] and Kort [8]. Since then these devices have been installed on a wide variety of vessels ranging from tugs and trawlers through to supertankers, submarines and torpedoes. This success can be explained by classifying ducted propulsors into flow-accelerating or flow-decelerating types depending upon whether the presence of the duct increases or decreases the flow velocities at the blading.

Flow-decelerating configurations tend to result in increased static pressure at the blading and aft-acting duct forces. Consequently, low propulsive efficiencies have restricted the use of this type of device to cases where cavitation is a problem. However, flow-accelerating configurations are associated with forward-acting duct forces, yielding high propulsive efficiencies at high thrust loadings, and as a result have been installed on vessels such as tugs, torpedoes, submarines and large tankers.

In addition to the above advantages, the duct affords the blading some degree of protection from damage, and, acting as a screen, can reduce noise radiation to the far field; indeed, careful design can lead to very quiet operation for military or oceanographic purposes [6]. Moreover, the presence of the duct allows the blade tips to sustain hydrodynamic loading, offering opportunities for reduced propulsor diameter and increased utilisation of boundary layer inflow. Further improvements in propulsive efficiency can be obtained by the addition of a second blade row, usually in the form of either pre- or post- swirl stator vanes (to the inclusion of which the duct readily lends itself.) There is a widely held view [9] that pre-swirl stator vanes reduce the circumferential variations in velocity encountered by the rotor, leading to reduced

propeller-induced noise and vibration; such vanes can also replace struts as a means of duct support.

Balanced against these advantages must be the additional cost associated with the installation of the duct, and inferior off-design performance (particularly when operating astern); problems of duct erosion caused by tip cavitation are well-documented [10] for large merchant ships and have never really been satisfactorily solved.

References

1) Rippon,P.M. "Evolution of Engineering in the Royal Navy Volume I: 1827-1939", p34, Spellmount Ltd., Kent, 1988

2) Glover,E.J. "Propulsive Devices for Improved Propulsive Efficiency", Trans. IMarE, Vol.99, Paper 31, 1987

3) Blaurock,J. "An Appraisal of Unconventional Aftbody Configurations and Propulsion Devices", Marine Technology (SNAME), Vol.27, No.6, November 1990

4) Silverleaf,A. "Prospects for Unconventional Marine Propulsion Devices", 7th Symposium on Naval Hydrodynamics, Office of Naval Research, Arlington Va., USA, August 1968

5) Clayton,B.R, Bishop,R.E.D. "Mechanics of Marine Vehicles", E. & F.N. Spon Ltd., London, 1982

6) Friedman,N. "Submarine Design and Development", p.88, Conway Maritime Press, 1984

7) Stipa,L. "Experiments with Intubed Propellers", 1 'Aerotechnica, pp923-953, August 1931, Translation: Dwight Miner, NACA-TM 655, January 1932.

8) Kort, L. "Der Neue Dusenschrauben-Antrieb", Werft-Reederei-Haven, Jahrgang 15, Heft 4, 15th February 1934

9) Burcher,R., Rydill,L. "Concepts In Submarine Design", p.121, Cambridge Ocean Technology Series No.2, Cambridge University Press, 1994

10) Okamoto, H., Okada, K., Saito, Y., Takahei, T. "A Cavitation Study of Ducted Propellers on Large Ships", Trans. SNAME, Vol.83, 1975

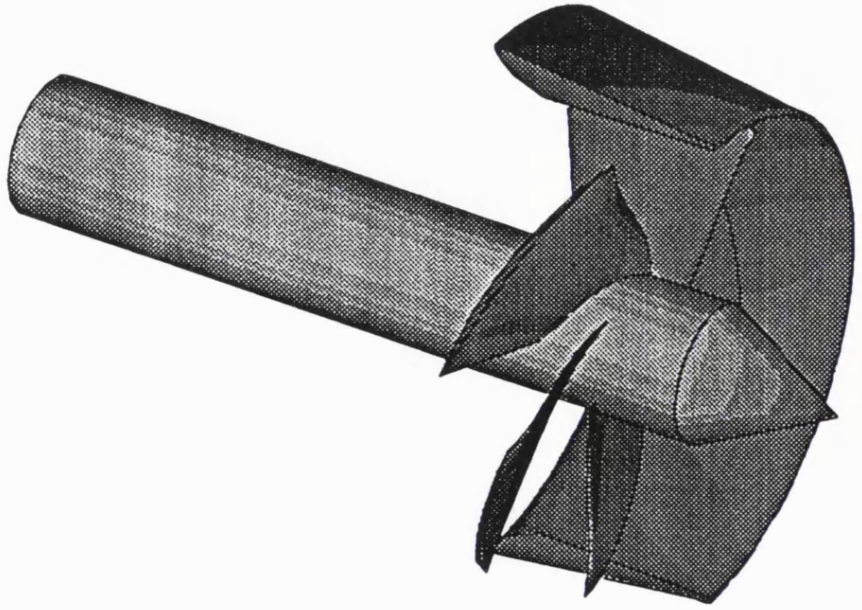

Figure 1.1: A Solid Model of a Five-Bladed Ducted Propeller
(Duct Cut Away and Duct Supports Omitted for Clarity)

CHAPTER 2 BACKGROUND ON DUCTED PROPULSOR DESIGN

2.1 Review of Previous Work On Ducted Propulsors

2.1.1 Introductory Works and General Reviews

Firstly, "Principles of Naval Architecture" [1] gives an excellent overview of ducted propeller theory and experiments, whilst Clayton and Bishop [2], using momentum theory, give a more theoretical introduction to ducted propulsor technology.

An interesting review of early ducted propulsor work is given by Dyne [3], in which the concept of the ducted propeller is traced back beyond the experimental work of Stipa [4] and Kort [5] to original British patents for a ducted propeller and a contra-rotating ducted propulsor by Ramsey (1792) and Church (1829) respectively!

A review of early (pre-1970s) ducted propeller theory is presented by Wessinger and Maass [6], critically appraising the early computation schemes that preceded the sophisticated lifting surface approaches of today.

The report of 1973 RINA Symposium On Ducted Propellers [7] provides a comprehensive, if somewhat dated, review of many now well-established methods and ideas, together with a wealth of experimental results.

Finally, more up to date reviews of ducted propulsor research, past and present, together with suggestions for future research, can be found in Reports of the International Towing Tank Conference (ITTC), such as [8].

2.1.2 General Experimental and Theoretical Studies

Due to the complexity of the ducted propulsor problem much of the research in this field has been based on highly simplified theories or experimental studies.

Typical of this work is that of Oosterveld and Van Manen [9]. Here the characteristics of both flow-accelerating and flow-decelerating ducted propellers are discussed using the results of experimental investigations and simplified theoretical studies. Experiments were carried out using the Ka Propeller Series and standard nozzles developed at the Netherlands Ship Model Basin (NSMB), good agreement

with momentum theory being reported. Criteria for the avoidance of flow separation on the duct are presented in diagrammatic form. For flow-accelerating nozzles the authors conclude that improvements in real efficiencies are only obtained at high screw loads, and that higher screw loads favour longer duct lengths. For flow-decelerating nozzles it is concluded that enhanced cavitation characteristics are only realised at low screw loadings, and that in such cases the nozzle must be relatively short to avoid large efficiency losses.

In [10] Oosterveld presents further results of experiments conducted using the Ka Screw Series. These standard screws developed at NSMB, were designed specifically for use within ducts, having wide blade tips to limit tip cavitation, with uniform pitch and flat face sections for ease of casting. A standard range of Nozzles for use with the Ka Series has also been developed. In this particular work open water results are presented for accelerating ducted propellers suitable for use on tugs and pushboats. The results show that conventional nozzles suffer from poor astern performance, and thus for vessels of this type it is desirable to fit nozzles with well-rounded, thick trailing edges. The performance of the ring propeller is also investigated. This device is essentially a ducted propeller with part or all of the duct fixed to the blade tips; problems associated with tip gaps are eliminated, but low efficiency due to viscous forces on the rotating duct has restricted full-scale application.

Optimum ducted propeller design charts based on standard screw series data are provided by Loukakis and Gelegnis [11], and Yosifov, Slatev and Staneva [12]. Whilst useful in preliminary ship design for machinery selection, such charts must be of limited use when designing propulsors for large ships.

Van Manen [13] investigates the effect of radial load distribution on the performance of ducted propellers, addressing such areas as flow separation on the duct, cavitation and efficiency, and the effects of blade tip clearance. The study is based on experiments conducted for a range of duct and screw combinations, with varying tip clearances. The author reports that the effect of blade tip loading on cavitation is significant, although radial load distribution has practically no effect on efficiency loss due to tip clearance. Suggested features for propeller ducts are given, together with design diagrams for achieving "optimum" ducted propeller performance.

Lewis [14] derives analytic expressions for ducted propeller performance prediction (including some account for viscous losses) in the absence of shear flow, and presents

design curves for both free-vortex and power law loading distributions. Some comparisons of surface vorticity numerical methods and experimental tests are also provided, reasonable agreement being found.

Lindgren et al [15] outline results of a study into the applicability of ducted and contra-rotating propellers to a 150,000 TDW tanker and a 12,000 TDW container ship using the design method outlined in [3]. The results indicate an improvement in open water efficiency of 7.5% and notably better cavitation characteristics by adopting a ducted propeller compared to a conventional propeller.

Several aspects of ducted propeller design, including hull-propeller interaction, tip clearance effects, and the beneficial effect of diffuser sections downstream of the blading are discussed by English and Rowe [7]. The authors postulate that the true benefit of ducted propellers in terms of efficiency is due to favourable hull-propeller interaction, arguing that open water efficiencies are generally no better than for open propellers. The advantages of steerable ducted propellers over conventional propeller-rudder combinations are highlighted, particularly in terms of propulsive efficiency and manoeuvrability, although costs seem to have prevented any large ship applications. By adopting a diffuser section on the duct downstream of the blading, slipstream velocity and hence jet losses can be reduced, and the authors present experimental results with various diffuser configurations to show this. The importance of keeping blade tip clearance to a minimum is also discussed, and proposals for reducing tip clearance losses using discharge jets on the duct are presented. Finally, the results of a slipstream survey of a model ducted propeller are given, circumferential mean velocities being shown.

Oosterveld [7] reviews a series of systematic open water ducted propeller experiments conducted at NSMB using both accelerating and decelerating nozzles (Figure 2.1). Attention is also given to right angle drives which allow for steerable ducted propellers. The application of ducted propellers to tugs, pushboats and large tankers is considered. The poor astern performance of ducted propellers is noted, and a nozzle with a well-rounded trailing edge (nozzle No. 37, Figure 2.1) is recommended for cases where this is a problem e.g. tugs; at high forward speeds this nozzle is quoted to be about 2% less efficient than the ubiquitous accelerating nozzle No. 19A. The concept of a non-axisymmetrical duct is outlined for reducing unsteady propeller forces and cavitation.

Results of a design study for a ducted propeller for a large OBO carrier are given by Glover and Ryan [7]. Some of the more important design decisions are explained, with the method outlined in [16] being used to select suitable configurations for model testing. Model tests show good agreement with theory.

Emerson and Sinclair [7] outline a feasibility study into the application of a ducted propeller to an OBO carrier, including structural and fabrication considerations, and economic factors. The study utilised the lifting line analysis method outlined by Ryan and Glover [16]. The results of model experiments conducted for the alternative configurations are given, together with the result of tests conducted on non-axisymmetric ducts.

Caster [7] outlines the design, predicted performance and open-water experimental tests of three accelerating ducted propellers designed for improved backing performance. Performance predictions were conducted using the method of Dyne [3]. Generally good agreement between theory and experiment are reported, particularly in terms of ahead and backing efficiencies.

Experiments on ducted propellers in axial and inclined flows conducted at the Swedish State Shipbuilding Experimental Tank are reported on by Dyne [7].

Flising [7] briefly describes the studies resulting in the installation of a ducted propeller on a 130,000 TDW tanker, and a summary of full scale trial measurements.

In another short paper, Titoff [7] makes recommendations for empirical factors for use in determining hull-propeller interaction for ducted propellers.

Minsaas, Jacobsen and Okamoto [7] present suggestions, based on experimental results, for determining propulsion factors for ducted propellers, with correlation of full scale and experimental results for a 215000 TDW tanker. The effect of the ducted propeller on manoeuvrability is also discussed.

The installation and trials of a ducted propeller on the SS Golar Nichu, a 215,000 TDW tanker (then the largest ship to have been fitted with such a device) is described by Andersen and Tani [7]. A detailed description of the design, along with masters' reports on ship handling and a comparison with sister ships fitted with conventional propellers are given. Results of manoeuvrability and hull vibration measurements are presented. The authors conclude that adopting the ducted propeller resulted in

overall improvements in propulsive efficiency (approximately 5-7% depending on load condition), manoeuvrability and hull vibration problems.

Shpakoff [7] analyses the results of a model study of ducted propeller performance both in still water and in a seaway, using both open water and behind hull test results. The effect of duct fouling on propulsive efficiency is also considered using full scale results.

A paper on the structural design of ducts and duct supports is presented by Caldwell and Andrew [7]. Design philosophy, choices of structural configuration, and means of structural analysis are discussed. The various possible load actions and their practical means of estimation are outlined.

Søntvedt et al [7] present a study of large ducted propellers with respect to loads and response, based on full-scale recordings of duct pressures, deformations and strains, together with data for propeller blade strains. Correlations with various theoretical models are made. The authors draw attention to the growth and collapse of cavitation in the blade tip region, which may produce significant dynamic duct stresses, although duct stress and deformation due to static wave encounter and blade frequency loads are reported to be small.

The causes and effects of air-drawing (natural ventilation) with particular reference to ducted propeller performance are discussed by Huse [7]. This fascinating phenomenon occurs in certain instances when the pressure in various parts of the propulsor flow field is less than atmospheric pressure, causing air to be drawn down from the free surface. Whilst the forced ventilation of propeller blades is a recognised means of reducing cavitation noise, in the case of natural ventilation the supply of air is out of control, and sudden reductions in thrust and torque may occur, resulting in severe noise and vibrations. The author presents the results of model tests where the effect of air drawing on thrust fluctuations and propeller-induced hull pressures were measured. Means of reducing ventilation, namely the use of hull-mounted fins and tilting the duct with its forward end downwards are assessed. It is concluded that ducted propellers are more prone to air drawing than equivalent open propellers at the same submergence. Duct tilting is shown to be more successful in reducing ventilation than the use of fins. In certain cases tilting of the duct was shown to improve propulsive efficiency by up to 6%. The problems of scale effects on predicting ventilation are highlighted, although it is argued that the general trends outlined are valid.

Biskup [7] briefly develops a theoretical analysis method for the variable forces arising on a duct due to a propeller, including the effect of oblique flow.

Theoretical studies by Van Gunsteren and Van Gunsteren [17] conclude that the effect of a fixed propeller duct is to increase the turning diameter of a vessel, and improve the response time and stability on a straight line course, as full scale trials have proved.

Okamoto et al [18] report on full scale observations of cavitation onboard VLCC's, bulk carriers and other large, full-form ships. Due to the confused flow fields associated with these large vessels, early applications of ducted propellers in these cases were dogged by problems of duct erosion caused by tip cavitation. Investigations to assess the potential of anti-erosive materials and air injection in reducing this problem were conducted, the results of the latter being presented in this paper. Air injection is shown to be an effective means of reducing propeller noise and vibration. In the discussion section, means of eliminating tip vortex cavitation, such as off-loading the tips and swept-forward blades, are suggested.

The experimental verification of the ducted propeller analysis method presented in [19] is described by Hughes et al [20]. These tests, conducted after the numerical verification of the program, were conducted in a water tunnel at MIT, USA. The forces on the propeller and duct were measured over a range of advance coefficients, with circumferential-average flow velocities being measured at various stations upstream and downstream of the duct using a Laser Doppler Velocimetry (LDV) system. The authors stress that the LDV system enables velocities to be determined to with one percent. Saturating the water in the tunnel with air bubbles enabled the presence of the flow separation on the duct to be detected. The computational predictions show very good agreement with experimental results for cases where the flow does not separate from the duct.

Finally, it is interesting to consider ducted propulsors in relation to the entire field of "alternative propulsion devices". Reviews of these devices are given by Glover [21] and Blaurock [22]. Of particular relevance are the Mitsui Integrated Duct [23] (where the duct is mounted immediately upstream of the propeller) and Schneekluth's Wake Equalising Duct [24] (where a non-axisymmetric duct is mounted on the hull some distance upstream of the propeller). Both these devices, it is claimed, offer

many of the benefits associated with ducted propeller installations at reduced cost and without many of the operating problems.

2.1.3 Computational Methods for Ducted Propulsors

Although theoretical studies such as the work of Morgan [25] lay the foundations for the numerical modelling of the ducted propulsor, the complexity of the ducted propulsor problem and the lack of powerful computing facilities meant that it was not until the first large ship applications in the late 1960's that the first computational schemes were developed.

One of the earliest computational schemes for the analysis of ducted propeller flow fields, based on the theory outlined in [25], is presented by Caster [26]. The so called Dickman-Wessinger mathematical model is adopted whereby the duct is represented by vortices and ring sources distributed along a circular cylinder of a diameter representative of the duct. The blading is represented using lifting line theory, developed by Lerbs [27] for moderately-loaded propellers. Only the steady components of velocity induced on the duct are considered. Comparisons with experimental results are given for a test propulsor at two operating conditions, showing good agreement.

Another early computational method for the design of ducted propellers is outlined by Dyne [3]. From inputs such as required thrust, tip diameter, shaft speed, blade number and circulation distribution, and cavitation margins, the method iteratively determines blade area, propulsive efficiency, duct thrust and shape, and blade camber and thickness until the required propulsive thrust is achieved. The duct is represented by ring source and vortex distributions along a cylindrical surface, the hub (assumed cylindrical) also being represented using ring sources. When determining certain features such as duct thrust and duct shape an assumption of an infinite number of blades is made, this being modelled using a uniform distribution of ring and rectilinear vortices; as a consequence this approach is applicable only to cases of moderate and light blade loadings. When determining such quantities as blade thrust and camber, the blades are represented as radial lifting lines. The approach cannot deal with shear flow and takes no account of viscous effects, and no experimental verification is given. As can be seen, this method involves a number of simplifying assumptions, although it represents one of the most advanced works of its time.

Morgan and Caster [28] assess the adequacies of the early ducted propeller theories in assessing ducted propeller and annular aerofoil performance. By comparison with experimental results they conclude that the theories available to them predicted forces and duct pressure distributions adequately provided flow separation did not occur on the duct surface. They emphasise the limited applicability of the results due to the limited number of geometries considered, and also areas where improvements in predictions were needed, such as the pressure distribution on the duct interior surface. The importance of the avoidance duct flow separation is also stressed.

Turbal [7] introduces the interesting concept of a non-axisymmetrical propeller duct, and describes a method for calculating flow characteristics of ducted propellers fitted with these ducts. The method involves a number of simplifying assumptions (notably "linearisation" of the governing equations), with the blading being represented by an actuator disc and the duct by a surface vorticity distribution. Such non-axisymmetrical propeller ducts offer the benefit of reduced circumferential variations in flow velocity encountered by the blading, and hence reduced unsteady propeller-induced vibration and noise. However, such ducts would require careful design to achieve satisfactory design performance, and the complexity of the design problem, and fabrication costs, seem to have prevented any large scale applications to date. The off-design performance of this type of device must be a source of concern, particularly avoidance of duct separation when manoeuvring; indeed, off-design unsteady propeller forces may be worse than for a conventional ducted or open propeller.

A method for the design of marine propeller ducts in shear flow is presented by Lee [29]. The duct thickness and loading distribution is specified, with an actuator disc model being used for the blading. This approach, which assumes inviscid, axisymmetric through flow, includes the effects of non-uniform blade loading[1]. Fourier transform techniques are used to reduce a simplified form of the Euler Equation to a series of linear simultaneous equations, enabling duct camber to be solved for iteratively. It should be noted, however, that the duct so obtained, whilst giving satisfactory performance at the design point, may well show undesirable behaviour off-design such as flow separation. If possible, it is desirable to adopt a "standard" duct that has been proven in an extensive series of experimental tests, such

[1] Here, as indeed throughout this thesis, the term "non-uniform blade loading" is used to refer to instances where spanwise variations of blade circulation are encountered, and thus cases where bound vorticity is shed from the blade trailing edge. Likewise, the term "uniform blade loading" is used to refer to instances where no spanwise variations in blade circulation occur, and thus where no bound vorticity is shed from the blade trailing edge. It should therefore be noted that cases of "uniform blade loading" do not necessarily correspond to cases of uniform blade pressure loading.

as the NSMB nozzles shown in Figure 2.1. None-the-less, computational duct design methods are still of considerable use in developing new duct profiles.

A significant development in the field of computational methods was the analysis method of Ryan and Glover [16]. Here the hub and shroud are represented by means of surface vorticity distributions (rather than by the less sophisticated Dickman-Wessinger model) with the propeller blades modelled as lifting lines. This approach yields both the flow through field around the propulsor and the duct pressure distribution. Although the effects of a non-uniform blade loading are included, the method cannot directly deal with cases of sheared inflow such as those encountered by a propulsor operating within the wake of a ship, and the effects of slipstream contraction and the circumferential variations of duct circulation are neglected.

Gibson and Lewis [7] (see also [30]) present a similar, but rather simpler approach, whereby the propeller is modelled by an actuator disc. Results obtained were similar to those above, and although later extended to include the effects of blade tip clearance [31], the method suffers from similar limitations.

More recently the analysis method of Robins [32], again using an actuator disc/surface vorticity model, includes the effects of sheared onset flow and slipstream contraction by imposing vortex sheets within the flow and applying a condition of zero pressure jump across these sheets. However, the swirl induced by the blading is neglected and the method suffers from the usual limitations of the actuator disc approach i.e. only circumferential mean velocities are obtained and only limited information regarding the required blade shapes can be found.

In one of the most extensive studies of its kind, Falcao de Campos [33] firstly develops a numerical procedure solving for the potential flow around isolated ducts using surface singularity distributions, and then outlines a means of introducing boundary layer displacement to account for viscous action. The author then formulates the ducted propeller analysis problem in terms of Stokes stream function, representing the blading by means of an actuator disc, and accounting for blade-induced swirl. Discrete vortex sheets are used to represent axisymmetric sheared onset flow, the entire problem being solved by an iterative procedure involving streamline tracing. The numerical methods described are then applied to investigate hull-propulsor interaction. Finally, a ducted propeller design procedure utilising the outlined numerical methods is given, the blades being designed using Lerbs' induction factor method; correction factors given for conventional propellers by Morgan et al

[34] are recommended. A wide range of experimental results are given throughout the report, with generally good agreement with numerical results being achieved.

Zchmiechen and Zhou [35] derive an optimum propulsion condition based on energy distribution in the jet wake for multi-blade row ducted propulsors, enabling the principal parameters of the propulsor, including mass flow, to be determined. An energy-based streamline iteration method is then used to determine the propulsor flow field, with the blading represented as a pump stage. Circumferential variations in flow velocity are neglected, although the method takes some account of viscous losses via loss factors, and can deal with sheared onset flow and slipstream contraction. As stated earlier, the propulsor mass flow rate is fixed as input to the streamline iterative procedure, rather than being determined interactively, and this must limit the accuracy of the results. As the approach accounts for finite blade chord, it should be possible to use the predicted streamline paths in the design of blading, although this is not highlighted by the authors.

A sophisticated analysis method is given by Kerwin et al [19], utilising a panel representation of the duct and hub, and a vortex lattice representation of the blading. The method is capable of modelling the periodic flow within the blade passages and accounts for circumferential variations in duct circulation. Since only the solid surfaces of the propulsor are represented and not the entire flow domain, this approach is potentially very fast. However, the method is potential-based and as such is unable to deal with sheared inflow. Slipstream contraction and other wake characteristics have to be specified by the user and the panel representation of the geometry is necessarily quite complicated.

Hughes and Kinnas [36] report on the extension of this analysis method to include pre-swirl stator vanes, although only the circumferentially averaged interactions between the propeller and stator are included, and again, shear flow effects are not included. The subsequent experimental verification of the method is outlined, this involving blade and duct force measurements for a model propulsor mounted in a water tunnel. The experimental results show very good agreement with the predictions of the method for the cases where the duct flow remains attached.

Szantyr and Glover [37] present a detailed analysis method based on unsteady, deformable lifting surface theory for ducted propellers operating in a three-dimensional, non-uniform velocity field. The duct and blades, together with their associated wakes, are represented by discrete vortex elements distributed on

representative surfaces, whilst blade and duct thickness are modelled by distributions of sources and sinks. This method, previously applied to open propellers, models the occurrence and extent of the different types of cavitation, and unsteady propeller and hull pressure forces can also be found. It would seem, however, that the effects of radial variations in onset flow are neglected, and again slipstream contraction is neglected.

An inverse design method based on a streamline curvature/blade-to-blade technique is presented by Furuja and Chiang [38]. The required blade shapes are obtained directly as an output from this method, and unlike most of the other methods reviewed, this approach explicitly includes a second blade row. However, it is by no means clear whether the method can model either shear flow or slipstream contraction, nor whether mass flow is specified as an input to the process. Three-dimensional effects in the blade passages are only partially accounted for.

Finally, there exists a number of methods concerned with the optimisation of ducted propeller blade circulation. Typical of this is the work of Kinnas and Coney ([39], [40]). Using a panel representation of the duct and representing the blades by radial lifting lines, a non-linear optimisation technique yields minimum torque for a prescribed blade thrust and optimum blade chords from specified blade cavitation criteria. Sanchez-Caja [41] has extended this work to include hub effects, although again it is assumed that the vortex wakes align with the undisturbed onset flow, and the method cannot model shear.

2.2 Classification of Computational Methods for Ducted Propulsors

From Section 2.1.3 it can be seen that computational methods for ducted propulsors generally fall into one of three categories:-

2.2.1 Analysis Methods

Analysis methods solve for the propulsor flow field for a given propulsor geometry and a specified operating condition, thus enabling the performance of a given propulsor (and hence its suitability) to be assessed for a range of operating conditions.

Inputs to analysis methods include the duct and hub geometry, the shaft speed and the velocity profile far upstream of the propulsor. For lifting surface methods it is also

necessary to specify the blade shapes, although this is generally not necessary for actuator disc and lifting line models which may therefore be used much earlier in the design process.

Typical output from an analysis method might include the duct pressure distribution, propulsor thrust and torque, and an estimate of propulsive efficiency. Whilst lifting surface methods also yield estimates of blade pressure distributions from which cavitation performance may be assessed, such detailed information cannot be derived directly from actuator disc or lifting line methods.

Typical analysis methods are the actuator disc models of [7] (Gibson and Lewis), [32] and [33], and the lifting line approaches of [16] and [26]. Here the computed flow field is based on either a specified blade circulation distribution or disc pressure loading, rather than on blade shapes.

More sophisticated analysis methods are typified by the lifting surface methods of [19] and [37] which fully account for blade both shapes and the effect of a finite number of blades.

2.2.2 Load Optimisation Methods

This group of methods, for use in the early stages of ducted propulsor design, is concerned with the optimisation of blade circulation distributions for either a specified blade thrust or torque. Such methods ([39], [40], [41]) typically use either actuator disc or lifting line models for the blading, with the duct and hub modelled by surface singularity distributions. Generally these methods cannot deal with either sheared onset flow or slipstream contraction.

2.2.3 Inverse Design Methods

Inverse design methods are used to determine some feature of a ducted propulsor design, such as blade shape or duct geometry. This is achieved by specifying some corresponding feature of the propulsor flow field, such as the required blade circulation distribution for blade design, or the duct pressure distribution if the duct shape is to be determined. By then specifying the remainder of the propulsor geometry, together with the operating condition for which the propulsor is to be designed, the entire ducted propulsor design and the associated design-point flow field can be obtained. The suitability of the synthesised design can then be assessed in

terms of cavitation, the likelihood of flow separation, and propulsor thrust and torque. Once a satisfactory design has been generated, off-design performance (which cannot normally be obtained from the inverse design method) can be appraised using either an analysis method or by experiment.

To date relatively little research has been directed at the development of inverse design methods for ducted propulsors. However, the few methods that exist have generally been applied to either duct design or blade design, as follows:-

(i) Duct Inverse Design Methods

The only methods of this type found were those by Lee [29], which solve for duct shape from a specified duct pressure distribution, and Dyne [3] (which also solves for blade shape). Whilst of considerable use in studies into duct shape, this class of method seems only to be of limited use in designing propulsor ducts for specific applications as they optimise duct shape for a single design point, and take no account of viscous action which may result in unsatisfactory duct performance even at this design point.

For most marine cases satisfactory off-design performance and ease of duct manufacture are of such importance that it seems to be common practice for designers instead to adopt "standard" duct profiles such as those presented in Figure 2.1; these have been proven to give satisfactory performance over a wide range of operating conditions by extensive experimental studies and numerous full-scale applications.

(ii) Blade Inverse Design Methods

Blade shapes are arguably the most crucial aspect of a ducted propulsor design, as it is the blading that absorbs the shaft power and typically generates over 80% of the propulsor thrust [9]. Once the duct geometry has been selected, it is blade performance that determines the efficiency of the propulsor. As a result it is the application of inverse design methods to blade design that shows the most promise, and indeed, it is in this area that the remainder of this thesis will concentrate.

Apart from the work of the author (see Roddis and Zangeneh [42], and Zangeneh and Roddis [43]) which is based on the approach outlined in Chapters 4 and 5, the only other inverse design methods of this type found were those of Dyne [3] (which also solves for duct shape), and Furuja and Chiang [38]. All

these methods determine blade shape from a specified blade circulation distribution.

2.3 Existing Techniques for the Design of Ducted Propulsor Blading

Some of the companies and institutions involved in the design of ducted propulsors are, perhaps understandably, rather secretive about the detailed techniques they employ in the design of ducted propulsor blading. However, based on published literature, and the rather limited knowledge of the author, the following alternative methods of blade design seem to be most widely employed:-

2.3.1 "Trial-and-Error"

It is usually possible to obtain an approximate blade design based either on some existing design or simplified theory. Using either experimental tests or a computational analysis method, this blade geometry can be systematically modified on a "trial-and-error" basis until the desired performance is achieved. This type of approach, which relies heavily on the experience of the designer, is time-consuming, and, if experimental techniques are employed, expensive. As such this approach is only normally used to "fine tune" a blade design during the later stages of the design process, immediately prior to construction.

2.3.2 Standard Series Data

Another approach to propulsor blading design is the use of standard propeller series data, such as the Ka ducted propeller series presented in [9]. However, considering the sensitivity of blade performance to the environment in which a particular propulsor operates, one might reasonably conclude that blade design from standard propeller series is unlikely to give optimum propulsive efficiency at the propulsor design point. Given the cost associated with the installation of a propulsor duct, one might conclude that a more sophisticated approach to design is warranted, at least for large-ship applications of ducted propulsors where the potential for fuel savings is huge. Additionally, for certain cases such as twin blade row propulsors, standard series data is not available, and therefore cannot be used.

2.3.3 Actuator Disc/Lifting Line Theory

Blading may be designed using the computational results of either actuator disc or lifting line based analysis methods (such those given in [16], [26], [32] and [33]), which compute the propulsor flow field based on a specified blade circulation or blade loading distribution rather than from input blade shapes. Alternatively, the output

from one of the load optimisation methods presented in [39], [40] and [41] may be used. In either instance the blade may be considered as series of "blade elements" [44], whereby at each radius the blade is assumed to act as a two-dimensional hydrofoil. There are then two possible approaches:-

1) From the analysis method the relative flow angles at the blade leading and trailing edges can be obtained, with the blade chord being selected from the pressure loading predictions. The camber line of each blade element can then be designed as a curve that aligns with the relative flow at the leading and trailing edges. These blade elements can then be combined to generate a surface which can be faired if required. A blade thickness distribution, based on structural considerations, can then be superimposed to obtain the final blade geometry.

The major disadvantage of this method is that away from the blade leading and trailing edges the choice of camber line path is completely arbitrary; considerable skill and experience must be involved in obtaining a satisfactory blade pressure distribution.

Although not mentioned explicitly in any of the literature reviewed, this approach, whilst rather crude, is highly plausible, and has probably been used in the past.

2) Utilising the output from the analysis method, each blade element can be designed by aligning its camber line with the predicted relative velocity field at the blade trailing edge, as outlined by Falcao de Campos [33]. Blade chord can then be chosen based on the estimated blade loading distribution, the final design being obtained by applying a suitable blade thickness distribution, such as those given for open propellers by O'Brien [44].

The resulting designs are, however, in many ways inferior to those obtained from 1) above, as the adoption of flat camber lines ensures a non-zero blade incidence at the design point. For highly loaded blades such a flow regime may result in a harsh pressure gradient around the blade leading edge, and such undesirable flow phenomena as cavitation or flow separation.

As a result, the elemental camber lines are often modified using lifting surface correction factors in order to achieve zero (ideal) incidence at the leading edge. Further correction factors, either theoretical or empirical, can be applied to account for errors associated with neglecting blade chord, blade thickness, blade number and skew. For ducted propellers Falcao de Campos [33] suggests the use of lifting surface correction factors given by Morgan et al [34] for open propellers.

If the effects of shear flow are not included in the analysis method, as is often the case, they are usually accounted for by superimposing some representative velocity profile onto the velocities predicted at the blading (see Dr. Falcao de Campos's contribution in [42]).

It is this type of approach that seems to be most widely used in ducted propulsor design. Although relatively simple to use, this technique relies on a rather confusing array of assumptions regarding slipstream contraction, wake geometry and blade shapes, the net effect of which is that blade shapes become increasingly inaccurate for higher blade loadings. Furthermore, once the radial distribution of circulation has been specified, the designer is left with very little control over blade shape.

Both the above blade element methods rely on the blade-induced swirl being either specified or computed by the analysis method.

2.3.4 Inverse Design

The final means of ducted propulsor blade design is the inverse design approach, as outlined in Section 2.2.3. Of the existing blade inverse design methods, that of Dyne [3] represents a computational implementation of the blade element/analysis method design procedure discussed in Section 2.3.3, with the addition of an iterative procedure to determine duct shape; as such it would be expected to suffer from similar limitations. Meanwhile the inverse design method given by Furuja and Chiang [38] seems to have a number of limitations, as summarised in Section 2.1.3, and, to date, appears not to have been widely adopted.

2.4 The Potential for the Application of Turbomachine Methods to the Design of Marine Ducted Propulsor Blading

Of the fundamental approaches to propulsor blade design listed in Section 2.3, it is perhaps the inverse design approach that is conceptually most neat, this approach also offering the best prospect for the rapid, low-cost generation of satisfactory designs.

It can be seen from Section 2.3.3 that existing inverse design methods for ducted propulsors are limited both in number and in application, and are based on somewhat restrictive and dated mathematical approaches.

However, as outlined by Borges [45] and Zangeneh [46], inverse design methods have found considerable application in the field of turbomachinery blade design. Typically, inverse design methods for turbomachinery blading utilise recent developments in computer power much more fully than corresponding ducted propulsor design methods, enabling the rapid generation of blade shapes whilst leaving the designer with considerable control over blade performance. As blade shapes are determined interactively with the associated flow field, a minimum of assumptions are involved, and full account of both finite blade number and blade chord can be made.

As will be outlined in the next Chapter, there is considerable scope for the application of turbomachinery methods to the inverse design of ducted propulsor blading. The extension of one such method to the design of ducted propulsor forms the basis of this thesis.

References

1) Various "Principles of Naval Architecture", Part II, Section 9, pp213-225, Editor: Edward V. Lewis, SNAME, 1988

2) Clayton,B.R, Bishop,R.E.D. "Mechanics of Marine Vehicles", E. & F.N. Spon Ltd., London, 1982

3) Dyne, G. "A Method for the Design of Ducted Propellers in a Uniform Flow", Publication No.62, Swedish State Shipbuilding Experimental Tank, Gothenburg, Sweden, 1967

4) Stipa,L. "Experiments with Intubed Propellers", l'Aerotechnica pp923-953, August 1931
Translation: Dwight D. Miner, NACA-TM 655, NACA, USA, January 1932

5) Kort,L. "Der Neue Dusenschrauben-Antrieb", Werft-Haven, Jahrgang 15, Heft 4, 15th February 1934

6) Wessinger,J., Maas,D. "Theory of the Ducted Propeller - a Review", 7th Symposium on Naval Hydrodynamics, Office of Naval Research, Arlington Va., USA, August 1968

7) Various, "Symposium on Ducted Propellers", RINA, Summer 1973:-
- Paper 1: Gibson,I.S., Lewis,R.I. "Ducted Propeller Analysis by Surface Vorticity and Actuator Disc Theory"
- Paper 2: Turbal,V.K. "Theoretical Solution of the Problem on the Action of a Non-Axisymmetrical Ducted Propeller System in a Non-Uniform Flow"
- Paper 3: English,J.W., Rowe,S.J. "Some Aspects of Ducted Propulsion"
- Paper 4: Oosterveld,M.W.C. "Ducted Propeller Characteristics"
- Paper 5: Glover,E.J., Ryan,P.G. "A Comparison of Theoretical and Experimental Performance of a Ducted Propeller System"
- Paper 6: Emerson,A., Sinclair,L. "Experimental and Practical Considerations in the Design of a Ducted Propeller System"
- Paper 7: Caster,E.B. "Ducted Propeller Designs for Improved Backing Performance"
- Paper 8: Dyne,G. "Systematic Studies of Accelerating Ducted Propellers in Axial and Inclined Flows"
- Paper 9: Flising,A. "A Ducted Propeller Installation on a 300 000 TDW Tanker - A Research and Development Project"
- Paper 10: Titoff,I.A. "Interaction Between Ducted Propeller System and Ship Hull"
- Paper 11: Minsaas,K.J., Jacobsen,G.M., Okamoto,H. "The Design of Large Ducted Propellers for Optimum Efficiency and

Manoeuvrability"
Paper 12: Andersen,O., Tani,M. "Experience with SS Golar Nichu"
Paper 13: Shpakoff,V.S "Hydrodynamic Characteristics of Ducted Propellers Affected by Environmental Conditions"
Paper 14: Caldwell,J.B., Andrew,R.N. "Structural Design of Ducts and Duct Supports"
Paper 15: Søndvedt,T., Johansson,P., Mugaas,B., Vaage,B. "Loads and Response of Large Ducted Propeller Systems"
Paper 16: Huse,E. "Performance of Tilted Ducts"
Paper 17: Biskup,B.A. "Periodic Forces Developing on a Propeller Duct"

8) Various, "19th International Towing Tank Conference Proceedings", Vols. I & II, ITTC, Madrid, 1990

9) Van Manen,J.D., Oosterveld,M.W.C. "Analysis of Ducted Propeller Design", Trans. SNAME, Vol. 74, 1966

10) Oosterveld,M.W.C. "Ducted Propeller Systems Suitable for Tugs and Pushboats", I.S.P., No 219, Vol 19, 1972

11) Loukasis,T., Gelegnis,G. "Optimisation Diagrams for the Selection of Ducted Propellers from the Ka Series", IMAEN '84, Athens, 1984

12) Yosifov,K., Zlatev,K., Staneva,A. "Optimum Characteristics Equations for the K-J Ducted Propeller Design Charts", IMAEN '84, Athens, 1984

13) Van Manen,J.D. "Effect of Radial Load Distribution on the Performance of Shrouded Propellers", RINA Transactions, 1962

14) Lewis,R.I. "Fluid Dynamic Design and Performance Analysis of Ducted Propellers", Vol. 88, No 3, Trans. NECIES, February 1972

15) Lindgren,H., Johnsson,C.-A., Dyne,G. "Studies in the Application of Ducted and Contra-Rotating Propellers on Merchant Ships", 7th Symposium on Naval Hydrodynamics, Office of Naval Research, Arlington Va., USA, August 1968

16) Ryan,P.G., Glover,E.J. "A Ducted Propeller Design Method: A New Approach Using Surface Vorticity Distribution Techniques and Lifting Line Theory", Trans. RINA, Vol. 114, 1972

17) Van Gunsteren,L.A., Van Gunsteren,F.F. "The Effect of a Nozzle On Steering Characteristics", I.S.P., Vol 19, May 1972

18) Okamoto,H., Okada,K., Saito,Y., Takahei,T. "A Cavitation Study of Ducted Propellers On Large Ships", Trans. SNAME, Vol.83, 1975

19) Kerwin,J.E., Kinnas,S.A., J-T Lee, W-Z Shih "A Surface Panel Method for Hydrodynamic Analysis of Ducted Propellers", P4, SNAME Annual Meeting, New York, November 1987

20) Hughes,M.J.,Kinnas,S.A., Kerwin,J.E. "Experimental Validification of a Ducted Propeller Analysis Method", pp214-219, Trans. ASME, June 1992

21) Glover,E.J. "Propulsive Devices for Improved Propulsive Efficiency", Trans. IMarE, Vol.99, Paper 31, 1987

22) Blaurock,J. "An Appraisal of Unconventional Aftbody Configurations and Propulsion Devices", Marine Technology (SNAME), Vol.27, No.6, November 1990

23) Narita,H., Yagi,H., Johnson,H.D., Breves,L.R. "Development and Full-Scale Experiences of a Novel Integrated Duct Propeller", Trans. SNAME, Vol.89, 1981

24) Stierman,E.J. "The Design of an Energy Saving Wake Adapted Duct", PRADS '87 (3rd International Symposium), Trondheim, Norway, June 1987

25) Morgan,W.B. "Theory of the Annular Aerofoil and Ducted Propeller", Fourth Symposium on Naval Hydrodynamics, pp151-207, 1962

26) Caster,E.B. "A Computer Program for Use In Designing Ducted Propellers", NSRDC Report 2507, October 1967

27) Lerbs,H.W. "Moderately Loaded Propellers with a Finite Number of Blades and an Arbitrary Distribution of Circulation", Trans. SNAME, Vol.60, pp73-117, 1952

28) Morgan,W.B., Caster,E.B. "Comparison of Theory and Experiment on Ducted Propellers", 7th Symposium On Naval Hydrodynamics, Office of Naval Research, Arlington Va., USA, August 1968

29) Lee,H. "The Effects of Radially Sheared Inflow On the Design of Propeller Ducts", PRADS '87 (3rd International Symposium), Vol. I, p143, Tronheim, Norway, June 1987

30) Lewis,R.I. "Vortex Element Methods for Fluid Dynamic Analysis of Engineering Systems", Cambridge Engine Technology Series, Cambridge University Press, 1991

31) Gibson,I.S. "Theoretical Studies of Tip Clearance and Radial Loading On the Operation of Ducted Fans and Propellers", Journal of Mechanical Engineering Sciences, Vol.16, 1974

32) Robins, A.J. "Through-Flow Calculations for a Ducted Propulsor Operating in a Thick Boundary Layer", International Conference On New Developments in Warship Propulsion, RINA, November 1989

33) Falcao de Campos,J.A.C. "On the Calculation of Ducted Propeller Performance in Axisymmetric Flows", Technical Report 696, Netherlands Ship Model Basin, Wageningen, The Netherlands, 1983

34) Morgan,W.B., Silovic,V., Denny,S.B. "Propeller Lifting Surface Corrections", Trans. SNAME, Vol. 76, pp309-347, 1968

35) Zchmiechen,M., Zhou,L. "An Advanced Method for Design of Optimal Ducted Propellers Behind Bodies of Revolution", SNAME STAR Symposium, Pittsburgh, Pennsylvania, June 8-10, 1988

36) Hughes, M.J., Kinnas,S.A. "An Analysis Method for a Ducted Propeller with Pre-Swirl Stator Blades", Proceedings of the Propellers/Shafting '91 Symposium, Paper No.15, SNAME, Virginia Beach Va., USA

37) Szantyr,J.A., Glover,E.J. "The Analysis of Unsteady Propeller Cavitation and Hull Surface Pressures for Ducted Propellers", Trans. RINA, Vol 132 (Part A), 1990

38) Furuja,O., Chiang,W.L. "A New Pumpjet Design Theory", Report No TC-3037, Tetra Tech. Inc., Pasadena Ca, 1986

39) Kinnas,S.A., Coney,W.B. "On the Optimum Ducted Propeller Loading", SNAME Propellers '88 Symposium, Virginia Beach, Virginia, September 1988

40) Kinnas,S.A., Coney,W.B. "The Generalised Image Model - An Application to the Design of Ducted Propellers", Journal of Ship Research, pp197 - 209, Vol 36, No 3, September 1992

41) Sanchez-Caja,A. "On the Optimum Ducted Propeller Loading with Inclusion of Duct and Hub", Trans. RINA, Vol 133 (Part B), 1991

42) Roddis,M.E., Zangeneh,M. "A Method for the Inverse Design of Ducted Propulsors Operating in Axisymmetric Shear Flows", Issued for written discussion, RINA, 1993

43) Zangeneh,M., Roddis,M.E. "A Three-Dimensional Method for the Inverse Design of Marine Ducted Propulsor Blading", to be presented at SNAME Propellers/Shafting '94, Virginia Beach, Va., USA, September 1994

44) O'Brien,T.P. "The Design of Marine Screw Propellers", Hutchinson Scientific and Technical, London 1962

45) Borges,J. "Three Dimensional Inverse Design of Turbomachinery", Ph.D. Thesis, Cambridge University Engineering Department, Cambridge, 1986

46) Zangeneh,M. "Three Dimensional Inverse Design of Radial-Inflow Turbines", Ph.D. Thesis, Cambridge University Engineering Department, Cambridge, 1988

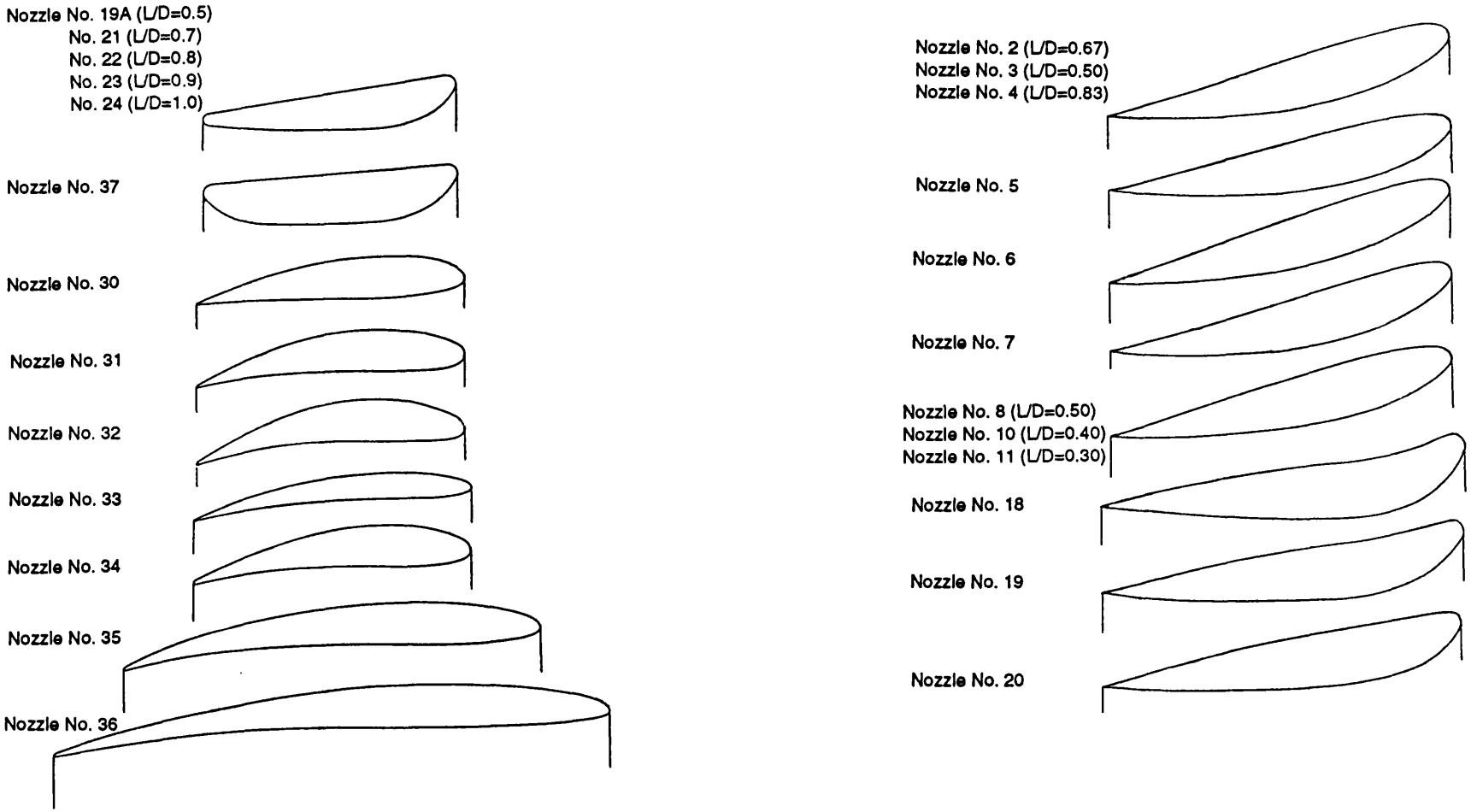

Figure 2.1: Profiles of Various Nozzles Tested at NSMB (See Oosterveldt [7])

CHAPTER 3 THE APPLICATION OF TURBOMACHINERY METHODS TO THE DESIGN OF DUCTED PROPULSOR BLADING

3.1 Introduction

The closing Section of the previous Chapter considered some of the inadequacies of existing techniques for the design of ducted propulsor blading, and noted the disparity between such methods and those used for the design of turbomachinery blading.

The present Chapter will consider the general applicability of turbomachine design methods to the ducted propulsor design problem. To these ends only blade design methods for internal flow turbomachines will be considered, as it is on the extension of one such method to ducted propulsor design that the remainder of this thesis will concentrate. The design method adopted for this thesis will then be considered in detail, along with the modifications required to enable ducted propulsor flows to be modelled satisfactorily.

3.2 Summary of the Ducted Propulsor and Turbomachine Design Problems

3.2.1 The Internal Flow Turbomachine Design Problem

Although the term "internal flow turbomachine" embraces a wide range of bladed devices including turbines, compressors, pumps and certain types of gas turbines (Figure 3.1), the design problem for all these cases may be represented in schematic form by Figure 3.2.

When designing these types of machine one generally only has to consider flow restricted between hub and shroud endwalls of arbitrary geometry. As a result the mass flow rate is usually specified as an input to the design procedure in terms of a velocity profile. This velocity profile is taken sufficiently far upstream of the blading as to be assumed independent of the actual blade design.

The design procedure must take account of whether the working fluid is either compressible or incompressible, and also any heat addition to the fluid by combustion or some other process. In many instances there may be more than one blade row, in

which case the design is usually considered as a series of rotor-stator or contra-rotating blade "stages".

3.2.2 The Ducted Propulsor Design Problem

The ducted propulsor design problem may be represented in schematic form by Figure 3.3.

Here the working fluid is sea water, which, under normal conditions is incompressible. All power is transmitted to the water via the blading, there being no combustion process or other form of large scale heat addition to consider. On grounds of efficiency there are normally no more than two blade rows, although in the past there have been proposals for triple blade row stator-rotor-stator ducted propulsors [1].

As marine propulsors generally operate deep within the boundary layer of the parent vessel not only do severe radial variations in onset flow need to be accounted for, but also large-scale circumferential variations in velocity due to the non-axisymmetry of the parent hull and the presence of control surface wakes.

The action of the propulsor blading generally induces a considerable flow incidence at the duct leading edge. Allied to this there is a tendency for the propulsor slipstream to contract downstream of the duct trailing edge. As a consequence, the flow velocities within the duct and the corresponding propulsor mass flow cannot be adequately predicted before the design has been generated. Accurate design therefore entails the determination of propulsor mass flow in conjunction with the propulsor flow field. This can only be achieved by modelling both the propulsor through flow ("core" flow) and bypass flow from far upstream of the propulsor (where the flow is unmodified by the presence of the propulsor) to far downstream into the wake (where the propulsor slipstream is fully contracted). Further complications may be associated with the presence of such physical boundaries as the free surface and the seabed.

Due to the "jet" of water expelled from the propulsor there is a continuous sheet of vorticity shed from the duct trailing edge. Full account of this "duct wake" must be taken if satisfactory estimates of propulsor mass flow and slipstream trajectory are to be obtained.

Generally, the design aim is to maximise overall propulsor thrust (and hence propulsive efficiency) for some specified shaft power and flow condition. However,

compromises are necessary to ensure that satisfactory performance is achieved at off-design conditions. In particular, the avoidance of blade and duct cavitation is highly desirable under all operating conditions, as its occurrence not only reduces propulsive efficiency, but also greatly increases noise and vibration problems, and can cause both duct and blade erosion. Perhaps of even greater importance is the avoidance of flow separation on the duct and blading, as this can have a catastrophic effect on propulsor performance.

3.3 The Applicability of Internal Flow Turbomachine Methods to the Design of Ducted Propulsor Blading

From Sections 3.2.1 and 3.2.2 it can be seen that there are considerable differences between the internal flow turbomachine and ducted propulsor design problems.

Firstly, due to the absence of flow compressibility and heat addition for the case of the ducted propulsor, the ducted propulsor design problem is, in many ways, much simpler than that for many types of internal flow turbomachines.

However, for the ducted propulsor problem the flow is not restricted between hub and shroud endwalls. Instead the problem domain has to be extended to incorporate both the propulsor through flow and bypass flow for considerable distances upstream and downstream of the duct. Consequently, there is a solid body (the duct) contained within the problem domain, which, together with the duct vortex wake, requires special treatment.

Furthermore, propulsor mass flow cannot be specified as an input to the design process, but rather must be determined in conjunction with the propulsor blade shapes and flow field.

The circumferential and radial variations in onset flow encountered by the blading are generally much greater for ducted propulsors than for most types of turbomachine; some account of these shear effects must be taken if satisfactory propulsor performance is to be achieved.

Despite these substantial differences, there is one fundamental principal common to both ducted propulsors and other turbomachine types; namely one of energy transfer between a fluid and rotating blading in close proximity to solid surfaces. As a result

blade design methods for internal flow turbomachines such as those that are outlined in the next section are fundamentally suitable for application to ducted propulsor design. The differences highlighted in the preceding paragraphs are relatively superficial in comparison to the underlying similarity, and can be dealt with by the appropriate application of mathematical and computational techniques.

3.4 Existing Blade Design Methods for Internal Flow Turbomachinery: The Benefits of the Clebsch Approach

A substantial amount of research has be done on the computational inverse design of turbomachinery blading, most of which is based on inviscid flow theories. Whilst it would be inappropriate to consider this work in depth here, extensive reviews are given by Borges [2] and Zangeneh [3]. It is, however, interesting to briefly consider some of the alternative approaches to the turbomachine design problem.

Firstly it should be noted that many authors (for example Zangeneh [3], and Lewis [4]) classify design methods for turbomachinery blading as either "true" or "semi" inverse design methods. "Semi" inverse design methods differ from "true" inverse design methods in that they employ existing analysis methods in conjunction with systematic modifications of some initial blade shape to meet the design criteria. This classification is, however, somewhat confusing and will not be used in this thesis, as many "true" inverse design methods also solve for blade shape iteratively. The net result is the same regardless of whether a "true" or "semi" inverse design approach is used; namely the design of blading in accordance with some specified design point condition.

In any case, the following fundamental approaches to the computational design of turbomachinery blading seem to be most common:-

1) Specification of a Blade Velocity Distribution

One approach to the blade inverse design problem is to specify the velocity distribution on both the pressure and suction surfaces of the blade. Such a method for the design of two-dimensional cascades is presented by Murgusen and Railly [5] who used a surface vorticity representation of the blading (the so-called "Martensen" technique [4]). At first sight this technique is rather appealing, as by specifying the velocity distribution one is, in effect, also specifying the blade pressure distribution. As a consequence the designer is left

with considerable control over both blade forces and the occurrence of such undesirable flow phenomena as flow separation and cavitation. However, this approach to the blade inverse design problem is far from ideal. As the velocity distribution on both sides of the blade is specified, the method solves for both blade camber and thickness. Consequently, the resulting blade thickness distribution is not related to structural considerations. Furthermore, as viscous effects are not included in the design procedure, it is possible to perceive situations, such as those discussed by Lewis ([4], p.301), where a wholly unsatisfactory thickness distribution would be obtained, resulting in the occurrence of flow separation on the blading.

The two dimensional method of Thompkins and Tong [6] attempts to address these severe limitations. Here an initial estimate of blade camber and thickness is systematically modified to achieve a given blade pressure distribution with a time-marching Euler solver. The main advantage this particular method offers is that it is possible to apply constraints to the blade geometry; if a geometry satisfying both the constraints and the pressure distribution cannot be found, a solution satisfying the constraints and a relaxed pressure distribution is found instead. However, for cases where the pressure distribution is relaxed the resulting blade performance may well be unsatisfactory.

2) Specification of a Velocity Distribution on One Side of the Blade Together with Blade Thickness

An alternative approach to inverse design is to specify the velocity distribution on one side of the blade together with blade thickness and iteratively solve for blade shape. In these cases it is generally the velocity distribution on the suction side of the blade that is specified, as this provides the most effective means of avoiding flow separation, and, where relevant, cavitation. This type of method is typified by the classic two-dimensional blade design method of Wilkinson [7], where the blading is modelled using surface vorticity distributions. The principal disadvantage of this technique is that it is difficult to relate the specified suction surface velocity distribution to the blade pressure distribution and blade forces that are obtained as output. Considerable experience must therefore be required if a satisfactory design is to be obtained with a single design run; this must, to some extent, detract from the arguments in favour of using such an inverse design method.

3) **Specification of Blade Pressure Loading and Blade Thickness**

It is possible to determine blade shapes from a specified blade pressure loading (i.e. the difference in pressure between the blade pressure and suction surfaces) and blade thickness. Whilst such an approach enables the blade forces to be specified as an input to the design procedure, cavitation performance and the likelihood of flow separation can only be assessed from the output blade pressure and velocity distributions. This type of method, which does not seem to have been widely employed in the field of turbomachinery design, is typified by the two-dimensional design method of Novak and Haymann-Haber [8] where the tangential variations in flow quantities are represented by Taylor series expansions.

4) **Specification of a Blade Circulation Distribution**

A final approach to the inverse design problem is to determine blade shape from a specified blade circulation distribution. As blade circulation is not normally used as an indicator of blade performance it might perhaps be regarded as a poor choice of design parameter. However, it can be related to blade force using estimates of flow velocity at the blade, and in practice is found to give the designer excellent control over the performance of the synthesised design. Typical of this kind of approach is the two-dimensional design method of Betz and Flugge-Lotz [9], where the blade circulation distribution is specified directly. A more recent example is the two-dimensional technique of Hawthorne et al [10], where blade circulation is specified in terms of the blade-induced tangential velocity (see Appendix VIII); such an approach is ideally suited to twin blade row designs where the downstream blade row is specifically designed to eliminate swirl from the efflux.

It will be noted that all the methods outlined in [5]..[10] are two-dimensional design methods. The design of a complete blade using these methods is very similar in overall terms to the propulsor blade design technique outlined in Section 2.3.3, and involves division of the blade into a series of two-dimensional blade elements which are designed independently and then "stacked" on top of each other.

This design procedure can be implemented computationally to give a quasi three-dimensional design method. Such methods determine blade shapes by iterating between a two-dimensional blade design method and an axisymmetric throughflow analysis program. Typical of such quasi three-dimensional design methods is the

procedure presented by Jennions and Stow ([11], [12]) which enables both the design and analysis of turbomachine blading.

These two-dimensional and quasi three-dimensional design methods offer some potential for application to ducted propulsor design. However, it is the use of three-dimensional blade design methods, whereby a blade is designed as a single entity rather than as a "stack" of independently-designed blade elements, that offers most promise for ducted propulsor applications. In particular, a three-dimensional approach enables the entire blade geometry to be determined in conjunction with the surrounding flow field, with the development of circumferential variations of flow quantities within the blade passages being accounted for. The resulting blade shapes are therefore based on a minimum number of assumptions.

As was noted by Zangeneh [3], and Dang [13], it is the circulation-based approach outlined in 4) above that lends itself most readily to the three-dimensional design of blading, and indeed, most existing methods of this type (such as those given by Zhao et al [14], Ockurounmu and McCune [15], and Tan et al [16]) are circulation-based.

Of these three-dimensional blade design techniques, it was the method of Tan et al [16], based on the Clebsch representation of vorticity [17], that was chosen for the ducted propulsor design method presented in this thesis. This method is well established in the field of turbomachinery design, and as will be outlined in the next two Sections, many of the techniques required to extend the approach to ducted propulsor flows have already been developed.

3.5 Background on the Clebsch Approach to Blade Design

The fundamental feature of the ducted propulsor design method presented in this thesis is its use of the Clebsch representation of vorticity. As will be detailed in Chapter 4, this approach (presented by Lamb [17]) enables flow velocities to be formulated in terms of a potential function (which represents the irrotational component of the velocity field) and a series of physically-significant scalar flow quantities (which describe the rotational component of flow). Provided that a suitable Clebsch formulation can be found for a given flow problem (as was the case with the ducted propulsor problem considered in this thesis), the end result is that the equations of motion of the fluid reduce to a form in which they may be solved.

It is through the use of this approach that the ducted propulsor design method presented in this thesis can be traced back to the work of Hawthorne et al [10] who applied the Clebsch representation to the inverse design of two dimensional cascades. Here the flow was assumed to be inviscid and incompressible, with blade thickness being neglected. Series expansions were used to represent the development of circumferential variations of velocity within the blade passages, enabling blade shape to be determined iteratively from a prescribed mean tangential velocity distribution and conditions of zero incidence and no flow normal to the blade camber line. As stated by the authors, the key advantage of the Clebsch-based formulation over the more traditional Biot-Savart approach to the inverse design problem (typified by the method of Betz and Flugge-Lotz [9]) is that it can readily be extended to three-dimensional blade design problems.

The extension of the Clebsch technique to the three-dimensional design of annular cascades is presented by Tan et al [16]. Again, blade thickness, flow compressibility and viscous effects were neglected, with further assumptions of uniform onset flow and uniform blade loading being made. The flow velocity was split into circumferentially averaged and periodic components, the former being represented using Stokes stream function and the latter using a Clebsch formulation and series expansions. As with the two-dimensional method [10], blade shape was determined iteratively from the blade boundary condition together with a condition of ideal incidence. An "actuator duct" simplification of the method (as originally outlined by Hawthorne [18]) is also presented, whereby the cascade is assumed to consist of an infinite number of blades of finite chord.

The approach was later extended to include blade thickness, as outlined by Dang and McCune [19] who considered the design of two-dimensional cascades. To these ends a mean tangential blockage factor similar to that employed by Denton [20] was used.

Further work by Dang and McCune [21] applied the Clebsch approach to the three-dimensional inverse design of rectilinear cascades for cases of incompressible shear flow. Here a Clebsch formulation for vorticity and velocity was employed, this being similar in overall form to that used in this thesis (see equations 4.16 and 4.22). The pitch-averaged component of the flow field was again modelled using a stream function, whilst the periodic component was represented using "smoothing" functions (i.e. series expansions). Blade shapes were obtained iteratively for a specified mean tangential velocity distribution, although blade thickness was neglected. The results presented clearly show both the development of secondary flow patterns within the

blade passages and the corresponding Bernoulli surface distortions, as discussed in the theoretical work of Hawthorne [22] and Horlock and Lakshminarayana [23].

Borges [2], again neglecting blade thickness, extended the work of Tan et al [16] to the inverse design of turbomachines of arbitrary meridional geometry for cases of incompressible flow. In a departure from the previously adopted solution procedure, a finite difference representation of the governing equations was used together with co-ordinate transformation techniques, this being necessary to simplify the application of boundary conditions to the arbitrary geometry problem. As with the earlier methods an iterative solution procedure was adopted. In order to validate the method, performance comparisons were made between two turbines, one designed using the Clebsch-based approach and the other using an existing design technique. Experimental results showed the Clebsch method to yield notable improvements in performance over the existing design method.

A summary of the Clebsch-based inverse design method is presented by Hawthorne and Tan [24]. A range of possible applications of the method are briefly discussed. Of particular relevance to the work presented in this thesis is the extension of the method to deal with non-uniform blade loading, axisymmetrically sheared onset flow, and multiple-blade row designs.

The work of Borges was further extended to deal with cases of compressible flow by Zangeneh ([3], [25]). Two alternative approaches are presented, one taking full account of the development of circumferential variations in fluid density, the other being a simplified approach where the circumferential variations in density are neglected. In both instances blade thickness effects were included via a mean blockage factor similar to that used by Dang and McCune [19]. Computational results for a practical subsonic test case show the simplified approach to provide a very good approximation to the fully three-dimensional method with significantly reduced computational requirements. The computational verification of the method using Denton's three-dimensional inviscid Euler solver [26] is outlined, very good agreement with the predictions of the inverse design method being obtained.

Zangeneh [27] later coupled this design method with a three-dimensional Navier-Stokes solver developed by Dawes [28] to enable the design procedure to take some account of viscous effects. Again two alternative approaches are presented. One accounts for viscous effects through the introduction of an aerodynamic blockage distribution throughout the meridional geometry, whilst the other approach

introduces a vorticity term that is related to entropy gradients. Results indicate that the entropy gradient approach represents viscous effects fairly accurately.

Finally, the work of Dang and Wang [29] extends the actuator duct approach given by Tan et al [16] to deal with blade thickness, flow compressibility and axisymmetrically sheared onset flow, with viscous effects being modelled through the use of blockage and entropy-increase terms. Solution of the problem is via a finite volume technique. The resulting design method can deal with multiple blade row designs, computational results being presented for a low-pressure multi-stage centrifugal compressor.

Numerous techniques from all the above works were utilised in the ducted propulsor design method presented in Chapters 4 and 5. However, due to the arbitrary nature of ducted propulsor geometries and the insignificance of flow compressibility, it is the inverse design method of Borges [2] that, in overall terms, represents the starting point from which the ducted propulsor design method was developed. It should be further noted, however, that the detailed formulation of the ducted propulsor design method and many of the computational techniques employed were based on the work of Zangeneh ([3], [25]), but with flow compressibility neglected.

3.6 Extension of the Clebsch Approach to the Inverse Design of Marine Ducted Propulsor Blading

With reference to the differences between the ducted propulsor and turbomachine design problems highlighted in Section 3.3, the extension of the turbomachine design method of Borges [2] to the case of ducted propulsor design involved the following fundamental modifications:-

1) Modifications to Account for Non-Uniformities of Onset Flow

For the reasons stated in Section 4.2, it was not possible to include the effects of circumferential variations in onset flow in the ducted propulsor design method. However, the effects of axisymmetrically sheared onset flow and the associated development of circumferential variations of rothalpy within the blade passages were fully included in the design procedure. This was achieved using a Clebsch formulation for vorticity similar to that employed by Dang and McCune [21], although the solution procedure adopted was considerably

different from these authors (who only considered the design of rectilinear cascades).

2) Inclusion of the Effects of Non-Uniform Blade Loading

For cases of non-uniform blade loading[2] not only is it necessary to satisfy the zero loading (Kutta) condition at the blade trailing edge explicitly, but it is also necessary to account for the sheets of vorticity that are shed from the blade trailing edges. To achieve this, techniques similar to those used by Dang and McCune [21], and Hawthorne and Tan [24] were employed, whereby the blade wakes are treated as extensions of the blade with zero pressure loading.

3) Inclusion of a Second Blade Row

To enable twin blade row propulsors to be designed it was necessary to allow for the presence of a second blade row of arbitrary speed downstream of the first. This was achieved using a development of the techniques outlined very briefly by Hawthorne and Tan [24], whereby the flow downstream of the upstream blade row is based on time-averaged quantities, with additional modifications to account for the presence of shear flow.

4) Modifications to the Problem Domain

The problem domain as presented for the turbomachine design problem required considerable modification to enable both the propulsor through flow and bypass flow to be modelled from far upstream of the propulsor to far downstream into the wake. This involved the inclusion of solid wall boundary conditions within the problem domain to model both the duct surface and the duct vortex wake. It was also necessary to apply a boundary condition of negligible flow disturbance at a suitably large value of radius. Further modifications were required to allow for both finite duct thickness (see Section 5.6) and the discontinuity in flow quantities across the duct wake (Section 5.5).

5) Determination of Propulsor Mass Flow

In order for propulsor mass flow to be determined in conjunction with the propulsor flow field, it was necessary to devise a computational scheme whereby a condition of zero pressure jump (i.e. the Kutta condition) was applied iteratively at the duct trailing edge.

---

2 See the footnote at the bottom of page 32.

6) **Propulsor Slipstream Contraction**

Due to the jump in velocity across the duct vortex wake (Figure 3.3) it was found necessary to adopt the procedure outlined in Section 5.5 to account for propulsor slipstream contraction.

These modifications together with the formulation of the ducted propulsor design method will now be detailed in the coming Chapters.

References

1) Silverleaf,A. "Prospects for Unconventional Marine Propulsion Devices", 7th Symposium on Naval Hydrodynamics, Office of Naval Research, Arlington Va., USA, August 1968

2) Borges,J. "Three Dimensional Inverse Design of Turbomachinery", Ph.D. Thesis, Cambridge University Engineering Department, Cambridge, 1986

3) Zangeneh,M. "Three Dimensional Design of Radial-Inflow Turbines", Ph.D. Thesis, Cambridge University Engineering Department, Cambridge, 1988

4) Lewis,R.I. "Vortex Element Methods for Fluid Dynamic Analysis of Engineering Systems", Cambridge Engine Technology Series, Cambridge University Press, 1991

5) Murugesan,K., Railly,J.W. "Pure Design Method for Aerofoils in Cascade", pp454-470, J. Mech. Eng. Sci., Vol.11, No.5, 1969

6) Thompkins,W.T., Tong,S.S. "Inverse or Design Calculations for Nonpotential Flow in Turbomachinery Blade Passages", p82, ASME Journal of Engineering for Gas Turbines and Power, Vol.104, April 1982

7) Wilkinson,D.H. "A Numerical Solution of the Analysis and Design Problems for the Flow Past One or More Aerofoils", Aeronautical Research Council Reports and Memoranda (ARC R & M) No. 3545, London, April 1967

8) Novak,R.A., Haymann-Haber,G. "A Mixed-Flow Cascade Passage Design Procedure Based on a Power Series Expansion", p231, ASME Journal of Engineering for Gas Turbines and Power, Vol.105, April 1983

9) Betz,A., Flugge-Lotz,I. "Design of Centrifugal Impeller Blades", NACA TM-902, 1939

10) Hawthorne,W.R., Wang,C., Tan,C.S., McCune,J.E. "Theory of Blade Design for Large Deflections: Part I - Two-Dimensional Cascade", ASME Journal of Engineering for Gas Turbines and Power, Vol.106, April 1984

11) Jennions,I.K., Stow,P. "A Quasi-Three-Dimensional Turbomachinery Blade Design System: Part I - Throughflow Analysis", p301, ASME Journal of Engineering for Gas Turbines and Power, Vol.107, April 1985

12) Jennions,I.K., Stow,P. "A Quasi-Three-Dimensional Turbomachinery Blade Design System: Part II - Computerised System", p308, ASME Journal of Engineering for Gas Turbines and Power, Vol.107, April 1985

13) Dang,T.Q. "A Fully Three-Dimensional Inverse Method for Turbomachinery Blading in Transonic Flows", ASME Paper 92-GT-209, 1992

14) Zhao,X., Sun,C., Wu,C. "A Simple Method for Solving Three-Dimensional Inverse Problems of Turbomachine Flow and the Annular Constraint Condition", p293, ASME Journal of Engineering for Gas Turbines and Power, Vol.107, April 1985

15) Okurounmou,O., McCune,J.E. "Lifting Surface Theory of Axial Compressor Blade Rows: Part I - Subsonic Compressor", p1363, AIAA Journal, Vol.12, No.10, October 1974

16) Tan,C.S., Hawthorne,W.R., McCune,J.E., Wang,C. "Theory of Blade Design for Large Deflections: Part II - Annular Cascades", ASME Journal of Engineering for Gas Turbines and Power, Vol.106, April 1984

17) Lamb,H. "Hydrodynamics", p248, Sixth Edition, Cambridge University Press, 1932

18) Hawthorne,W.R. "The Actuator Duct Representation of Turbomachinery Blade Rows", CUED/A - Turbo/TR 119, Cambridge University Engineering Department, Cambridge, 1983

19) Dang,T.Q., McCune,J.E. "Design Method for Highly-Loaded Blades with Blockage in Cascade", presented at the Symposium on Computation of Internal Flows: Methods and Applications", New Orleans, 11-16th February, 1984

20) Denton,J.D. "Throughflow Calculations for Transonic Axial Flow Turbines", ASME Journal of Engineering for Power, Vol.100, April 1978

21) Dang,T.Q., McCune,J.E. "A Three-Dimensional Blade Design Method in Rotational Flow", Proc. Intl. Conference on Inverse Design Concepts in Engineering Sciences, University of Texas, Austin, USA, 1984

22) Hawthorne,W.R. "Rotational Flow Through Cascades. Part I : The Components of Vorticity", p266-279, Quart. Journ. of Mech. & Appl. Math., Vol.8, 1955

23) Horlock,J.H., Lakshminarayana,B. "Secondary Flows: Theory, Experiment, and Application in Turbomachinery Aerodynamics", Annual Review of Fluid Mechanics, Vol.5, 1973

24) Hawthorne,W.R., Tan,C.S. "Design of Turbomachinery Blading in 3D Flow by the Circulation Method: A Progress Report", International Conference On Inverse Design In Engineering Sciences (ICIDES), 1987

25) Zangeneh,M. "A Compressible Three-Dimensional Inverse Design Method for Radial and Mixed Flow Turbomachinery", International Journal of Numerical Methods in Fluids, Vol.13, pp599-624, 1991

26) Denton,J.D. "An Improved Time Marching Method for Turbomachinery Flow Calculations", ASME Journal of Engineering for Power, p514, Vol.105, No.3, 1983

27) Zangeneh,M. "Inviscid-Viscous Interaction Method for 3D Inverse Design of Centrifugal Impellers", ASME Paper 93-GT-103, ASME, 1993

28) Dawes,W.N. "Application of Full Navier-Stokes Solvers to Turbomachinery Flow Problems", VKI Lecture Series 2: Numerical Techniques for Viscous Flow Calculations in Turbomachinery Blading, 1986

29) Dang,T.Q., Wang,T. "Design of Multi-Stage Turbomachinery Blading by the Circulation Method: Actuator Duct Limit", ASME Paper 92-GT-286, 1992

30) Dixon,S.L. "Fluid Mechanics, Thermodynamics of Turbomachinery", p2, Third Edition, Pergamon Press, 1978

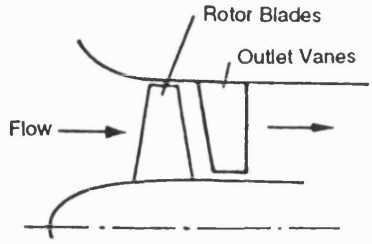

(a) Single Stage Axial Flow Compressor or Pump

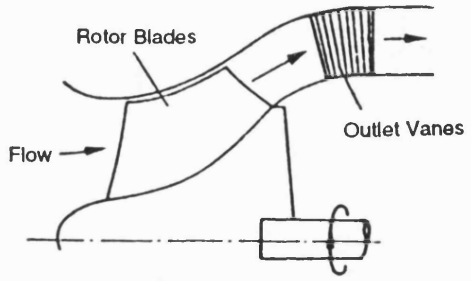

(b) Mixed Flow Pump

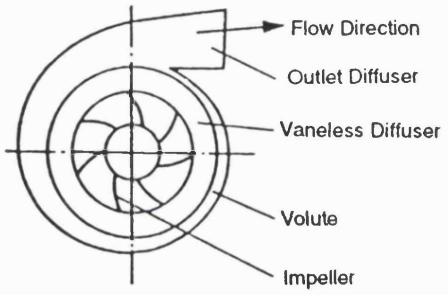

(c) Centrifugal Compressor or Pump

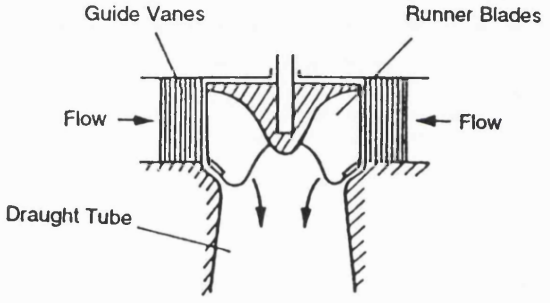

(d) Francis Turbine (Mixed Flow Type)

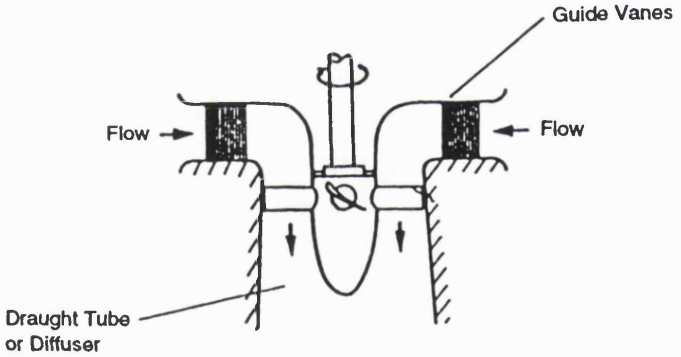

(e) Kaplan Turbine

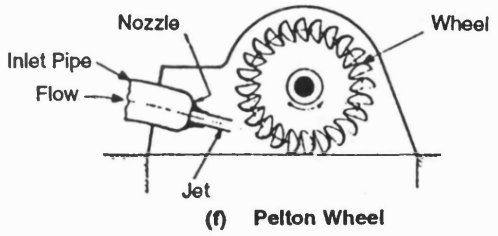

(f) Pelton Wheel

Figure 3.1: Diagrammatic Form of Various Types of Turbomachine (as Presented by Dixon [30])

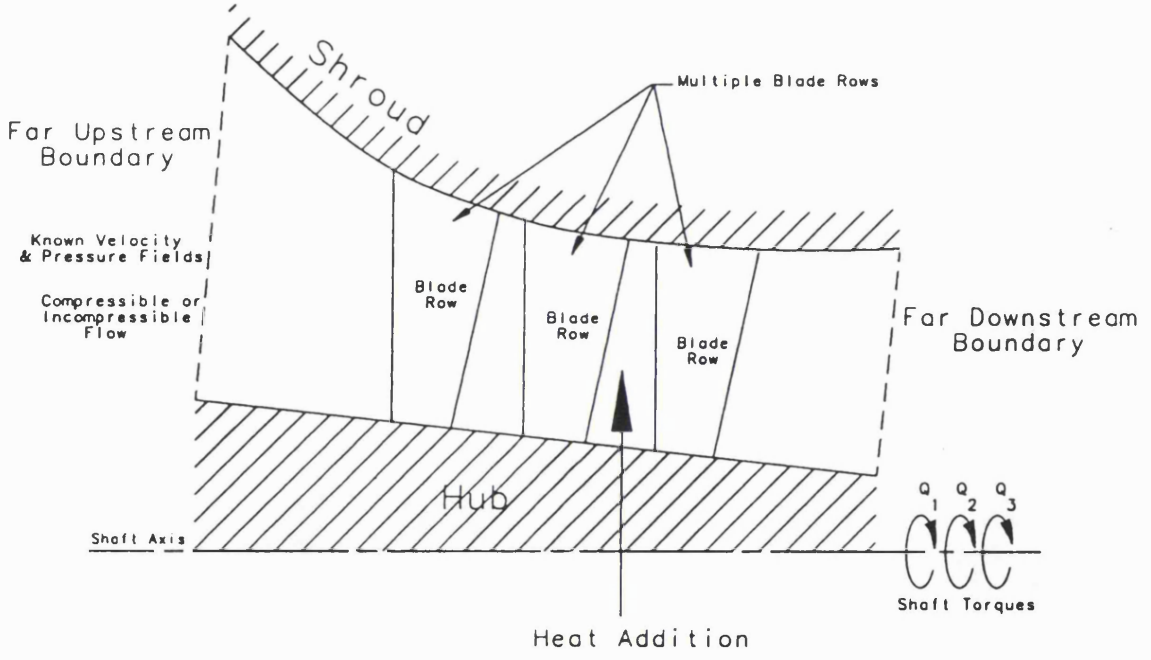

Figure 3.2: Schematic of the Internal Flow Turbomachine Design Problem

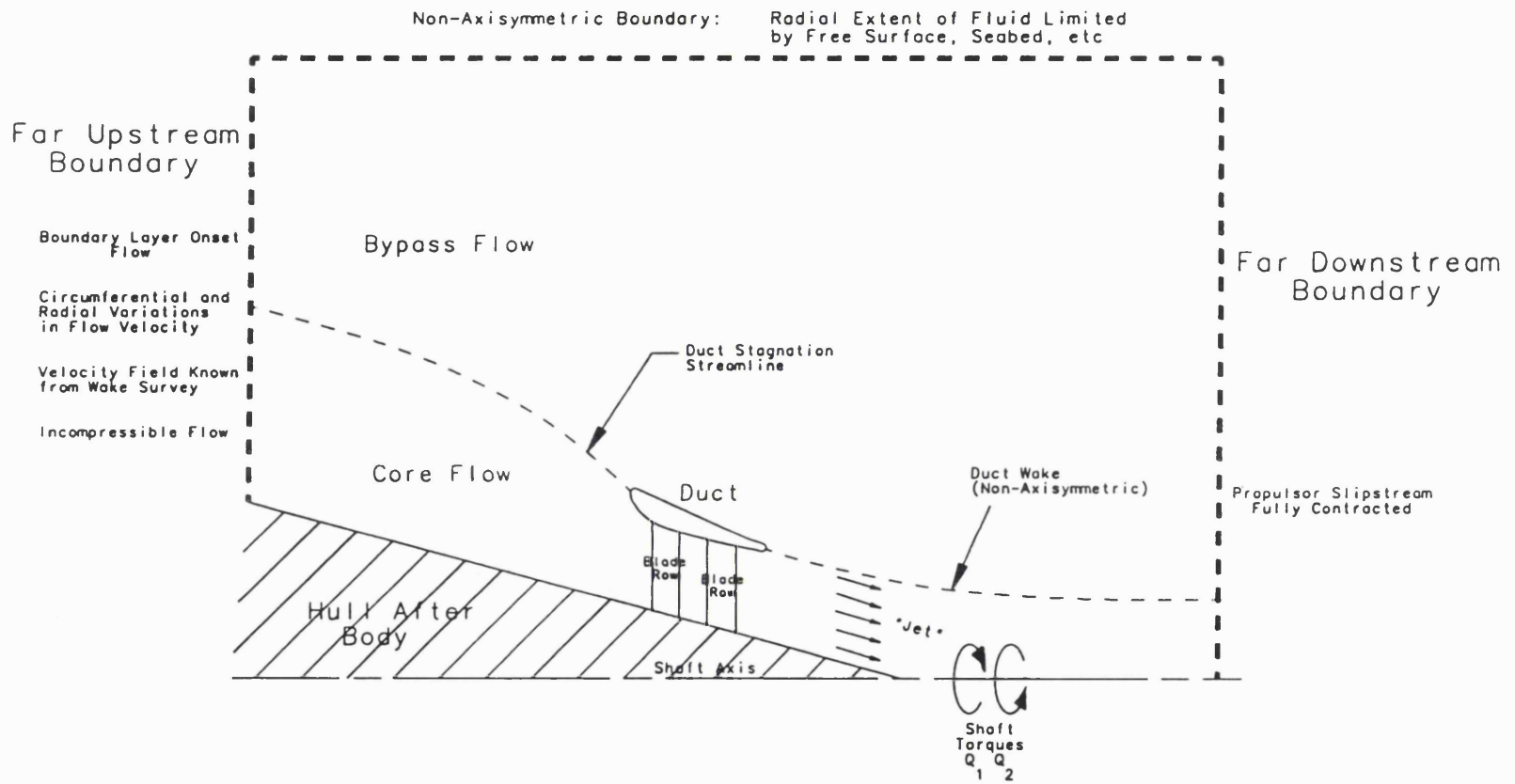

Figure 3.3: Schematic of the Ducted Propulsor Design Problem

CHAPTER 4 PROBLEM FORMULATION FOR THE INVERSE DESIGN METHOD

4.1 Introduction

This chapter will outline the algebraic formulation of the computational inverse design method for marine ducted propulsors that forms the basis of this thesis. This method offers a number of advantages over the existing techniques described in Chapter 2.

Firstly, the method can not only deal with axisymmetric sheared onset flow, but also allows for the development of a three-dimensional velocity field within the blade passages, and the corresponding three-dimensional shear effects. Employing assumptions of inviscid, incompressible flow and using the Clebsch representation of vorticity, both the propulsor through flow and bypass flow are described by partial differential equations in terms of Stokes stream function, a potential function and Clebsch variables. By modelling the region of flow from far upstream of the propulsor to far downstream into the wake the effects of slipstream contraction are fully included. The approach can deal with multiple-component designs such as rotor-stator and contra-rotating propulsors, as well as simpler single blade row designs, and the effects of non-uniform blade loading[1] and finite blade chord are fully included.

As an inverse design method, the required blade shapes are obtained directly as an output from the numerical procedure together with the complete propulsor flow field. From this output the blade pressure jumps, propulsor thrust and torque, and the duct pressure distribution can be calculated at the design point enabling the suitability of the synthesised design to be assessed. It is felt that such an approach is more appropriate to the early stages of design than some of the analysis methods listed in Chapter 2 which require blade shapes to be provided as input.

4.2 Underlying Assumptions of the Inverse Design Method

With reference to the simplified problem domain for the ducted propulsor shown in Figure 4.1, it is necessary to make the following assumptions regarding the propulsor and its associated flow field:-

---

[1] See the footnote at the bottom of page 32.

(a) **Inviscid flow**

Whilst undesirable, it is necessary to assume that the flow is inviscid in order to reduce the computational task to a manageable size.

(b) **Incompressible flow**

This is not perceived as a problem, as sea water largely satisfies this condition.

(c) **Axisymmetric Onset Flow**

In order to obtain a unique solution for blade shape, it is necessary to assume that the velocity profile on the far upstream boundary is axisymmetric.

(d) **Fluid of Infinite Extent**

Allied to the assumption of axisymmetric onset flow, it is necessary to assume that the fluid is of infinite extent, and therefore that the presence of such boundaries as the sea surface and the seabed may be neglected.

(e) **Negligible Tip Clearance**

The clearance between the blade tips and the duct is assumed to be small, in keeping with good design practice.

(f) **Axisymmetric Duct Wake**

For simplicity, the duct wake is assumed to be axisymmetric, its trajectory and the propulsor mass flow rate being determined from consideration of the mean (circumferential-average) flow quantities.

(g) **Cavitation Absent**

The occurrence of cavitation on the duct and blading is neglected. This is not deemed to be too great a limitation, as it is generally desirable to avoid cavitation at the design point on grounds of efficiency, and also to prevent blade and duct erosion.

It is further necessary to extrapolate the duct trailing edge to a sharp point in order to achieve satisfactory convergence of the propulsor mass flow.

4.3 Representation of Vorticity

The key feature of the entire method is that the flow vorticity is modelled using the Clebsch representation of vorticity (see Lamb [1]). This approach is already well established in the field of general turbomachine design, previous applications having

included the inverse design of cascades for cases of incompressible flow ([2], [3]), compressible flow [4] and shear flow [5] (see Section 3.5).

This transformation enables the vorticity to be written in the form

$$\Omega = \nabla\lambda \times \nabla\mu \qquad 4.1$$

where the intersection of the surfaces λ=constant and μ=constant define the vortex lines within the flow.

For a given vortex line there are generally an infinity of Clebsch variables that satisfy this relationship. However, for equation 4.1 to be valid throughout the flow domain, the Clebsch variables λ and μ must be chosen to be fully compatible with the equations of motion of the fluid. If this is the case it then follows (Appendix X) that

$$\mathbf{V} = \nabla\Phi + \lambda\nabla\mu \qquad 4.2$$

where Φ is a potential function representing the irrotational component of the velocity field, and the second term represents the rotational component.

4.4 Derivation of the Governing Equations

Adopting the cylindrical polar co-ordinate system shown in Figure 4.2, a relative velocity **W** may be defined relative to the blading, viz:-

$$\mathbf{W} = \mathbf{V} - \omega r\hat{\mathbf{e}}_\theta \qquad 4.3$$

Defining the blade surfaces by

$$\alpha = \theta - f(r,z) = \frac{2\pi m}{N_b} \;:\; m = 0,1,2,\ldots,N_b - 1 \qquad 4.4$$

the condition of no flow normal to the blade may then be expressed

$$\mathbf{W}_{bl} \cdot \nabla\alpha = 0 \qquad 4.5$$

Now, the Euler Equation maybe written [6]

$$\rho \mathbf{W} \times \Omega = \rho \nabla H + \rho F \nabla \alpha \qquad 4.6$$

where H is rothalpy and the term $\rho F \nabla \alpha$ represents the blade force on the fluid which must act normal to the blade on the blade surface.

Taking the tangential component of equation 4.6 at the blade surface, it can be seen that

$$V_{zbl}\frac{\partial V_z}{\partial \theta} + V_{rbl}\frac{\partial V_r}{\partial \theta} - V_{zbl}\frac{\partial r V_\theta}{dz} - V_{rbl}\frac{\partial r V_\theta}{\partial r} = \frac{\partial H}{\partial \theta} + F \qquad 4.7$$

Now, as it can be shown that

$$\overline{\left(V_{zbl}\frac{\partial V_z}{\partial \theta}\right)} = \overline{\left(V_{rbl}\frac{\partial V_r}{\partial \theta}\right)} = \overline{\frac{\partial H}{\partial \theta}} = 0$$

circumferentially averaging equation 4.7 over one blade pitch (i.e. over the range $0 \le \theta < 2\pi/N_b$) yields

$$\overline{F} = -\mathbf{W}_{bl} \cdot \nabla \overline{r V_\theta}$$

As the blade force is exerted at the blade surfaces, it follows that

$$F = \overline{F}\delta_p(\alpha) = -\left(\mathbf{W}_{bl} \cdot \nabla \overline{r V_\theta}\right)\delta_p(\alpha) \qquad 4.8$$

with equation 4.6 becoming

$$\mathbf{W} \times \Omega = \nabla H - \left(\mathbf{W}_{bl} \cdot \nabla \overline{r V_\theta}\right)\delta_p(\alpha)\nabla \alpha \qquad 4.9$$

where $\delta_p(\alpha)$ is the periodic delta function given in Appendix II.

Now, taking the dot product of equation 4.9 with $\mathbf{W}$ and applying condition 4.5 it follows that

$$\mathbf{W} \cdot \nabla H = 0 \qquad 4.10$$

The flow vorticity is now split into components as follows:-

$$\Omega = \Omega_b + \Omega_S \qquad 4.11$$

where Ω_b represents the blade bound/shed vorticity, and Ω_S is the additional component of vorticity associated with the presence of shear flow. Decomposing each component of vorticity as in equation 4.1, and noting that Ω_b is only non-zero on the blade/blade wake surface, equation 4.11 may be written

$$\Omega = (\nabla\lambda_b \times \nabla\mu_b)\delta_p(\alpha) + \nabla\lambda_s \times \nabla\mu_s \qquad 4.12$$

provided λ_b, λ_s, μ_b and μ_s are chosen from considerations of the equations of motion. Since the blade bound/shed vorticity must lie on the blade surfaces/wakes, it is immediately apparent that $\lambda_b = \alpha$ may be chosen. Additionally, setting $\lambda_s = H$, equation 4.9 may be written

$$\Omega = (\nabla\alpha \times \nabla\mu_b)\delta_p(\alpha) + \nabla H \times \nabla\mu_s \qquad 4.13$$

Substituting equation 4.13 into 4.9 and applying condition 4.10 now yields

$$F = (\mathbf{W}_{bl} \cdot \nabla\mu_b)\delta_p(\alpha) \qquad 4.14$$

$$\mathbf{W} \cdot \nabla\tau = 1 \qquad 4.15$$

where $\tau = \mu_s$

Comparing equation 4.14 with equation 4.8 it can be seen that

$$\mu_b = -\overline{rV_\theta}$$

Likewise from equation 4.15 it can be seen that τ is the "Drift Function" given by Hawthorne [7]. This quantity represents the time between fluid particles passing some reference plane and reaching the point of concern in the fluid, as can be seen by expressing equation 4.15 in the integral form

$$\tau = \int_0^s \frac{ds}{|\mathbf{W}|}$$

where s is distance along the particle path.

The full Clebsch representation of vorticity is therefore

$$\Omega = \left(\nabla \overline{rV_\theta} \times \nabla\alpha\right)\delta_p(\alpha) + \nabla H \times \nabla\tau \qquad 4.16$$

At this stage it should be stressed that swirl is assumed to be absent from the onset flow. As a result the first term on the right hand side of this equation is zero upstream of the blading and in the bypass flow.

Furthermore, it should be noted that equation 4.16 is almost identical to the Clebsch formulation used (without derivation) by Dang and McCune [5], the only difference being that they use a tangential velocity term relevant to the design of rectilinear cascades in place of $\overline{rV_\theta}$. Additionally, the first term on the right hand side of equation 4.16 is identical to the expression for vorticity derived by Borges [3] which has been widely applied to the design of turbomachinery blading in the absence of shear flow ([2], [3], [4]).

Now, whilst $\overline{rV_\theta}$ on the blading is specified as an input to the design process, $\overline{rV_\theta}$ downstream of the blading is determined by the condition that the blade wakes cannot sustain a pressure jump. Thus substituting F=0 into equation 4.8, $\overline{rV_\theta}$ downstream of the blading can be determined from

$$\mathbf{W}_{bl} \cdot \nabla \overline{rV_\theta} = 0 \qquad 4.17$$

the implication of this being that the trailing vortex lines lie along the wake streamlines.

At this stage it is convenient to split the velocity field into circumferential mean and periodic components along similar lines to Tan et al [2], viz

$$\mathbf{V} = \overline{\mathbf{V}} + \tilde{\mathbf{V}} \qquad 4.18$$

For computational convenience the velocity field $\overline{\mathbf{V}}$ is formulated in terms of Stokes stream function, ψ, as follows:-

$$\overline{V}_r = -\frac{1}{rB_t}\frac{\partial \psi}{\partial z} \qquad 4.19a$$

$$\overline{V}_z = +\frac{1}{rB_t}\frac{\partial \psi}{\partial r} \qquad 4.19b$$

where B_t is a mean tangential blockage function introduced to account for blade thickness:-

$$B_t = 1 - \frac{N_b T_t}{2\pi r}$$

T_t = tangential blade thickness

$$= T_n \sqrt{1 + r^2\left(\frac{\partial f}{\partial r}\right)^2 + r^2\left(\frac{\partial f}{\partial z}\right)^2}$$

T_n = blade thickness normal to mean camberline
(determined from structural considerations)

N_b = number of blades

This model for blade thickness, previously employed by Dang and McCune [8], and Zangeneh [9], represents the blade thickness as a circumferentially-distributed blockage. As a consequence blade thickness is only accounted for in the circumferential mean component of velocity.

Now, the periodic velocity field $\tilde{\mathbf{V}}$ is formulated in terms of a periodic potential function $\Phi(r,\theta,z)$, as follows. Firstly, using the fundamental definition of vorticity

$$\Omega = \nabla \times \mathbf{V} \qquad 4.20$$

it can be shown that

$$\overline{\Omega} = \nabla \times \overline{\mathbf{V}} \qquad 4.21a$$

$$\tilde{\Omega} = \nabla \times \tilde{\mathbf{V}} \qquad 4.21b$$

Therefore, from equations 4.21b and 4.16 it can be seen that one formulation for the periodic velocity field is

$$\tilde{\mathbf{V}} = \nabla\Phi - S(\alpha)\nabla\overline{rV_\theta} + \tilde{H}\nabla\tilde{\tau} - \tilde{\tau}\nabla(\overline{H}+\tilde{H}) + \overline{\tilde{\tau}\nabla\tilde{H}} \qquad 4.22^{2}$$

where $S(\alpha)$[3] is the sawtooth function defined in Appendix II, and $\Phi(r,\theta,z)$ is a purely periodic potential function representing the irrotational component of the flow field.

Now, since the mean velocity $\overline{\mathbf{V}}$ is represented using Stokes stream function and therefore automatically satisfies the condition

$$\nabla.\overline{\mathbf{V}} = 0 \qquad 4.23$$

the condition of Continuity reduces to

$$\nabla.\tilde{\mathbf{V}} = 0 \qquad 4.24$$

which when combined with of equation 4.22 gives

$$\begin{aligned}\nabla^2\Phi = {} & S(\alpha)\nabla^2\overline{rV_\theta} + \left(\nabla\overline{rV_\theta}.\nabla\alpha\right)S'(\alpha) - \tilde{H}\nabla^2\tilde{\tau} - \nabla\tilde{H}\cdot\nabla\tilde{\tau} \\ & + \tilde{\tau}\nabla^2\left(\overline{H}+\tilde{H}\right) + \nabla\tilde{\tau}\cdot\nabla\left(\overline{H}+\tilde{H}\right) - \overline{\tilde{\tau}\nabla^2\tilde{H}} + \overline{\nabla\tilde{\tau}\cdot\nabla\tilde{H}}\end{aligned} \qquad 4.25$$

The one remaining condition for the formulation to be valid is that the mean velocities as given in equations 4.19a,b must satisfy equation 4.21a. Since the radial and axial components of equation 4.21a are independent of Stokes Stream function, this condition may be stated as

$$\left(\nabla\times\overline{\mathbf{V}}\right)\cdot\hat{\mathbf{e}}_\theta = \left[\nabla\overline{rV}_\theta\times\nabla\alpha + \overline{\nabla H\times\nabla\tau}\right]\cdot\hat{\mathbf{e}}_\theta \qquad 4.26$$

At this stage it is convenient to introduce the Discrete Fourier Transform (DFT) to represent the tangential variations in the flow quantities (see Appendix I). This approach, previously used by Borges [3] and Zangeneh [4], allows the equations to

---

2 Equation 4.22 can easily be proved, since taking the curl of both sides yields equation 4.16, as required

3 It can be shown (see Appendix II) that $S'(\alpha) = \delta_p(\alpha) - 1$

be solved on a two-dimensional meridional mesh and thus offers a number of benefits in terms of computational speed and efficiency.

So, representing H, τ and Φ by Inverse Discrete Fourier Transforms (IDFTs):-

$$\Phi(r,\theta,z) = \sum_{\substack{n=-N/2 \\ n\neq 0}}^{N/2-1} \Phi^n(r,z) e^{i2\pi k n/N} \qquad 4.27$$

$$H(r,\theta,z) = \sum_{n=-N/2}^{N/2-1} H^n(r,z) e^{i2\pi k n/N} \qquad 4.28$$

$$\tau(r,\theta,z) = \sum_{n=-N/2}^{N/2-1} \tau^n(r,z) e^{i2\pi k n/N} \qquad 4.29$$

It will be noted that as the flow in the tangential direction is of period equal to the blade pitch,

$$\theta = \frac{2\pi k}{NN_b} \quad : k = 1,2,\ldots,N \qquad 4.30$$

Additionally, the sawtooth function $S(\alpha)$ and its first derivative $S'(\alpha)$ may be written (Appendix II)

$$S(\alpha) = \sum_{\substack{n=-N/2 \\ n\neq 0}}^{N/2-1} \frac{-i}{nN_b} e^{iN_b n\alpha} \qquad 4.31$$

$$S'(\alpha) = \sum_{\substack{n=-N/2 \\ n\neq 0}}^{N/2-1} e^{iN_b n\alpha} \qquad 4.32$$

Substituting equations 4.27..4.32 into equation 4.22, utilising equations 4.18, 4.19a,b and 4.30, and using the Frequency Convolution Theorem (Appendix I), it will be seen that the formulation for the velocities on the blade (where $S(\alpha)=0$ *and* $\theta=f(r,z)$) are

$$V_{rbl} = -\frac{1}{rB_t}\frac{\partial\psi}{\partial z} + \sum_{\substack{n=-N/2\\ n\neq 0}}^{N/2-1}\left(\frac{\partial\Phi^n}{\partial r} + H^n\frac{\partial\tau^0}{\partial r} - \sum_{\substack{p=-N/2\\ q\neq 0}}^{N/2-1}\tau^q\frac{\partial H^p}{\partial r}\right)e^{iN_b n\theta} \qquad 4.33a$$

$$V_{\theta bl} = \frac{\overline{rV_\theta}}{r} + \sum_{\substack{n=-N/2\\ n\neq 0}}^{N/2-1}\left(n\Phi^n - \sum_{\substack{p=-N/2\\ q\neq 0}}^{N/2-1}pH^p\tau^q\right)\frac{iN_b e^{iN_b n\theta}}{r} \qquad 4.33b$$

$$V_{zbl} = +\frac{1}{rB_t}\frac{\partial\psi}{\partial r} + \sum_{\substack{n=-N/2\\ n\neq 0}}^{N/2-1}\left(\frac{\partial\Phi^n}{\partial z} + H^n\frac{\partial\tau^0}{\partial z} - \sum_{\substack{p=-N/2\\ q\neq 0}}^{N/2-1}\tau^q\frac{\partial H^p}{\partial z}\right)e^{iN_b n\theta} \qquad 4.33c$$

where

$$q = \begin{cases}(n-p+N): & (n-p) < -N/2\\ (n-p-N): & (n-p) > N/2-1\\ (n-p) & : \ -N/2 \le (n-p) \le N/2-1\end{cases} \qquad 4.34$$

Likewise, applying IDFTs to equations 4.25, the condition of continuity becomes

$$\sum_{\substack{n=-N/2\\ n\neq 0}}^{N/2-1}\left(\frac{\partial^2\Phi^n}{\partial r^2} + \frac{\partial^2\Phi^n}{\partial z^2} + \frac{1}{r}\frac{\partial\Phi^n}{\partial r} - \frac{N_b^2 n^2}{r^2}\Phi^n\right)e^{i2\pi k n/N}$$

$$=$$

$$\sum_{\substack{n=-N/2 \\ n\neq 0}}^{N/2} \left[\begin{array}{l} -\left(\frac{\partial^2 \overline{rV_\theta}}{\partial r^2} + \frac{1}{r}\frac{\partial \overline{rV_\theta}}{\partial r} + \frac{\partial^2 \overline{rV_\theta}}{\partial z^2}\right)\frac{ie^{-iN_b nf}}{nN_b} \\ \quad -\left(\frac{\partial \overline{rV_\theta}}{\partial r}\frac{df}{dr} + \frac{\partial \overline{rV_\theta}}{\partial z}\frac{\partial f}{\partial z}\right)e^{-inN_b f} \\ \quad -\left(\frac{\partial^2 \tau^0}{\partial r^2} + \frac{1\partial \tau^0}{r\partial r} + \frac{\partial^2 \tau^0}{\partial z^2}\right)H^n \\ \quad -\left(\frac{\partial H^n}{\partial r}\frac{\partial \tau^0}{\partial r} + \frac{\partial H^n}{\partial z}\frac{\partial \tau^0}{\partial z}\right) \\ \quad + \sum_{\substack{p=-N/2 \\ q\neq 0}}^{N/2-1}\left(\frac{\partial^2 H^p}{\partial r^2} + \frac{1\partial H^p}{r\partial r} + \frac{\partial^2 H^p}{\partial z^2} - \frac{N_b^2 p^2 H^p}{r^2}\right)\tau^q \\ \quad + \sum_{\substack{p=-N/2 \\ q\neq 0}}^{N/2-1}\left(\frac{\partial H^p}{\partial r}\frac{\partial \tau^q}{\partial r} + \frac{\partial H^p}{\partial z}\frac{\partial \tau^q}{\partial z} - \frac{pqN_b^2 H^p \tau^q}{r^2}\right) \end{array} \right] e^{\frac{i2\pi kn}{N}}$$

where q is as defined in equation 4.34.

By inspection, the only way this relationship can hold is if the $n^{\underline{th}}$ component of the LHS corresponds directly to the $n^{\underline{th}}$ component of the RHS. Hence, dropping the summation,

$$\left(\frac{\partial^2 \Phi^n}{\partial r^2} + \frac{\partial^2 \Phi^n}{\partial z^2} + \frac{1}{r}\frac{\partial \Phi^n}{\partial r} - \frac{N_b^2 n^2}{r^2}\Phi^n\right) \qquad 4.35$$

$$=$$

$$-\left(\frac{\partial^2 \overline{rV_\theta}}{\partial r^2} + \frac{1}{r}\frac{\partial \overline{rV_\theta}}{\partial r} + \frac{\partial^2 \overline{rV_\theta}}{\partial z^2}\right)\frac{ie^{-iN_b nf}}{nN_b} - \left(\frac{\partial \overline{rV_\theta}}{\partial r}\frac{df}{dr} + \frac{\partial \overline{rV_\theta}}{\partial z}\frac{\partial f}{\partial z}\right)e^{-inN_b f}$$

$$-\left(\frac{\partial^2 \tau^0}{\partial r^2} + \frac{1\partial \tau^0}{r\partial r} + \frac{\partial^2 \tau^0}{\partial z^2}\right)H^n - \left(\frac{\partial H^n}{\partial r}\frac{\partial \tau^0}{\partial r} + \frac{\partial H^n}{\partial z}\frac{\partial \tau^0}{\partial z}\right)$$

$$+ \sum_{\substack{p=-N/2 \\ q\neq 0}}^{N/2-1}\left(\frac{\partial^2 H^p}{\partial r^2} + \frac{1\partial H^p}{r\partial r} + \frac{\partial^2 H^p}{\partial z^2} - \frac{N_b^2 p^2 H^p}{r^2}\right)\tau^q$$

$$+ \sum_{\substack{p=-N/2 \\ q\neq 0}}^{N/2-1}\left(\frac{\partial H^p}{\partial r}\frac{\partial \tau^q}{\partial r} + \frac{\partial H^p}{\partial z}\frac{\partial \tau^q}{\partial z} - \frac{pqN_b^2 H^p \tau^q}{r^2}\right)$$

where $n \neq 0$ and q is as defined in equation 4.34.

By applying Stokes stream function, IDFTs and the Frequency Convolution Theorem, equation 4.26 reduces to

$$-\frac{1}{rB_t}\frac{\partial^2\psi}{\partial z^2} - \frac{1}{r}\frac{\partial(1/B_t)}{\partial z}\frac{\partial\psi}{\partial z} - \frac{1}{rB_t}\frac{\partial^2\psi}{\partial r^2} - \frac{1}{r}\frac{\partial(1/B_t)}{\partial r}\frac{\partial\psi}{\partial r} + \frac{1}{r^2B_t}\frac{\partial\psi}{\partial r} = \frac{\partial\overline{rV_\theta}}{\partial r}\frac{\partial f}{\partial z} - \frac{\partial\overline{rV_\theta}}{\partial z}\frac{\partial f}{\partial r} + \sum_{p=-N/2}^{N/2-1}\left(\frac{\partial H^p}{\partial z}\frac{\partial\tau^{-p}}{\partial r} - \frac{\partial H^p}{\partial r}\frac{\partial\tau^{-p}}{\partial z}\right) \quad 4.36$$

with equations 4.5 and 4.17 expanding as

$$V_{rbl}\frac{\partial f}{\partial r} + V_{zbl}\frac{\partial f}{\partial z} = \frac{1}{r}\left[V_{\theta bl} - \omega r\right] \quad 4.37$$

$$V_{rbl}\frac{\partial\overline{rV_\theta}}{\partial r} + V_{zbl}\frac{\partial\overline{rV_\theta}}{\partial z} = 0 \quad 4.38$$

It can be seen that equations 4.35 and 4.36 are similar to expressions presented by Zangeneh [4] for compressible flow, but with additional terms included to account for the presence of shear, and some simplification due to the absence of flow compressibility.

Now, representing the fully three-dimensional relative velocity field using IDFTs

$$\mathbf{W}(r,\theta,z) = \sum_{n=-N/2}^{N/2-1}\left(W_r^n\hat{\mathbf{e}}_r + W_\theta^n\hat{\mathbf{e}}_\theta + W_z^n\hat{\mathbf{e}}_z\right)e^{i2\pi k n/N} \quad 4.39$$

it can be seen from equations 4.3, 4.18, 4.19a, b, and 4.34 that

$$W_r^n = \left(\frac{\partial\Phi^n}{\partial r} + \frac{ie^{-iN_b n f}}{nN_b}\frac{\partial\overline{rV_\theta}}{\partial r} + H^n\frac{\partial\tau^0}{\partial r} + \sum_{\substack{p=N/2\\ q\neq 0}}^{N/2-1}\tau^q\frac{\partial H^p}{\partial r}\right) \quad : n \neq 0 \quad 4.40a$$

$$W_r^n = -\frac{1}{rB_t}\frac{\partial \psi}{\partial z} \quad : n = 0$$

$$W_\theta^n = \frac{iN_b n \Phi^n}{r} - \sum_{\substack{p=-N/2 \\ q\neq 0}}^{N/2-1} \frac{iN_b p H^p \tau^q}{r} \quad : n \neq 0$$

4.40b

$$W_\theta^n = \frac{\overline{rV_\theta}}{r} - \omega r \quad : n = 0$$

$$W_z^n = \left(\frac{\partial \Phi^n}{\partial z} + \frac{ie^{-iN_b nf}}{nN_b}\frac{\partial \overline{rV_\theta}}{\partial z} + H^n \frac{\partial \tau^0}{\partial z} + \sum_{\substack{p=N/2 \\ q\neq 0}}^{N/2-1} \tau^q \frac{\partial H^p}{\partial z} \right) \quad : n \neq 0$$

4.40c

$$W_z^n = +\frac{1}{rB_t}\frac{\partial \psi}{\partial r} \quad : n = 0$$

Using the Frequency Convolution Theorem and equations 4.28, 4.29 and 4.34 therefore enables equations 4.10 and 4.15 to be rewritten

$$\sum_{n=-N/2}^{N/2-1} \sum_{p=-N/2}^{N/2-1} W_r^q \frac{\partial H^p}{\partial r} + \frac{iN_b p W_\theta^q}{r} H^p + W_z^q \frac{\partial H^p}{\partial z} = 0$$

$$\sum_{n=-N/2}^{N/2-1} \sum_{p=-N/2}^{N/2-1} W_r^q \frac{\partial \tau^p}{\partial r} + \frac{iN_b p W_\theta^q}{r} \tau^p + W_z^q \frac{\partial \tau^p}{\partial z} = 1$$

Since in each instance the right hand side of each equation does not vary circumferentially, it follows that

$$\sum_{p=-N/2}^{N/2-1} W_r^q \frac{\partial H^p}{\partial r} + \frac{iN_b p W_\theta^q}{r} H^p + W_z^q \frac{\partial H^p}{\partial z} = 0 \qquad 4.41$$

$$\sum_{p=-N/2}^{N/2-1} W_r^q \frac{\partial \tau^p}{\partial r} + \frac{iN_b p W_\theta^q}{r} \tau^p + W_z^q \frac{\partial \tau^p}{\partial z} = \begin{cases} 1 & : n = 0 \\ 0 & : n \neq 0 \end{cases} \qquad 4.42$$

where $-N/2 < n < N/2-1$.

4.5 Determination of Propulsor Mass Flow and Relocating the Duct Wake

The mass flow through the propulsor and the corresponding duct circulation must be such that the Kutta condition is satisfied at the duct trailing edge. This is essentially a requirement that the duct trailing edge cannot sustain a pressure jump, and is formulated as follows.

Firstly, for simplicity it is necessary to base this condition on circumferentially-averaged flow quantities. Such an approach still allows for circumferential variations in duct circulation, yet failure to do so would result in a non-cylindrical duct wake which would hugely increase the computational requirements.

Thus, applying the Bernoulli Streamline Theorem to the core and bypass flows at the duct trailing edge

$$\overline{H}_b = \frac{\overline{P}_b}{\rho} + \frac{\overline{V}_{r_b}^2 + \overline{V}_{z_b}^2}{2}$$

and

$$\overline{H}_c = \frac{\overline{P}_c}{\rho} + \frac{\overline{V}_{r_c}^2 + \overline{V}_{z_c}^2 + \overline{V}_{\theta_c}^2}{2} - \omega\left(\overline{rV_\theta}\right)_c$$

where subscripts b and c refer to the bypass and core flows respectively.

For the case of a single blade row, $\overline{H}_b = \overline{H}_c$ at the duct trailing edge, and the Kutta condition requires that $\overline{P}_b = \overline{P}_c$, giving

$$\overline{V_{rc}^2} + \overline{V_{zc}^2} - \overline{V_{rb}^2} - \overline{V_{zb}^2} = 2\omega\overline{rV_{\theta c}} - \left(\overline{V}_\theta\right)_c^2$$

which using the equations 4.19(a), (b) may be re-written

$$\left(\frac{\partial\psi}{\partial z}\right)_c^2 + \left(\frac{\partial\psi}{\partial r}\right)_c^2 - \left(\frac{\partial\psi}{\partial z}\right)_b^2 - \left(\frac{\partial\psi}{\partial r}\right)_b^2 = r^2\left(2\omega(\overline{rV_\theta})_c - (\overline{V_\theta})_c^2\right) \qquad 4.43$$

This equation is used to determine the value of ψ on the duct (i.e. propulsor mass flow).

Now, for the general case of finite blade tip loading there is a discontinuity in both meridional and tangential flow velocity along the length of the duct wake (the interface between the duct through flow and bypass flow, as shown in Figure 4.1). This prevents the value of stream function here being updated using equation 4.36, since the mean vorticity (and thus the right hand side of equation 4.36) tend to infinity here. This problem is dealt with by applying a condition of zero pressure jump, identical to equation 4.43, along this discontinuity, the justification being that a streamline (i.e. the duct wake) cannot sustain a finite pressure jump.

4.6 Summary

It can be seen here that the ducted propulsor inverse design problem has reduced to a series of seven simultaneous non-linear partial differential equations, which can be solved for the unknown flow variables as follows:-

Unknown Quantity	Equation No.
Stokes Stream Function ψ	4.43 on Duct and Duct Wake
	4.36 Elsewhere
3-D Potential Function Φ	4.35
3-D Rothalpy H	4.41
3-D Drift Function τ	4.42
Blade Shape f	4.37
Mean Swirl $\overline{rV_\theta}$	4.38

References

1) Lamb,H. "Hydrodynamics", p248, Sixth Edition, Cambridge University Press, 1932

2) Tan,C.S., Hawthorne,W.R., McCune,J.E., Wang,C. "Theory of Blade Design for Large Deflections: Part II - Annular Cascades", ASME Journal of Engineering for Gas Turbines and Power, Vol. 106, April 1984

3) Borges,J. "Three Dimensional Inverse Design of Turbomachinery", Ph.D. Thesis, Cambridge University Engineering Department, Cambridge, 1986

4) Zangeneh,M. "A Compressible Three-Dimensional Inverse Design Method for Radial and Mixed Flow Turbomachinery", International Journal of Numerical Methods in Fluids, Vol. 13, pp599-624, 1991

5) Dang,T.Q., McCune,J.E. "A Three-Dimensional Blade Design Method in Rotational Flow", Proc. Intl. Conference on Inverse Design Concepts in Engineering Sciences, University of Texas, Austin, USA, 1984

6) Vavra,M.H. "Aero-thermodynamics and Flow in Turbomachines", Wiley, 1960

7) Hawthorne,W.R. "The Actuator Duct Representation of Turbomachinery Blade Rows", CUED/A - Turbo/TR 119, Cambridge University Engineering Department, Cambridge, 1983

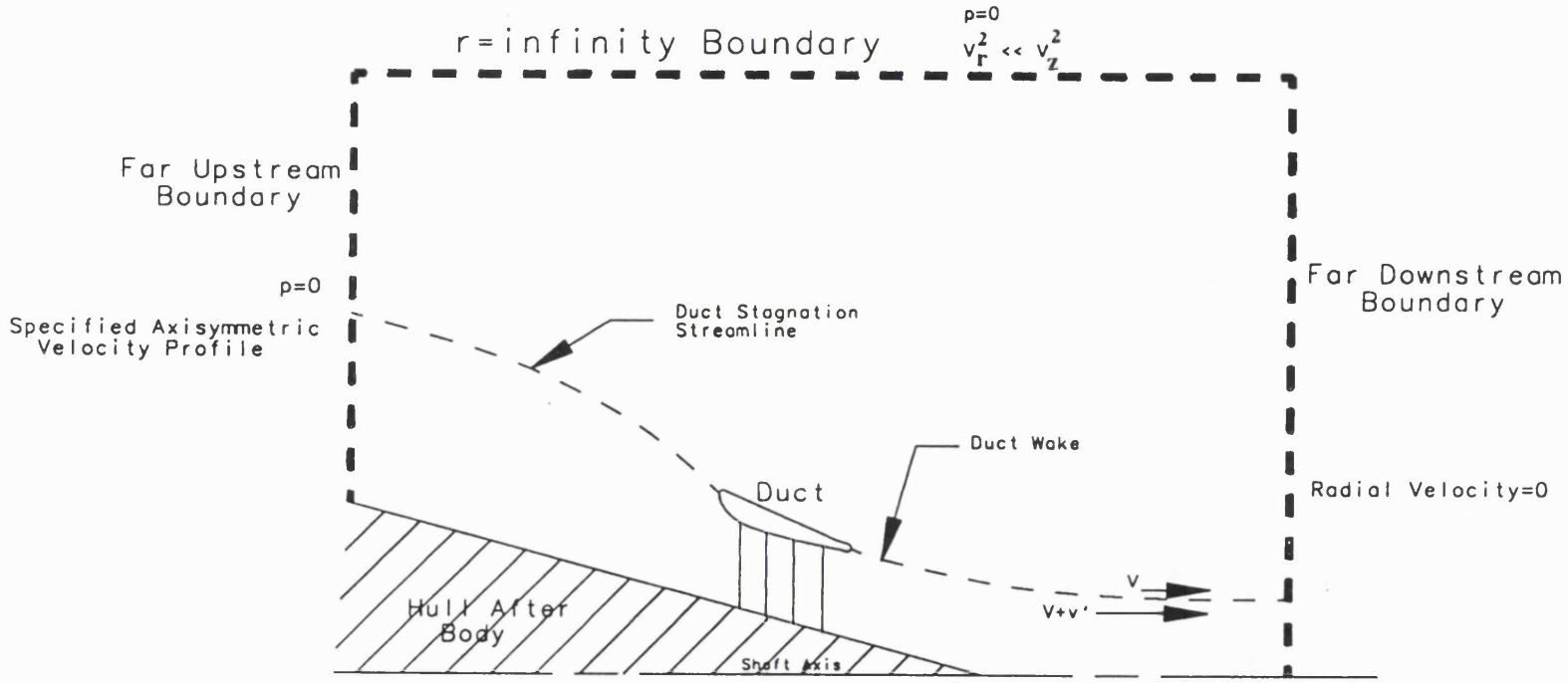

Figure 4.1: Simplified Problem Domain for the Ducted Propulsor Design Problem

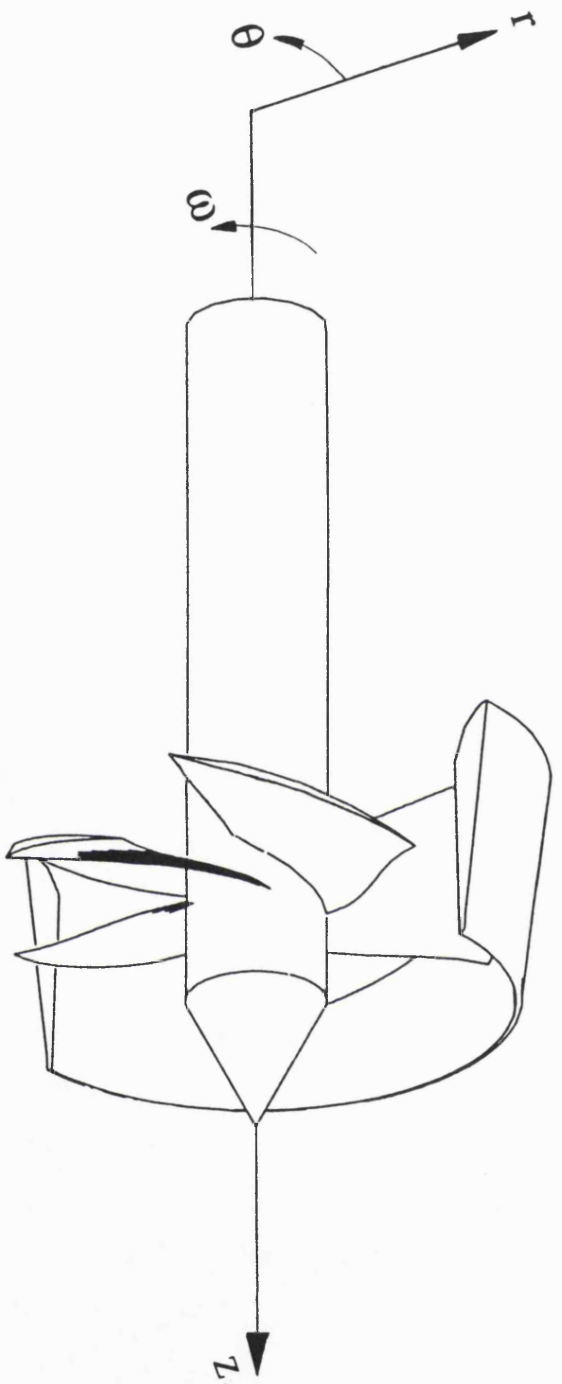

Figure 4.2: The Adopted Cylindrical Polar Coordinate System

CHAPTER 5 NUMERICAL SOLUTION OF THE GOVERNING EQUATIONS

5.1 Equation Transformation

The governing equations of the inverse design problem, as given in Chapter 4, are solved at each point on a meridional mesh of quasi-streamlines and quasi-orthogonals, typical meshes being shown in Figures 6.4 and 6.18 (note that solid boundaries such as the hub and duct always lie along quasi-streamlines).

To ease the solution process, with particular reference to the application of boundary conditions, this mesh is mapped onto a rectangular "computational" mesh using co-ordinate transform techniques ([1], [2]). This is achieved in a manner similar to that employed in the blade design method of Borges [3], and proceeds as follows.

Firstly, a body-fitted co-ordinate system (ξ,θ,η) is chosen according to the transformation

$$(r,\theta,z) \rightarrow (\xi,\theta,\eta)$$

such that the lines η=constant and ξ=constant lie along the quasi-streamlines and quasi-orthogonals of the meridional mesh respectively (see Figure 6.4). Defining the transformation parameters by

$$J = z_\xi r_\eta - z_\eta r_\xi \tag{5.1}$$

$$\alpha = z_\eta^2 + r_\eta^2 \tag{5.2}$$

$$\beta = z_\xi z_\eta + r_\xi r_\eta \tag{5.3}$$

$$\gamma = z_\xi^2 + r_\xi^2 \tag{5.4}$$

$$DR = \alpha r_{\xi\xi} - 2\beta r_{\xi\eta} + \gamma r_{\eta\eta} \tag{5.5}$$

$$DZ = \alpha z_{\xi\xi} - 2\beta z_{\xi\eta} + \gamma z_{\eta\eta} \tag{5.6}$$

$$T = \left(z_\eta DR - r_\eta DZ\right)/J \tag{5.7}$$

$$\Sigma = \left(r_\xi DZ - z_\xi DR\right)/J \tag{5.8}$$

which are identical to those used by Borges [3], it can be shown that for *any* variable f (r,z)

$$\frac{\partial f}{\partial z} = \left(r_\eta f_\xi - r_\xi f_\eta\right)/J \qquad 5.9$$

$$\frac{\partial f}{\partial r} = \left(z_\xi f_\eta - z_\eta f_\xi\right)/J \qquad 5.10$$

$$\frac{\partial^2 f}{\partial z^2} + \frac{\partial^2 f}{\partial r^2} = \left(\alpha f_{\xi\xi} - 2\beta f_{\xi\eta} + \gamma f_{\eta\eta} + \mathrm{T} f_\xi + \Sigma f_\eta\right)/J^2 \qquad 5.11$$

and also that

$$\hat{\mathbf{e}}^t_\xi = -\left(r_\eta \hat{\mathbf{e}}_r + z_\eta \hat{\mathbf{e}}_z\right)/\sqrt{\alpha} \qquad 5.12$$

$$\hat{\mathbf{e}}^t_\eta = \left(r_\xi \hat{\mathbf{e}}_r + z_\xi \hat{\mathbf{e}}_z\right)/\sqrt{\gamma} \qquad 5.13$$

$$\hat{\mathbf{e}}^n_\xi = \left(-z_\eta \hat{\mathbf{e}}_r + r_\eta \hat{\mathbf{e}}_z\right)/\sqrt{\alpha} \qquad 5.14$$

$$\hat{\mathbf{e}}^n_\eta = \left(z_\xi \hat{\mathbf{e}}_r - r_\xi \hat{\mathbf{e}}_z\right)/\sqrt{\gamma} \qquad 5.15$$

$$\hat{\mathbf{e}}_r = \left(r_\xi \sqrt{\alpha}\, \hat{\mathbf{e}}^n_\xi + r_\eta \sqrt{\gamma}\, \hat{\mathbf{e}}^n_\eta\right)/J \qquad 5.16$$

$$\hat{\mathbf{e}}_z = \left(z_\xi \sqrt{\alpha}\, \hat{\mathbf{e}}^n_\xi + z_\eta \sqrt{\gamma}\, \hat{\mathbf{e}}^n_\eta\right)/J \qquad 5.17$$

where $\hat{\mathbf{e}}^t_\xi$ and $\hat{\mathbf{e}}^t_\eta$ are unit tangent vectors to ξ=constant and η=constant respectively, and $\hat{\mathbf{e}}^n_\xi$ and $\hat{\mathbf{e}}^n_\eta$ are the corresponding unit normals.

Applying these relationships to equations 4.40a..c yields

$$\mathbf{W}^n \cdot \hat{\mathbf{e}}^n_\eta = \frac{1}{J\sqrt{\gamma}} \left(\begin{array}{l} \gamma \Phi^n_\eta - \beta \Phi^n_\xi \\ + \dfrac{ie^{-in N_b f}}{n N_b} \left(\gamma (\overline{rV_\theta})_\eta - \beta (\overline{rV_\theta})_\xi \right) \\ + H^n \left(\gamma \tau^0_\eta - \beta \tau^0_\xi \right) \\ - \displaystyle\sum_{\substack{p=-N/2 \\ q \neq 0}}^{N/2-1} \tau^q \left(\gamma H^p_\eta - \beta H^p_\xi \right) \end{array} \right) \quad : n \neq 0 \qquad 5.18a$$

$$\mathbf{W}^n \cdot \hat{\mathbf{e}}^n_\eta = \frac{-\Psi_\xi}{r B_t \sqrt{\gamma}} \quad : n = 0$$

$$W_\theta^n = \frac{iN_b}{r}\left(n\Phi^n + \sum_{\substack{p=-N/2 \\ q\neq 0}}^{N/2-1} pH^p\tau^q \right) \quad : n \neq 0$$

$$W_\theta^n = \left(\frac{\overline{rV_\theta}}{r} - \omega r \right) \quad : n = 0 \qquad \text{5.18b}$$

$$\mathbf{W}^n \cdot \hat{\mathbf{e}}_\xi^n = \frac{1}{J\sqrt{\alpha}} \left(\begin{array}{l} \alpha\Phi_\xi^n - \beta\Phi_\eta^n \\ + \dfrac{ie^{-inN_b f}}{nN_b}\left(\alpha(\overline{rV_\theta})_\xi - \beta(\overline{rV_\theta})_\eta\right) \\ + H^n\left(\alpha\tau_\xi^0 - \beta\tau_\eta^0\right) \\ - \displaystyle\sum_{\substack{p=-N/2 \\ q\neq 0}}^{N/2-1} \tau^q\left(\alpha H_\xi^p - \beta H_\eta^p\right) \end{array} \right) \quad : n \neq 0$$

$$\mathbf{W}^n \cdot \hat{\mathbf{e}}_\xi^n = \frac{\Psi_\eta}{rB_t\sqrt{\alpha}} \quad : n = 0 \qquad \text{5.18c}$$

where q is as defined in equation 4.34.

By transforming equations 4.33a..c it can be shown that

$$\mathbf{V}_{bl} \cdot \hat{\mathbf{e}}_\xi^n = \frac{\Psi_\eta}{rB_t\sqrt{\alpha}} + \sum_{\substack{n=-N/2 \\ n\neq 0}}^{N/2-1} \frac{e^{inN_b f}}{J\sqrt{\alpha}} \left(\begin{array}{l} \alpha\Phi_\xi^n - \beta\Phi_\eta^n \\ + H^n\left(\alpha\tau_\xi^0 - \beta\tau_\eta^n\right) \\ - \displaystyle\sum_{\substack{p=-N/2 \\ q\neq 0}}^{N/2-1} \tau^q\left(\alpha H_\xi^p - \beta H_\eta^p\right) \end{array} \right) \qquad \text{5.19a}$$

$$\mathbf{V}_{bl} \cdot \hat{\mathbf{e}}_\eta^n = \frac{-\Psi_\xi}{rB_t\sqrt{\gamma}} + \sum_{\substack{n=-N/2 \\ n\neq 0}}^{N/2-1} \frac{e^{inN_b f}}{J\sqrt{\gamma}} \left(\begin{array}{l} \gamma\Phi_\eta^n - \beta\Phi_\xi^n \\ + H^n\left(\gamma\tau_\eta^0 - \beta\tau_\xi^n\right) \\ - \displaystyle\sum_{\substack{p=-N/2 \\ q\neq 0}}^{N/2-1} \tau^q\left(\gamma H_\eta^p - \beta H_\xi^p\right) \end{array} \right) \qquad \text{5.19b}$$

$$\mathbf{V}_{\theta\, bl} = \frac{\overline{rV_\theta}}{r} + \sum_{\substack{n=-N/2 \\ n\neq 0}}^{N/2-1} \frac{iN_b e^{inN_b f}}{r} \left(n\Phi^n - \sum_{\substack{p=-N/2 \\ q\neq 0}}^{N/2-1} pH^p \tau^q \right) \qquad 5.19c$$

with equations 4.37, 4.38, 4.41 and 4.42 becoming

$$\sqrt{\alpha}\left(\mathbf{V}_{bl}\cdot\hat{\mathbf{e}}_\xi^n\right) f_\xi + \sqrt{\gamma}\left(\mathbf{V}_{bl}\cdot\hat{\mathbf{e}}_\eta^n\right) f_\eta = \frac{J}{r}(V_{\theta\, bl} - \omega r) \qquad 5.20$$

$$\sqrt{\alpha}\left(\mathbf{V}_{bl}\cdot\hat{\mathbf{e}}_\xi^n\right) \overline{(rV_\theta)}_\xi + \sqrt{\gamma}\left(\mathbf{V}_{bl}\cdot\hat{\mathbf{e}}_\eta^n\right) \overline{(rV_\theta)}_\eta = 0 \qquad 5.21$$

$$\sum_{p=-N/2}^{N/2-1} \left(\begin{array}{l} \sqrt{\alpha}\left(\mathbf{W}^q\cdot\hat{\mathbf{e}}_\xi^n\right) H_\xi^p + \sqrt{\gamma}\left(\mathbf{W}^q\cdot\hat{\mathbf{e}}_\eta^n\right) H_\eta^p \\ \quad + \dfrac{iN_b JpW_\theta^q}{r} H^p \end{array} \right) = 0 \qquad 5.22$$

for $-N/2 \le n \le N/2-1$

$$\sum_{p=-N/2}^{N/2-1} \left(\begin{array}{l} \sqrt{\alpha}\left(\mathbf{W}^q\cdot\hat{\mathbf{e}}_\xi^n\right) \tau_\xi^p + \sqrt{\gamma}\left(\mathbf{W}^q\cdot\hat{\mathbf{e}}_\eta^n\right) \tau_\eta^p \\ \quad + \dfrac{iN_b JpW_\theta^q}{r} \tau^p \end{array} \right) = \left\{ \begin{array}{l} 1 : n = 0 \\ 0 : n \neq 0 \end{array} \right. \qquad 5.23$$

for $-N/2 \le n \le N/2-1$

where again q is as given in equation 4.34.

The transformed version of equation 4.36 is

$$\begin{aligned} &\alpha\psi_{\xi\xi} - 2\beta\psi_{\xi\eta} + \gamma\psi_{\eta\eta} \\ &+ \left(\alpha B_t(1/B_t)_\xi - \beta B_t(1/B_t)_\eta + \mathrm{T} + Jz_\eta/r\right)\psi_\xi \\ &+ \left(\gamma B_t(1/B_t)_\eta - \beta B_t(1/B_t)_\xi + \Sigma + Jz_\xi/r\right)\psi_\eta \\ &\qquad = \end{aligned} \qquad 5.24$$

$$-rB_t J\left((\overline{rV_\theta})_\eta f_\xi - (\overline{rV_\theta})_\xi f_\eta + \sum_{p=-N/2}^{N/2-1}\left(H_\xi^p \tau_\eta^{-p} - H_\eta^p \tau_\xi^{-p}\right)\right)$$

where now $B_t = 1 - \frac{N_b T_t}{2\pi r}$ and $T_t = T_n\sqrt{1 + \frac{r^2(\alpha f_\xi^2 - 2\beta f_\xi^2 f_\eta + \gamma f_\eta^2)}{J^2}}$.

In a similar fashion, equation 4.35 becomes

$$\alpha\Phi_{\xi\xi} - 2\beta\Phi_{\xi\eta} + \gamma\Phi_{\eta\eta} + \left(T - \frac{Jz_\eta}{r}\right)\Phi_\xi + \left(\Sigma + \frac{Jz_\xi}{r}\right)\Phi_\eta - \frac{n^2 N_b^2 J^2 \Phi^n}{r^2} =$$

5.25

$$-\frac{ie^{-inN_b f}}{nN_b}\begin{pmatrix}\alpha\,\overline{rV}_{\theta_{\xi\xi}} - 2\,\beta\overline{rV}_{\theta_{\xi\eta}} + \gamma\,\overline{rV}_{\theta_{\eta\eta}} \\ +\left(T - \frac{Jz_\eta}{r}\right)\overline{rV}_{\theta_\xi} + \left(\Sigma + \frac{Jz_\xi}{r}\right)\overline{rV}_{\theta_\eta}\end{pmatrix}$$

$$-e^{-inN_b f}\left(\alpha\,\overline{rV}_{\theta_\xi} f_\xi - \beta\,\overline{rV}_{\theta_\xi} f_\eta - \beta\,\overline{rV}_{\theta_\eta} f_\xi + \gamma\,\overline{rV}_{\theta_\eta} f_\eta\right)$$

$$-H^n\begin{pmatrix}\alpha\tau^0_{\xi\xi} - 2\beta\tau^0_{\xi\eta} + \gamma\tau^0_{\eta\eta} \\ +\left(T - \frac{Jz_\eta}{r}\right)\tau^0_\xi + \left(\Sigma + \frac{Jz_\xi}{r}\right)\tau^0_\eta\end{pmatrix}$$

$$-\left(\alpha\,\tau^0_\xi H^n_\xi - \beta\,\tau^0_\xi H^n_\eta - \beta\,\tau^0_\eta H^n_\xi + \gamma\,\tau^0_\eta H^n_\eta\right)$$

$$+\sum_{\substack{p=-N/2\\ q\neq 0}}^{N/2-1}\tau^q\begin{pmatrix}\alpha H^p_{\xi\xi} - 2\beta H^p_{\xi\eta} + \gamma H^p_{\eta\eta} - \frac{J^2N_b^2p^2}{r^2}H^p \\ +\left(T - \frac{Jz_\eta}{r}\right)H^p_\xi + \left(\Sigma + \frac{Jz_\xi}{r}\right)H^p_\eta\end{pmatrix}$$

$$+\sum_{\substack{p=-N/2\\ q\neq 0}}^{N/2-1}\left(\alpha\,\tau^q_\xi H^p_\xi - \beta\,\tau^q_\xi H^p_\eta - \beta\,\tau^q_\eta H^p_\xi + \gamma\,\tau^q_\eta H^p_\eta - \frac{J^2N_b^2pq}{r^2}H^p\tau^q\right)$$

where $-N/2 < n < N/2-1 \ : \ n \neq 0$, and q is as defined in equation 4.34.

Finally, noting that the duct and duct wake always lie along the duct quasi-streamline due to the re-meshing procedure, $\psi_\xi = 0$ here, and the duct Kutta condition for a single blade row propulsor (equation 4.43) becomes

$$\psi^2_{\eta c} - \psi^2_{\eta b} = \frac{r^2 J^2}{\gamma} (2\omega \overline{rV}_{\theta c} - \overline{V}^2_{\theta c}) \qquad 5.26$$

Thus, it can be seen that the inverse design problem for a single blade row ducted propulsor has been reduced to a series of seven partial differential equations (5.20..5.26) which can be solved for f, $\overline{rV}_\theta$ downstream of the blading, $H^n : n = -N/2, N/2-1$, $\tau^n : n = -N/2, N/2-1$, ψ off the duct/duct wake, $\Phi^n : n = -N/2, N/2-1$, and ψ on the duct/duct wake respectively upon discretisation and application of the appropriate boundary and initial conditions.

5.2 Numerical Solution of the Transformed Equations[1]

The governing equations were solved using finite difference techniques ([2], [4]) to represent the meridional derivatives of the flow variables.

Equations 5.24 and 5.25 are elliptic in nature, and as such were discretised using the second order accurate central difference expressions given in Appendix III. Both equations were then solved throughout the mesh using the "Cycle C" Multigrid Algorithm given by Brandt [5]. This iterative method, previously used in Clebsch-based blade design methods by Borges [3] and Zangeneh [6], offers a significant increase in computational speed when compared to more conventional Successive Over Relaxation (SOR) Schemes [4]. This approach does, however, place some restrictions on the choice of mesh, especially the total number of quasi-orthogonals and quasi-streamlines chosen.

At this stage it should be noted that the potential function, $\Phi(r, \theta, z)$ is, by definition, real. Thus the positive half of the frequency spectrum $\Phi^n(r,z)$: n=-N/2, N/2-1 can be found as the complex conjugate of the negative half of the spectrum, as outlined by Zangeneh [6]

---

[1] The discretised forms of the governing equations are given in Appendix VI.

i.e. $\Phi^{-n}(r,z) = \mathbf{Re}\,(\Phi^{n}(r,z)) - i\,\mathbf{Im}(\Phi^{n}(r,z)) \quad : \quad -N/2 \le n \le -1$ 5.27

rather than by direct solution of equation 5.25.

Equations 5.20 and 5.21 are hyperbolic in nature, and were discretised using the Crank-Nicholson Implicit Scheme outlined in [4]. This approach, previously employed by Borges [3] and Zangeneh [6] results in these equations being satisfied at the midpoints of the grid rather than at the grid points themselves. The result is two equations which enable $\overline{rV_\theta}$ and the blade wrap angle f to be solved at each quasi-orthogonal by solving a tridiagonal system of equations (Appendix VI). Using this technique $\overline{rV_\theta}$ is marched downstream of the blade trailing edge within the core flow, whilst f is marched upstream and downstream of the blade "stacking condition" (see Section 5.4).

Equations 5.22 and 5.23 are also hyperbolic in nature, and as such were also discretised using a Crank-Nicholson Implicit Scheme. Since H and τ are three-dimensional functions, this approach yields a block tridiagonal system of equations (see Appendix VI) for both H^n and τ^n : n=-N/2, N/2-1 at each quasi-orthogonal. This enables both H^n and τ^n to be marched downstream of initial conditions on the far upstream boundary.

It should be noted that solving the block tridiagonal equations for H and τ is a time-consuming process. Although the time taken can be reduced by some 40% by processing the right hand side vectors of the H and τ equations together (the coefficient matrix is identical for both equations 5.22 and 5.23), solving for H and τ dominates the computational procedure in terms of CPU time. An efficient Fortran77 routine for solving block tridiagonal systems of equations is given by Anderson, Tannehill and Pletcher [2], and can easily be modified to deal with complex elements and a second right hand side vector.

Finally, it was found necessary to smooth the velocity, rothalpy and drift function fields given by equations 5.18a..c, 5.19a..c, 5.22 and 5.23 by multiplying the n^{th} harmonics of each of these quantities by the "sigma" factor

$$\frac{N}{2\pi n}\mathrm{SIN}\left(\frac{2\pi n}{N}\right) \quad : \quad -N/2 \le n \le N/2-1 \quad \text{where } n \neq 0$$

given by Lanczos [7]. This approach, as used by Zangeneh [8], significantly reduces the distortions of these quantities which result from the occurrence of Gibbs' Phenomena [9] in the vicinity of the blade jumps in velocity, rothalpy and drift function.

5.3 Boundary Conditions

5.3.1 Stream Function ψ (Equation 5.24):-

a) As there is no flow through the hub, a condition of constant stream function is applied along the hub quasi-streamline.

b) On the far upstream boundary it is assumed that the flow velocities are unaffected by the presence of the blading, enabling stream function to be determined from a specified velocity profile.

c) On the far downstream boundary, it is assumed that the propulsor slipstream is fully contracted and therefore that $V_r=0$

i.e. $\frac{\partial \psi}{\partial z} = 0.$

d) Since there can be no flow through the duct surface, a condition of constant stream function is applied along the duct and duct wake, the value of which is determined by applying equation 4.43 (the Kutta Condition) at the duct trailing edge.

e) It is assumed that the r = ∞ boundary is sufficiently far from the propulsor for the pressure here to be unmodified by the presence of the propulsor, and for the velocity field to be axisymmetric

i.e. $H^0 = \frac{\overline{V_r^2} + \overline{V_z^2}}{2}$

Further assuming that $\overline{V_r^2} << \overline{V_z^2}$ and formulating V_z in terms of Stokes stream function, it follows that

$$\frac{\partial \psi}{\partial z} = r\sqrt{2H^0} \qquad 5.28$$

5.3.2 Potential Function Φ (Equation 5.25)

a) Since the onset flow is assumed axisymmetric and swirl is assumed absent from the onset flow, a Dirichlet condition of $\Phi=0$ (i.e. $\Phi^n=0$) is applied on the far upstream boundary, which corresponds to $\tilde{\mathbf{V}} = 0$.

b) It is assumed that the r = ∞ boundary is sufficiently far from the propulsor for the periodic velocities to be very small here (i.e. $\tilde{\mathbf{V}} = 0$), thus a boundary condition of $\Phi^n=0$ is applied here.

c) On the hub, duct and duct wake surfaces a condition of $\tilde{\mathbf{V}}.\hat{\mathbf{e}}_\eta'' = 0$ is applied, which when combined with the corresponding ψ boundary conditions corresponds to a condition of no flow across these surfaces.

d) On the far downstream boundary, the second derivative of Φ along quasi-streamlines is set to zero i.e. a condition of $\Phi''_{\xi\xi} = 0$ is satisfied.

Whilst this is only an approximate boundary condition, it enables a periodic potential function caused by trailing vortex sheets to be sustained, and was adopted in the absence of a more appropriate condition. It should be noted that for the case of uniform blade loading, the circumferential variations in velocity decay to zero as the far downstream boundary is approached, and thus this von Neuman boundary condition may be replaced by a much simpler Dirichlet condition of $\Phi^n=0$ in such cases.

5.4 Initial Conditions

5.4.1 Blade Wrap Angle f (Equation 5.20)

Here the initial condition takes the form of a "stacking" condition (see Tan et al [10]), whereby the blade wrap angle f is fixed at one station along the blade chord, relative to which the values of f at all other points on the blade/wake are determined. In the simplest case, a radial stacking condition may be applied, although greater degrees of skew can be obtained by the specification of a non-radial stacking condition.

5.4.2 Mean Swirl $\overline{rV_\theta}$ (Equation 5.21)

This equation is used only to determine $\overline{rV_\theta}$ downstream of the blading and thus the specified $\overline{rV_\theta}$ distribution at the blade trailing edge serves as the initial condition for this equation.

5.4.3 Rothalpy H (Equation 5.22)

The value of rothalpy on the far upstream boundary can be determined from the specified velocity profile, and this forms the initial condition for equation 5.22. Since swirl is assumed absent from the onset flow, rotary stagnation pressure equates to the absolute stagnation pressure at the far upstream boundary, and, by defining this boundary as a static pressure reference (i.e. p=0), the initial condition for H may be expressed

$$H^0 = \frac{p_0}{\rho} = \frac{V_r^2 + V_z^2}{2} \qquad 5.29$$

with $H^n : n \neq 0$ since the onset flow is axisymmetric.

5.4.4 Drift Function τ (Equation 5.23)

The far upstream boundary is used as the reference for drift function. Its value is set to zero here, this forming the initial condition for τ.

5.5 Solving for Propulsor Mass Flow and Tracing the Duct Wake Trajectory

Equation 5.26 (the duct Kutta Condition) is applied at the duct trailing edge in order to update the value of ψ here (and hence propulsor mass flow).

Equation 5.26 is also applied at each point along the assumed position of the duct wake to obtain a value of ψ consistent with the current position. Applying a condition of no flow across the wake, it then becomes possible to trace an updated trajectory consistent with the current value of ψ on the duct. To ease the implementation of this procedure, the downstream portion of the solution grid is remeshed each time the trajectory is updated in order to ensure that the duct wake (and hence the discontinuity in flow quantities) remains on the duct quasi-streamline. The overall procedure for determining propulsor mass flow and slipstream trajectory is as shown in Figure 5.1.

At this point it should be noted that as velocity, rothalpy, drift function and potential function are, in general, discontinuous on both the duct and duct wake, both the upper and lower surface values of these quantities have to be calculated and used as appropriate in the computational scheme.

5.6 Modelling Duct Thickness

The finite difference approach together with the duct boundary condition enables two alternative definitions of the duct surface to be used; one corresponding to the duct upper surface and one the lower surface. When solving at mesh points above the duct, the upper surface definition and its associated geometric derivatives are used, whilst beneath the duct the lower surface definitions are used. Thus, by the inclusion of extra logic structures into the program code, it becomes possible to model the effects of finite duct thickness in addition to infinitesimal duct thicknesses.

5.7 Satisfying the Kutta Condition at the Blade Trailing Edge

For the Kutta condition to be satisfied at the blade trailing edge equation 5.21 must hold here. For cases of uniform blade loading this can be achieved implicitly by specifying a blade circulation distribution that satisfies $(\overline{rV_\theta})_\xi = 0$ at the blade trailing edge. However, for cases of non-uniform blade loading the following scheme for explicitly satisfying the Kutta condition after each blade shape iteration was developed:-

a) Marching $\overline{rV_\theta}$ one quasi-orthogonal upstream from the trailing edge using equation 5.21.

b) Scaling the blade $\overline{rV_\theta}$ distribution along each quasi-streamline to match the updated values obtained in a) above.

c) Smoothing the blade $\overline{rV_\theta}$ distribution along quasi-streamlines to remove the resulting discontinuity in slope immediately upstream of the blade trailing edge. This is achieved by assuming a cubic variation in $\overline{rV_\theta}$ between this discontinuity and a point typically four or five points upstream of the trailing edge. This

cubic distribution is applied to each quasi-streamline individually in such a way that the value $\overline{rV_\theta}$ and its slope $\left(\overline{rV_\theta}\right)_\xi$ remain unaltered, both at the trailing edge and at the other end of the spline.

Although by necessity the blade $\overline{rV_\theta}$ distribution is modified by this process, the values of $\overline{rV_\theta}$ at the leading and trailing edges (and thus the overall blade circulation distribution) remain unmodified. The smoothing process adopted ensures that the slope of the $\overline{rV_\theta}$ distribution at the trailing edge is unmodified, thereby ensuring that the blade Kutta condition is still satisfied after smoothing.

5.8 Solution Procedure

The iterative procedure adopted for the solution of the single blade row ducted propulsor inverse design problem, as implemented in a Fortran77 code, is shown in Figure 5.1.

It should be noted that this procedure determines blade shape for a specified blade circulation distribution. However, if, as is often the case, blade shape is to be determined for a specified shaft torque, it is possible to envisage an extra tier being added to the iterative procedure whereby the blade $\overline{rV_\theta}$ distribution is successively scaled to achieve the desired torque.

5.9 Inputs and Outputs From the Design Process

The inputs to and outputs from the inverse design problem for single blade row ducted propulsors can be summarised as follows:-

5.9.1 Inputs

a) Velocity profile on the far upstream boundary (as obtained from a wake survey or Computational Fluid Dynamics (CFD) estimates);
b) Blade circulation distribution in terms of $\overline{rV_\theta}$ (see Appendix VIII);
c) Axial blade chord and location;
d) Duct and hub geometry;

e) Shaft angular velocity;
f) Blade thickness distribution (based on structural considerations);
g) Fluid density;
h) Number of blades.

5.9.2 Outputs

a) Propulsor mass flow.
b) Blade and blade wake shapes (in terms of the wrap angle f);
c) Fully three-dimensional velocity field;
d) Fully three-dimensional drift function and rothalpy fields;
e) $\overline{rV_\theta}$ downstream of the blading;

From the above it is possible to determine all flow pressures. Of particular interest is the blade pressure distribution which can be computed using equation A5.2 (Appendix V); this can be used to assess cavitation performance at the design point, and also integrated to yield blade thrust and torque. Additionally, the blade relative velocity distribution can be calculated from equation A5.4, enabling the likelihood of flow separation on the blades to be predicted.

5.10 Addition of a Second Blade Row

5.10.1 Modifications to the Computational Procedure

The inclusion of a second (downstream) blade row in the computational procedure involves only a small increase in computational time, and involves the following modifications to the design process:-

a) Specification of the shaft speed, number of blades, axial chord, location, and thickness and $\overline{rV_\theta}$ distributions for the additional blade row.

b) For there to be a unique solution for blade shape, it is necessary for the downstream blade row to encounter axisymmetric onset flow. Therefore, a "mixing" plane, similar to that used by Hawthorne and Tan [11], is defined on one quasi-orthogonal between the trailing edge of the upstream blade row and the leading edge of the downstream row (see Section 5.10.3). At the mixing plane both the flow velocity and the flow vorticity are circumferentially-averaged, this being achieved as outlined in Section 5.10.2.

c) At the mixing plane the relative co-ordinate system is changed from that of the upstream blade row to that of the downstream row. Thus the values of rothalpy here are reset in accordance with

$$H^0 \rightarrow H^0 + \overline{rV_\theta}(\omega_1 - \omega_2) \qquad 5.30$$

where subscripts 1 and 2 refer to the upstream and downstream blade rows respectively.

d) Downstream of the mixing plane the number of blades is taken to be that for the downstream blade row.

e) It is necessary to march $\overline{rV_\theta}$ downstream between the two blade rows using equation 5.21. The $\overline{rV_\theta}$ distribution on the downstream blade row is then scaled in such a way as to match the updated values of $\overline{rV_\theta}$ at its leading edge, whilst maintaining the specified values of $\overline{rV_\theta}$ at its trailing edge.

f) To give an extra degree of control over blade shapes, an independent stacking condition is specified for the downstream blade row, this being used to determine all blade/wake shapes downstream of the mixing plane.

g) In addition to the Kutta condition at the trailing edge of the upstream blade row it is necessary to satisfy a zero-incidence condition at the leading edge of the downstream blade row. This essentially involves marching $\overline{rV_\theta}$ one quasi-streamline downstream from the leading edge of the downstream row (using equation 5.21), and then scaling and smoothing the new $\overline{rV_\theta}$ distribution using similar techniques to those employed for the blade Kutta condition (see Section 5.7). Additionally, if a non-uniform swirl distribution is chosen at the trailing edge of the downstream row, it is further necessary to satisfy the Kutta condition here explicitly.

h) Since rothalpy is reset at the mixing plane in accordance with c) above, there is generally a jump in rothalpy across the duct wake. Therefore the duct Kutta condition (equation 5.26) for multiple blade row propulsors is modified to

$$\psi_{\eta c}^2 - \psi_{\eta b}^2 = \frac{r^2 J^2}{\gamma}\left(2(H_c^0 - H_b^0 + \omega\overline{rV}_{\theta c}) - \overline{V}_{\theta c}^2\right) \qquad 5.31$$

From the procedure outlined above it should be apparent that it would be a relatively simple matter to include even more blade rows in the computational procedure if required.

5.10.2 Circumferentially-Averaging Velocity at the Mixing Plane

As stated in section 5.10.1, for the twin blade row problem the velocity field is circumferentially averaged at the mixing plane using the following procedure:-

1) From equations 4.16 and 5.18a..c it can be seen that the shear component of the periodic velocity and vorticity fields can be circumferentially-averaged at the mixing plane by circumferentially-averaging rothalpy and drift function here i.e. setting

$$H^n = \tau^n = 0 \quad : n \neq 0 \tag{5.32}$$

2) A downstream potential function Φ_2 is defined which replaces the upstream potential Φ within the core flow downstream of the mixing plane. This dissociates the periodic potential function downstream of the mixing plane from that upstream. The upstream potential function Φ is modified so that it satisfies a downstream boundary condition of $\Phi_{\xi\xi} = 0$ at the mixing plane.

3) From equations 4.16 and 4.22 it can be seen that the only general means of circumferentially-averaging the remainder of the velocity and vorticity fields is if Φ_2 satisfies

$$\nabla\Phi_2 = S(\alpha)\nabla\overline{rV_\theta} \tag{5.33}$$

at the mixing plane.

Unfortunately, not only would such a potential function require Von Neuman conditions on each boundary (highly undesirable from the point of view of numerical stability), but worse still it would seem that no such function that satisfies this relationship exists.

The solution adopted therefore was for Φ_2 to satisfy the Dirichtlet condition $\Phi_2 = 0$ at the mixing plane (its far upstream boundary), and the Von Neuman condition $\Phi_{2_{ds}} = 0$ on the far downstream boundary.

From equations 4.16 and 4.22 it can be seen that this approach is sufficient for both the velocity and vorticity fields to be purely axisymmetric immediately downstream of the mixing plane, provided that:-

(a) the upstream blade row is uniformly loaded (i.e. $\nabla\overline{rV_\theta} = 0$ at the mixing plane);

(b) the mixing plane is sufficiently far (typically half a blade chord) upstream of the downstream blade row leading edge (see Section 5.10.3).

However, for cases of a non-uniformly loaded upstream blade row ($\nabla\overline{rV_\theta} \neq 0$ at the mixing plane), the resulting velocity at the mixing plane is clearly non-axisymmetric (equation 4.22 gives $\tilde{\mathbf{V}} = -S(\alpha)\nabla\overline{rV_\theta}$). As a result the velocity and vorticity downstream of the mixing plane were formulated as:-

$$\mathbf{V} = \nabla\Phi_2 - S(\alpha)\,\nabla\left(\overline{rV_\theta} - \overline{rV_{\theta m}}\right) + \tilde{H}\nabla\bar{\tau} + \tilde{\tau}\,\nabla\left(\bar{H}+\tilde{H}\right)\bar{\tau} + \overline{\tilde{\tau}\,\nabla\tilde{H}} \qquad 5.34a$$

$$\Omega = \nabla\overline{rV_\theta}\times\nabla\alpha + \nabla\left(\overline{rV_\theta} - \overline{rV_{\theta m}}\right)\times\nabla\alpha\left(\delta_p(\alpha)-1\right) + \nabla H\times\nabla\tau \qquad 5.34b$$

where $\overline{rV_\theta} = \overline{rV_{\theta m}}$ at the mixing plane, and is assumed to be convected along mean streamlines to points downstream of this plane, satisfying

$$\overline{\mathbf{W}}\cdot\nabla\overline{rV_{\theta m}} = 0 \qquad 5.35$$

Whilst this "induced swirl" formulation ($(\overline{rV_\theta} - \overline{rV_{\theta m}})$ is, in effect, the mean swirl induced by the downstream blade row) is not strictly mathematically rigorous, it does ensure that the velocity and vorticity fields are axisymmetric at the mixing plane, and prevents the periodic component of the shed vorticity from being transferred across

the mixing plane. Furthermore, for cases of uniform blade loading this approach yields identical solutions to those obtained from steps 1...3 above.

Considerable time and thought was devoted to the problem of the non-uniformly loaded upstream blade row, and this solution was the best that could be found bearing in mind the limitations imposed by the concept of the mixing plane.

5.10.3 Positioning of the Mixing Plane

It is generally desirable to position the mixing plane as far downstream of the upstream blade row as possible to prevent the downstream boundary condition of Φ (which is only approximate - see Section 5.3.2) from significantly affecting the three-dimensional velocity field around the upstream blade row. However, it is also desirable for the mixing plane to lie far upstream of the downstream blade row so that the upstream boundary condition on the downstream potential function Φ_2, does not inhibit the development of three-dimensional velocities around the downstream blade row.

Results of studies on the positioning of the mixing plane are too lengthy to present in detail here. However, it was found that for loading distributions such as those used in Chapter 6 the errors (as reflected in blade shape predictions) associated with the proximity of the mixing plane to the blading are small, provided that the mixing plane is no closer than one quarter of a blade chord to either blade row.

5.11 Simplified Computational Runs

Three types of computational run of the inverse design method can be conducted, each of differing complexity and CPU time requirements:-

5.11.1 Fully Three-Dimensional Runs

As described in the preceding pages.

5.11.2 Three-Dimensional Mean Shear Runs

Here rothalpy and drift function are assumed to remain axisymmetric throughout the flow domain, being determined using the mean flow velocities rather than from the three-dimensional velocity field.

Thus equations 5.22 and 5.23, used to determine rothalpy H and drift function τ, simplify to

$$\sqrt{\alpha}\left(\mathbf{W}^0\cdot\hat{\mathbf{e}}_\xi^n\right)H_\xi^0 + \sqrt{\gamma}\left(\mathbf{W}^0\cdot\hat{\mathbf{e}}_\eta^n\right)H_\eta^0 = 0 \qquad 5.36$$

$$\sqrt{\alpha}\left(\mathbf{W}^0\cdot\hat{\mathbf{e}}_\xi^n\right)\tau_\xi^0 + \sqrt{\gamma}\left(\mathbf{W}^0\cdot\hat{\mathbf{e}}_\eta^n\right)\tau_\eta^0 = J \qquad 5.37$$

with $H^n = \tau^n = 0 \;:\; n \neq 0$.

This results in equations 5.18...5.21 and 5.24...5.26 reducing to

$$\mathbf{W}^n\cdot\hat{\mathbf{e}}_\eta^n = \frac{1}{J\sqrt{\gamma}}\left(\begin{array}{l}\gamma\,\Phi_\eta^n - \beta\,\Phi_\xi^n \\ + \dfrac{ie^{-inN_b f}}{nN_b}\left(\gamma\,\overline{rV_{\theta\eta}} - \beta\overline{rV_{\theta\xi}}\right)\end{array}\right) \;:\; n\neq 0$$

$$\mathbf{W}^n\cdot\hat{\mathbf{e}}_\eta^n = \frac{-\Psi_\xi}{rB_t\sqrt{\gamma}} \;:\; n=0 \qquad 5.38a$$

$$W_\theta^n = \frac{iN_b\,n\Phi^n}{r} \;:\; n\neq 0$$

$$W_\theta^n = \frac{\overline{rV_\theta}}{r} - \omega r \;:\; n=0 \qquad 5.38b$$

$$\mathbf{W}^n\cdot\hat{\mathbf{e}}_\xi^n = \frac{1}{J\sqrt{\alpha}}\left(\begin{array}{l}\alpha\Phi_\xi^n - \beta\Phi_\eta^n \\ + \dfrac{ie^{-inN_b f}}{nN_b}\left(\alpha\,\overline{rV_{\theta\xi}} - \beta\,\overline{rV_{\theta\eta}}\right)\end{array}\right) \;:\; n\neq 0$$

$$\mathbf{W}^n\cdot\hat{\mathbf{e}}_\xi^n = \frac{\Psi_\eta}{rB_t\sqrt{\alpha}} \;:\; n=0 \qquad 5.38c$$

$$\mathbf{V}_{bl}\cdot\hat{\mathbf{e}}_{\xi}^{n}=\frac{\psi_{\eta}}{rB_{t}\sqrt{\alpha}}+\sum_{\substack{n=-N/2\\ n\neq 0}}^{N/2-1}\frac{e^{inN_{b}f}}{J\sqrt{\alpha}}\left(\alpha\,\Phi_{\xi}^{n}-\beta\,\Phi_{\eta}^{n}\right) \tag{5.39a}$$

$$\mathbf{V}_{bl}\cdot\hat{\mathbf{e}}_{\eta}^{n}=\frac{-\psi_{\xi}}{rB_{t}\sqrt{\gamma}}+\sum_{\substack{n=-N/2\\ n\neq 0}}^{N/2-1}\frac{e^{inN_{b}f}}{J\sqrt{\gamma}}\left(\gamma\,\Phi_{\eta}^{n}-\beta\,\Phi_{\xi}^{n}\right) \tag{5.39b}$$

$$V_{\theta\,bl}=\frac{\overline{rV_{\theta}}}{r}+\sum_{\substack{n=-N/2\\ n\neq 0}}^{N/2-1}\frac{iN_{b}n\,e^{inN_{b}f}}{r}\Phi^{n} \tag{5.39c}$$

$$\sqrt{\alpha}\left(\mathbf{V}_{bl}\cdot\hat{\mathbf{e}}_{\xi}^{n}\right)f_{\xi}+\sqrt{\gamma}\left(\mathbf{V}_{bl}\cdot\hat{\mathbf{e}}_{\eta}^{n}\right)f_{\eta}=\frac{J}{r}(V_{\theta\,bl}-\omega r) \tag{5.40}$$

$$\sqrt{\alpha}\left(\mathbf{V}_{bl}\cdot\hat{\mathbf{e}}_{\xi}^{n}\right)\left(\overline{rV_{\theta}}\right)_{\xi}+\sqrt{\gamma}\left(\mathbf{V}_{bl}\cdot\hat{\mathbf{e}}_{\eta}^{n}\right)\left(\overline{rV_{\theta}}\right)_{\eta}=0 \tag{5.41}$$

$$\begin{aligned}&\alpha\psi_{\xi\xi}-2\beta\psi_{\xi\eta}+\gamma\psi_{\eta\eta}\\&+\left(\alpha B_{t}(1/B_{t})_{\xi}-\beta B_{t}(1/B_{t})_{\eta}+\mathrm{T}+Jz_{\eta}/r\right)\psi_{\xi}\\&+\left(\gamma B_{t}(1/B_{t})_{\eta}-\beta B_{t}(1/B_{t})_{\xi}+\Sigma+Jz_{\xi}/r\right)\psi_{\eta}\\&\qquad=\\&-rB_{t}J\left((\overline{rV_{\theta}})_{\eta}f_{\xi}-(\overline{rV_{\theta}})_{\xi}f_{\eta}+H_{\xi}^{0}\tau_{\eta}^{0}-H_{\eta}^{0}\tau_{\xi}^{0}\right)\end{aligned} \tag{5.42}$$

$$\begin{aligned}&\alpha\Phi_{\xi\xi}-2\beta\Phi_{\xi\eta}+\gamma\Phi_{\eta\eta}+\left(T-\frac{Jz_{\eta}}{r}\right)\Phi_{\xi}\\&+\left(\Sigma+\frac{Jz_{\xi}}{r}\right)\Phi_{\eta}-\frac{n^{2}N_{b}^{2}J^{2}\Phi^{n}}{r^{2}}\\&\qquad=\\&-\frac{ie^{-inN_{b}f}}{nN_{b}}\begin{pmatrix}\alpha\,\overline{rV}_{\theta_{\xi\xi}}-2\,\beta\overline{rV}_{\theta_{\xi\eta}}+\gamma\,\overline{rV}_{\theta_{\eta\eta}}\\+\left(T-\frac{Jz_{\eta}}{r}\right)\overline{rV}_{\theta_{\xi}}+\left(\Sigma+\frac{Jz_{\xi}}{r}\right)\overline{rV}_{\theta_{\eta}}\end{pmatrix}\\&-e^{-inN_{b}f}\left(\alpha\,\overline{rV}_{\theta_{\xi}}f_{\xi}-\beta\,\overline{rV}_{\theta_{\xi}}f_{\eta}-\beta\,\overline{rV}_{\theta_{\eta}}f_{\xi}+\gamma\,\overline{rV}_{\theta_{\eta}}f_{\eta}\right)\quad(\text{for n}\neq 0)\end{aligned} \tag{5.43}$$

$$\psi_{\eta c}^2 - \psi_{\eta b}^2 = \frac{r^2 J^2}{\gamma} (2\omega \overline{rV}_{\theta c} - \overline{V}_{\theta c}^2) \qquad 5.44$$

Upon discretisation, equations 5.36 and 5.37 enable H and τ to be marched downstream from the initial conditions by solving a simple tridiagonal system of equations on each quasi-orthogonal rather than a complex block tridiagonal system. Further reductions in computational time are associated with the absence of convolved terms in the right hand sides of equations 5.38...5.43. The net result, as will be shown in Chapter 6, is a huge saving in computational time when compared to the fully three-dimensional approach, with little difference in blade shape predictions apparent.

It should be noted that this mean shear approach still makes allowance for the three-dimensional velocity field that develops in the blade passages.

However, the shear vorticity associated with the development of circumferential variations in drift function and rothalpy within the blade passages (i.e. the component $\nabla H \times \nabla \tau - \nabla \overline{H} \times \nabla \overline{\tau}$ of the right hand side of equation 4.16) is neglected. As a consequence no account is taken of the circumferential variations of shear vorticity (outlined in [12],[13] and [14]) that develop within the blade passages. In particular, no allowance is made for the filaments of shear vorticity that develop at the blade surface and are ultimately shed from the blade trailing edge (the occurrence of this type of vorticity, which is due to "vortex-stretching", is discussed by Hawthorne [12]).

In many ways this "mean shear" approach is analogous to the "mean density" approach to blade design suggested by Zangeneh [6] where circumferential variations in density were neglected but circumferential variations in velocity were included.

5.11.3 Actuator Duct Runs

With this approach, originally presented by Hawthorne [15], the propulsor velocity field is assumed to remain axisymmetric. Thus all flow quantities also remain axisymmetric, and equations 5.18..5.21 and 5.24..5.26 reduce to

$$\mathbf{W}^0.\hat{\mathbf{e}}^n_\eta = \mathbf{V}_{bl}.\hat{\mathbf{e}}^n_\eta = \frac{-\psi_\xi}{rB_t\sqrt{\gamma}} \qquad 5.45a$$

$$\mathbf{W}^0_\theta = \mathbf{V}_{\theta\, bl} - \omega r = \left(\frac{\overline{rV_\theta}}{r} - \omega r\right) \qquad 5.45b$$

$$\mathbf{W}^0.\hat{\mathbf{e}}^n_\xi = \mathbf{V}_{bl}.\hat{\mathbf{e}}^n_\xi = \frac{\psi_\eta}{rB_t\sqrt{\alpha}} \qquad 5.45c$$

$$\mathbf{W}^n.\hat{\mathbf{e}}^n_\eta = \mathbf{W}^n_\theta = \mathbf{W}^n.\hat{\mathbf{e}}^n_\xi = 0 \quad : n \neq 0 \qquad 5.45d$$

$$\sqrt{\alpha}\left(\mathbf{V}_{bl}\cdot\hat{\mathbf{e}}^n_\xi\right) f_\xi + \sqrt{\gamma}\left(\mathbf{V}_{bl}\cdot\hat{\mathbf{e}}^n_\eta\right) f_\eta = \frac{J}{r}(V_{\theta\, bl} - \omega r) \qquad 5.46$$

$$\sqrt{\alpha}\left(\mathbf{V}_{bl}\cdot\hat{\mathbf{e}}^n_\xi\right) \overline{(rV_\theta)}_\xi + \sqrt{\gamma}\left(\mathbf{V}_{bl}\cdot\hat{\mathbf{e}}^n_\eta\right) \overline{(rV_\theta)}_\eta = 0 \qquad 5.47$$

$$\sqrt{\alpha}\left(\mathbf{W}^0\cdot\hat{\mathbf{e}}^n_\xi\right) H^0_\xi + \sqrt{\gamma}\left(\mathbf{W}^0\cdot\hat{\mathbf{e}}^n_\eta\right) H^0_\eta = 0 \qquad 5.48a$$

$$H^n = 0 \quad : n \neq 0 \qquad 5.48b$$

$$\sqrt{\alpha}\left(\mathbf{W}^0\cdot\hat{\mathbf{e}}^n_\xi\right) \tau^0_\xi + \sqrt{\gamma}\left(\mathbf{W}^0\cdot\hat{\mathbf{e}}^n_\eta\right) \tau^0_\eta = J \qquad 5.49a$$

$$\tau^n = 0 \quad : n \neq 0 \qquad 5.49b$$

$$\begin{aligned} &\alpha\psi_{\xi\xi} - 2\beta\psi_{\xi\eta} + \gamma\psi_{\eta\eta} \\ &+ \left(\alpha B_t(1/B_t)_\xi - \beta B_t(1/B_t)_\eta + \mathrm{T} + Jz_\eta/r\right)\psi_\xi \\ &+ \left(\gamma B_t(1/B_t)_\eta - \beta B_t(1/B_t)_\xi + \Sigma + Jz_\xi/r\right)\psi_\eta \\ &\qquad = \\ &-rB_tJ\left((\overline{rV_\theta})_\eta f_\xi - (\overline{rV_\theta})_\xi f_\eta + H^0_\xi\tau^0_\eta - H^0_\eta\tau^0_\xi\right) \end{aligned} \qquad 5.50$$

$$\psi_{\eta c}^2 - \psi_{\eta b}^2 = \frac{r^2 J^2}{\gamma} (2\omega \overline{rV}_{\theta c} - \overline{V}_{\theta c}^2) \qquad 5.51$$

Note that equation 5.25 is no longer used as Φ is set to zero for axisymmetric flow. This approach is even faster than the three-dimensional mean shear run, since the potential function and the associated three-dimensional terms are not evaluated. Large reductions in storage requirements are also realised, with all flow variables being of the real rather than complex type. Whilst significantly less accurate than the three-dimensional methods for highly-loaded blades due to the absence of periodic effects, this approach is none-the-less very fast and robust, and is ideal for use in the early stages of design.

5.12 Numerical Problems Associated with the Normal Derivative of $\overline{rV_\theta}$ at the Endwalls

Research on Clebsch-based blade inverse design methods has shown there to be numerical problems associated with three-dimensional runs for cases where the tangential component of bound vorticity (i.e. the component $\frac{\partial \overline{rV_\theta}}{\partial n}\frac{\partial f}{\partial s} - \frac{\partial \overline{rV_\theta}}{\partial s}\frac{\partial f}{\partial n}$ of the right hand side of equation 4.16) is non-zero at the endwalls.

The presence of this endwall singularity, which is discussed in detail by Borges [3] and Zangeneh ([6], [8]), would seem to be a result of the assumption of inviscid flow which makes no allowance for the presence of wall boundary layers. Both these authors attribute these numerical difficulties to the large velocities at the endwalls resulting from the blades (which are modelled as vortex sheets) intersecting the endwalls obliquely.

This type of problem, as encountered with the Clebsch-based approach to blade design, was first reported by Tan et al [10]. Here it was found necessary to force the tangential component of bound vorticity to zero at the endwalls in order to achieve satisfactory numerical convergence of an inverse design method for axial machines. As only cases satisfying $\frac{\partial \overline{rV_\theta}}{\partial n} = 0$ at the endwalls were considered, this was achieved by forcing the normal derivative of wrap angle, $\frac{\partial f}{\partial n}$, to zero at the endwalls.

Later, Borges [3] encountered similar problems with his arbitrary geometry inverse design method, and as a result found it necessary to adopt two approximations to achieve numerical convergence. Firstly, the second term on the left hand side of equation 5.20 was neglected when determining blade wrap angle f within three mesh points of the endwalls. Then, having achieved numerical convergence, the value of $\frac{\partial f}{\partial n}$ was gradually extrapolated from an unaltered value three grid points from the endwalls down to zero at the endwalls. It was argued that these approximations were reasonable as they were only applied close to the endwalls where viscous effects (which were not modelled) would be expected to dominate.

However, for the ducted propulsor design method outlined in this thesis the solution adopted was identical to that suggested by Zangeneh [6], whereby the normal derivatives of both $\overline{rV_\theta}$ and wrap angle f are assumed to be zero when enforcing the endwall boundary condition for the potential function (as given in Section 5.3.2) along the hub and duct. Although it is not strictly mathematically rigorous, it is found that by satisfying this simplified boundary condition, computational problems for both the fully three-dimensional and three-dimensional mean shear runs are avoided. This procedure is much simpler to implement than the approach of Borges [3], and, since it is only applied at the endwalls, is arguably more accurate.

5.13 Numerical Problems Associated with Fully Three-Dimensional Runs

A number of numerical problems were encountered during the development of the ducted propulsor inverse design codes. It should be stressed that these problems, which are outlined below, were encountered only with fully three-dimensional runs of the program, and not the actuator duct or three-dimensional mean shear runs:-

a) Preliminary work suggested that it was necessary to specify a far upstream velocity profile which resulted in a condition of zero derivative of velocity normal to the endwalls in order to achieve convergence of fully three-dimensional runs for all but the most gentle cases of shear.

As this problem was not encountered with three-dimensional mean shear runs, the cause would seem to be associated with the development of circumferential variations of shear vorticity within the blade passages. In particular, it seems

likely that the problem is a result of the concentrated sheets of shear vorticity that develop on the blade ("filament" vorticity using the terminology of Hawthorne [12]) rather than due to the circumferentially-distributed component of shear vorticity ("distributed secondary circulation" [12]).

By a similar arguments used by Borges [3] and Zangeneh [6] (Section 5.12) to account for an endwall singularity associated with bound vorticity, a sheet of filament vorticity would be expected to generate a singularity at the endwalls for cases where the blade intersects the endwall obliquely.

No matter, it was found that by using the technique given in Appendix VII to force the normal derivative of rothalpy along the endwalls to zero (i.e. $\partial H^* / \partial n = 0 : -N/2 \le n \le N/2 - 1$) prior to evaluating the potential function Φ, convergence could be achieved for more general runs where the normal derivative of velocity at the endwalls was non-zero. In effect, what this procedure amounts to is gradually decaying the periodic component of shear vorticity down to zero at the endwalls from an unaltered value typically four or five mesh points away. Whilst this approach is not, mathematically-speaking, accurate, since H near the endwalls should be determined from equations 5.22, it enables solutions to be obtained for a wide range of cases in which otherwise none could be obtained. Any associated errors should be located close to the endwalls where one would expect viscous effects (which are not included in the inverse design method) to dominate blade performance.

b) In equation 4.22 the shear component of the periodic velocity field is written

$$\tilde{H}\nabla\tilde{\tau} - \tilde{\tau}\nabla(\overline{H} + \tilde{H}) + \overline{\tilde{\tau}\nabla\tilde{H}}$$

However, it could have been written more simply as

$$H\nabla\tau - \overline{H\nabla\tau}$$

or alternatively as

$$\tau\nabla H - \overline{\tau\nabla H}$$

Whilst this would simplify the problem formulation, all attempts to implement this in a computer program resulted in numerical problems. The cause of these

problems seems to be that rothalpy and drift function are discontinuous on the blade surface, and as a result any attempt to evaluate the terms $\overline{H}\nabla\tilde{\tau}$ and $\overline{\tau}\,\nabla\tilde{H}$ using Fourier techniques results in large-amplitude spiked functions which cause the program to "crash". By formulating the velocity field as in equation 4.22, which is equally valid, these problems are avoided. Although one remaining term, $\tilde{\tau}\,\nabla\tilde{H}$, might be expected to cause similar numerical problems, results indicate that this term is always very small since $\tilde{\tau} << \overline{\tau}$, and thus its presence does not affect the convergence of the problem.

c) Generally for the ducted propulsor problem the mesh boundary is taken as far downstream as practical to allow for slipstream contraction, and this led to numerical problems resulting in the design program "crashing". Attempts to locate the root cause of this difficulty, which generally occurs several blade iterations into the iterative procedure (Figure 5.1), were hampered by the vast quantity of data used by the computer programs. However, one of the following possible causes seem likely:-

1) The circumferential variations in rothalpy and drift function (which continue to develop indefinitely downstream of the propulsor) become very large close to the outlet boundary. This leads to problems in evaluating the derivatives of rothalpy and drift function using Fourier techniques for the reasons outlined in b) above, resulting in the program crashing.

2) The circumferential variations in rothalpy and drift function become very large close to the outlet boundary for the reasons stated in 1) above, and become incompatible with the far downstream boundary condition for the potential function (see Section 5.3.2) which is only approximate. This results in numerical instability which causes the program to crash.

3) Successively solving for the fully three-dimensional rothalpy and drift function at each quasi-orthogonal is a numerically-intensive task. It may be that the round-off errors associated with this procedure accumulate to such an extent that spurious values of these variables are calculated towards the downstream boundary, causing the program to crash.

   This would explain why this problem was not encountered when the design method presented in this thesis was applied to the design of pump

blading; for the pump problem one generally requires fewer than half the number of quasi-orthogonals used in ducted propulsor design. Additionally, it could also account for why it was necessary to freeze the development of the periodic rothalpy and drift function fields (see below) even for lightly-loaded propulsors where the circumferential variations of these quantities would be expected to be small.

Unfortunately it was difficult to investigate this theory of failure because the use of double precision complex variables is not permitted [16] in FORTRAN 77 (the programming language used for the inverse design codes). Even if this were possible, the already vast storage requirements associated with the fully three-dimensional code would double along with the computational time, and this would have been beyond the capabilities of the available computing facilities.

Whilst it was also conceivable that the cause was flow reversal within the blade passages (which would have involved modifications to the marching routines used to solve for H and τ), the occurrence of the problem for lightly-loaded test cases made this seem unlikely, and indeed computational tests for flow-reversal confirmed that this was not the cause.

In any case, it was found necessary to freeze the development of the periodic components of rothalpy and drift function within the core flow at some quasi-orthogonal downstream of the duct trailing edge in order to achieve convergence. This was achieved by forcing H^n and τ^n (where $n \neq 0$) to be constant along quasi-streamlines downstream of this quasi-orthogonal, and then applying the appropriate frequency shift to ensure that the jumps in rothalpy and drift function in this region remained at the blade surface.

Computational results have shown that if it is implemented only "far" downstream of the blading (typically downstream of the duct trailing edge), then freezing the development of rothalpy and drift function in this manner does not noticeably alter the predicted blade shapes.

References

1) Thomson,J.F. "Numerical Grid Generation, Foundations and Applications", North Holland, Amsterdam, 1985

2) Anderson,A., Tannehill,J.C., Pletcher,R.H. "Computational Fluid Mechanics and Heat Transfer", Series in Computational Methods in Mechanics and Thermal Sciences, McGraw Hill, 1984

3) Borges,J. "Three-Dimensional Inverse Design of Turbomachinery", Ph.D. Thesis, Cambridge University Engineering Department, Cambridge, 1986

4) Smith,G.D. "Numerical Solution of Partial Differential Equations: Finite Difference Methods", Third Edition, Oxford Applied Mathematics and Computing Science Series, Oxford University Press, 1985

5) Brandt,A. "Multi-Level Adaptive Solutions to Boundary Value Problems", Mathematics and Computation, Vol. 31, No. 138, pp333-390, April 1977

6) Zangeneh,M. "A Compressible Three-Dimensional Design Method for Radial and Mixed Flow Turbomachinery Blades", pp599-624, International Journal of Numerical Methods in Fluids", Vol.13, 1991

7) Lanczos,C. "Discourse On Fourier Series", p65, Oliver & Boyd Ltd., London, 1966

8) Zangeneh,M. "Three Dimensional Design of Radial-Inflow Turbines", Ph.D. Thesis, Cambridge University Engineering Department, Cambridge, 1988

9) Stroud,K.A. "Fourier Series and Harmonic Analysis", Stanley Thornes (Publishers) Ltd., Cheltenham, 1984

10) Tan,C.S., Hawthorne,W.R., McCune,J.E., Wang,C., "Theory of Blade Design for Large Deflections: Part II - Annular Cascades", ASME Journal of Engineering for Gas Turbines and Power, Vol. 106, April 1984

11) Hawthorne,W.R., Tan,C.S. "Design of Turbomachinery Blading in 3D Flow by the Circulation Method: A Progress Report", International Conference On Inverse Design In Engineering Sciences (ICIDES), 1987

12) Hawthorne,W.R. "Rotational Flow Through Cascades. Part I : The Components of Vorticity", pp266-279, Quart. Journ. of Mech. & Appl. Math., Vol.8, 1955

13) Hawthorne,W.R., Armstrong,W.D. "Rotational Flow Through Cascades. Part II : The Circulation About the Cascade", pp280-292, Quart. Journ. of Mech. & Appl. Math., Vol.8, Part 3, 1955

14) Horlock,J.H., Lakshminarayana,B. "Secondary Flows: Theory, Experiment, and Application in Turbomachinery Aerodynamics", Annual Review of Fluid Mechanics, Vol.5, 1973

15) Hawthorne,W.R. "The Actuator Duct Representation of Turbomachinery Blade Rows", CUED/A - Turbo/TR 119, Cambridge University Engineering Department, Cambridge, 1983

16) Monro,D.M. "Fortran 77", Edward Arnold Publishers, London, 1982

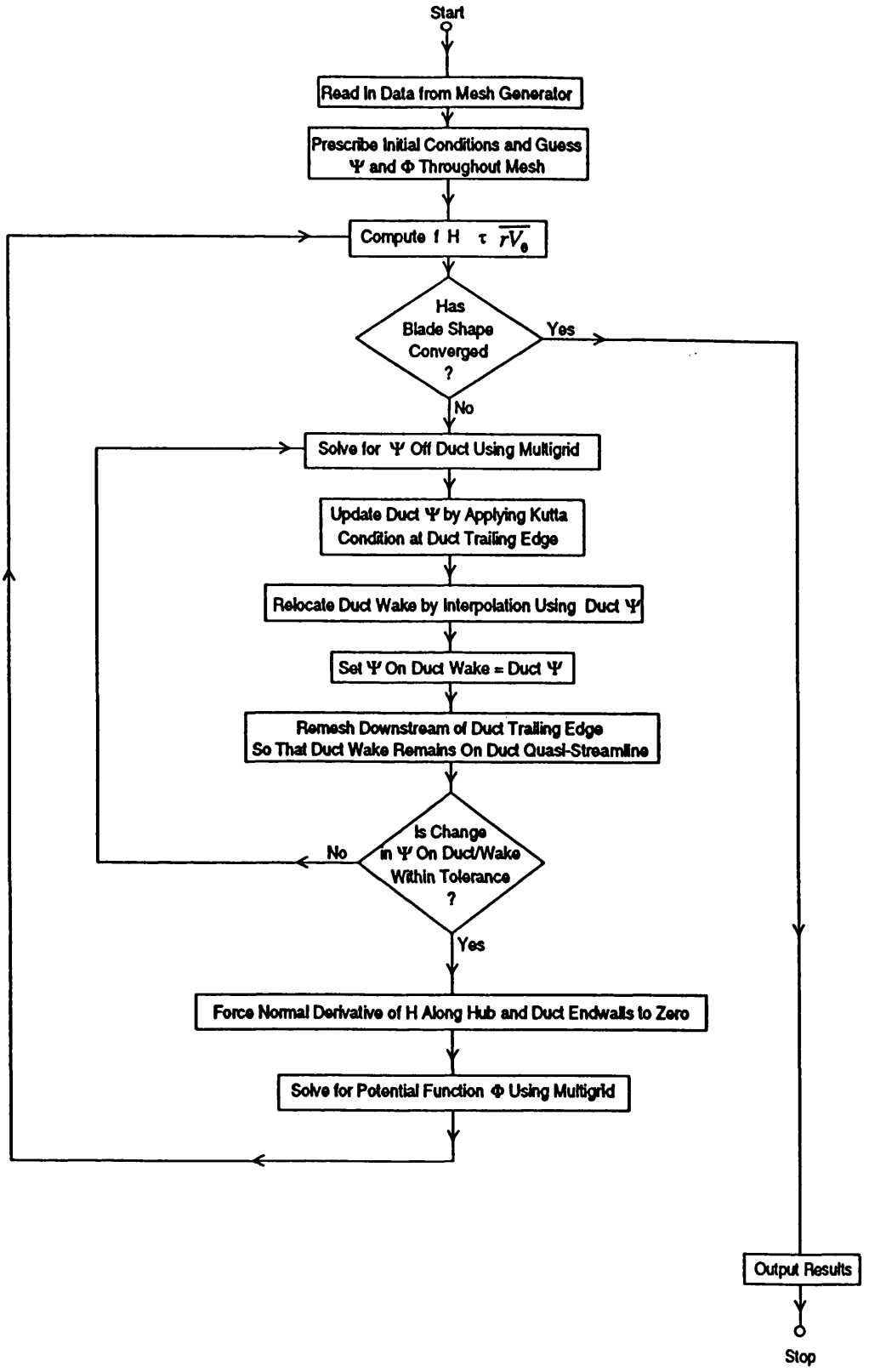

Figure 5.1: Simplified Flow Chart for the Fully Three-Dimensional Ducted Propulsor Inverse Design Program

CHAPTER 6: COMPUTATIONAL RESULTS

In order to illustrate of the capabilities of the ducted propulsor inverse design method outlined in Chapters 4 and 5, computational results are presented for the following cases:-

6.1 Merchant Ship Ducted Propeller

This single blade row propulsor, suitable for a 200 000 TDW tanker, has principal particulars based broadly on data presented by Andersen and Tani [1], consisting of a six-bladed propeller with a shaft speed of 135rpm mounted on a cylindrical hub of diameter 1.81m. The blading is enshrouded by an NSMB No 19A nozzle (Figure A9.1, Appendix IX) of tip diameter 7.8m. The meridional outline of each blade is defined by

Leading Edge:	$z = -0.07513\,r + 1.5680$
Trailing Edge:	$z = +0.07513\,r + 2.3321$

where z=0 corresponds to the duct leading edge and r and z are in m. The blade normal thickness corresponds to the NACA C4 distribution shown in Figure A9.3 (Appendix IX), where x is the axial distance from the blade leading edge.

The far downstream boundary is taken to be 5.1m downstream of the duct trailing edge. The far upstream boundary is taken to be 6.0m upstream of the duct leading edge, the circumferential-average velocity profile here being defined by

$$V_z = -0.2982\,r^2 + 2.9817\,r + 1.0458 \quad \text{m/s} \quad : r \leq 5.0\text{m}$$

$$V_z = 8.5 \quad \text{m/s} \quad : r > 5.0\text{m}$$

$$V_r = 0.0 : \text{all } r$$

the meridional velocity varying between a value of 6.796 Knots on the hub and a free stream value of 16.505 Knots at a radius of 5.0m, as shown in Figure 6.1.

The circulation distribution on the blading is defined by

$$\overline{rV}_\theta = 6K(r)\left(\frac{z'^2}{2} - \frac{z'^3}{3}\right) \quad \mathrm{m}^2/s$$

where $z' = \dfrac{(z - z_{le})}{(z_{le} - z_{te})}$

$$K(r) = 2.15 + 2.05(r - r_{hub})SIN\left(\pi\left(\frac{r - r_{hub}}{r_{tip} - r_{hub}} - 0.5\right)\right)$$

as shown in Figures 6.2 and 6.3. Note that the hub is not fully off-loaded, but is instead assigned a very small loading (through $\overline{rV}_\theta$) in order to avoid numerical problems during the implementation of the blade Kutta Condition.

A fully three-dimensional run, a three-dimensional mean shear run, and an actuator duct run were conducted on the 257 x 65 meridional mesh shown in Figure 6.4. Four multigrid levels were used, with sixteen harmonics (N=16) being used for the three-dimensional runs. Since the blades are non-uniformly loaded, the Kutta Condition was enforced explicitly at the blade trailing edge using the technique outlined in Section 5.7.

The final meridional mesh for the fully three-dimensional run, as output from the computational procedure is shown in Figure 6.5. Comparing this with Figure 6.4, the effect of the remeshing procedure outlined in Section 5.5 can be seen to be very small, a slight divergence of the propulsor slipstream being predicted.

The mean streamline patterns predicted by the fully three-dimensional run is shown in Figure 6.6, the corresponding mean velocity vectors being shown in Figure 6.7; these give a very good indication of the overall propulsor flow field, the latter plot clearly showing the jump in velocity across the duct wake. Note that the corresponding plots for the actuator duct and three-dimensional mean shear runs are not presented as they are indistinguishable from those presented here.

The predicted mean duct pressure distributions for the three runs are shown in Figure 6.8, and are essentially indistinguishable from each other. As can be seen from Figure 6.9, which compares the pressure distribution for the fully three-dimensional run with a comparable run conducted with zero blade thickness, the effect of blade thickness on the mean duct pressure distribution seems to be much greater than the presence of

any three-dimensional effects. Blade thickness also seems to account for the rather "bumpy" appearance of the inner surface pressure distributions shown in Figure 6.8.

The blade shapes predicted by the three types of run are compared in figure 6.10 and 6.11. Here the predictions of the fully three-dimensional and three-dimensional mean shear runs differ significantly only in the region of the hub; this could well be a result of the forced modifications to the rothalpy field in the vicinity of the hub for the fully three-dimensional run (see Section 5.13), rather than due to fully three-dimensional shear phenomena. Furthermore, even the actuator duct blade shapes differ only slightly from the three-dimensional predictions.

Predicted blade static pressure distributions (calculated using equation A5.2, Appendix V) are shown in Figure 6.12, these being of particular use in assessing the likelihood of blade cavitation, and, when applied to equation A5.5, the likelihood of flow separation on the blades. In these plots the radial variation of loading on the blades is readily apparent. As with the blade shapes, it can be seen that the blade pressure distributions for the fully three-dimensional and three-dimensional mean shear runs are almost identical. However, the pressure distributions given by the actuator duct run differ significantly from either of these three-dimensional runs.

A comparison of the initial (specified) blade $\overline{rV_\theta}$ distribution with the final distribution as output from the computational procedure is given in Figure 6.2, showing the modifications associated with the enforcement of the Kutta condition at the blade trailing edge to be small.

It will be seen in Figure 6.12 that the result of enforcing the Kutta condition (using the method outlined in Section 5.7), together with the solution of equation 5.21 downstream of the blading, is that the Kutta condition is not satisfied at the blade trailing edge, but rather half a mesh point upstream of it and half a mesh point downstream of it. This is because the adopted Crank-Nicholson discretisation results in equation 5.21 being satisfied at the mid-point between quasi-orthogonals, rather than at the trailing edge mesh points themselves. The resulting blade pressure jump at the trailing edge is non-zero, although it can be reduced in magnitude by reducing the quasi-orthogonal spacing on the blade.

Figure 6.13, shows the development of circumferential variations in velocity within the core flow for both the fully three-dimensional and three-dimensional mean shear runs. Not only are these two sets of plots indistinguishable, but there also seems to

be no appreciable circumferential variations in radial and tangential velocity, implying that three-dimensional effects are weak.

From Figure 6.14, the development of circumferential variations in rothalpy within the core flow can be seen to be very small in comparison with the circumferential average values of rothalpy. Given the small differences in blade shape and flow field predictions between the fully three-dimensional and three-dimensional mean shear runs, the development of circumferential variations in shear vorticity (outlined in the theoretical work of Hawthorne [2], Hawthorne and Armstrong [3] and Horlock and Lakshminarayana [4]) would therefore appear to be negligible.

From Table 6.1 it can be seen that both the mass flows and propulsor forces predicted by the three types of run are identical to within 0.5%, again this suggesting that three-dimensional flow effects are not significant for this propulsor.

Some words of caution are warranted regarding the values of duct thrust shown in Table 6.1. Much of the axial duct force for the propulsor is borne by the duct leading edge, where rather poor resolution of the duct pressure distribution (Figure 6.8) is obtained due to the high curvature and slope of the duct profile. Thus, integration of the duct pressure distribution to yield duct thrust/drag often results in spurious values; this, to some extent, seems to account for the rather large values of duct thrust presented in Table 6.1. Although this problem can to some extent be alleviated by adopting close quasi-orthogonal spacings around the duct leading edge, this leads to problems in generating the mesh, and can also cause computational problems associated with the variable spacing of quasi-orthogonals.

Finally, from Figure 6.15 it can be seen that the computational time requirement of three-dimensional mean shear run was only marginally (around 10%) greater than the actuator duct run, and yet this run yielded notably improved estimates of such features as blade shapes and the blade pressure distribution. The fully three-dimensional run, which took more than twice as long to converge as either of the these two runs, yielded no significant improvement in flow field or blade shape predictions compared to the much faster three-dimensional mean shear run.

6.2 Submarine Propulsors

(a) Rotor-Stator Submarine Propulsor

This propulsor, suitable for a submarine of 5000 Tonnes submerged displacement, consists of a 14-bladed rotor of shaft speed 95.5rpm mounted upstream of an 17-bladed stator. The leading and trailing edges of the upstream blade row are defined by z=0.67m and z=1.34m, and those for the downstream row by z=2.01m and z=2.68m respectively, where z=0.0 m corresponds to the duct leading edge. The normal thickness of the blading is as shown in Figure A9.3 (Appendix IX) where A=0.75 and x is the axial distance from the blade leading edge. A radial stacking condition is applied at the trailing edge of each blade row.

The far upstream velocity profile (taken at z=-5.0m) varies from a value of 2.07m/s (4.02 Knots) on the hub to a free stream value of 10.35m/s (20.10 Knots) at a radius of 6.9m, being defined by

$$V_z = -0.468111\, r^2 + 6.459932\, r - 12.286766 \quad \text{m/s} \quad : r \le 6.9\text{m}$$
$$V_z = 10.0 \quad \text{m/s} \quad : r > 6.9\text{m}$$

$$V_r = -0.125454\, r^2 + 1.731262\, r - 3.292853 \quad \text{m/s} \quad : r \le 6.9\text{m}$$
$$V_r = 10.0 \quad \text{m/s} \quad : r > 6.9\text{m}$$

as shown in Figure 6.16.

The circulation distribution (Figure 6.17) on the upstream blade row is defined by

$$\overline{rV}_\theta = 8.5\left(3z'^2 - 2z'^3\right) \quad \text{m}^2/\text{s}$$

and that on the downstream blade row by

$$\overline{rV}_\theta = 8.5\left(1 - 3z'^2 + 2z'^3\right) \quad \text{m}^2/\text{s}$$

where $z' = \dfrac{(z - z_{le})}{(z_{le} - z_{te})}$

c = blade chord

It should be noted that both these $\overline{rV_\theta}$ distributions implicitly satisfy the Kutta condition at their respective blade trailing edges.

The hub is defined by

$$r = -0.268z + 1.426 \quad m \quad : \quad z < 4.612 \text{ m}$$

with

$$r = 0.2 \text{ m} \quad : \quad z \geq 4.612 \text{ m}$$

in order to avoid numerical problems associated with computing stream function and at very small values of radius.

The duct (a much-modified NSMB No.19A nozzle) is defined as shown in Figure A9.2 (Appendix IX).

(b) Contra-Rotating Submarine Propulsor

The particulars for this propulsor are as for the rotor-stator propulsor given in (a) above, but with shaft speeds of 47.75rpm and -47.75rpm for the upstream and downstream blade rows respectively.

For both these propulsors fully three-dimensional, three-dimensional, and actuator duct runs were conducted on a VAXstation 4000vlc using the 257x65 meridional mesh shown in Figure 6.18. For the three-dimensional runs 16 Fourier harmonics were used due to the limitations of the available computing facilities.

The predicted mean streamline patterns for the fully three-dimensional runs are shown in Figure 6.20, the corresponding mean velocity vectors being presented in Figure 6.21.

Figure 6.19 shows the modified meridional mesh as output from the fully three-dimensional run of the rotor-stator propulsor. Comparing with Figure 6.18, the effects of remeshing the downstream portion of the mesh to allow for slipstream contraction (see Section 5.5) are clearly visible.

Figure 6.22 shows the predicted duct pressure distributions (based on the mean flow variables) for the two propulsors. As with the merchant ship propulsor in Section 6.1, the difference between the predictions of the actuator duct runs and the three-dimensional runs is negligible.

The mean duct pressure distributions predicted by the fully three-dimensional runs are compared with equivalent runs conducted in the absence of blade thickness in Figure 6.23. As for the merchant ship ducted propeller, this shows the "bumpy" appearance of the pressure distributions on the duct inner surface in Figure 6.23 to be associated with the blade thickness. This also serves to emphasise the significant effect blade thickness has on the duct pressure distribution, at least for the idealised case of inviscid flow and zero tip clearance.

Predicted blade shapes are shown in Figures 6.24, 6.25, 6.26 and 6.27. It can be seen that there are noticeable differences between the actuator duct blade shapes and those given by the three-dimensional runs. However, there is no appreciable difference between the blade shapes predicted by the fully three-dimensional and three-dimensional mean shear runs except close to the endwalls, and this difference is probably attributable to forcing the normal derivative of rothalpy at the hub and duct to zero for the fully three-dimensional runs (see Section 5.13) rather than any three-dimensional shear phenomena.

Figures 6.28 and 6.29 show the corresponding blade pressure distributions for the rotor-stator and contra-rotating propulsors respectively. In each instance the differences between the actuator duct results and the three-dimensional runs are far greater than the slight differences between the fully three-dimensional and three-dimensional mean shear results. This would seem to imply that the three-dimensional shear phenomena discussed in Section 5.11.2 are not significant for these two propulsors.

The development of circumferential variations in velocity predicted by the fully three-dimensional runs for the rotor-stator and contra-rotating propulsors are shown in Figures 6.30 and 6.31 respectively, the periodic flow within the blade passages being clearly visible in Figure 6.31; the results of the three-dimensional mean shear runs are indistinguishable from these plots, and so will not be presented here.

Figures 6.32, 6.33, 6.34 and 6.35 show the corresponding contours of rothalpy and drift function for both propulsors, the effect of circumferentially-averaging rothalpy

and drift function at the mixing plane (see Section 5.10) being visible in each instant. The development of circumferential variations in both rothalpy and drift function within the core flow can be seen to be very small for both propulsors. These plots are further evidence that the circumferential variations in shear vorticity are small for these propulsors. It should also be noted that the lack of significant circumferential variations in drift function is indicative of the relative unimportance of circumferential variations in velocity with these designs, and would suggest that the blades are lightly loaded.

The predicted mass flow and propulsor forces for the rotor-stator propulsor are given in Table 6.2, and those for the contra-rotating propulsor in Table 6.3. It will be seen that there is virtually no difference in both mass flow predictions between the fully three-dimensional, three-dimensional mean shear and actuator duct runs for either propulsor. Additionally, it will be noted that the two propulsors have near-identical (i.e. within less that 0.5%) mass flow rates; this perhaps would be expected they have a common duct and hub geometry, absorb the same shaft power, and have zero swirl at the duct trailing edge.

The shaft torques calculated by integrating the blade pressure jumps can be seen to differ by up to 7.5% from the theoretical values (obtained as the product of mass flow, shaft speed, and the overall change in $\overline{rV_\theta}$ induced by the blading). It must also be assumed that the values of blade thrust are similarly inaccurate, as these are calculated using a similar technique. Improved estimates of blade thrust and torque could have been obtained by conducting runs with additional mesh points on the blade, thereby improving the accuracy of the pressure integration. However, the limitations of the available computing facilities prevented this.

The values of shaft torque and overall propulsor thrust given by the fully three-dimensional, three-dimensional mean shear and actuator duct runs are within 0.5% of each other. In the case of the contra-rotating propulsor the predicted total propulsor thrust is some 7% higher than the rotor-stator propulsor (which absorbs almost the same shaft power), this being directly attributable to the quite substantial thrust sustained on its duct; the rotor-stator propulsor has a net drag on the duct, although its blades sustain a greater thrust than the contra-rotating propulsor.

It is interesting to note that although the two blade rows of the contra-rotating propulsor absorb the same shaft power, the downstream blade row's contribution to

the overall propulsor thrust is over 1.5 times that of the upstream blade row, due to the different blade angles on the downstream row.

Finally, a summary of computational times for the rotor-stator and contra-rotating propulsors is presented in Figures 6.36 and 6.37 respectively, showing the three-dimensional mean shear runs to be only marginally more time consuming than the actuator duct runs. The fully three-dimensional runs, which seem to offer no noticeable improvement in accuracy over the three-dimensional mean shear runs, require roughly 2.5 times as much computer time to converge.

6.3 Duct Only Runs

Actuator duct runs were conducted for the following interesting cases:-

(a) **Duct and Hub in a Sheared Onset Flow**
As for the merchant ship propulsor in Section 6.1, but in the absence of the blading i.e. no work done on the fluid.

(b) **Duct and Hub in a Uniform Onset Flow**
As for the arrangement outlined in Section 6.3.1, but with a uniform axial flow velocity on the far upstream boundary of 8.5m/s (16.5 Knots)

As in each of these cases there is no mechanism for the development of three-dimensional flow phenomena, actuator duct runs suffice.

The predicted streamline patterns, velocity vectors, and duct pressure distributions for the two cases are shown in Figures 6.38..6.40 and 6.41..6.43 respectively.

In each instance no work is done on the fluid, and as a result one would expect the velocity profile on the far downstream boundary to be identical to that far upstream, with zero jump in velocity across the duct wake. From figures 6.39 and 6.40 it can be seen that it is this which the method predicts. As a consequence these simple cases proved to be an ideal means of verifying both the implementation of the duct Kutta condition (as outlined in Section 5.5) and the corresponding mass flow predictions of the design method.

The duct pressure distributions (Figures 6.40 and 6.43) compare very well in overall form to that given by Falcao de Campos [5] for an isolated duct in uniform flow. In each instance a duct thrust is predicted (Table 6.4), although as with all the other runs, attention is drawn to the rather poor resolution of pressure close to the duct leading edge.

6.4 Concluding Comments

Due to the largely confidential nature of military and commercial applications of ducted propulsors, it has proved very difficult to obtain detailed full-scale design data for comparison with numerical results from the inverse design method. However, the author is confident that the generic test cases presented in Sections 6.1 and 6.2 are representative of existing full-scale propulsors. With respect to these results, the author offers the following concluding comments:-

1) In the numerical solution of the actuator duct and three-dimensional mean shear runs it is the determination of propulsor mass flow that dominates the computational procedure in terms of CPU time requirements. As a result the computational times for the three-dimensional mean shear runs presented in Figures 6.15, 6.36 and 6.37 are little different from the corresponding actuator duct runs that do not include three-dimensional effects.

   However, for the fully three-dimensional runs it is the solution of the block tridiagonal systems of equations (equations A6.5 and A6.6, Appendix VI) that dominates the solution process, resulting in the much greater computational times required for the fully three-dimensional runs when compared to the simplified runs. Additionally, storing the three-dimensional rothalpy and drift function fields is memory-intensive.

   When solving the block tridiagonal equations, storage requirements vary roughly in proportion to the number of Fourier harmonics taken, N, with solution times varying approximately in proportion to N^2. Thus, due to the limitations of the available computing facilities it was found necessary to limit N to no greater than 16, resulting in relatively poor resolution of the jumps in rothalpy at the blade (Figures 6.14, 6.32 and 6.33).

2) When compared to the three-dimensional runs, the actuator duct runs produce a very good estimate of overall propulsor performance (i.e. propulsor thrust, torque, mass flow, etc.), with reasonable estimates of such detailed characteristics such as blade shapes and blade pressure jumps being obtained.

3) The fully three-dimensional runs seem to yield little improvement in propulsor flow field and blade shape estimates over the three-dimensional mean shear runs which neglect the circumferential variations in rothalpy and drift function.

   The only noticeable differences between the predictions of the two three-dimensional approaches are in the vicinity of the hub and duct, and would seem to be more a result of forcing the normal derivative of rothalpy to zero here (see Section 5.13 and Appendix VII), than due to any three-dimensional shear phenomena.

4) Bearing in mind the above comments, it might reasonably be concluded that for practical marine ducted propulsor design three-dimensional mean shear runs of the inverse design method generally suffice.

   Allied to this, the effects of circumferential variations in shear vorticity suggested by the theoretical work of Hawthorne [2], Hawthorne and Armstrong [3], and Horlock and Lakshminarayana [4] would seem to be sufficiently small to be neglected in ducted propulsor blade design, at least for cases of axisymmetric onset flow.

   It should be noted, however, that no conclusions can be drawn regarding the significance of three-dimensional shear phenomena at off-design conditions.

5) For submarine propulsors restrictions on propulsor weight together with the desire to utilise boundary layer inflow to best effect [6] mean that duct diameter is limited, and as a consequence the mass flow rate is relatively low for the shaft power. However, minimising acoustic signature is of prime concern for this type of application, and therefore a relatively large number of lightly loaded blades is usually adopted.

   One might also reach similar conclusions for surface warships, where although duct diameter is restricted by both the relatively shallow draught of these

vessels and the twin shaft configuration usually adopted, limiting propulsor noise is again of key importance.

For large merchant ships of deep draught, restrictions on propulsor diameter and weight are less pressing. Consequently large duct diameters and correspondingly high propulsor mass flows are desirable on grounds of propulsive efficiency (i.e. minimising "jet wake loss") [7]. Whilst usually only a single blade row configuration with a maximum of six blades is adopted on grounds of cost, avoidance of cavitation is a key factor in the choice of blade loading. Thus for large merchant ship applications one might assume that a relatively small number of large area, relatively lightly-loaded blades are adopted.

The adoption of relatively light blade loadings in each of these instances in some way helps to explain the relative insignificance of three-dimensional flow phenomena in the ducted propulsor designs outlined in this Chapter.

However, it should be noted that ducted propulsors for towing vessels such as a tugs or trawlers may be designed for a static ("bollard pull") condition (the extension of the inverse design method to deal with such cases is considered in Chapter 8). Under such circumstances the undisturbed onset flow is zero, and very high blade loadings may result. Thus, three-dimensional shear effects may well be significant in such instances, although it is quite likely that flow cavitation would be more of a concern.

6) It is generally found that using the procedure outlined in Section 5.7 to explicitly satisfy the Kutta condition at the blade trailing edge involves only slight modifications to the specified blade $\overline{rV_\theta}$ distribution provided that:-

   (a) The specified $\overline{rV_\theta}$ distribution satisfies the condition $\overline{rV_{\theta_\xi}}=0$ at the blade trailing edge;

   (b) The mesh quasi-streamlines align approximately with the final meridional velocity at the blade trailing edge.

7) It should be noted that, taken in isolation, circumferential variations in drift function are not indicative of the three-dimensional shear effects discussed in

[2], [3] and [4], as they occur even in cases where shear is absent (i.e. $\nabla H = 0$).

8) Whilst for brevity the duct pressure distributions presented in this Chapter are based on mean flow variables, it should be noted that the three-dimensional methods enable the circumferential variation of duct pressure to be evaluated if required.

9) Unfortunately little information on the avoidance of flow separation on propulsor ducts was found in the available literature (Chapter 2). As a consequence no assessment of the suitability of the duct profiles adopted in this Chapter can be made. However, the duct pressure distributions for the merchant ship propulsor (Figures 6.8 and 6.9) compare well in overall form to those presented by Gibson and Lewis [8] and Falcao de Campos [5] for ducted propellers mounted on afterbodies in the absence of shear flow.

10) It should also be stressed that the results presented in this Chapter are based on an assumption of inviscid flow. Unfortunately no means were available for assessing the effect flow viscosity and the associated duct, hub and blade boundary layers would have on the predicted results, although it would certainly be wrong to assume that these effects are negligible.

References

1) Andersen,O., Tani,M. "Experience with S.S. Golar Nichu", Symposium On Ducted Propellers, RINA, Summer 1973

2) Hawthorne,W.R. "Rotational Flow Through Cascades. Part I : The Components of Vorticity", pp266-279, Quart. Journ. of Mech. & Appl. Math., Vol.8, 1955

3) Hawthorne,W.R., Armstrong,W.D. "Rotational Flow Through Cascades. Part II : The Circulation About the Cascade", pp280-292, Quart. Journ. of Mech. & Appl. Math., Vol.8, Part 3, 1955

4) Horlock,J.H., Lakshminarayana,B. "Secondary Flows: Theory, Experiment, and Application in Turbomachinery Aerodynamics", Annual Review of Fluid Mechanics, Vol.5, 1973

5) Falcao de Campos,J.A.C., "On the Calculation of Ducted Propeller Performance in Axisymmetric Flows", Technical Report 696, Netherlands Ship Model Basin, Wageningen, The Netherlands, 1983

6) Friedman,N. "Submarine Design and Development", p.88, Conway Maritime Press, 1984

7) Clayton,B.R, Bishop,R.E.D. "Mechanics of Marine Vehicles", p.358, E. & F.N. Spon Ltd., London, 1982

8) Gibson,I.S., Lewis,R.I. "Ducted Propeller Analysis by Surface Vorticity and Actuator Disc Theory", Symposium on Ducted Propellers, RINA, Summer 1973

Run Type:	Actuator Duct	3D Mean Shear	Fully 3D
Mass Flow Rate (Tonnes/Second)	556.09	556.23	556.52
Shaft Torque (kNm)	1805.0	1806.8	1807.1
Shaft Power (MW)	25.518	25.543	25.547
Total Blade Thrust (kN)	1748.8	1744.3	1744.3
Duct Thrust (kN)	847.90	847.57	847.91

NB

1) Values Based On a Sea Water Density of 1.025 Tonnes/m^3.

2) The values of duct thrust shown are based on circumferentially-averaged flow quantities.

Table 6.1: Predicted Mass Flow Rates, Propulsor Forces and Shaft Power for the Merchant Ship Ducted Propulsor

Run Type:	Actuator Duct	3D Mean Shear	Fully 3D
Mass Flow Rate (Tonnes/Second)	130.27	130.17	130.15
Rotor Torque (kNm)	1217.4	1212.8	1214.5
Theoretical Rotor Torque (kNm)	1107.3	1106.5	1106.4
Stator Torque (kNm)	-1188.5	-1188.0	-1187.5
Theoretical Stator Torque (kNm)	-1107.3	-1106.5	-1106.4
Theoretical Shaft Power (MW)	11.073	11.065	11.064
Rotor Thrust (kN)	1176.0	1166.8	1166.1
Stator Thrust (kN)	236.7	236.0	236.8
Duct Thrust (kN)	-35.9	-25.8	-24.8
Total Thrust (kN)	1376.8	1377.0	1378.1

NB

1) Values Based On a Sea Water Density of 1.025 Tonnes/m^3.

2) The values of duct thrust shown are based on circumferentially-averaged flow quantities.

Table 6.2: Predicted Mass Flow Rates, Propulsor Forces and Shaft Power for the Rotor-Stator Submarine Propulsor

Run Type:	Actuator Duct	3D Mean Shear	Fully 3D
Mass Flow Rate (Tonnes/Second)	130.29	130.21	130.22
Upstream Blade Row Torque (kNm)	1166.1	1158.8	1160.5
Theoretical Upstream Blade Row Torque (kNm)	1107.5	1106.8	1106.9
Downstream Blade Row Torque (kNm)	-1223.2	-1220.0	-1219.2
Theoretical Downstream Blade Row Torque (kNm)	-1107.5	-1106.8	-1106.9
Theoretical Total Shaft Power (MW)	11.075	11.068	11.069
Upstream Blade Row Thrust (kN)	478.9	472.5	471.3
Downstream Blade Row Thrust (kN)	784.5	782.2	781.5
Duct Thrust (kN)	208.7	211.5	221.4
Total Thrust (kN)	1472.1	1466.2	1474.2

NB

1) Values Based On a Sea Water Density of 1.025 Tonnes/m^3.

2) The values of duct thrust shown are based on circumferentially-averaged flow quantities.

Table 6.3: Predicted Mass Flow Rates, Propulsor Forces and Shaft Power for the Contra-Rotating Submarine Propulsor

Run Type:	Duct & Hub in Shear Flow	Duct & Hub in Uniform Flow
Mass Flow Rate (Tonnes/s)	310.48	406.43
Duct Thrust (kN)	391.11	394.72

(Values Based On a Sea Water Density of 1.025 Tonnes/m^3)

Table 6.4: Predicted Mass Flow Rates and Duct Forces for the Duct Only Runs

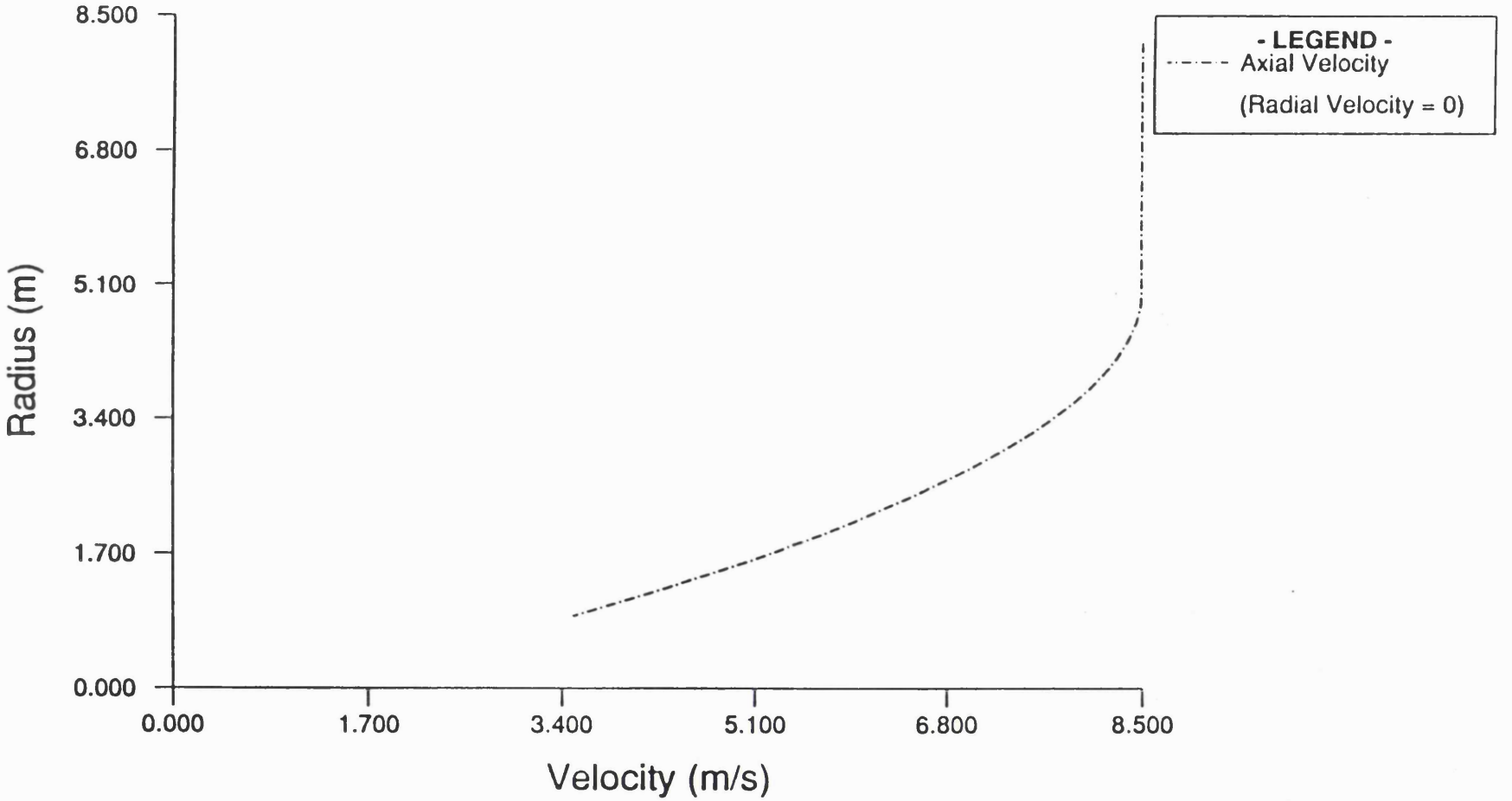

Figure 6.1: Far Upstream Velocity Profile for the Merchant Ship Propulsor

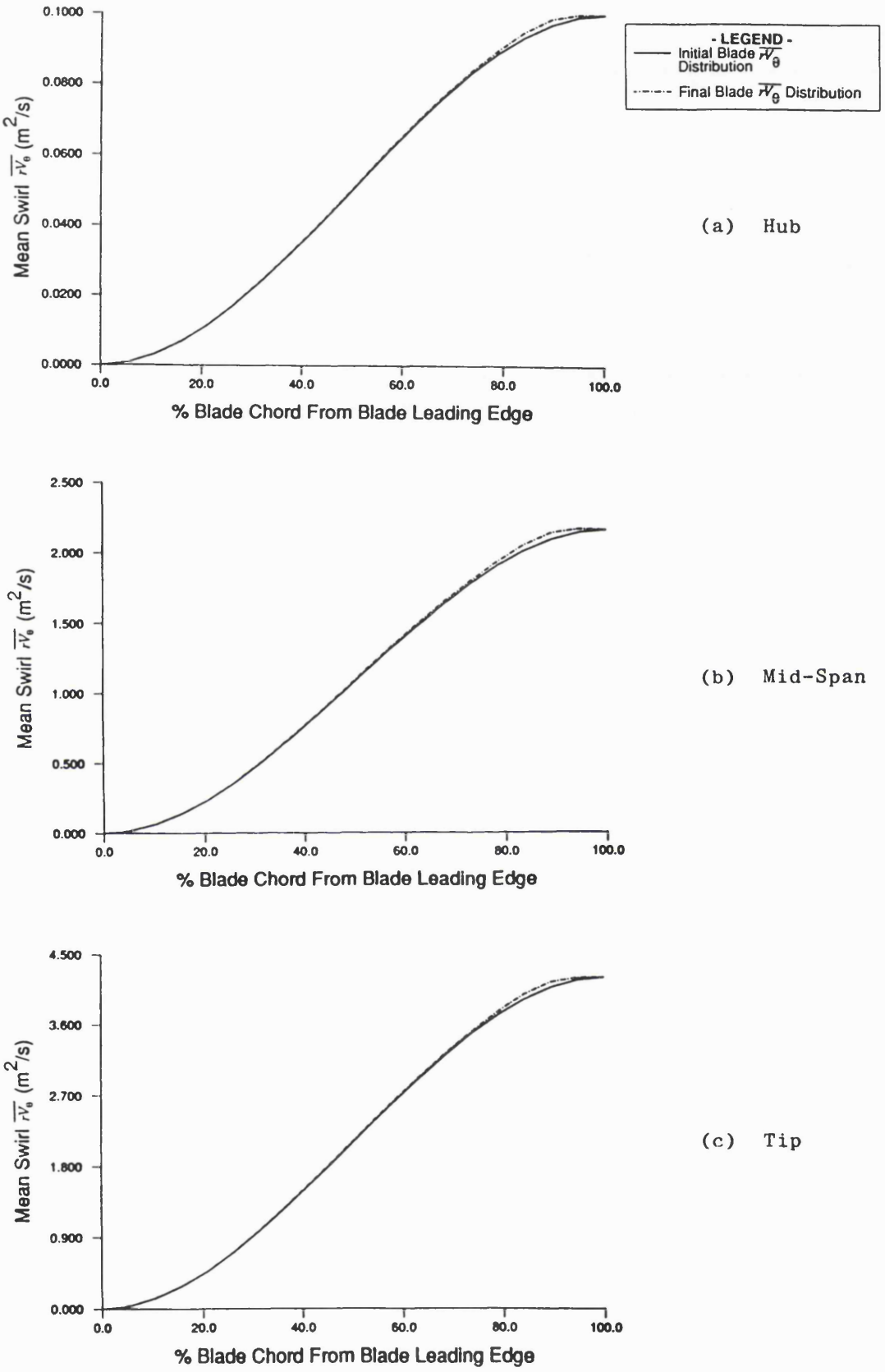

Figure 6.2: Comparison of Initial and Final $\overline{rV_\theta}$ Distributions for the Fully Three-Dimensional Run of the Merchant Ship Propulsor

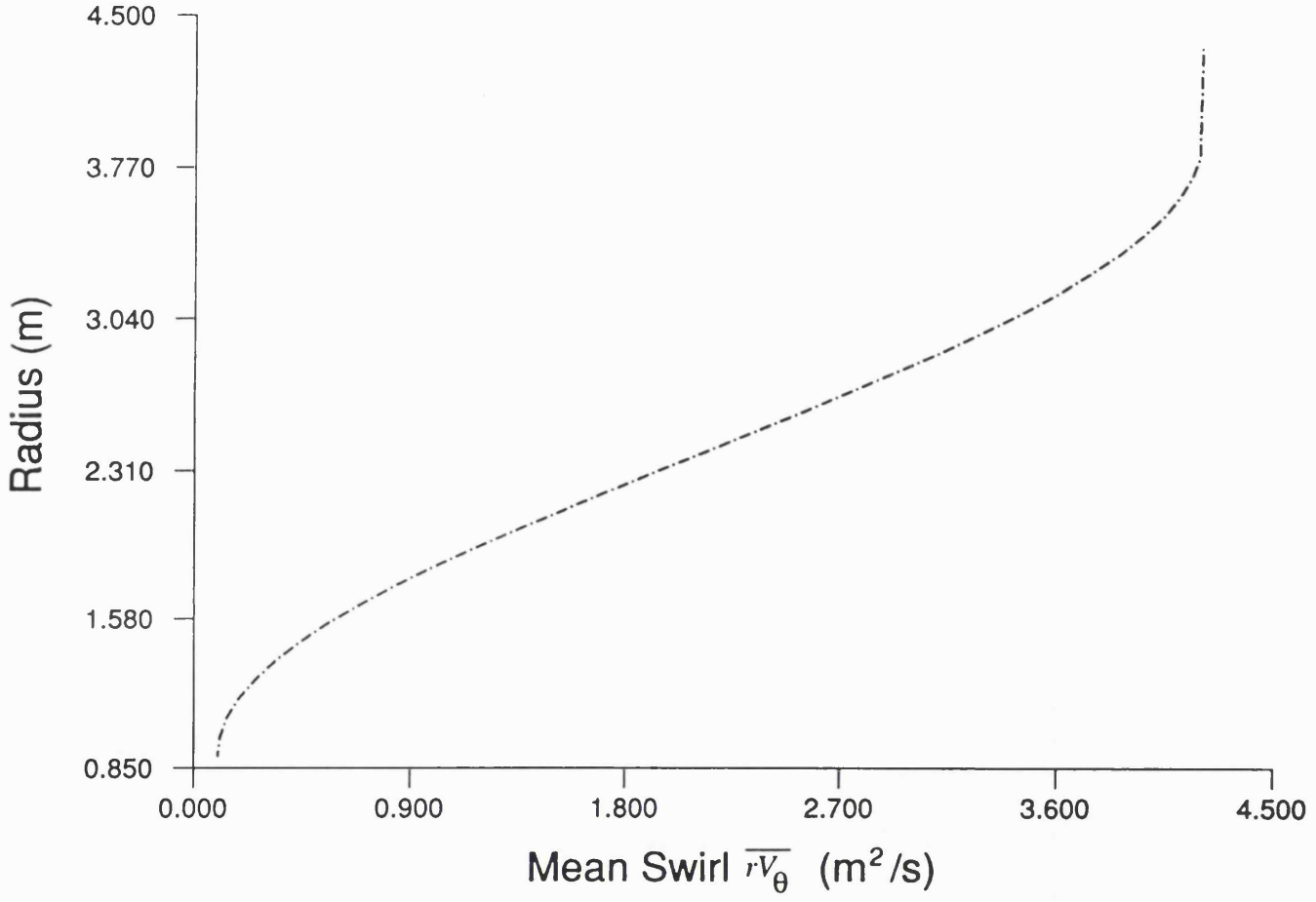

Figure 6.3: The $\overline{rV_\theta}$ Distribution at the Blade Trailing Edge for the Merchant Ship Propulsor

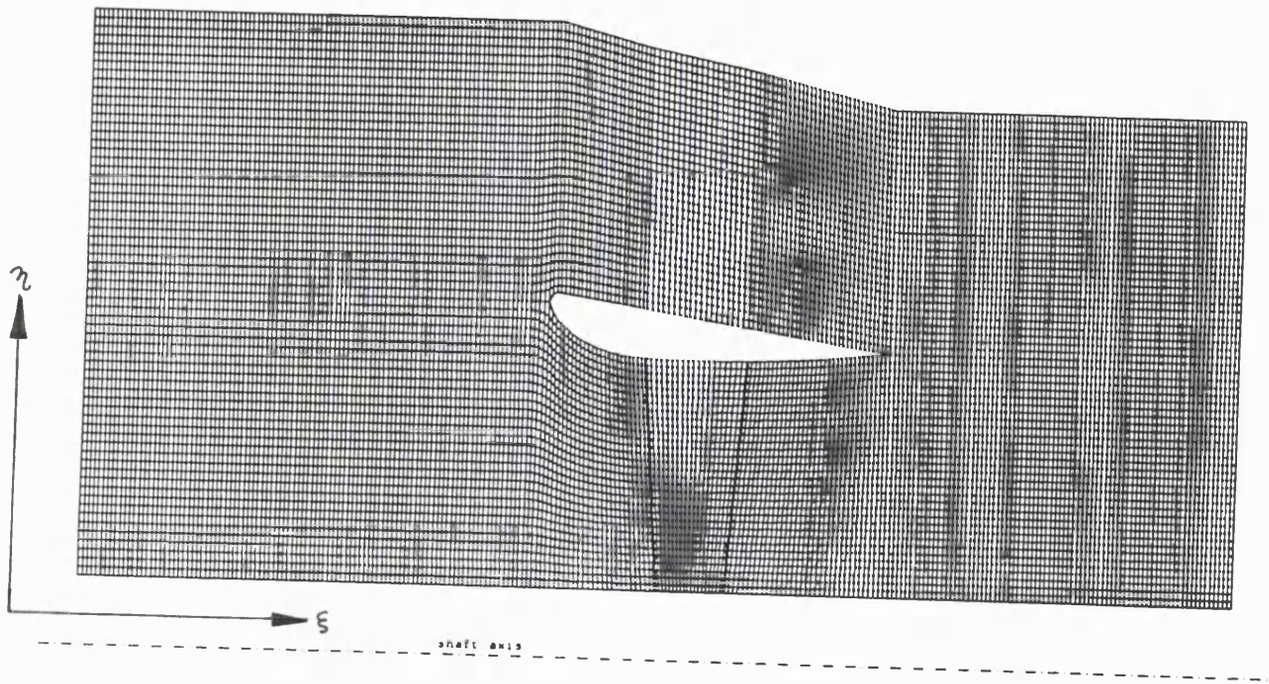

Figure 6.4: Initial Meridional Mesh for the Merchant Ship Propulsor

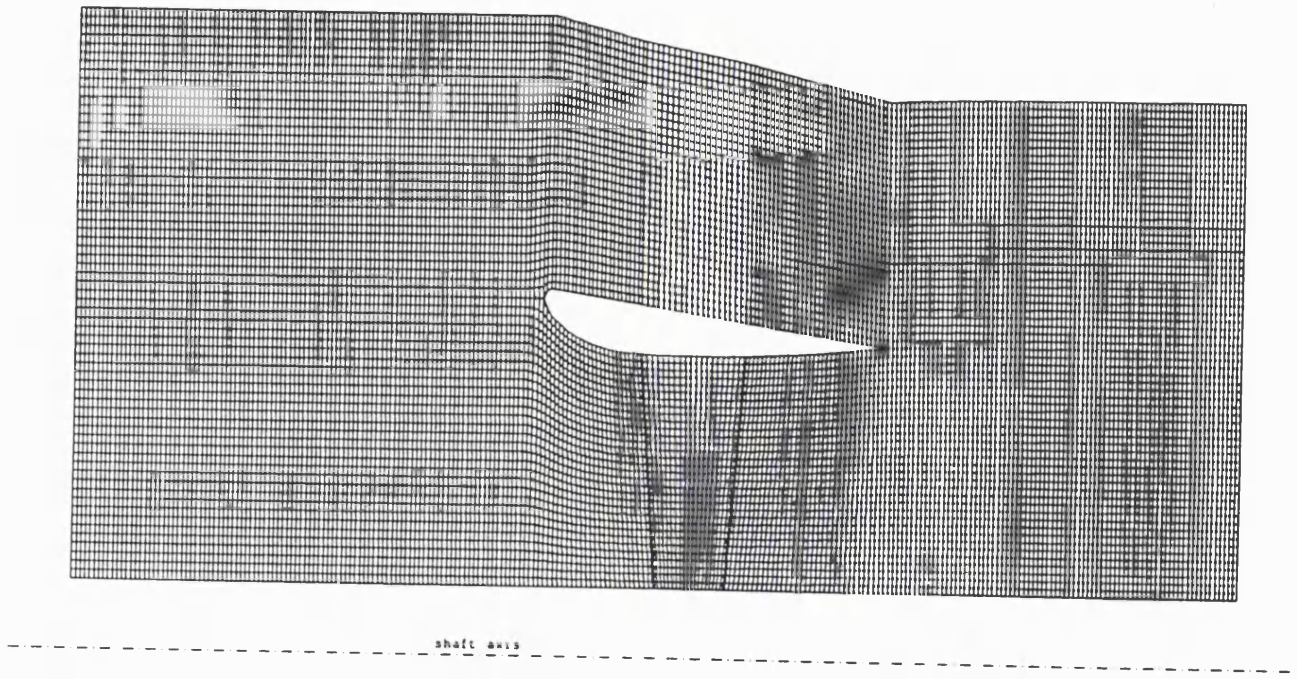

Figure 6.5: Meridional Mesh as Output from the Fully Three-Dimensional Run of the Merchant Ship Propulsor

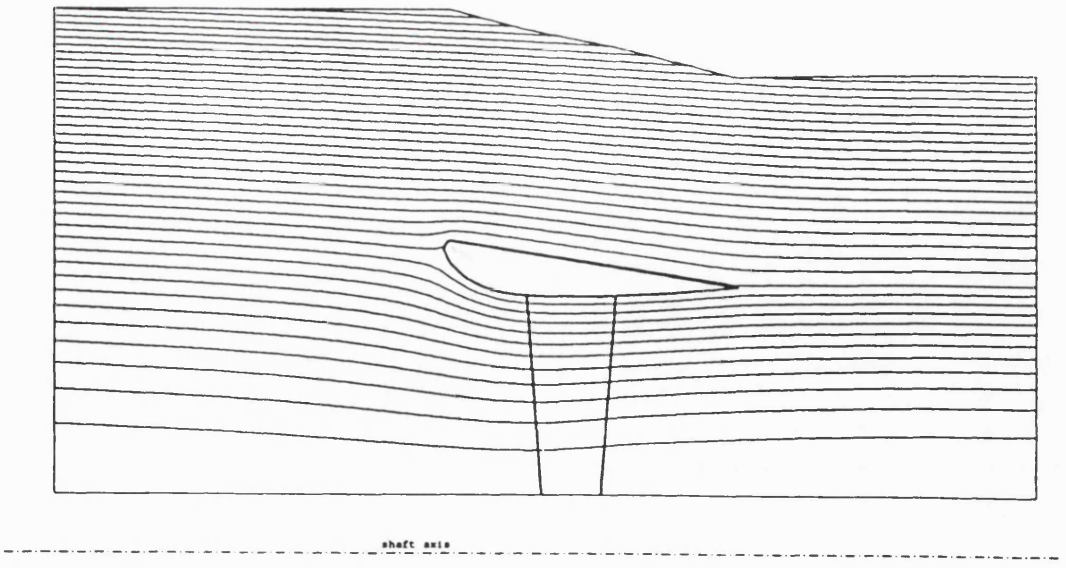

Figure 6.6: Mean Streamline Patterns Predicted by the Fully Three-Dimensional Run of the Merchant Ship Propulsor

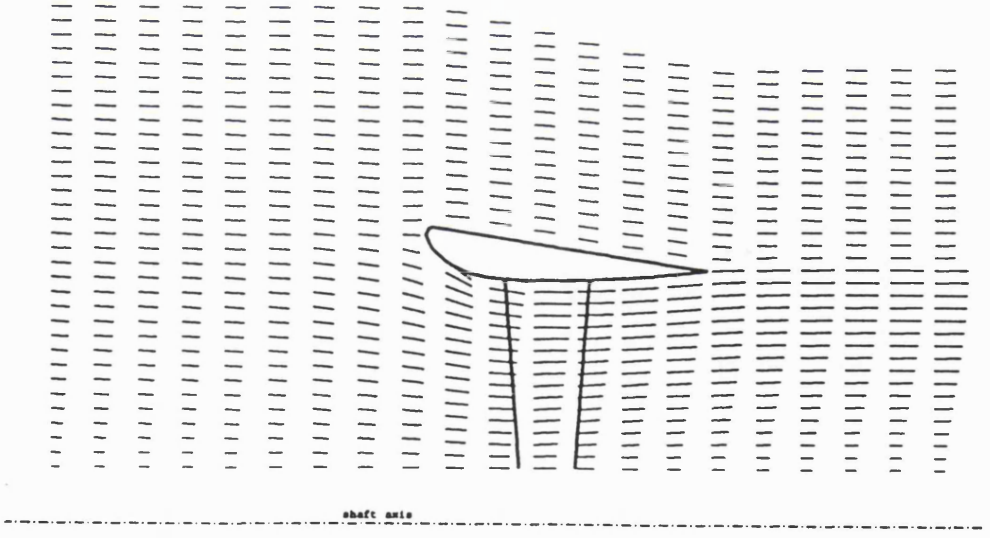

Figure 6.7: Mean Velocity Vectors Predicted by the Fully Three-Dimensional Run of the Merchant Ship Propulsor

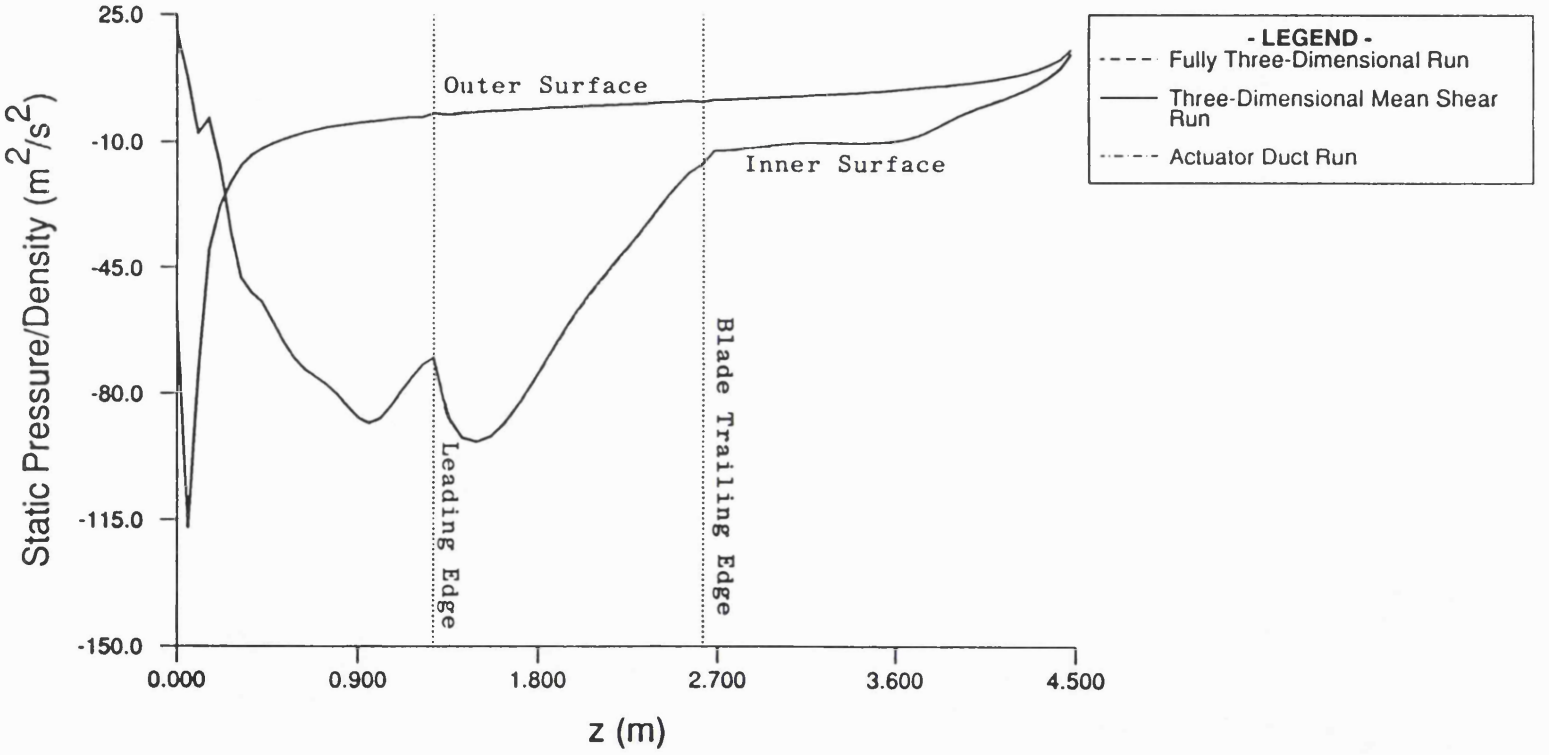

Figure 6.8: Predicted Duct Pressure Distribution (Based on Mean Flow Quantities) for the Merchant Ship propulsor

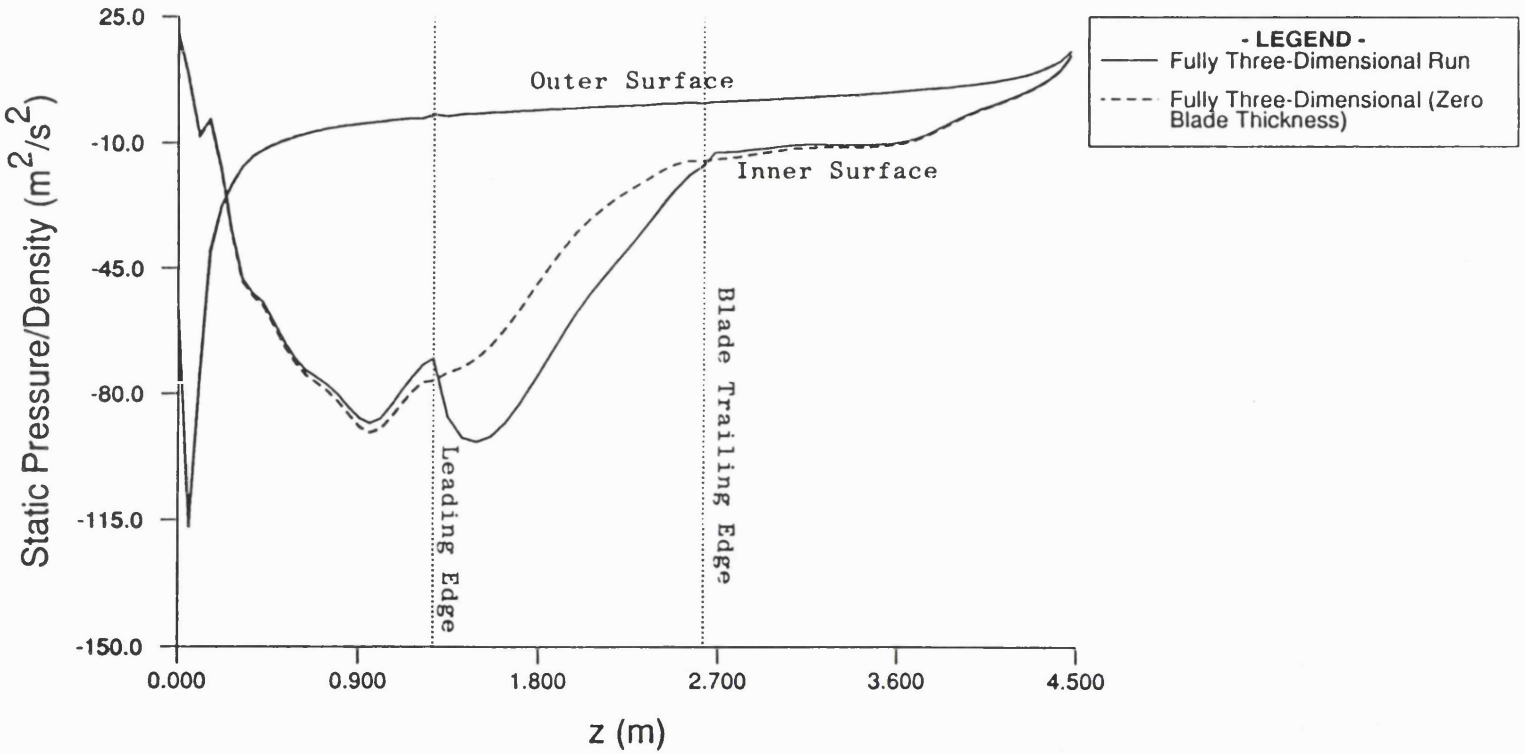

Figure 6.9: The Effect of Blade Thickness on the Predicted Duct Pressure Distribution Shown in Figure 6.8

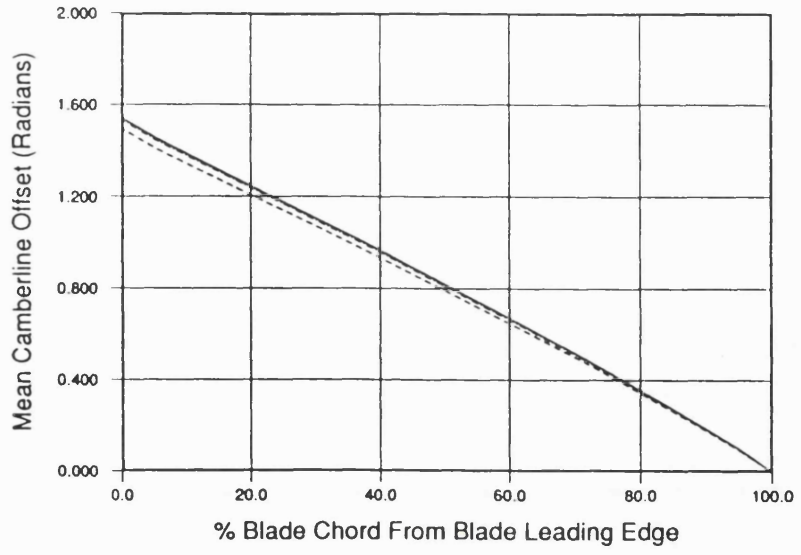

(a) Hub

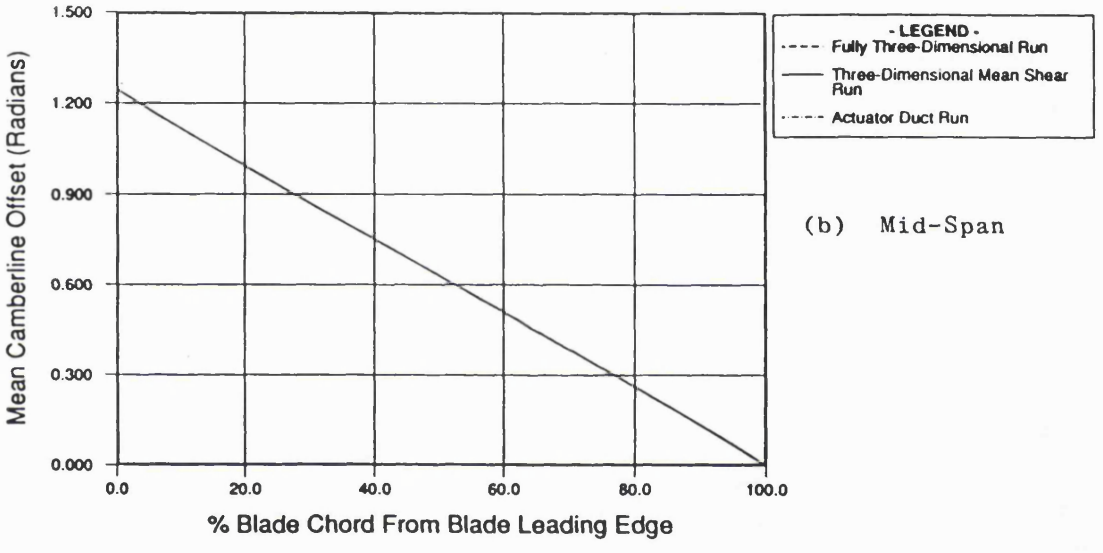

(b) Mid-Span

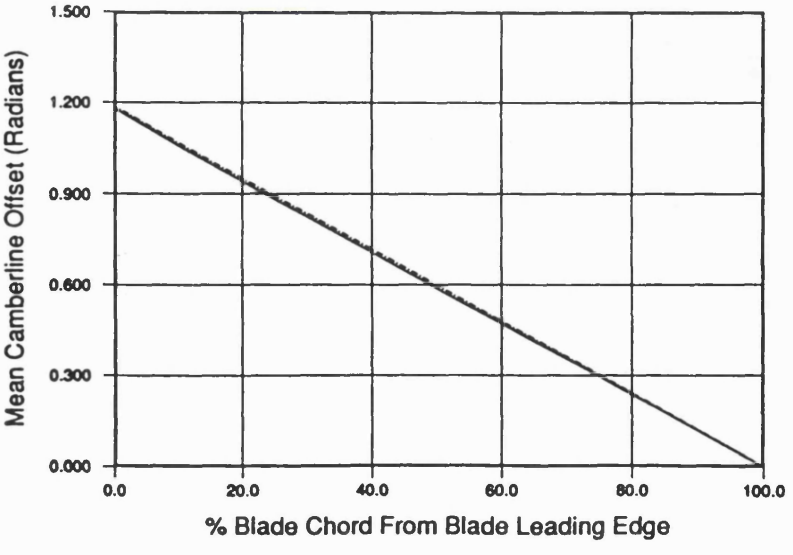

(c) Tip

Figure 6.10: Predicted Blade Shapes for the Merchant Propulsor (Plots Along Quasi-Streamlines)

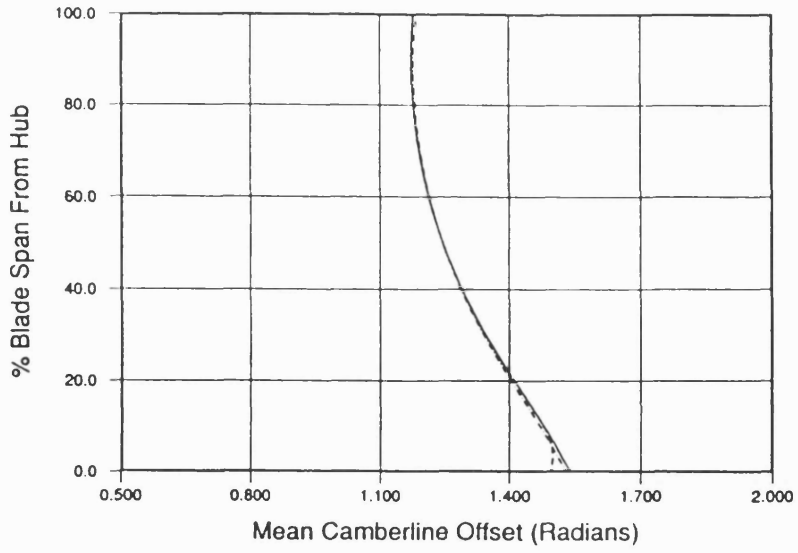

(a) Blade Leading Edge

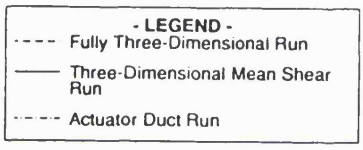

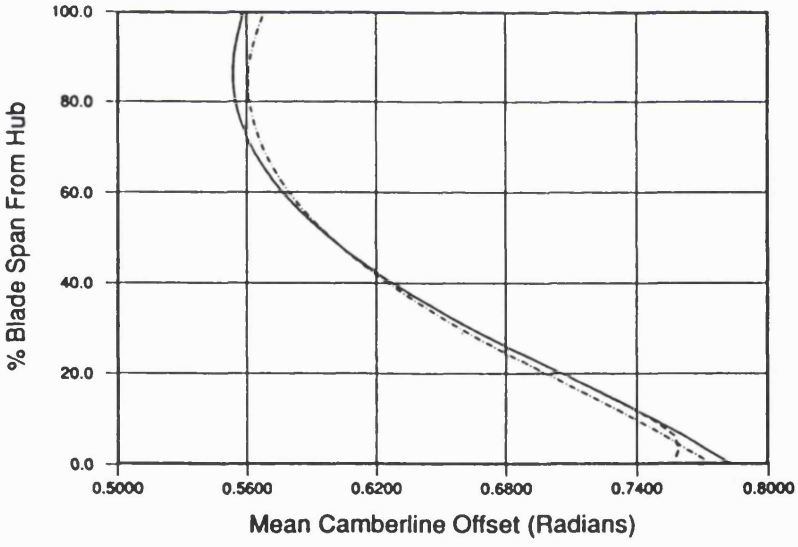

(b) Blade Mid-Chord

Figure 6.11: Predicted Blade Shapes for the Merchant Ship Propulsor (Plots Along Quasi-Orthogonals)

NB The Blade Trailing Edge is Defined to be Radial

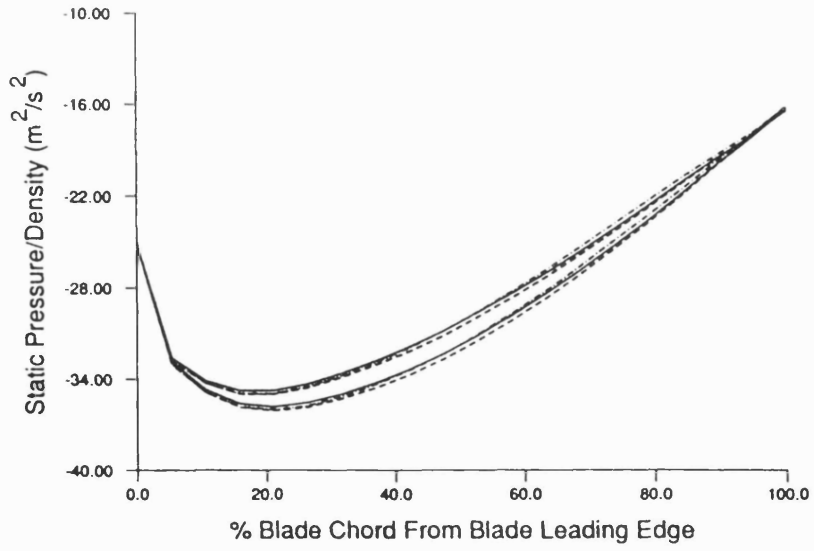

(a) Hub

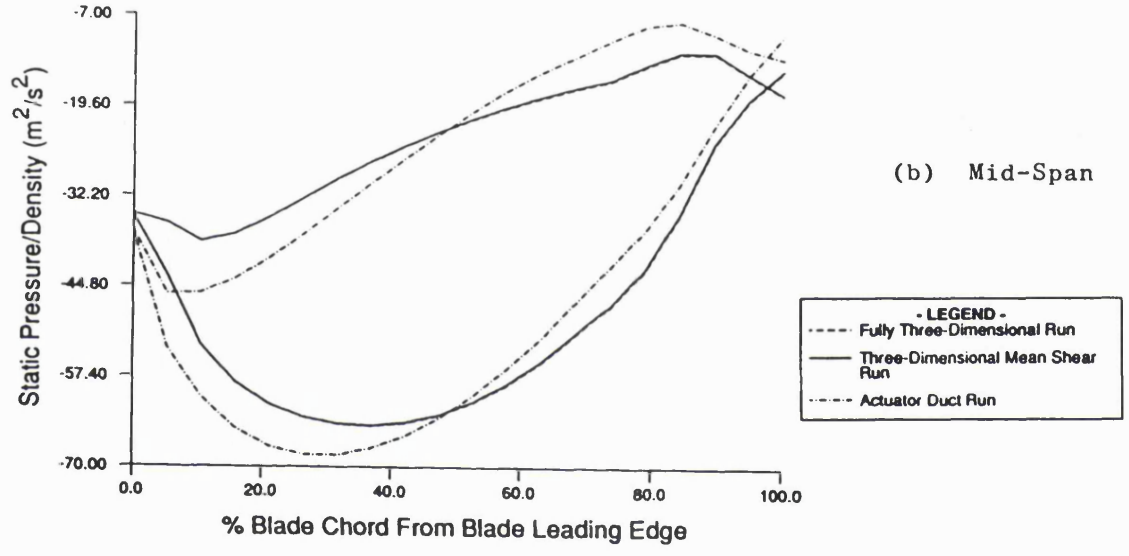

(b) Mid-Span

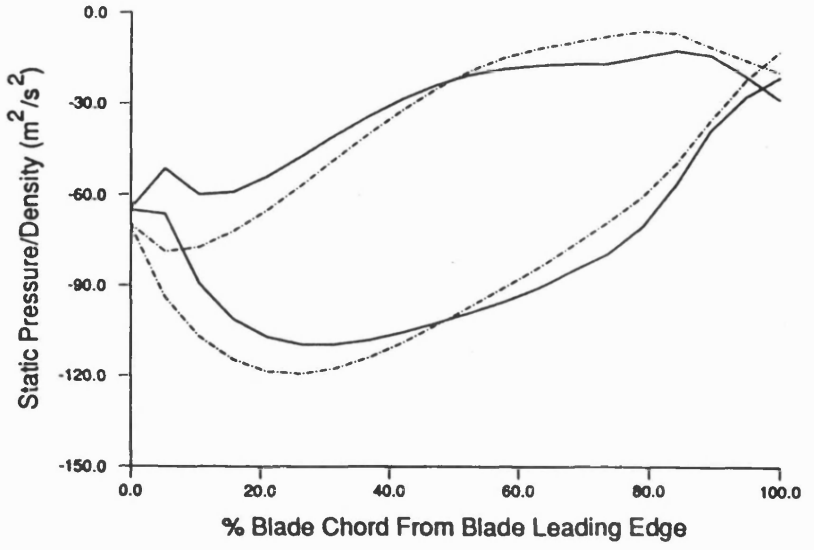

(c) Tip

Figure 6.12: Predicted Blade Pressure Distributions for the Merchant Ship Propulsor

Figure 6.13: Relative Velocity Vectors in the Transverse (r-θ) Plane as Predicted by the Three-Dimensional Runs of the Merchant Ship Propulsor

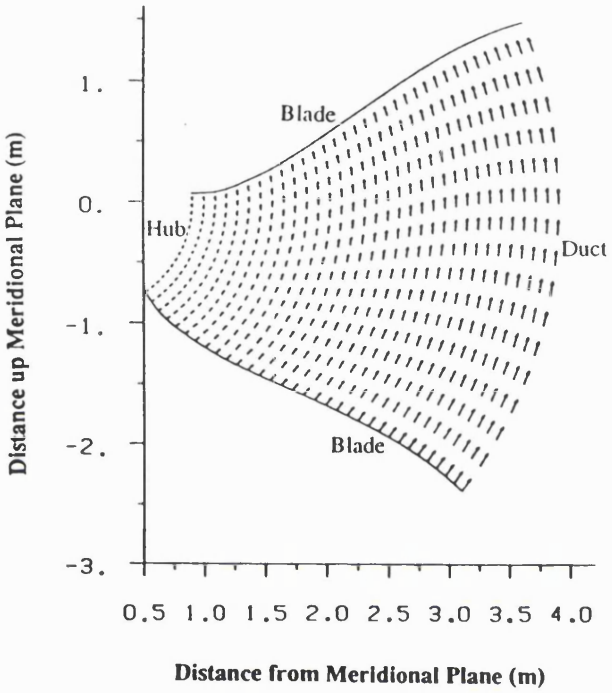

Fully 3D Run

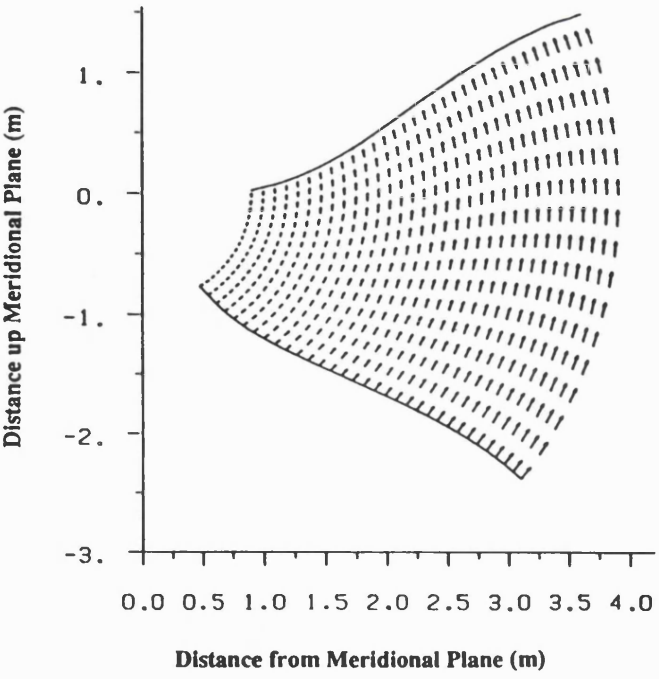

3D Mean Shear Run

(a) Blade Leading Edge

Figure 6.13 (Continued)

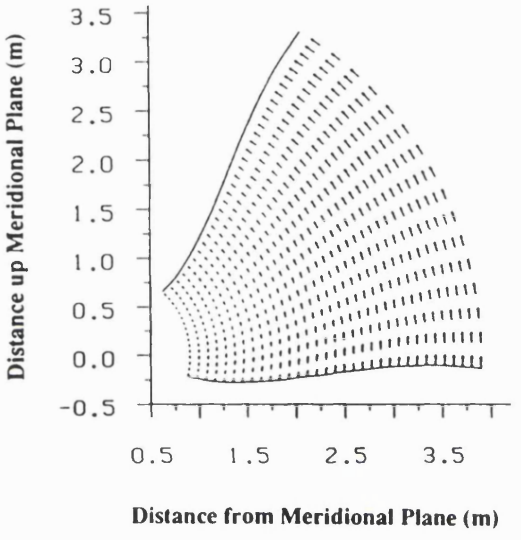

Fully 3D Run

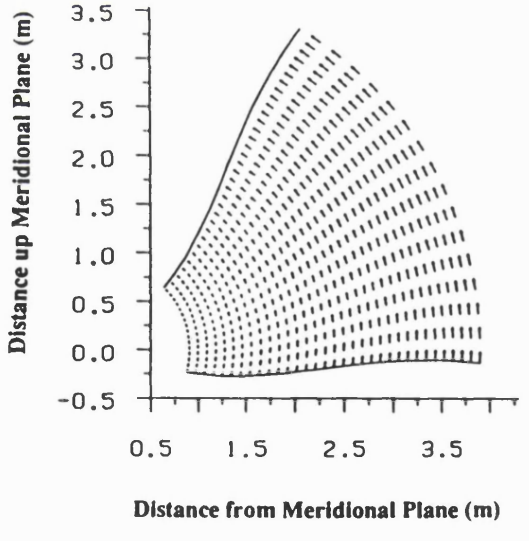

3D Mean Shear Run

(b) Blade Mid-Chord

Figure 6.13 (Continued)

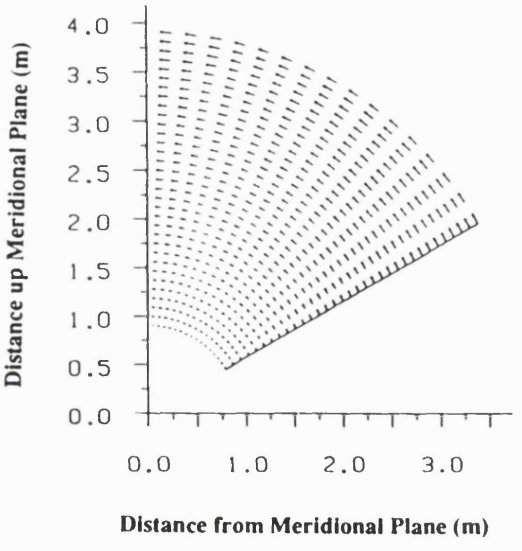

Fully 3D Run

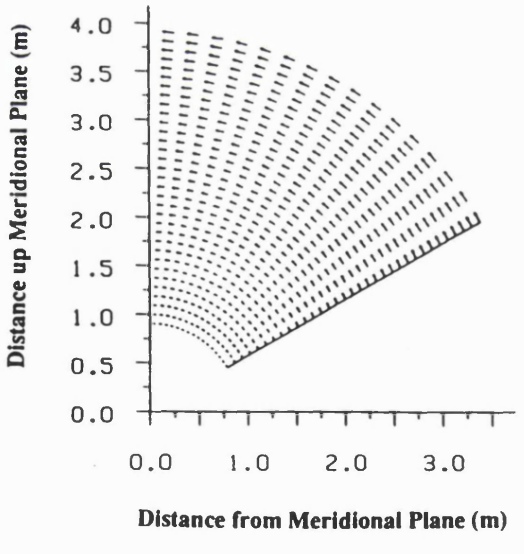

3D Mean Shear Run

(c) Blade Trailing Edge

Figure 6.13 (Continued)

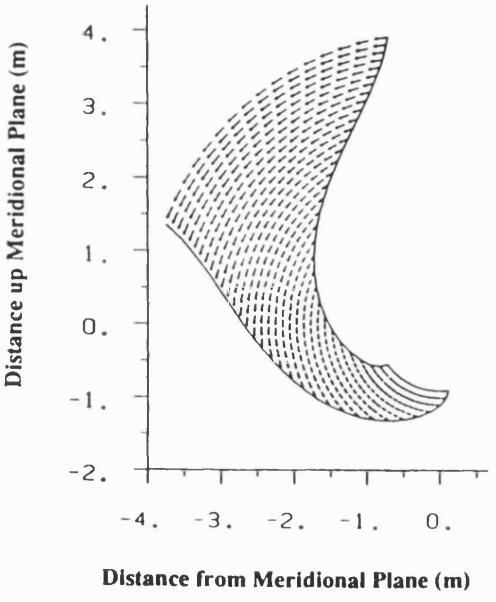

3D Mean Shear Run

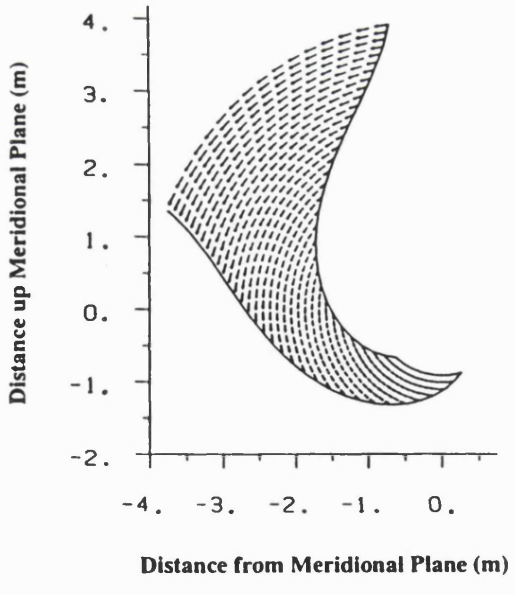

3D Mean Shear Run

(d) Duct Trailing Edge

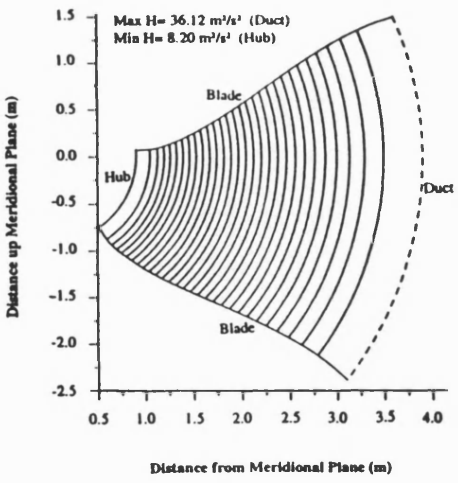

(a) Blade Leading Edge

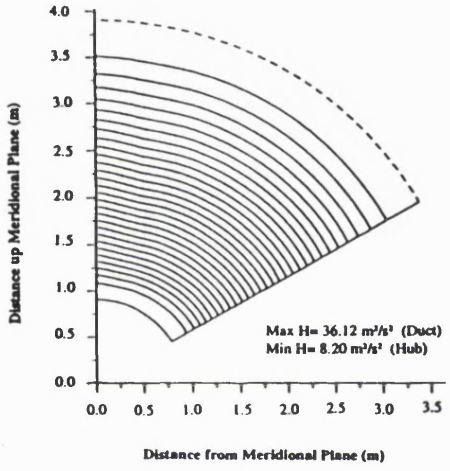

(b) Blade Trailing Edge

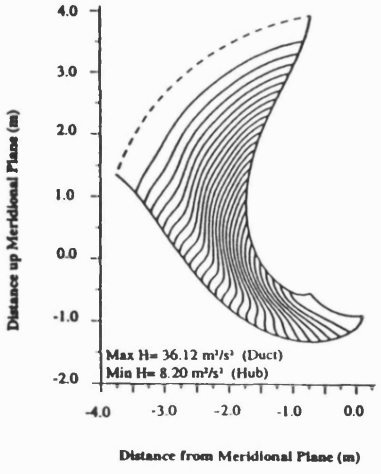

(c) Duct Trailing Edge

NB

Number of Contours per Plot = 30

Figure 6.14: Contours of Rothalpy in the Transverse (r-θ) Plane for the Merchant Ship Propulsor

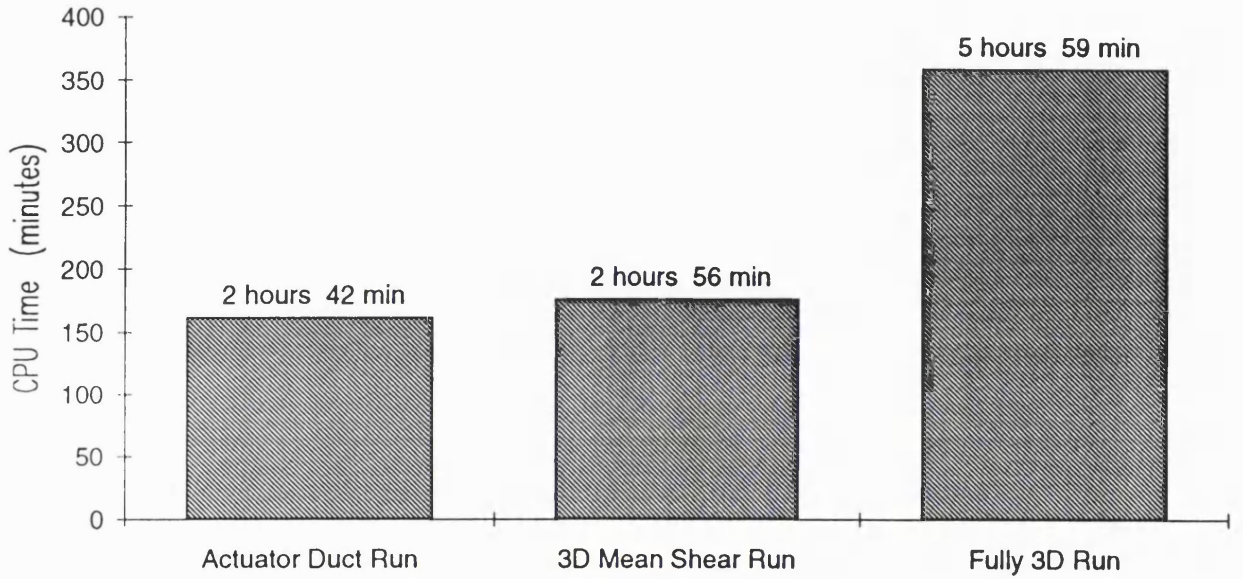

NB

1) Runs Conducted on a VAXstation 4000VLC
2) Times Based on an Initial Estimate for Propulsor Mass Flow of 502 Tonnes/second

Figure 6.15: Computational Times for the Merchant Ship Propulsor

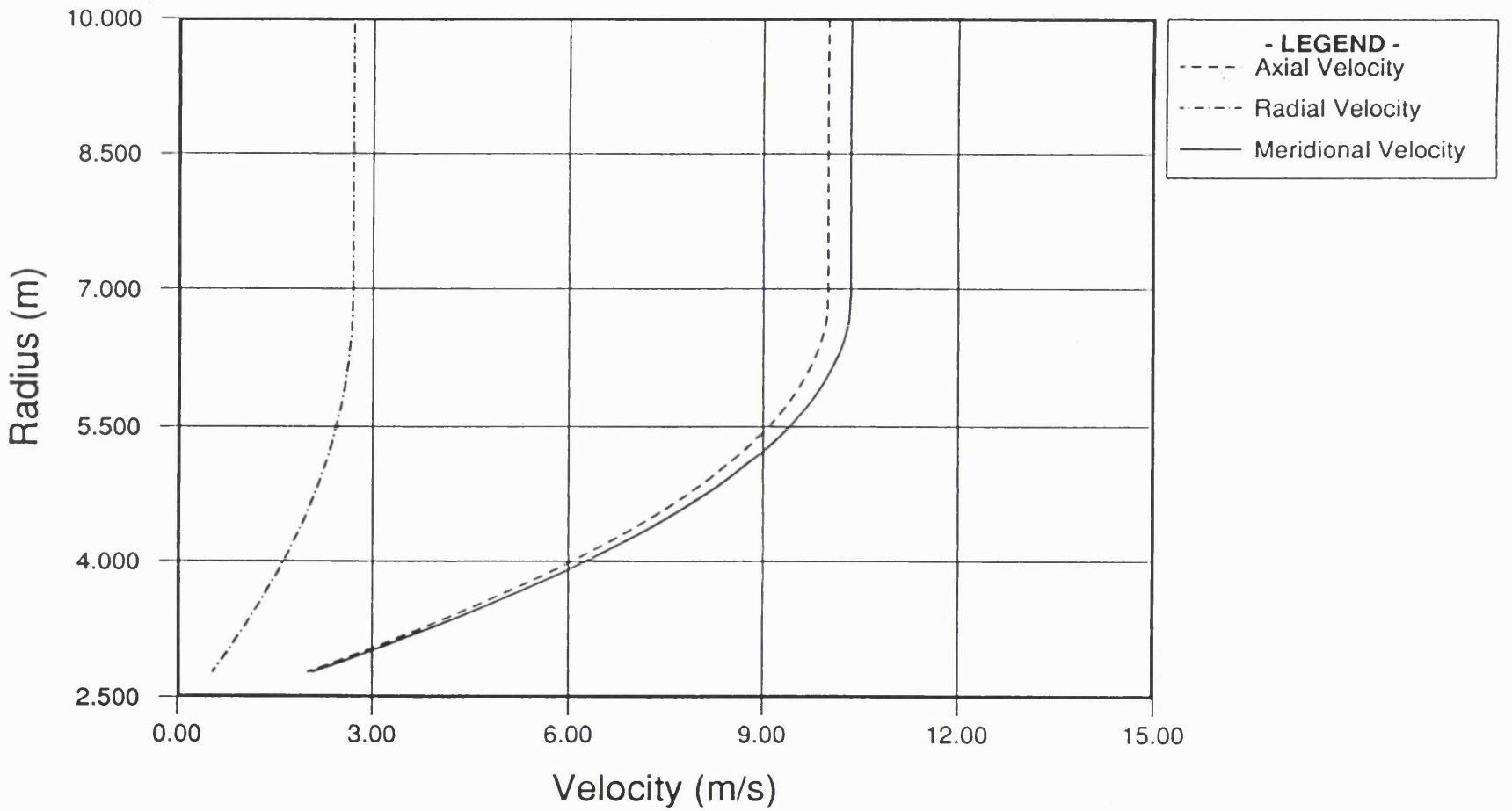

Figure 6.16: Far Upstream Velocity Profile for the Generic Submarine Propulsors

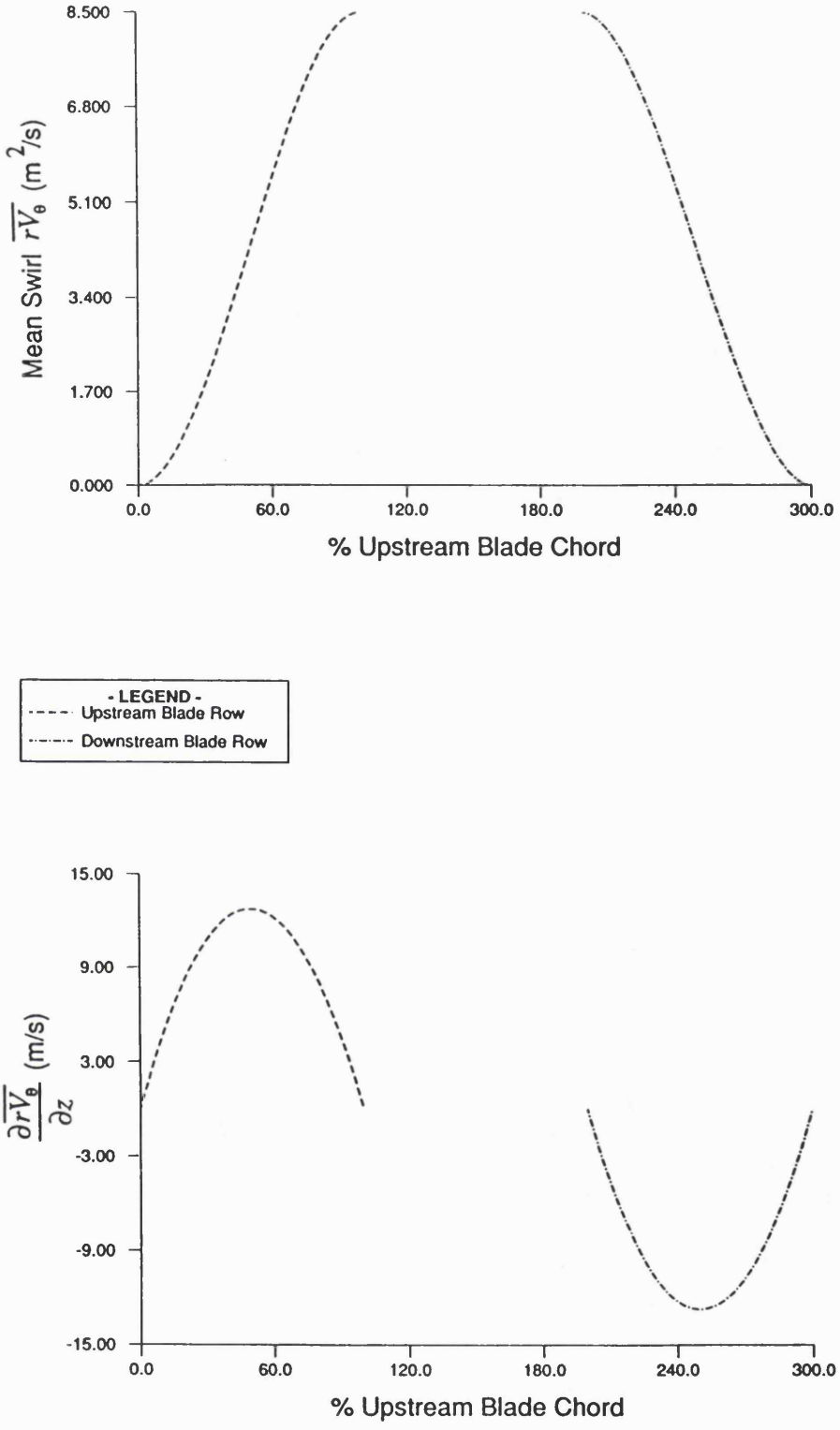

Figure 6.17: Blade Circulation Distribution (in Terms of $\overline{rV_\theta}$) for the Generic Submarine Propulsors

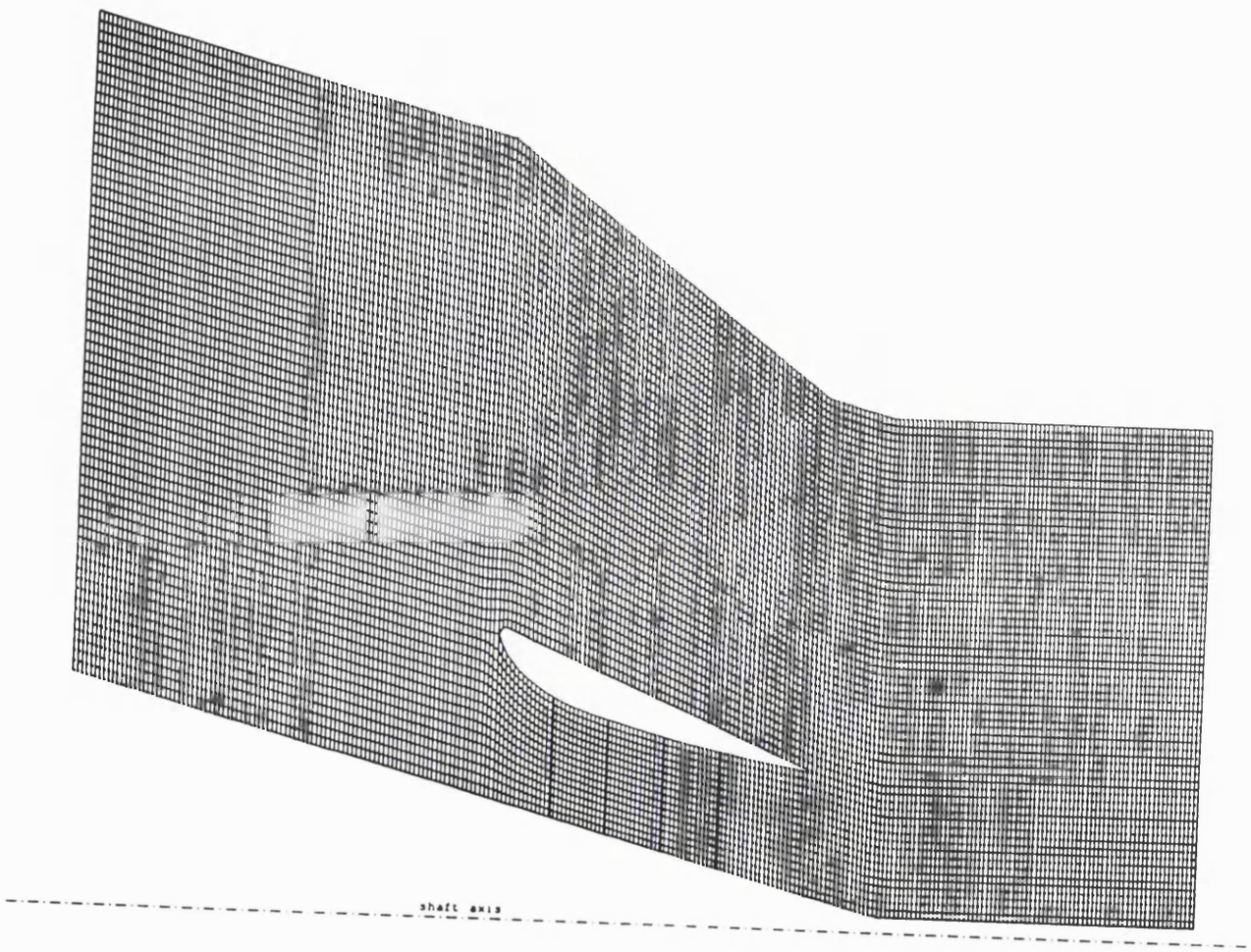

Figure 6.18: Meridional Mesh for the Rotor-Stator and Contra-Rotating Submarine Propulsors

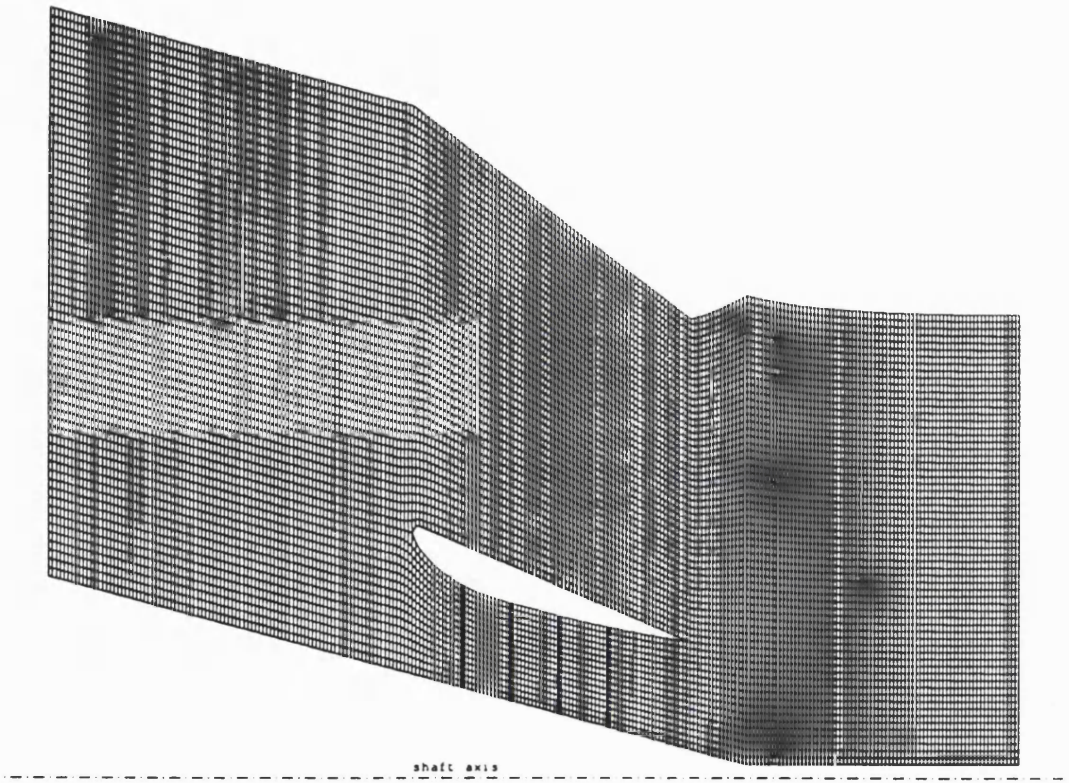

Figure 6.19: Meridional Mesh as Output from the Fully Three-Dimensional Run of the Rotor-Stator Submarine Propulsor

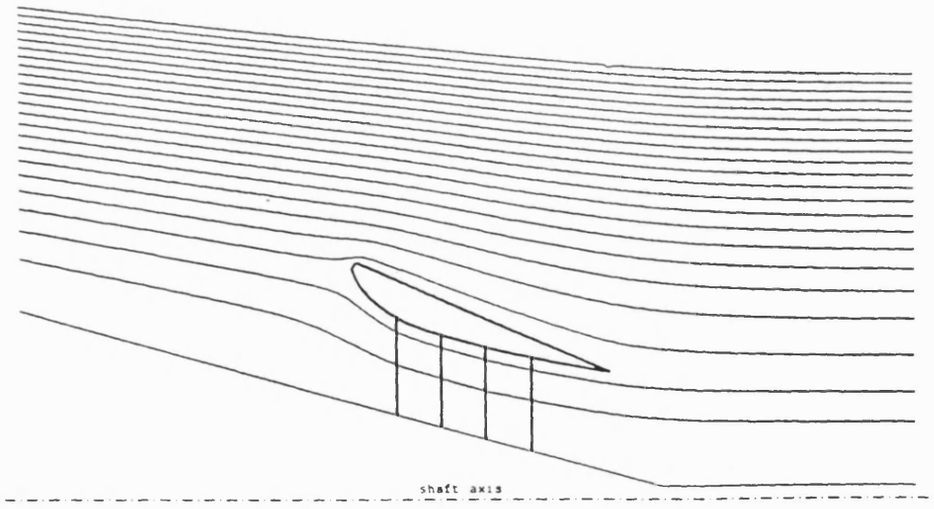

(a) Rotor-Stator Propulsor

Figure 6.20: Mean Streamline Patterns Predicted by the Fully Three-Dimensional Runs of the Generic Submarine Propulsors

(b) Contra-Rotating Propulsor

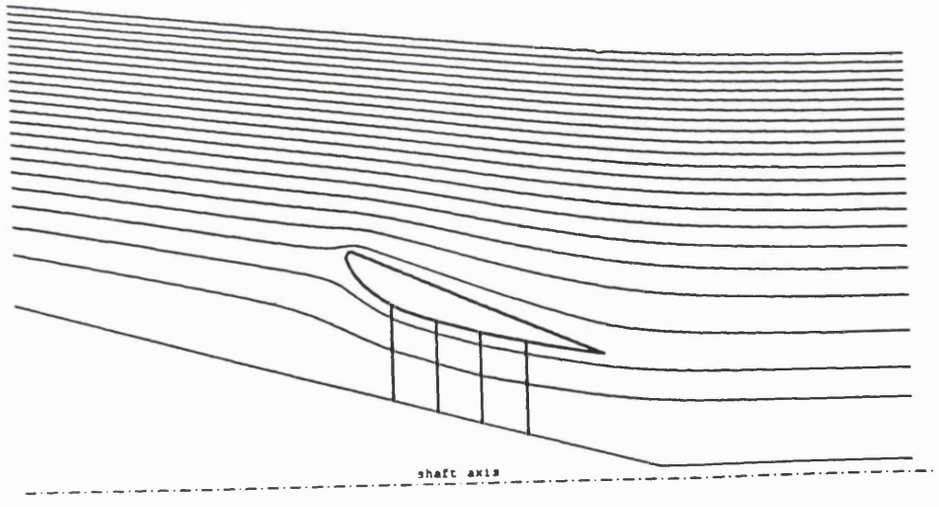

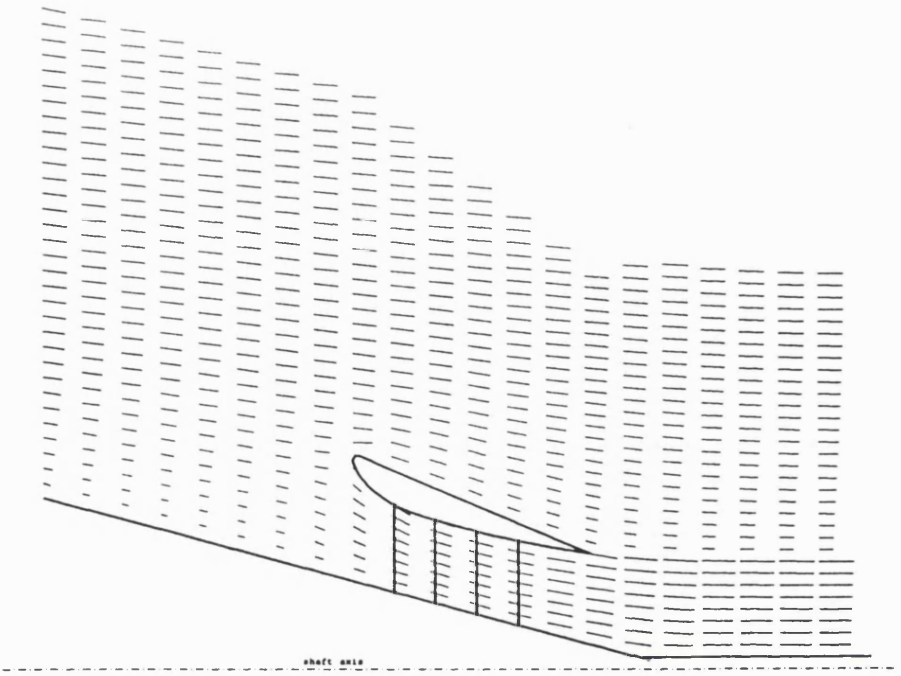

(a) Rotor-Stator Propulsor

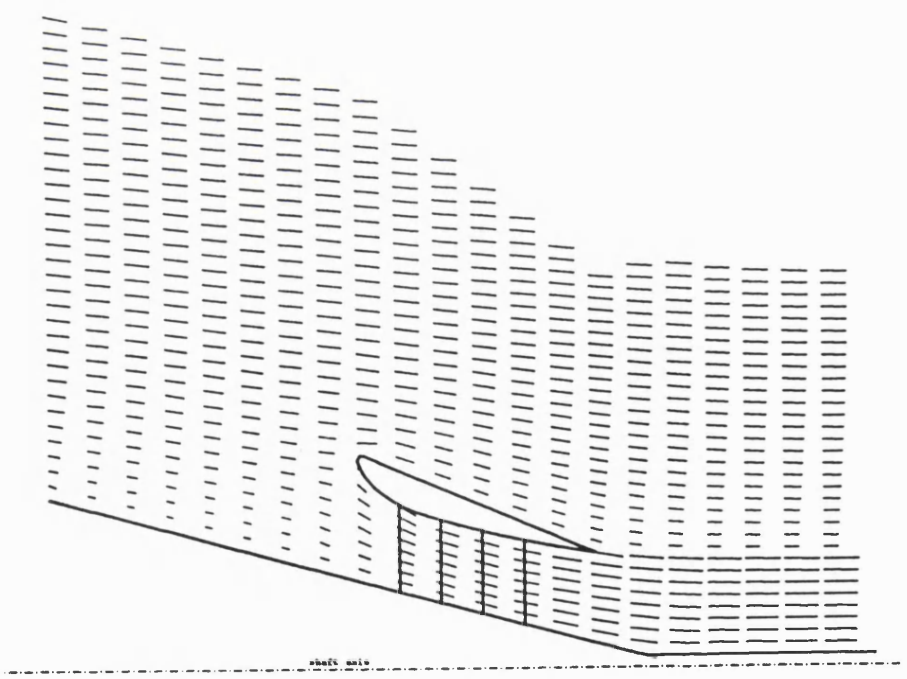

(b) Contra-Rotating Propulsor

Figure 6.21: Mean Velocity Vectors Predicted by the Fully Three-Dimensional Runs of the Generic Submarine Propulsors

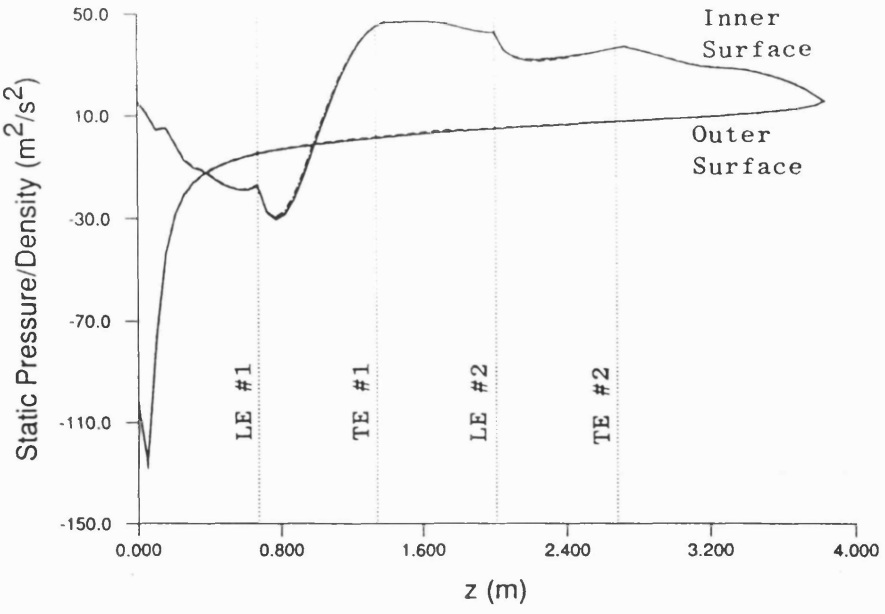

(a) Rotor-Stator Propulsor

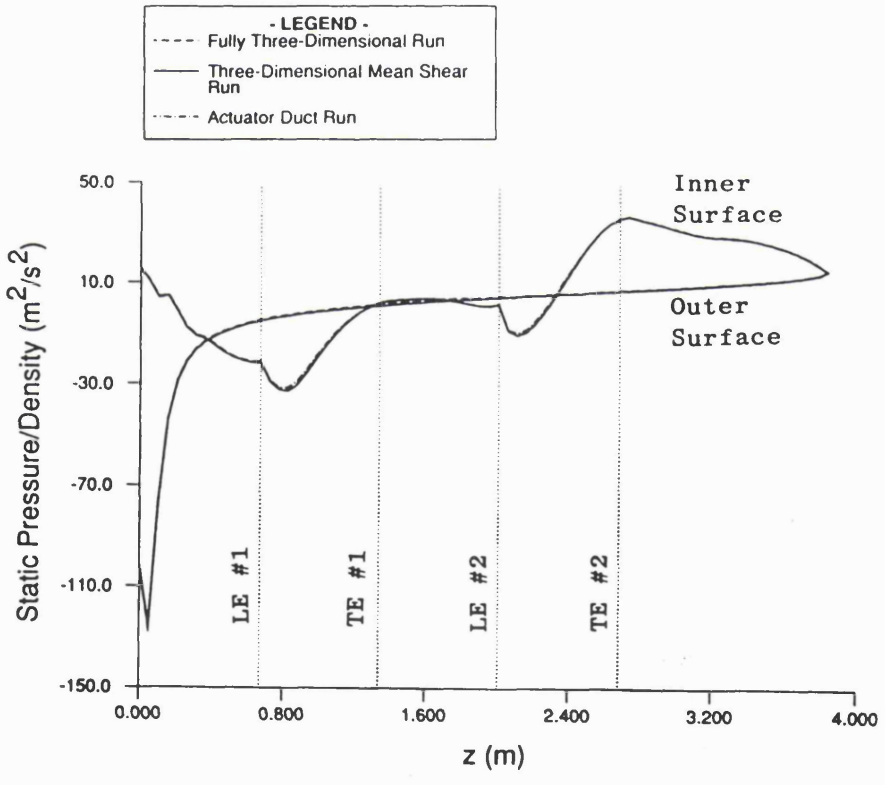

(b) Contra-Rotating Propulsor

Figure 6.22: Predicted Duct Pressure Distributions (Based on Mean Flow Quantities) for the Generic Submarine Propulsors

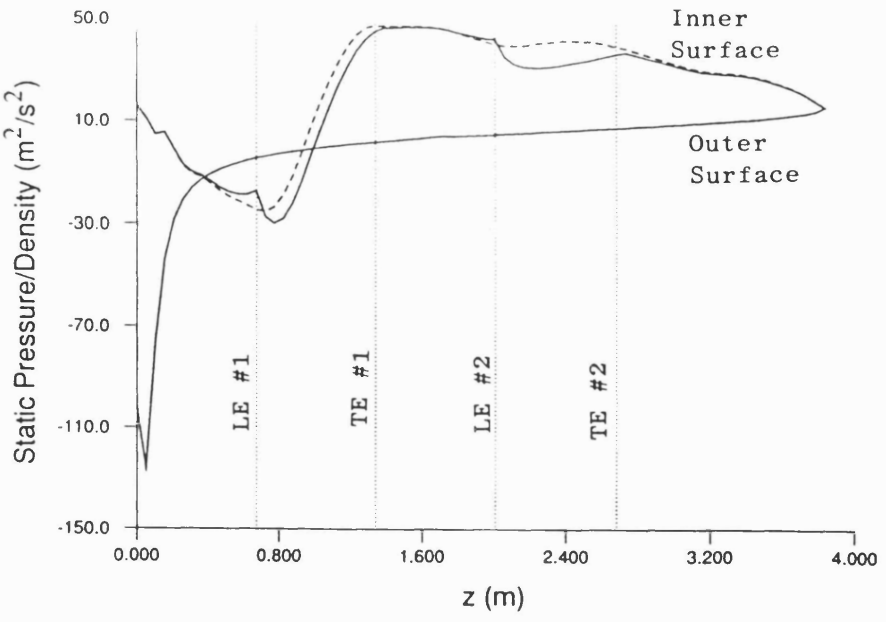

(a) Rotor-Stator Propulsor

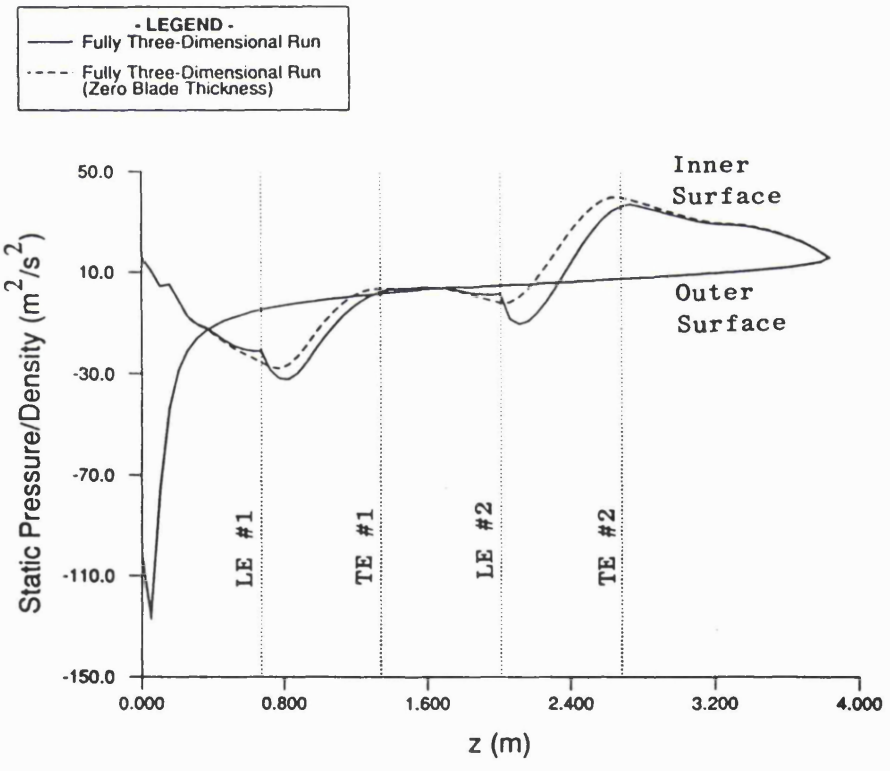

(b) Contra-Rotating Propulsor

Figure 6.23: The Effect of Blade Thickness on the Predicted Duct Pressure Distributions Shown in Figure 6.21

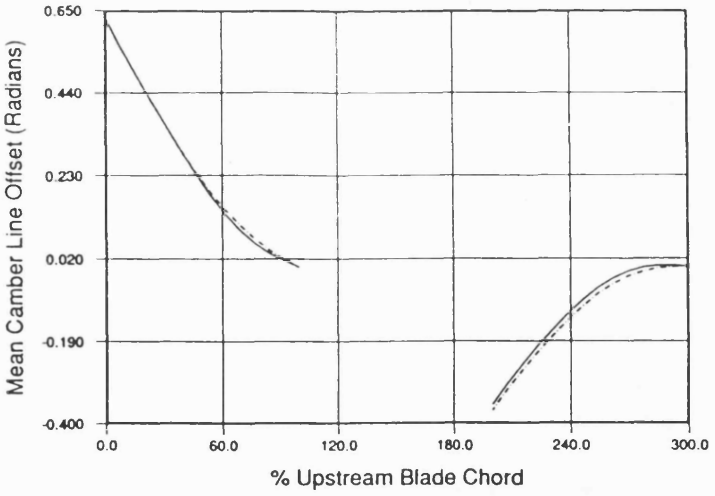

(a) Hub

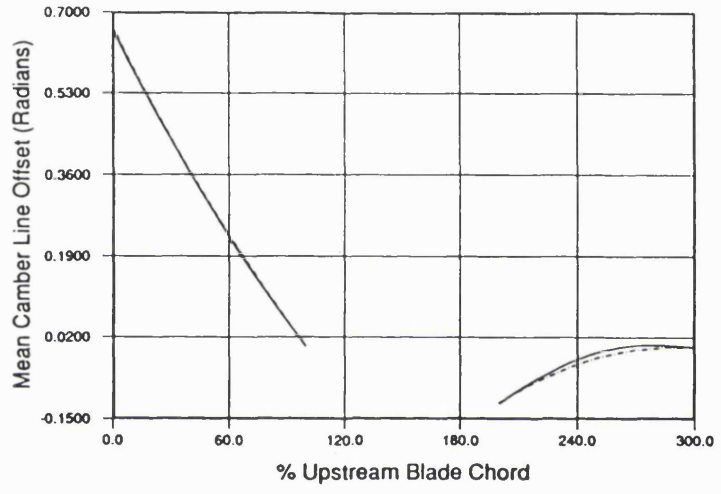

(b) Mid-Span

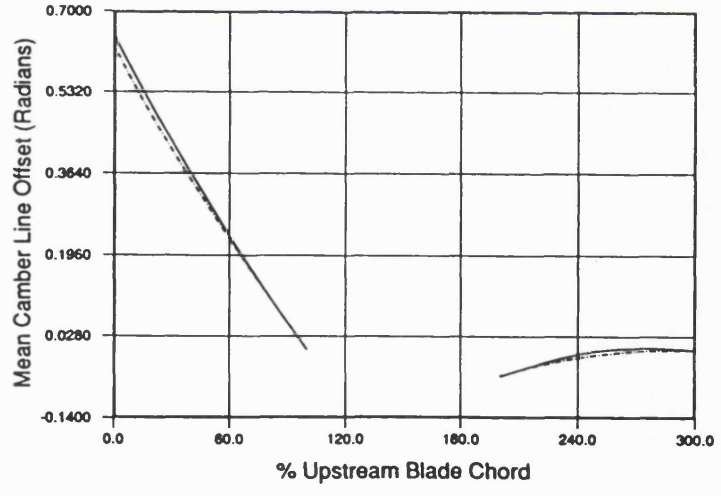

(c) Tip

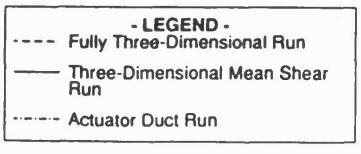

Figure 6.24: Predicted Blade Shapes for the Rotor-Stator Propulsor (Plots Along Quasi-Streamlines)

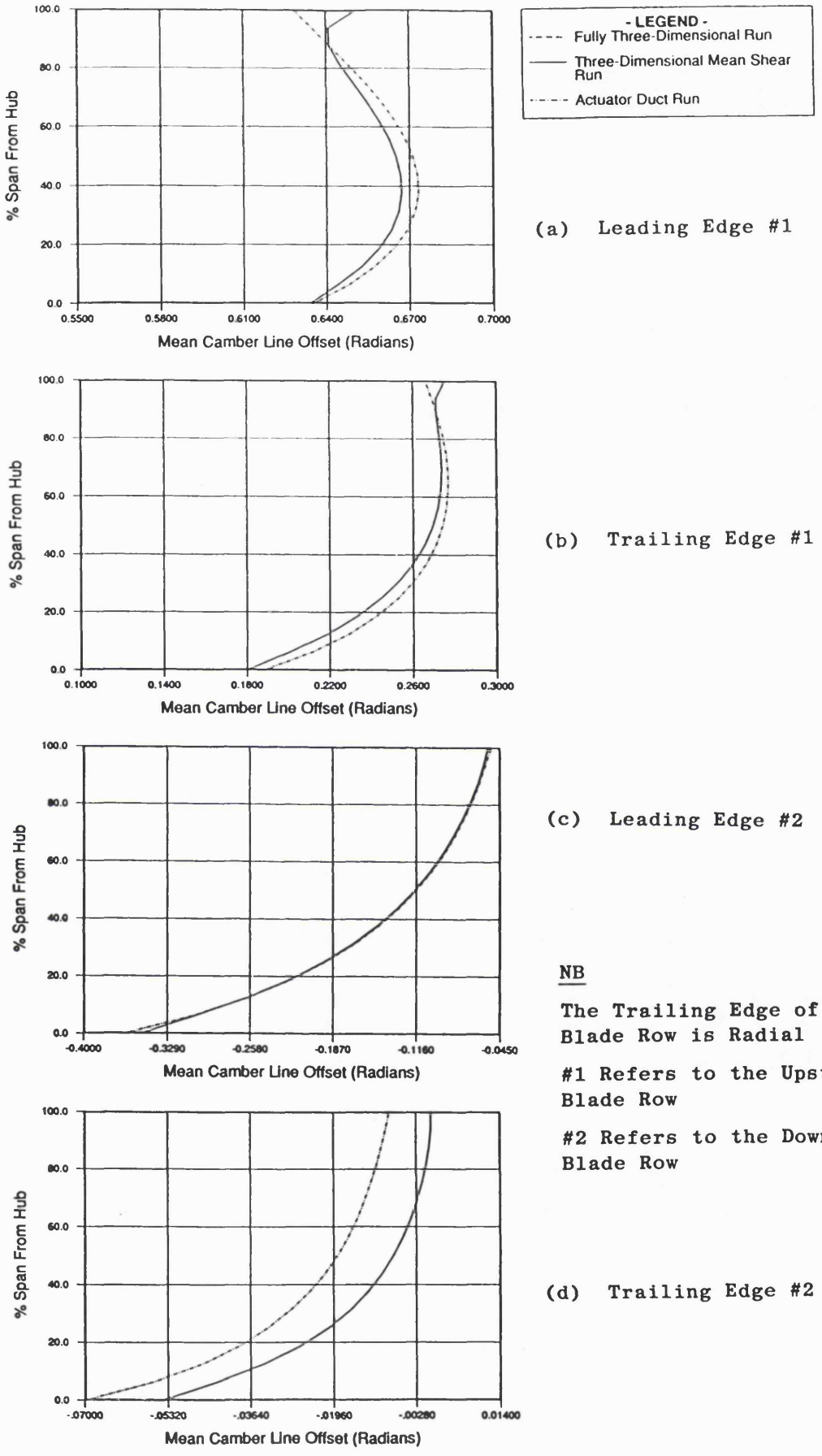

(a) Leading Edge #1

(b) Trailing Edge #1

(c) Leading Edge #2

NB

The Trailing Edge of Each Blade Row is Radial

#1 Refers to the Upstream Blade Row

#2 Refers to the Downstream Blade Row

(d) Trailing Edge #2

Figure 6.25: Predicted Blade Shapes for the Rotor-Stator Propulsor (Plots Along Quasi-Orthogonals)

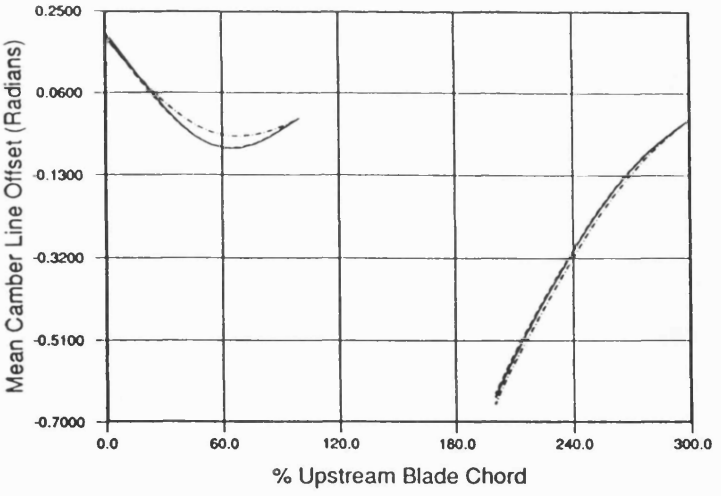

(a) Hub

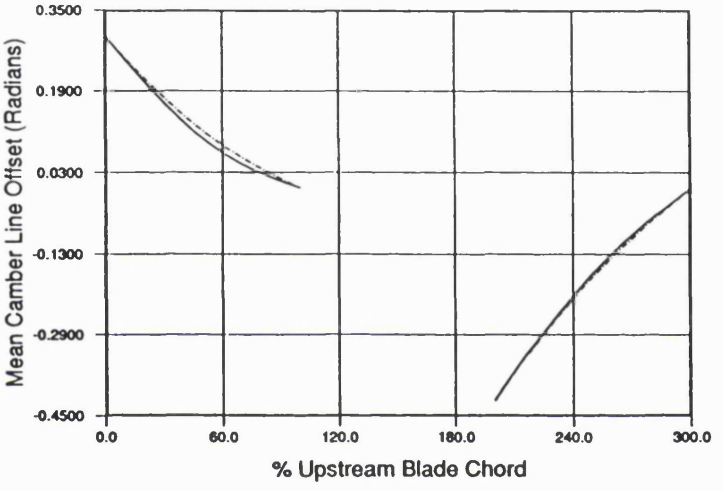

(b) Mid-Span

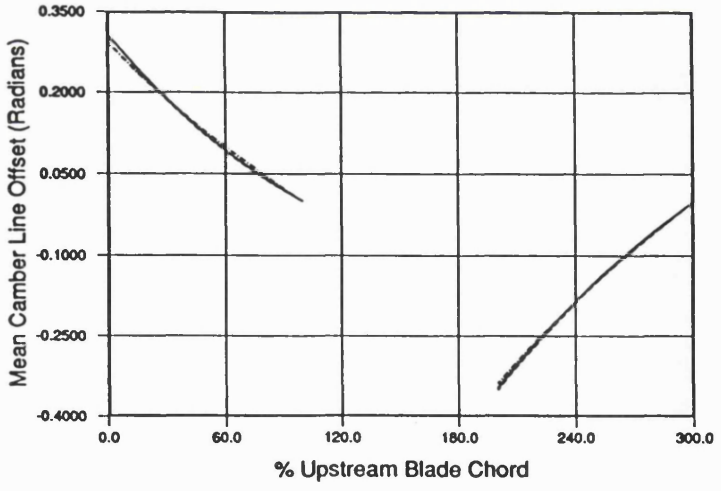

(c) Tip

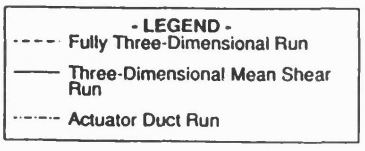

Figure 6.26: Predicted Blade Shapes for the Contra-Rotating Propulsor (Plots Along Quasi-Streamlines)

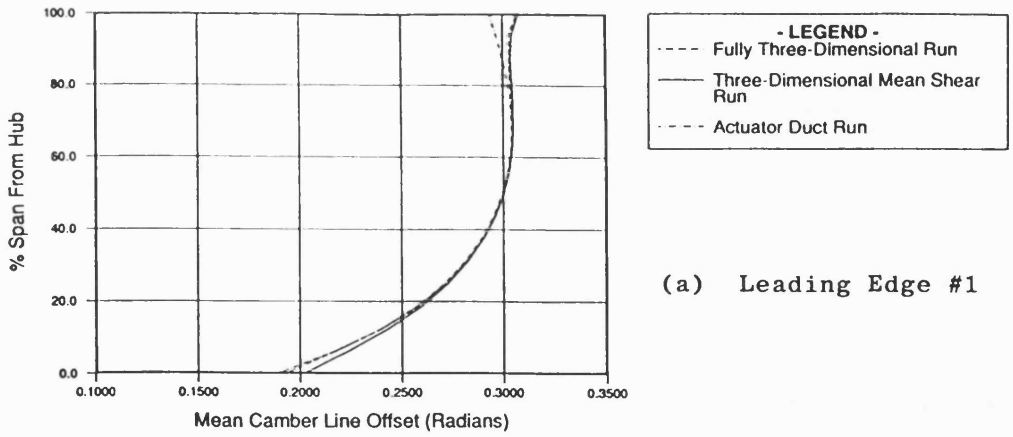

(a) Leading Edge #1

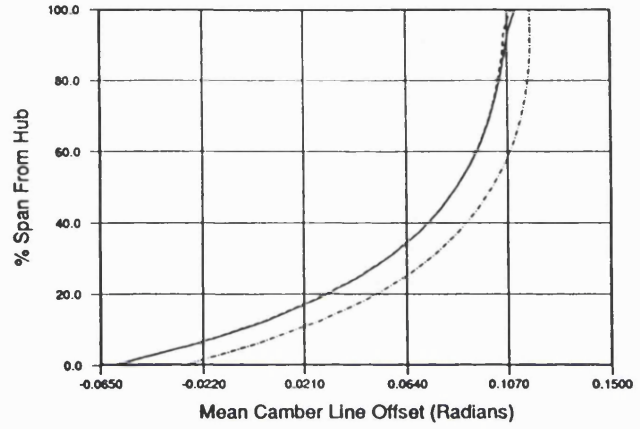

(b) Trailing Edge #1

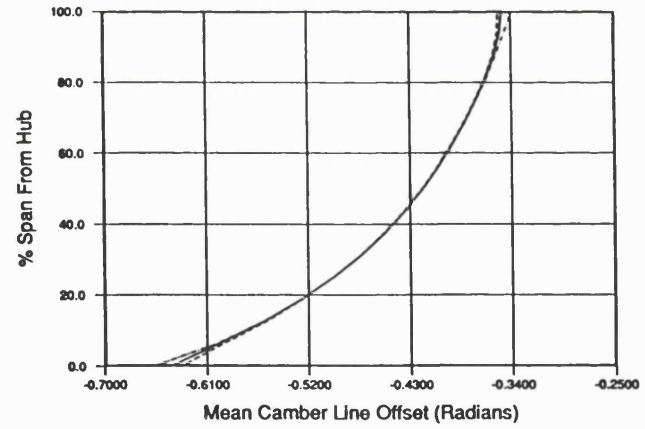

(c) Leading Edge #2

NB
The Trailing Edge of Each Blade Row is Radial

#1 Refers to the Upstream Blade Row

#2 Refers to the Downstream Blade Row

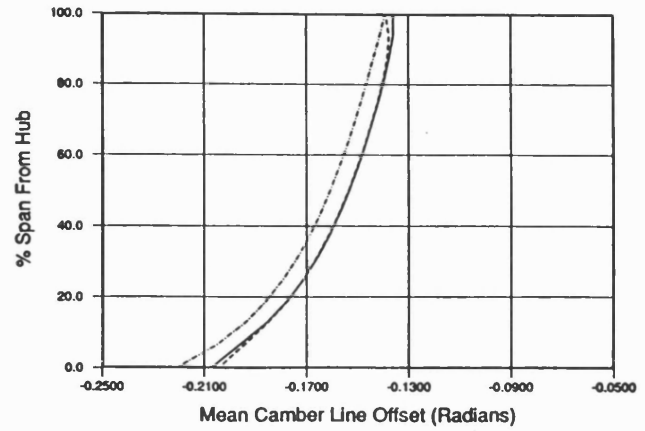

(d) Trailing Edge #2

Figure 6.27: Predicted Blade Shapes for the Contra-Rotating Propulsor (Plots Along Quasi-Orthogonals)

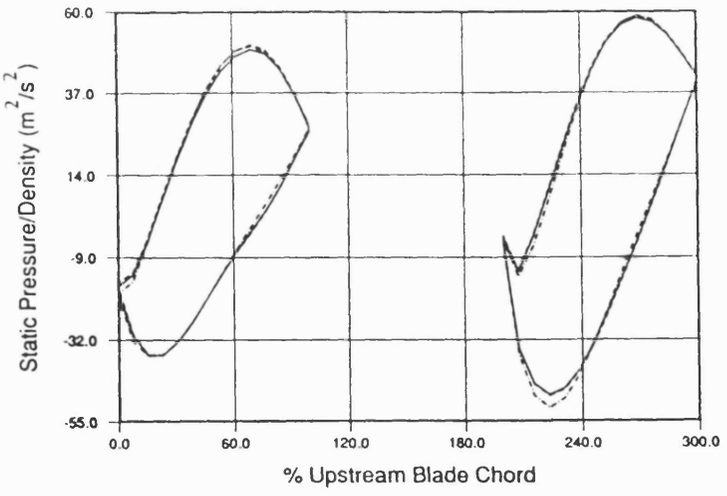

(a) Hub

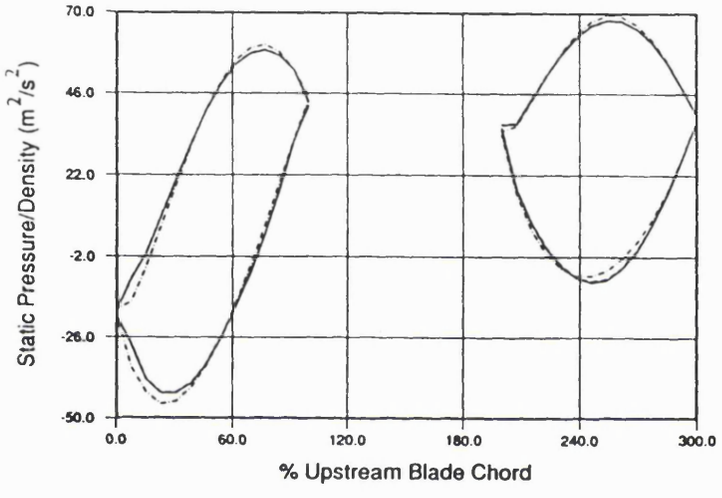

(b) Mid-Span

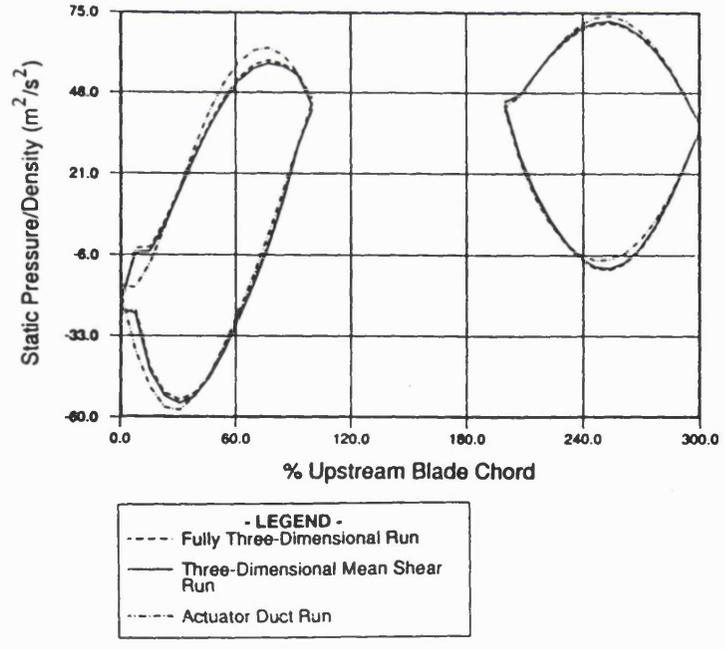

(c) Tip

Figure 6.28: Predicted Blade Pressure Distributions for the Rotor-Stator Propulsor

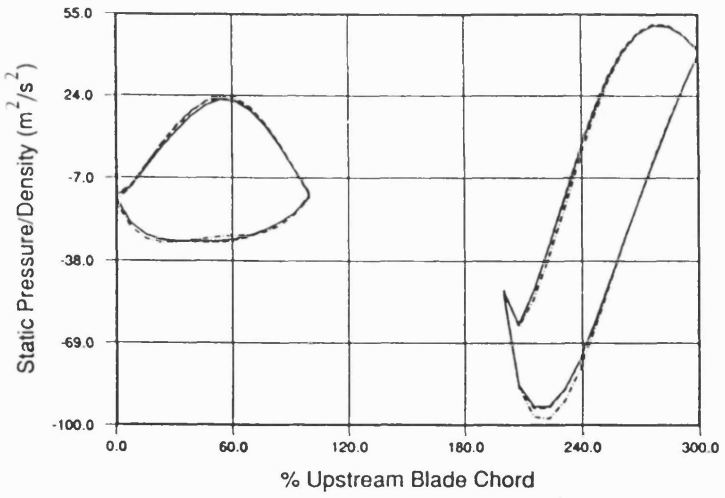

(a) Hub

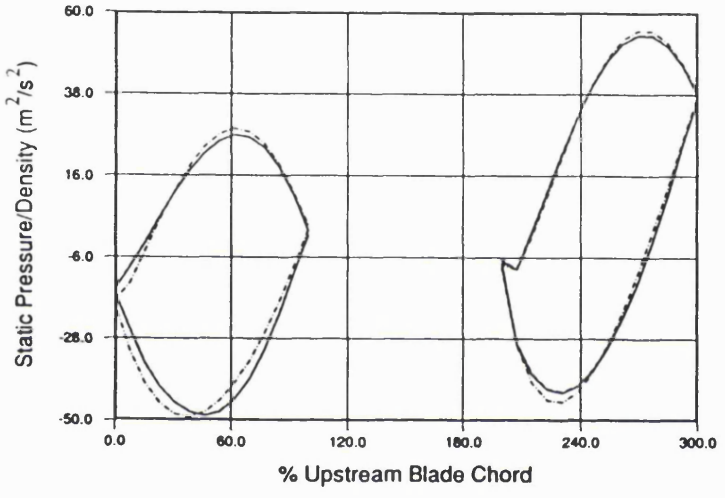

(b) Mid-Span

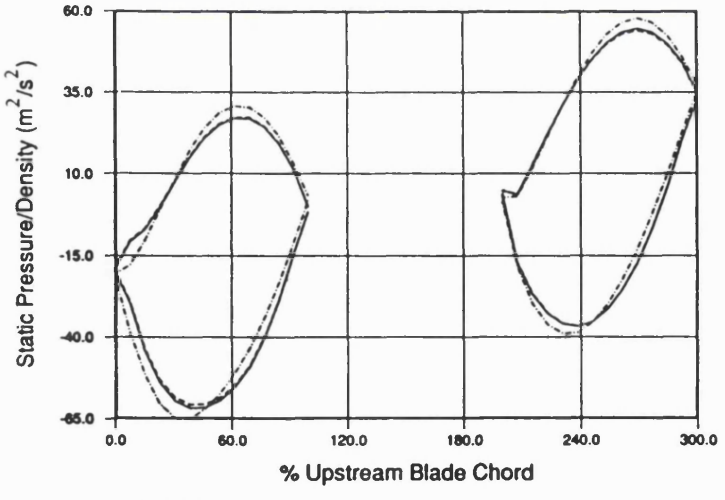

(c) Tip

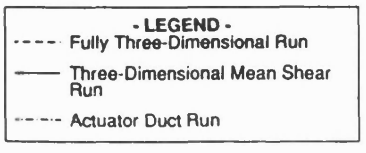

Figure 6.29: Predicted Blade Pressure Distributions for the Contra-Rotating Propulsor

Figure 6.30: Relative Velocity Vectors in the Transverse (r-θ) Plane as Predicted by the Fully Three-Dimensional Run of the Rotor-Stator Propulsor

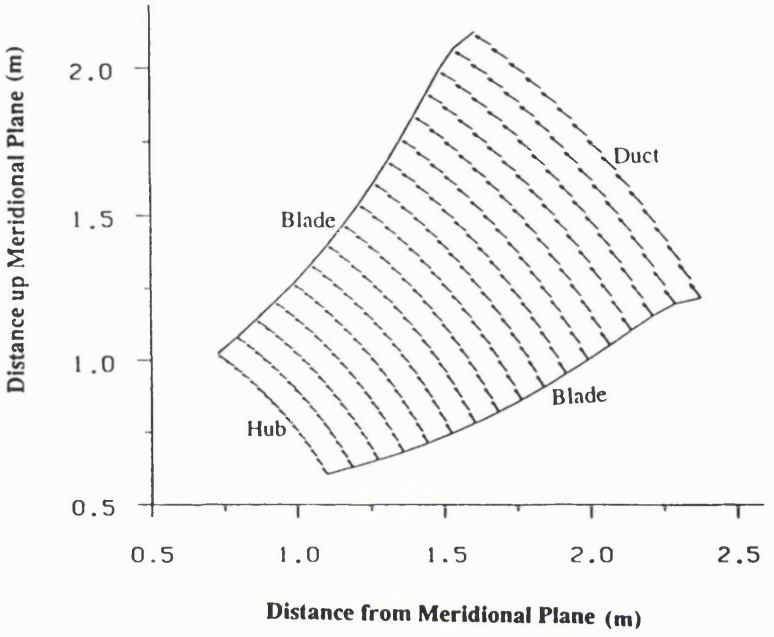

(a) Leading Edge #1

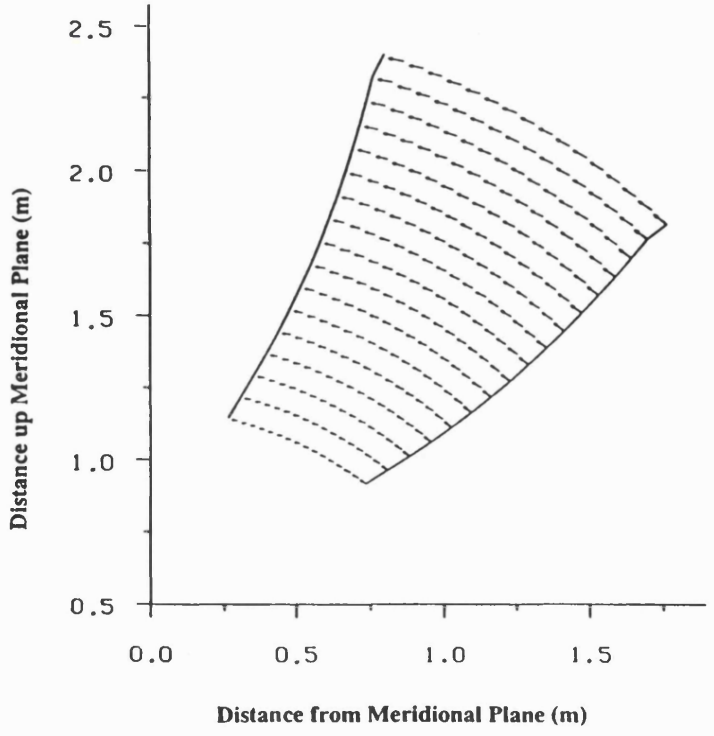

(b) Mid-Chord #1

Figure 6.30 (Continued)

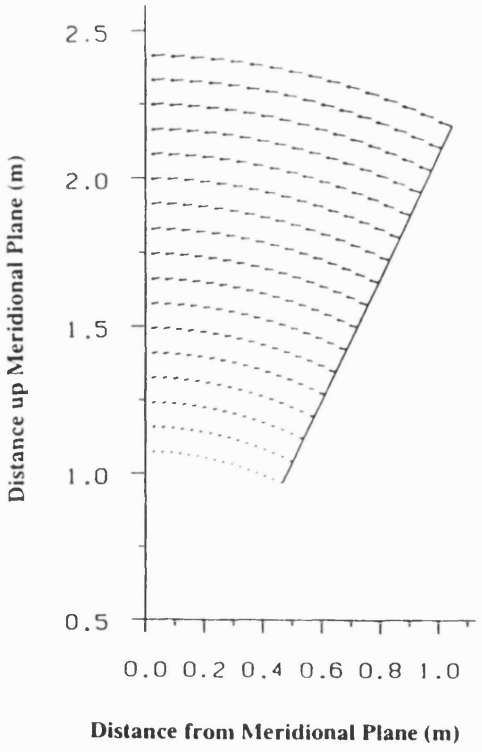

(c) Trailing Edge #1

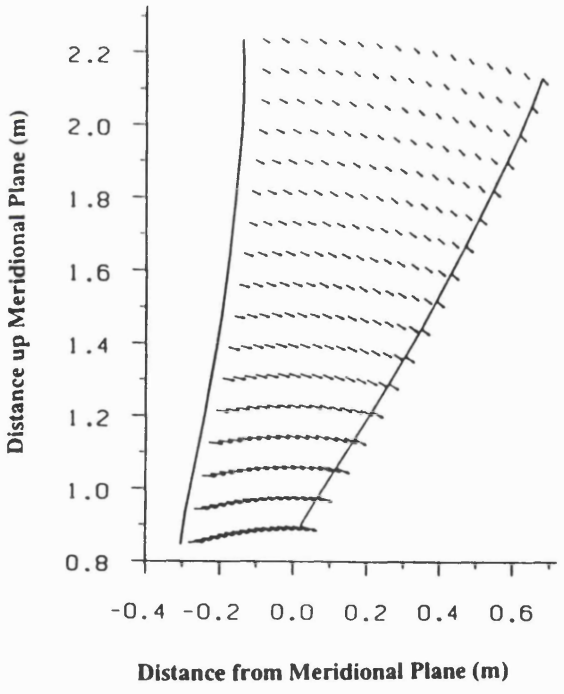

(d) Leading Edge #2

Figure 6.30 (Continued)

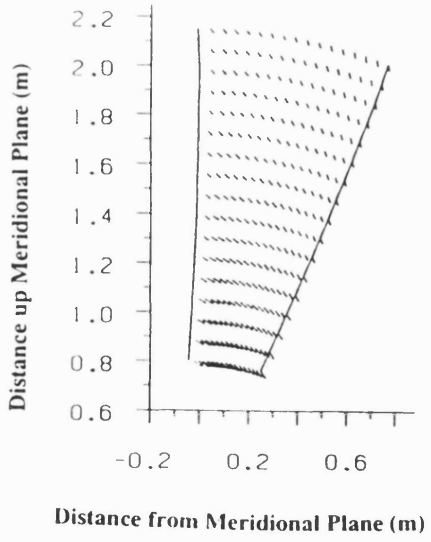

(e) Mid-Chord #2

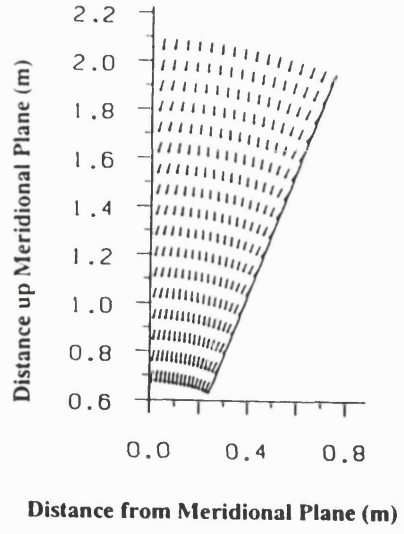

(f) Trailing Edge #2

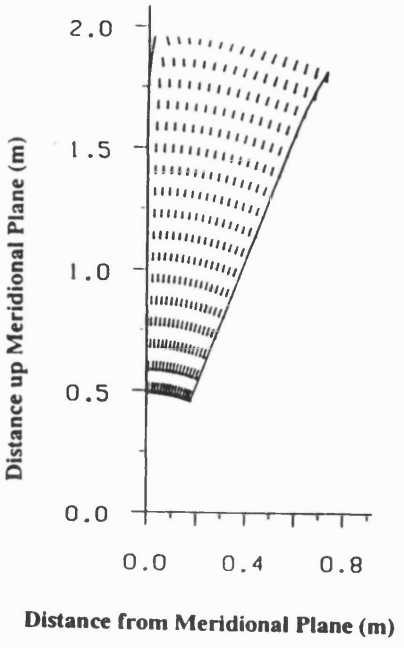

(g) Duct Trailing Edge

NB

#1 Refers to the Upstream Blade Row

#2 Refers to the Downstream Blade Row

Figure 6.31: Relative Velocity Vectors in the Transverse (r- θ) Plane as Predicted by the Fully Three-Dimensional Run of the Contra-Rotating Propulsor

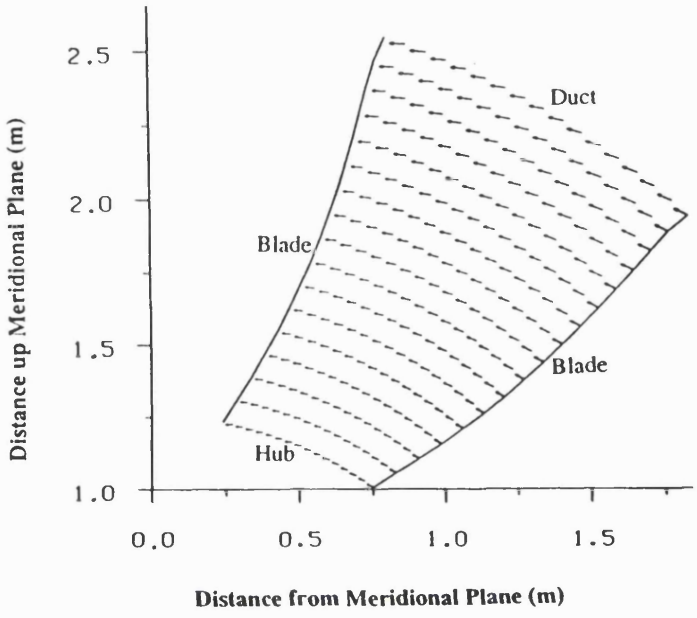

(a) Leading Edge #1

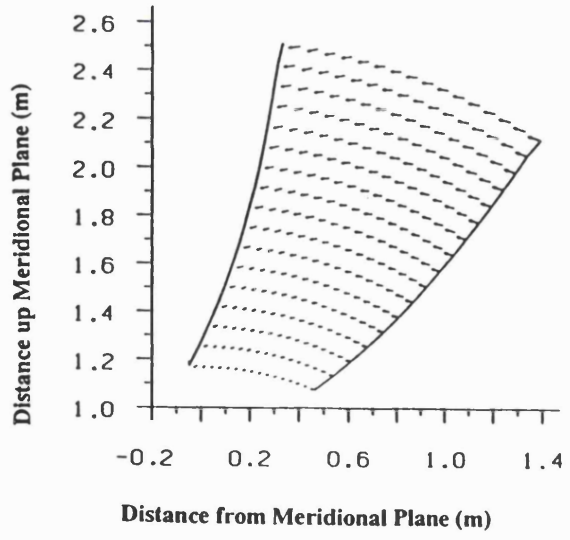

(b) Mid-Chord #1

Figure 6.31 (Continued)

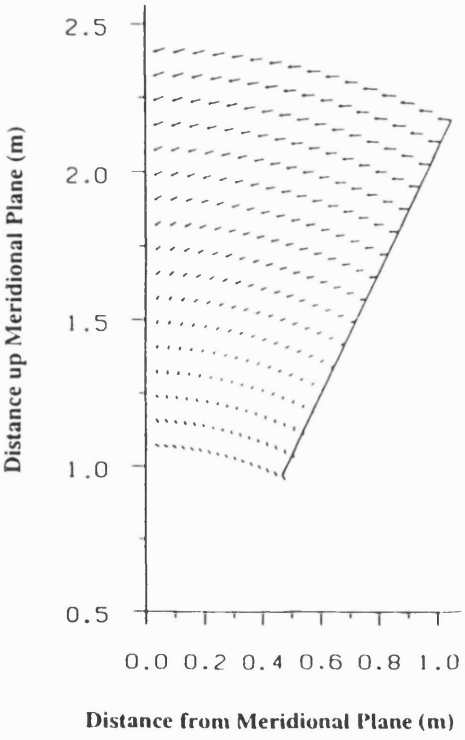

(c) Trailing Edge #1

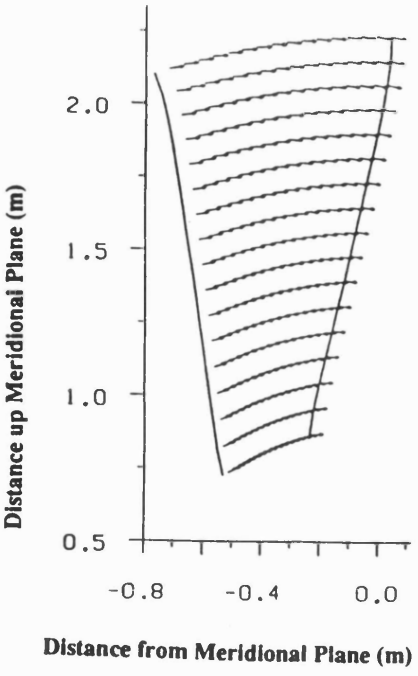

(d) Leading Edge #2

Figure 6.31 (Continued)

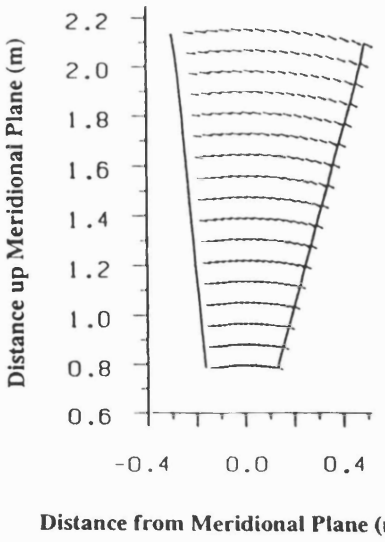

(e) Mid-Chord #2

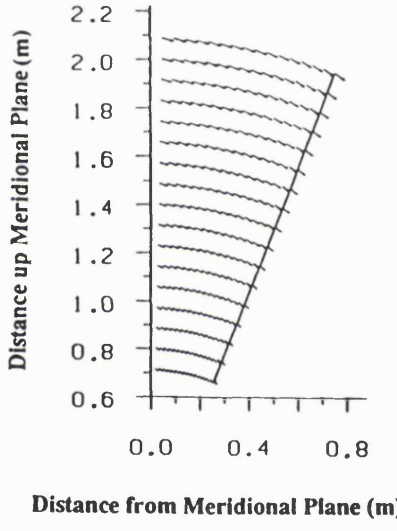

(f) Trailing Edge #2

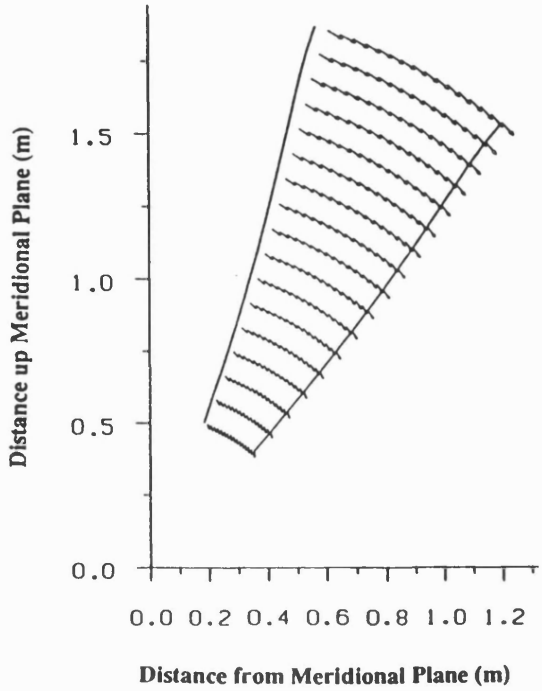

(g) Duct Trailing Edge

NB

#1 Refers to the Upstream Blade Row

#2 Refers to the Downstream Blade Row

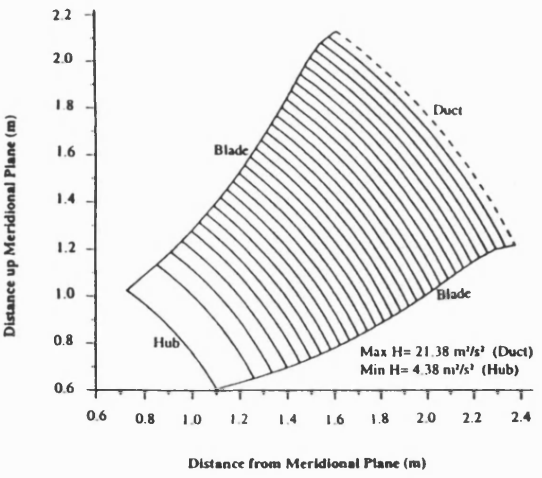

(a) Leading Edge #1

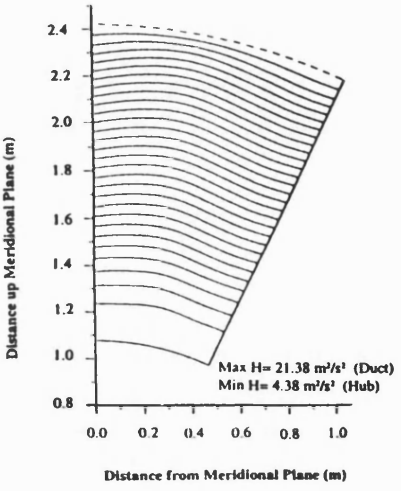

(b) Trailing Edge #1

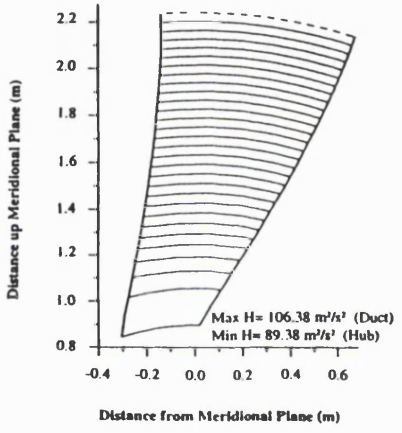

(c) Leading Edge #2

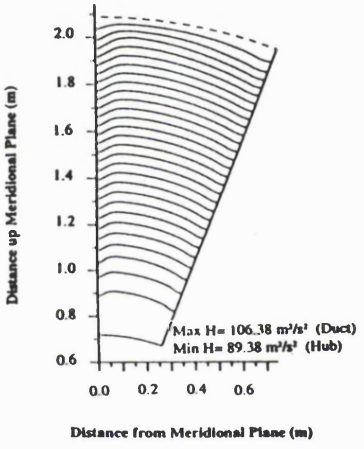

(d) Trailing Edge #2

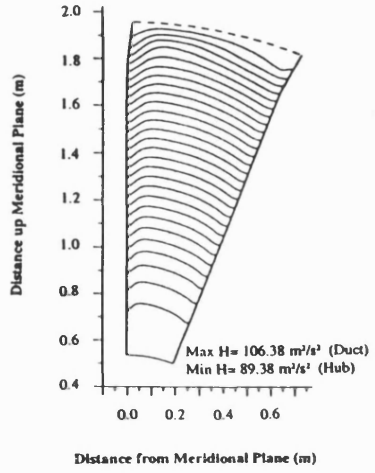

(e) Duct Trailing Edge

NB

1) Number of Contours per Plot = 30
2) #1 Refers to the Upstream Blade Row
   #2 Refers to the Downstream Blade Row

Figure 6.32: Contours of Rothalpy in the Transverse (r- θ) Plane for the Rotor-Stator Propulsor

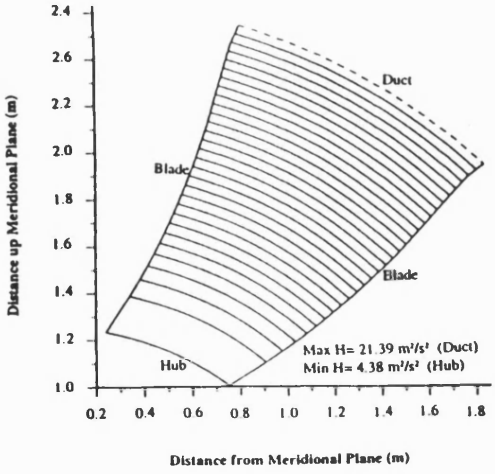

(a) Leading Edge #1

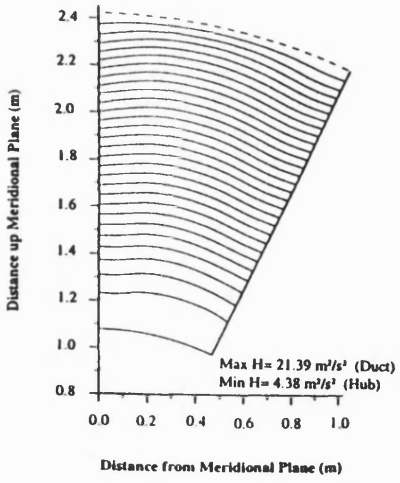

(b) Trailing Edge #1

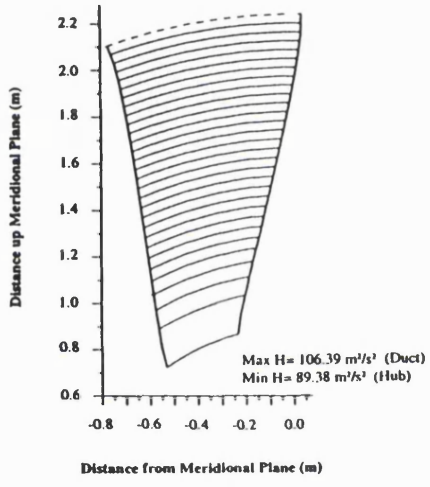

(c) Leading Edge #2

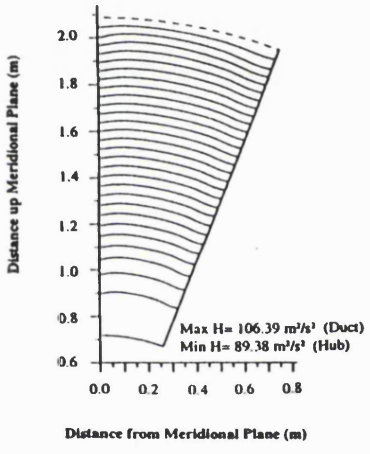

(d) Trailing Edge #2

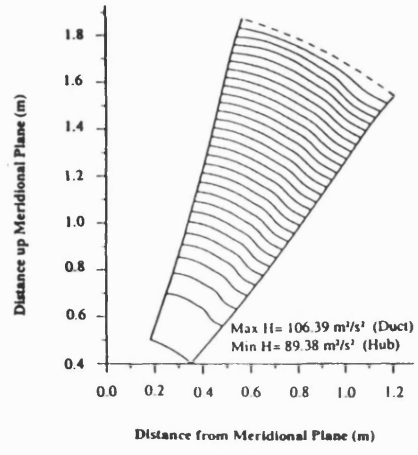

(e) Duct Trailing Edge

NB

1) Number of Contours per Plot = 30
2) #1 Refers to the Upstream Blade Row
   #2 Refers to the Downstream Blade Row

Figure 6.33: Contours of Rothalpy in the Transverse (r-θ) Plane for the Contra-Rotating Propulsor

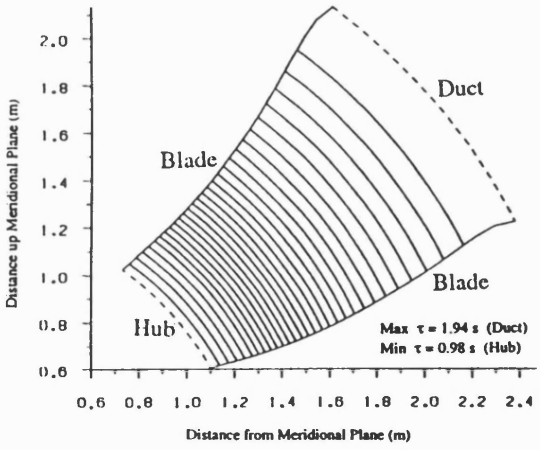

(a) Leading Edge #1

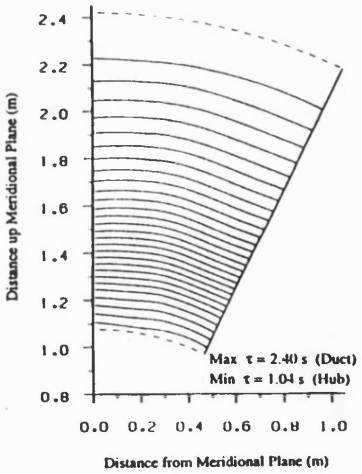

(b) Trailing Edge #1

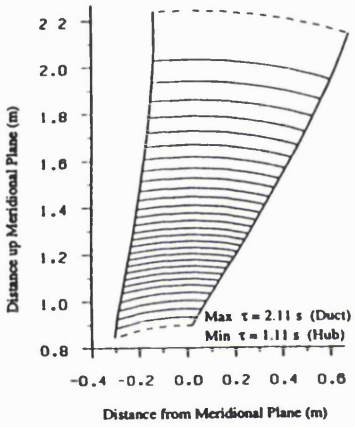

(c) Leading Edge #2

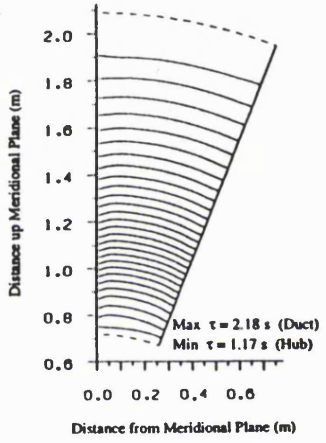

(d) Trailing Edge #2

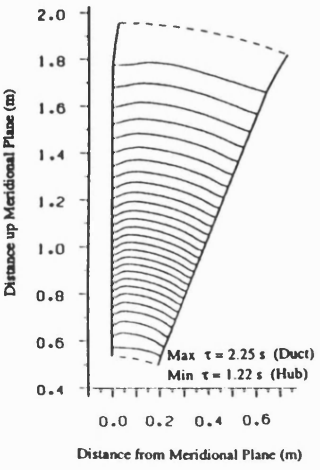

(e) Duct Trailing Edge

NB

1) Number of Contours per Plot = 30
2) #1 Refers to the Upstream Blade Row
   #2 Refers to the Downstream Blade Row

Figure 6.34: Contours of Drift Function in the Transverse (r-θ) Plane for the Rotor-Stator Propulsor

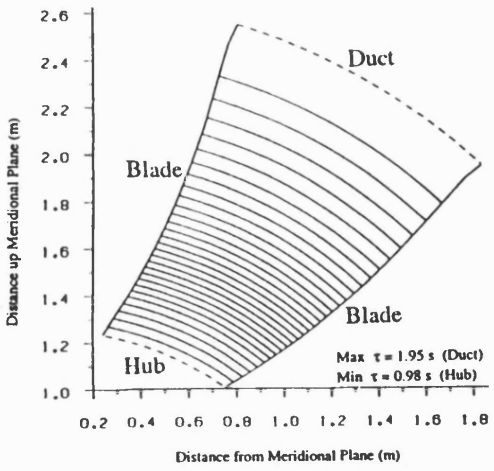

(a) Leading Edge #1

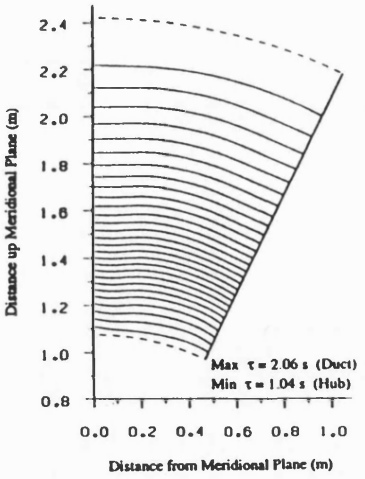

(b) Trailing Edge #1

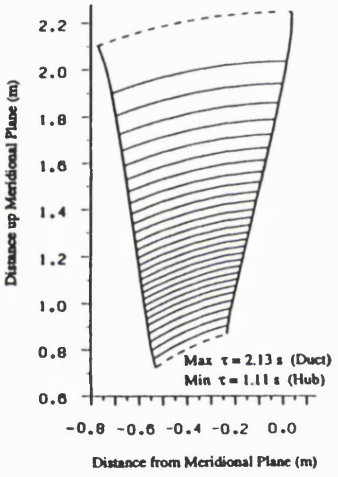

(c) Leading Edge #2

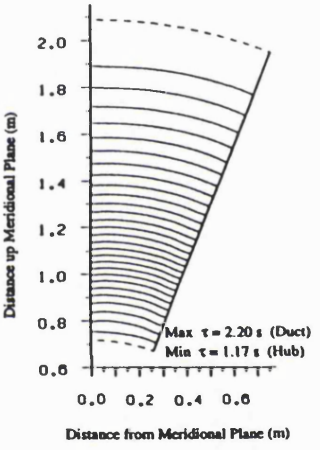

(d) Trailing Edge #2

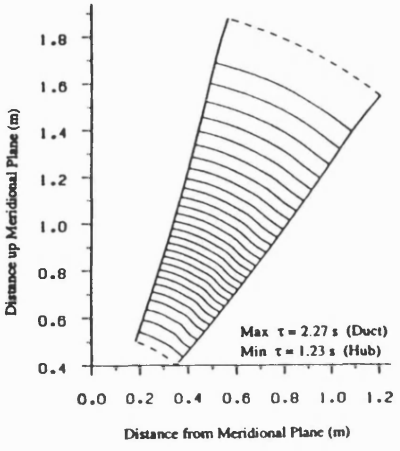

(e) Duct Trailing Edge

NB

1) Number of Contours per Plot = 30
2) #1 Refers to the Upstream Blade Row
   #2 Refers to the Downstream Blade Row

Figure 6.35: Contours of Drift Function in the Transverse (r-θ) Plane for the Contra-Rotating Propulsor

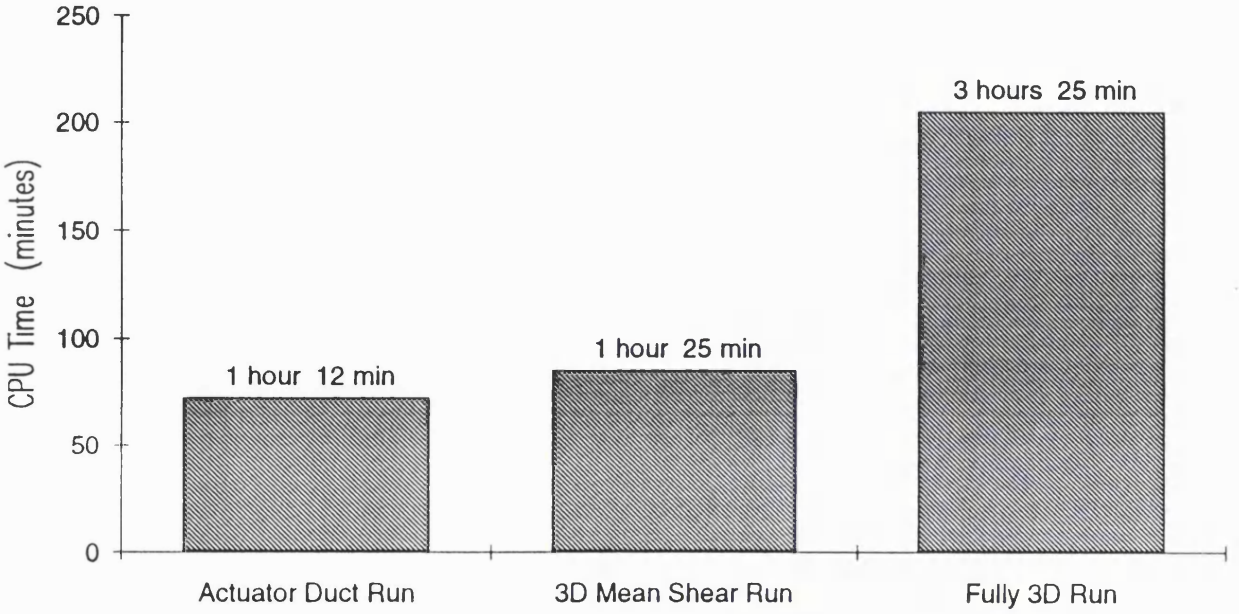

NB

1) Runs Conducted on a VAXstation 4000VLC
2) Times Based on an Initial Estimate for Propulsor Mass Flow of 120 Tonnes/second

Figure 6.36: Computational Times for the Rotor-Stator Propulsor

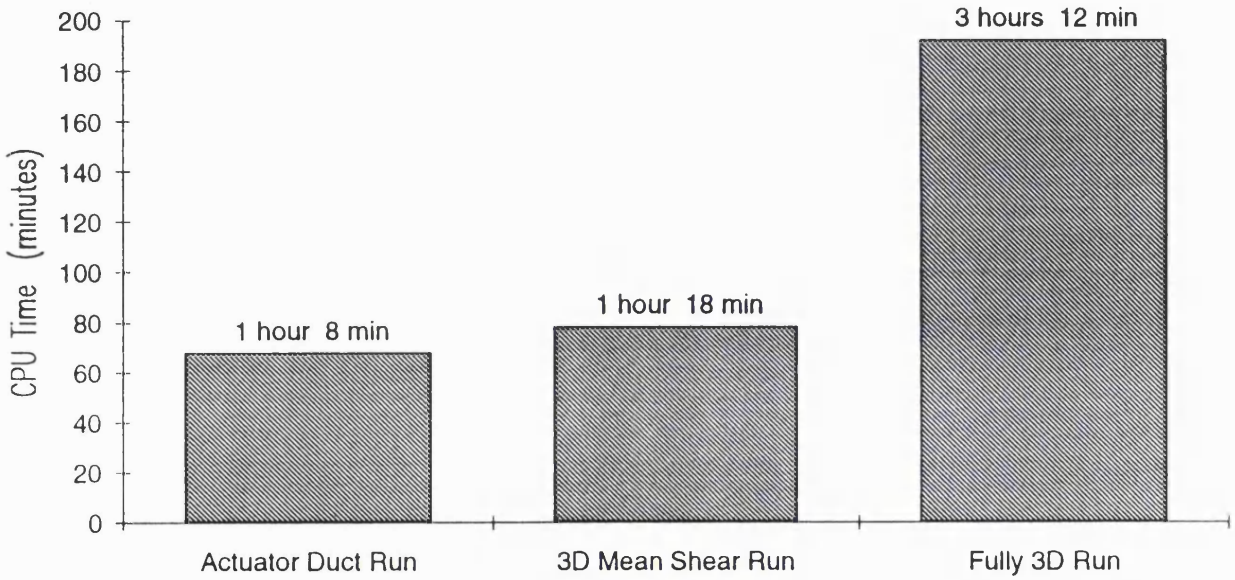

NB

1) Runs Conducted on a VAXstation 4000VLC

2) Times Based on an Initial Estimate for Propulsor Mass Flow of 120 Tonnes/second

Figure 6.37: Computational Times for the Contra-Rotating Propulsor

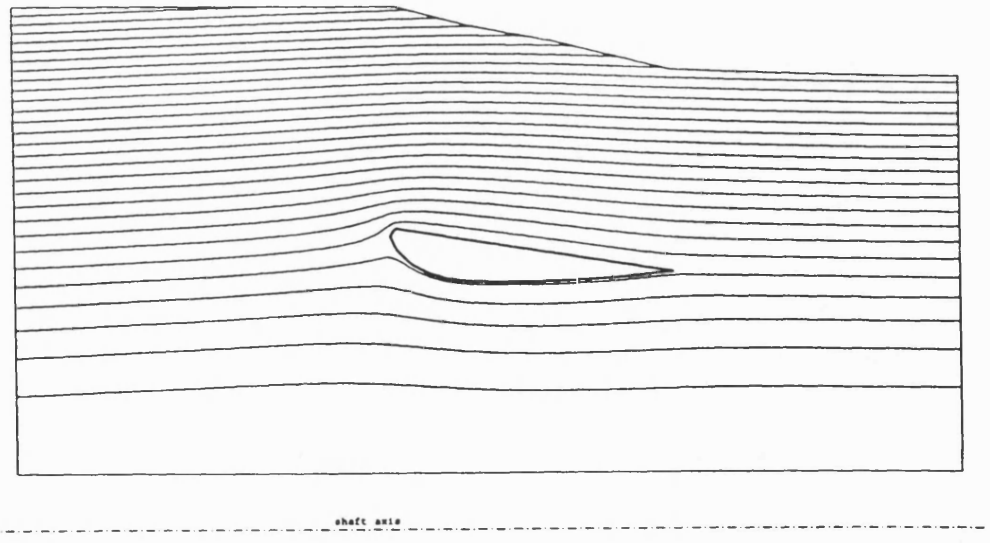

Figure 6.38: Predicted Streamline Patterns for the Merchant Ship Duct and Hub in Shear Flow

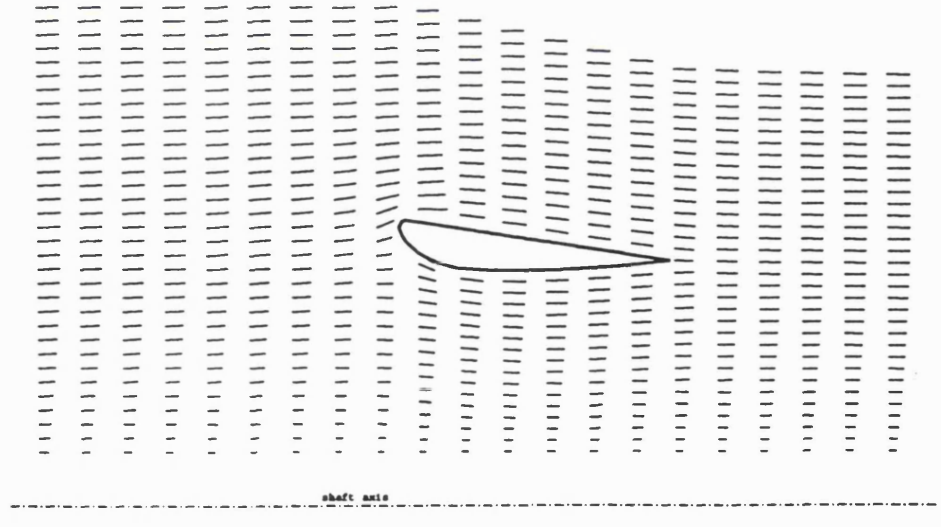

Figure 6.39: Predicted Velocity Vectors for the Merchant Ship Duct and Hub in Shear Flow

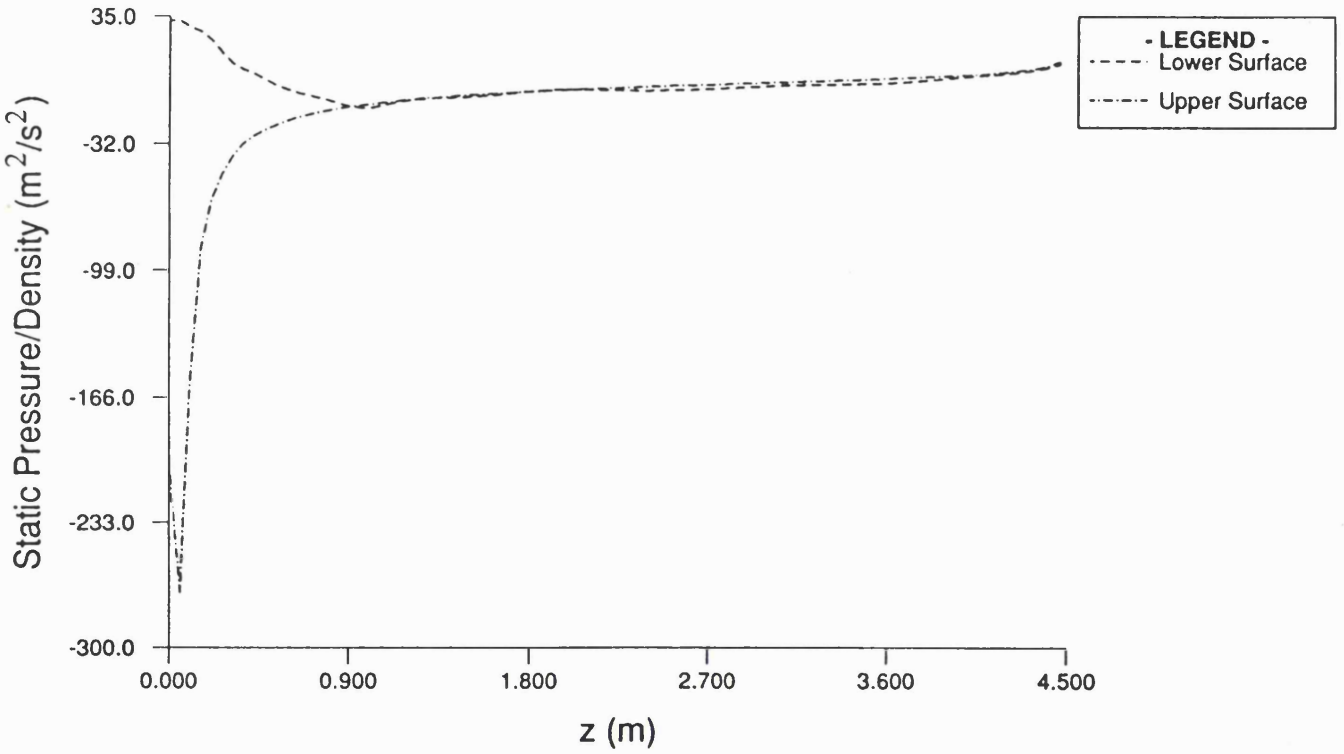

Figure 6.40: Predicted Duct Pressure Distribution for the Merchant Ship Duct and Hub in Shear Flow

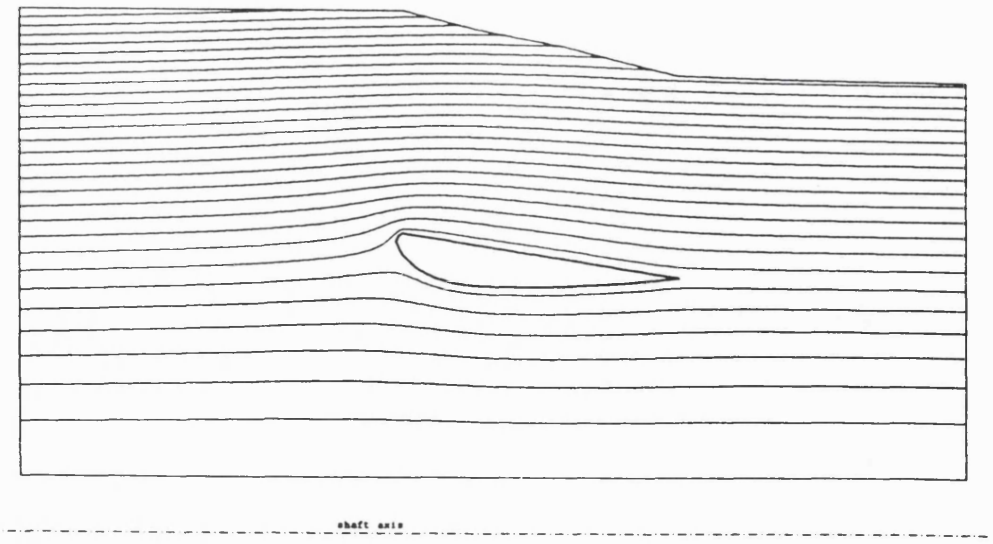

Figure 6.41: Predicted Streamline Patterns for the Merchant Ship Duct and Hub in Uniform Flow

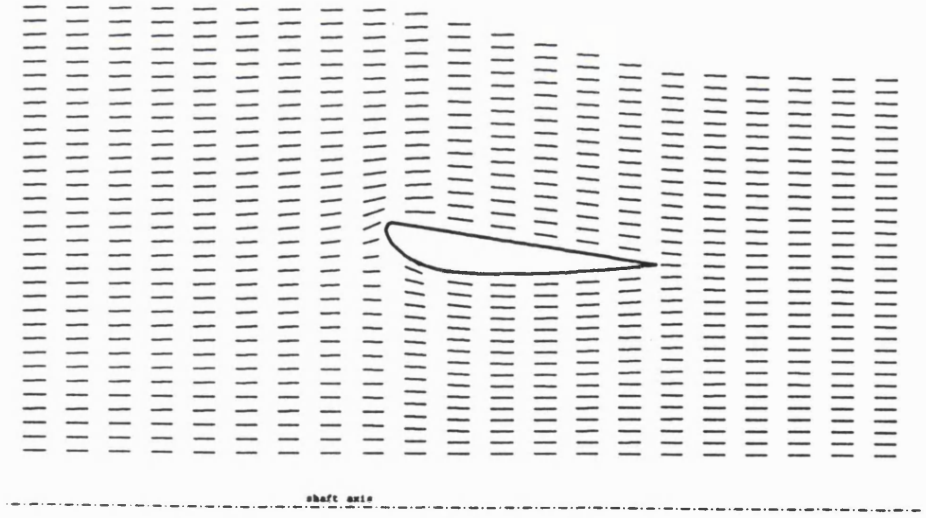

Figure 6.42: Predicted Velocity Vectors for the Merchant Ship Duct and Hub in Uniform Flow

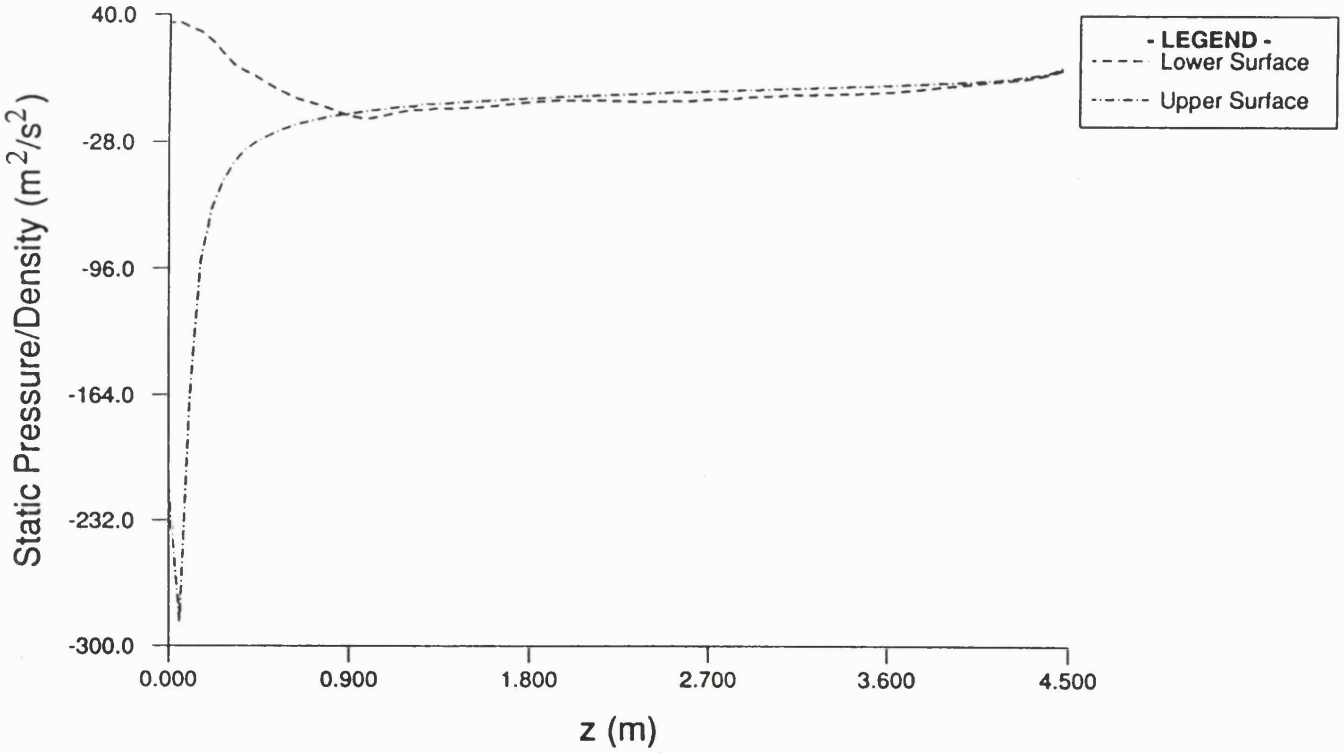

Figure 6.43: Predicted Duct Pressure Distribution for the Merchant Ship Duct and Hub in Uniform Flow

CHAPTER 7 EXPERIMENTAL VERIFICATION OF THE INVERSE DESIGN METHOD

7.1 Introduction

With work on the ducted propulsor design method complete, attention turned to the verification of the computational results. Three means of achieving this were considered:-

(a) Verification Using a Computational Analysis Method

This approach would have involved designing a test propulsor using the ducted propulsor design method, and then comparing the resulting flow field predictions with those of a computational analysis method.

Such an approach was particularly attractive in terms of both time requirements and cost. However, a ducted propeller analysis code that could model both three-dimensional phenomena and shear flow was not available.

Some consideration was given to verifying the design method using a pump analysis method based on a finite volume method [1]. This was rejected, however, as only the propulsor through flow could have been modelled, and no assessment of mass flow predictions could have been made from such an approach. Additionally, in its present form, this analysis method was reported to be ill-suited to modelling incompressible flow.

(b) Experimental Verification Using a Cavitation Tunnel

This approach would have entailed mounting a test propulsor (with blading designed by the inverse design method) and afterbody in a cavitation tunnel, with mesh screens upstream to stimulate the required far upstream velocity profile. Flow measurements using Laser Doppler Velocimetry (LDV) together with pressure taps on the duct surface would then enable the three-dimensional flow field and duct pressure measurements to be compared with the predictions of the inverse design method. Alternatively, a simpler, but cheaper, less time-consuming series of experiments could have been conducted based on measurements of shaft torque and the duct pressure distribution.

Whilst this was the preferred means of verification, unfortunately no cavitation tunnel was available at UCL, and construction of such a facility, or use of one outside UCL was deemed unacceptable due to limitations of both cost and time scale.

(c) Experimental Verification Using a Low Speed Wind Tunnel

This proposal involved recommissioning a low speed wind tunnel that had lain idle at UCL for some years (Figure 7.1). A test propulsor would be mounted within a lengthened working section with mesh screens mounted at the upstream entrance to the working section to stimulate an axisymmetric sheared onset flow.

Initial plans were to measure the three-dimensional velocity field around the propulsor using either Hot Wire Anemometry (HWA) or Laser Doppler Velocimetry (LDV) techniques. However, due to the limited time and funding available for the verification work, these sophisticated measurements were rejected in favour of much simpler measurements of the time-averaged propulsor flow field using a pitot probe. It was also hoped that flow visualisation tests could be conducted using either tufts or smoke, and that the absorbed shaft power and the duct pressure distribution could be measured.

There were a number of disadvantages associated with this approach. In particular, the limited dimensions of the wind tunnel working section (Section 7.2) and the desire to minimise wall interference effects restricted the maximum permissible propulsor diameter to an estimated 0.2m. Not only did the use of such a small test propulsor limit the accuracy of the flow measurements, but also necessitated certain compromises in the selection of a shaft speed; achieving turbulent flow on the blades implied the selection the highest possible shaft speed, whilst the need to avoid the effects of flow compressibility suggested that a low shaft speed should be adopted. Ultimately a compromise shaft speed of 4000rpm was selected (see Section 7.2.3), although this was far from ideal from the point of view of either Mach Number or Reynolds Number. The high shaft speed meant that a high performance motor would have to be used, increasing costs significantly.

Despite these problems, this proposal was the means finally chosen for verifying the inverse design method on grounds of both time and cost.

7.2 Verification using a Low Speed Wind Tunnel

As stated in the previous section, verification of the ducted propulsor inverse design method was conducted using a low speed open suction wind tunnel available at UCL. Details of this facility as originally constructed can be found in [2], and may be summarised as follows:-

Working Section: Cross Sectional : 0.61m x 0.61m
Length = 1.2m

Speed Range On Longitudinal Centre Line: 1.5 to 23.0 m/s

The experimental work consisted of the following stages:-

7.2.1 Recommissioning the Wind Tunnel

This work entailed constructing a lengthened (2.4m vice 1.2m) working section to satisfactorily house the propulsor assembly (Figure 7.2), and modifying the automated traverse rig (which was unserviceable) to allow for manual traverse and an increased traverse range.

It is interesting to note that doubling the working section length was found to have negligible effect on the air speed range that could be achieved in the working section.

7.2.2 Preliminary Measurements

In the absence of the propulsor rig, the wind tunnel was run with overlaid discs of wire mesh placed at the upstream end of the tunnel working section, the objective being to generate an axisymmetric velocity profile. The axial velocity field was measured at various stations along the length of the working section using a simple pitot-static probe (Figure 7.3). Having ascertained that the decay of the velocity profile over the centre portion of the working section (where the propulsor was to be mounted) was small, the velocity profile to be used as input to the inverse design method was measured together with the position of its minimum velocity. As can be seen from Figure 7.4, this profile deviated slightly from axisymmetry, and was therefore circumferentially-averaged using a Least Squares approach (NAG routine E02BAF given in [3]). The resulting axisymmetric velocity profile as input to the

inverse design method (together with the original velocity measurements) are shown in Figure 7.5.

7.2.3 Propulsor Design

Using the final velocity profile obtained from the procedure given in Section 7.2.2, a single blade row propulsor was designed using the ducted propulsor inverse design method outlined in Chapters 4 and 5.

An NSMB No.19A duct profile (Figure A9.1, Appendix IX) was selected for the test propulsor, this duct profile having found widespread application on merchant ships. However, the length to diameter ratio (L/D) of the Duct was increased from 0.5 to 0.6 to allow for the installation of a second blade row at a later date if required. In order to minimise wall-interference effects which affect propulsor mass flow, the interior diameter of the duct was set to 0.2m, thereby allowing a clearance of approximately 1.5D between the duct and tunnel walls (Figure 7.6).

Minimising blade tip clearance diameter in accordance with good design practice, a blade tip diameter of 0.198m was then selected.

At this stage a hub diameter of 0.08m (corresponding to a hub to tip ratio of 0.404), and a constant axial blade chord c=0.03m (=D/4) were chosen, both being representative of full scale ducted propulsors. Additionally, the blade leading edges were chosen to be 3c/2 downstream of the duct leading edge so that the blading was mounted centrally within the duct.

A seven-bladed design was chosen, so as to represent both merchant ship propulsors which may have as few as four blades, and propulsors for military applications which may have more than ten blades on each blade row. Adopting more blades would have increased the time required to manufacture the propulsor, and could have led to "blade overlap" which would have complicated the mounting arrangements for the blades.

At this point it was necessary to select a shaft speed for the design. It was essential to select the shaft speed in such a way that the blade flow would be fully turbulent; failure to do so could have resulted in laminar or transitional flow phenomena which are not encountered on full scale propulsors, rendering any results invalid. However, it was also necessary to keep the blade Mach Number as low as possible (ideally less

than 0.3) to prevent flow compressibility from affecting the performance of the propulsor. Thus, using the definition of blade Reynolds Number given by O'Brien [4]

$$R_n = \frac{V_{0.7} C_{0.7}}{\upsilon} \qquad 7.1$$

and defining blade Mach Number by

$$M = \frac{V_{tip}}{a} \qquad 7.2$$

where $V_{0.7} = \sqrt{V_{a_{0.7}}^2 + \omega^2 r_{0.7}^2}$

$V_{tip} = \sqrt{V_{a_{tip}}^2 + \omega^2 r_{tip}^2}$

$r_{0.7}$ = 70% of Tip Radius

r_{tip} = Tip Radius (0.099m)

$V_{a_{0.7}}$ = Axial Velocity at 70% of Tip Radius (Taken to be 10m / s)

$V_{a_{tip}}$ = Axial Velocity at Blade Tip (Taken to be 30m / s)

$C_{0.7}$ = Blade Chord at 70% Tip Radius

ω = Shaft Angular Speed (Rads / s)

ν = Kinematic Viscosity of the Flow Medium

(Typically 1.461×10^{-5} m^2 / s for Air at Room Temperature)

a = Speed of Sound in the Flow Medium

(Typically 340.3m / s for Air at Room Temperature)

a shaft speed of 4000rpm was selected using the plots shown in Figures 7.7 and 7.8, corresponding to M=0.15 and R_n=6.3×10^4; this was deemed to be the best compromise between viscous and compressibility considerations.

Although Reynolds Numbers for full scale propulsors are typically as high as 3×10^7, such a value could not be achieved in the wind tunnel without there being supersonic flow on the blades. In any case, it was hoped that any problems with laminar or transitional flow on the blades could have been solved using turbulent trips.

The blade normal thickness distribution adopted is as given in Figure A9.3 (Appendix IX), where x is the axial distance from the blade leading edge. Once computational results were available the suitability of this thickness distribution was assessed using

simple one-dimensional methods for blade strength assessment similar to those presented by Marscher [5].

Some consideration was given to adopting a cantilevered shaft arrangement whereby both shaft supports would have been located downstream of the duct. However, whirling analyses showed such an arrangement to be impractical as it would have entailed positioning the shaft supports and bearing housings (with their associated aerodynamic interference) close to the duct trailing edge. Therefore, the shaft support arrangement shown in Figure 7.2 was adopted, albeit reluctantly, as the presence of the upstream shaft support (which was fitted with a fairing) would inevitably have some effect on propulsor performance.

A shaft length of 1.0m was chosen to ensure minimum aerodynamic interference between the shaft mounts and drive mechanism, and the propulsor. A simple whirling analysis was conducted using the Rayleigh method outlined in [6]; this showed that if a solid steel shaft was adopted, shaft whirl (which could cause the blading to contact with the duct) would be avoided. Beam calculations showed both the static bending stresses in the shaft and the associated shaft deflection to be negligible.

The "far upstream" velocity profile adopted for the computational runs is as shown in Figure 7.5, the variation in velocity between the hub and tunnel wall being representative of that experienced within the afterbody boundary layer of a ship. For computational purposes the "far upstream" boundary was taken to be 0.24m upstream of the duct leading edge.

After considering a number of alternative blade $\overline{rV_\theta}$ distributions, that shown in Figure 7.9 and defined by

$$\overline{rV_\theta}(z) = \begin{cases} -212137.563z^3 - 5341.301z^2 & : z < -0.008\text{m} \\ -17.046z + 0.230 & \\ -250.0z^2 + 23.684z + 0.339 & : -0.008\text{m} < z < 0.008\text{m} \\ -110096.711z^3 + 2392.321z^2 & : z > 0.008\text{m} \\ +2.546z + 0.395 & \end{cases} \quad 7.3$$

was adopted as it was felt, having considered the blade velocity distribution, that this would minimise the risk of flow separation on the blades. It will be noted that for

simplicity, this distribution was chosen to give zero radial variation in $\overline{rV_\theta}$, and, taking the density of air to be 1.225 kg / m^3, resulted in a torque coefficient

$$k_Q = \frac{Q}{\rho\omega^2 D^5} = 0.267$$

which is representative of full scale propulsors.

The initial design of the blading was obtained using the ducted propulsor design method outlined in Chapters 4 and 5 and the 257×65 meridional mesh shown in Figure 7.10. The mean streamlines, velocity vectors, duct pressure distribution and blade shapes as predicted by the method are shown in Figures 7.11, 7.12, 7.13 and 7.14 respectively.

To achieve improved resolution for the manufacture of the blading, the final blade design was generated using a simplified version of the inverse design method that only modelled the flow within the duct from just downstream of the duct leading edge to just upstream of the duct trailing edge. This run was conducted on the 113×49 meridional mesh shown in Figure 7.15, using the mass flow and velocity estimates of the previous runs as input. Due to the relative insignificance of three-dimensional shear effects (suggested by Figure 7.14) the final design was generated using a three-dimensional mean shear run and 16 Fourier harmonics (N=16). The final blade shapes used in the manufacture of the blading (based on an estimated propulsor mass flow of 0.911 kg/s) are shown in Figures 7.16 and 7.17.

7.2.4 Selection of a Suitable Drive Mechanism

Due to the high shaft speed required a high performance DC servo-motor was selected to drive the propulsor shaft, with speed control being achieved using a thyristor drive. Although motor manufacturers suggested that a conventional servo-amplifier might give greater speed control, the thyristor drive was selected on grounds of cost, and, when combined with an in-line choke was found to give speed control well within the ±1% accuracy of the hand-held photo-electric tachometer used to measure shaft speed.

For simplicity a belt drive was used to transmit power to the propulsor shaft, with the motor being mounted at the downstream end of the shaft so as to minimise the effect of its presence on propulsor performance.

The shaft was mounted on deep groove ball bearings situated in bearing housings at each end of the shaft. This type of bearing was chosen as it was cheap, compact, and well able to transmit the shaft thrust without the need for a dedicated thrust bearing.

7.2.5 Manufacture of the Propulsor Test Rig

Each of the propulsor blades was machined as an individual blade segment on a Cincinnati CIM-X three-axis NC milling machine, sufficiently small machining steps being taken so as to eliminate the need for hand finishing of the blade surfaces. The blades were machined with a 5mm root radius, both for ease of manufacture and reasons of blade strength. Each blade (Figure 7.18) was then bolted into a recessed pocket on the shaft.

The duct was also machined on the NC milling machine prior to hand-finishing on a lathe, with the remainder of the design being manufactured using conventional workshop techniques.

The entire ducted propulsor assembly (as shown in Figure 7.2) was then mounted on an aluminium base plate for alignment purposes, and end-loaded into the tunnel working section (Figure 7.6).

7.2.6 Selection of a Probe for the Propulsor Flow Field Measurements

Having decided (for the reasons outlined in Section 7.1(c)) to measure only the time averaged velocity field around the test propulsor, it was decided that these measurements could best be conducted using some form of pitot probe.

Although the use of a simple pitot-static probe was briefly considered, several factors all but excluded the use of this type of device:-

1) As the total pressure tube is coaxially housed within the outer (static pressure) tube, pitot-static probes are generally larger than some of the other types of probe available. It was felt, given the small size of the test propulsor, that a pitot-static probe (and its supports) would cause unnecessary disturbance to the propulsor flow field, thereby impairing its own performance, and possibly that of the propulsor.

2) For accuracy, the static pressure taps of a pitot-static probe are generally located several probe diameters (see Chue [7]) downstream of the total pressure tap (which lies at the tip). As a consequence this type of device is

rather ill-suited to cases where rapid spatial variations of flow velocity are encountered, such as downstream of the test propulsor.

3) Measurements of axial and tangential velocity downstream of the propulsor would entail incrementally yawing the probe to obtain a "null" reading (whereby the probe is aligned with the flow). Whilst this in itself would be rather tedious, the use of a conventional "L" shaped probe (such as that shown in Figure 7.3) would also necessitate repositioning the probe to maintain the spatial position of the probe tip,

4) As pitot-static probes generally display poor sensitivity to yaw, the measurement of the downstream velocity field as outlined in 3) above was deemed to be insufficient accurate for the purposes of the experiments.

As a consequence the use of a five-hole pitot probe (see [7], [8]) was considered. Use of such a probe would have enabled all three components of time-averaged velocity (i.e. V_r, V_θ and V_z) to be measured simultaneously. Furthermore, all measurements could have been conducted with the probe at fixed angles of yaw and pitch, eliminating the tedious task of nulling the probe at each measurement position. Additionally the close spacing of the pressure taps around the tip of the five-hole probe minimises measurement errors associated with the tap spacing. However, this type of probe generally requires empirical calibration over a range of pitch and yaw angles, which means that the probe support structure must allow for both pitch and yaw.

After considering the difficulty of incorporating a calibrated yaw and pitch mechanism into the probe traverse system, and having noted the insignificance of radial velocities predicted by the blade design method (Figures 7.11 and 7.12), use of a five-hole probe was rejected in favour of the three-hole Cobra (Conrad) probe shown in Figure 7.19.

As outlined by Chue [7], the three-hole Cobra probe (as opposed to the two-hole variant) enables both components of flow velocity in the plane of the probe head (i.e. normal to the stem) to be measured simultaneously provided the third component of velocity (parallel to the stem) remains small. For the purposes of measuring the propulsor flow field, this involved measuring the axial and tangential components of velocity, whilst neglecting the radial component. The Cobra probe shares the compact tap spacing of five-hole probes, and as with five hole probes, measurements

can be conducted with the probe at a fixed angle of yaw. Whilst it is still necessary to empirically calibrate the probe over a range of yaw angles (Section 7.3), there is no need to pitch the probe, resulting in both a simpler traverse mechanism and a simpler calibration procedure.

7.2.7 Experimental Readings

The following experimental measurements were made with the ducted propulsor operating at its design point:-

1) Velocity Measurements

Having calibrated the Cobra probe (see Section 7.3.1), a series of radial traverses were conducted above the shaft at various stations around the test propulsor (Figure 7.23), throughout which time the probe remained aligned with the shaft axis. Upon completion of the traverses, the probe pressures (which were measured using a bank of U-tube manometers inclined at 20° to the horizontal) were converted into axial and tangential velocity components using the technique outlined in Section 7.3.2, and compared with the predictions of the blade design method as shown in Figures 7.24..7.27.

In addition, using the results shown in Figures 7.25(f) and 7.27(a) the flow angles ($\tan^{-1}(V_\theta/V_z)$) were calculated 8mm (0.067 duct lengths) upstream of the duct trailing edge, these being compared with the predictions of the design method in Figure 7.28.

Finally, the velocity measurements shown in Figure 7.25(f) were integrated to yield propulsor mass flow, this being compared with the computational prediction in Table 7.1.

2) Shaft Power Measurements

In addition to the detailed flow measurements outlined in 1) above, it was thought worthwhile to obtain a more general indication of overall propulsor performance.

To these ends the electrical power absorbed by the shaft motor was measured under design conditions, firstly with the duct and blading in place, and then with these items removed. By subtracting the latter result (which represents, at least approximately, the transmission losses in the drive mechanism) from the

first, an estimate of the power absorbed by the blading was obtained, as shown in Tables 7.2 and 7.3.

In addition to the above measurements, some attempt was made at flow visualisation using both smoke traces and tufts, although for the reasons given in Section 7.6.7, little was obtained in terms of meaningful results.

Additionally, the installation of pressure taps on the duct surface was considered to enable the duct pressure distribution to be measured and compared with computational predictions. However, this would have entailed machining a trench in the outer surface of the duct to conceal the necessary pressure tubes. Thus, due to limitations of time and concerns regarding the effect of this machining operation on duct circularity (and therefore blade tip clearance), these measurements were removed from the experimental schedule.

7.3 Use of the Three-Hole Cobra Probe for Measuring the Test Propulsor Flow Field

7.3.1 Calibration of the Three-Hole Cobra Probe

The Cobra probe was calibrated using the procedure outlined by Chue [7], which in turn is attributable to the work of Rajaratnam and Muralidhar [9].

This calibration assumes that when the probe is yawed at an angle α to the flow direction, the pressures p_A, p_B and p_C recorded by the three pressure taps A, B and C (Figure 7.19) may be written

$$p_A = p_{static} + K_A(\alpha)p_{dynamic} \qquad 7.4$$

$$p_B = p_{static} + K_B(\alpha)p_{dynamic} \qquad 7.5$$

$$p_C = p_{static} + K_C(\alpha)p_{dynamic} \qquad 7.6$$

where p_{static} and $p_{dynamic}$ are the true static and dynamic pressures at the probe tip, and K_A, K_B and K_C are calibration factors that are assumed to be functions of yaw angle α only.

Having made this assumption, the probe was mounted in the wind tunnel working section and aligned with the shaft axis to provide a yaw reference. The probe was then positioned towards the upstream end of wind tunnel working section, well clear of the test propulsor and tunnel walls, and the mesh screens (Section 7.2.2) removed (temporarily) from the entrance to the working section. Upon operating the wind tunnel fan, a uniform stream would now be encountered by the probe, and the calibration could begin.

The probe pressure readings (p_A, p_B and p_C) were measured at successive yaw angles in the range $-60° < \alpha < 60°$. With these measurements complete, the static and dynamic pressures (p_{static} and $p_{dynamic}$) of the uniform stream were measured using the pitot-static probe shown in Figure 7.3, enabling the variation of the calibration coefficients (K_A, K_B and K_C) with yaw angle α to be determined from equations 7.4..7.6. The resulting calibration coefficients, as shown in Figure 7.20, are almost identical to those presented by Chue [7].

Now, by combining equations 7.4..7.6 it was possible to define an additional calibration coefficient

$$K_0(\alpha) = \left(\frac{K_B - K_A}{K_C - K_A}\right) = \left(\frac{p_B - p_A}{p_C - p_A}\right) \qquad 7.7$$

As with K_A, K_B and K_C, this coefficient is purely a function of yaw angle α. However, unlike these other coefficients it can be determined solely from probe pressure readings, without the need for prior knowledge of the local static and dynamic flow pressures.

The full range of $K_0(\alpha)$ values determined from the calibration readings is shown in Figure 7.21. However, for the purposes of the propulsor flow measurements, it was expected that the flow incidence onto the probe would lie within the range $-10° < \alpha < 60°$, and as a consequence only the range of K_0 values shown in Figure 7.22 were used in interpreting the results of these measurements.

Having obtained this truncated range of K_0 values the probe calibration was complete.

However, in closing, it is interesting to note that as an alternative to the form given in equation 7.7, K_0 could have been defined as

$$K_0(\alpha)=\left(\frac{K_C-K_A}{K_B-K_A}\right)=\left(\frac{p_C-p_A}{p_B-p_A}\right)$$

$$K_0(\alpha)=\left(\frac{K_A-K_B}{K_C-K_B}\right)=\left(\frac{p_A-p_B}{p_C-p_B}\right)$$

or

$$K_0(\alpha)=\left(\frac{K_A-K_C}{K_B-K_C}\right)=\left(\frac{p_A-p_C}{p_B-p_C}\right)$$

Nevertheless, the combination given in equation 7.7 was adopted as its denominator is non-zero over the range of values (Figure 7.22) considered for the propulsor flow field measurements. Additionally, unlike some of these other forms, each value of K_0 defined by equation 7.7 can be associated with a unique value of yaw angle α over the range of α encountered during the propulsor measurements; this latter property is essential to the determination of flow velocity using the technique outlined in Section 7.3.2.

7.3.2 Determination of Axial and Tangential Velocity Around the Test Propulsor Using the Cobra Probe

Having calibrated the Cobra probe as outlined above, the probe traverses described in Section 7.2.7 were conducted. For each position of the probe tip the tap pressures p_A, p_B and p_C were recorded, enabling the time-averaged axial and tangential velocities to be determined as follows:-

1) Using equation 7.7, the value of K_0 was calculated.

2) Using this value of K_0 and the calibration results shown in Figure 7.22, the value of probe yaw angle α was determined using linear interpolation.

3) Using this value of α and the calibration results shown in Figure 7.20, K_A, K_B and K_C were determined using linear interpolation.

4) Having thus determined the values of K_A, K_B and K_C, the dynamic pressure $p_{dynamic}$ could then be obtained by combining any two of equations 7.4..7.6. In practice equations 7.4 and 7.6 were used in order to avoid arithmetical problems, resulting in the expression

$$p_{dynamic} = \left(\frac{p_C - p_A}{K_C(\alpha) - K_A(\alpha)} \right) \qquad 7.8$$

Additionally, although the static pressure p_{static} was not required for the verification of the ducted propulsor design method, it could, none-the-less, have been calculated from equation 7.4, viz

$$p_{static} = p_A - K_A(\alpha) p_{dynamic} \qquad 7.9$$

5) Having determined $p_{dynamic}$, the magnitude of the time-averaged flow velocity, $|\mathbf{V}|$, was calculated from

$$|\mathbf{V}| = \sqrt{\frac{2p_{dynamic}}{\rho}} \qquad 7.10$$

where ρ is the density of the air in the wind tunnel.

6) Noting that α was measured relative to the shaft axis, the time averaged velocity was be resolved into axial and tangential components, viz:-

$$V_z = |\mathbf{V}| \cos(\alpha) \qquad 7.11$$

$$V_\theta = |\mathbf{V}| \sin(\alpha) \qquad 7.12$$

which could then be compared with the predictions of the inverse design method.

7.4 Measurement Errors Associated with the Use of the Cobra Probe

There are a number of errors associated with the use of the three-hole Cobra probe for measuring the propulsor flow field, and it is worthwhile considering these before

the flow field results are considered. The possible sources of error are similar to those presented by Blake [8] for the measurement of time-averaged and steady flow pressures, and may be summarised as:-

1) Probe Alignment Errors

Prior to calibration it was necessary to physically align the probe with the shaft axis (the yaw reference). The delicate construction of the probe somewhat hindered this procedure, and as a result this alignment was only accurate to an estimated tolerance of ±1.5°.

Likewise, in order to correlate the probe readings with the predictions of the blade design method it was necessary to position the probe tip at a known distance forward of the blading and above the shaft axis before commencing experimental readings. Again the fragility of the probe precluded the use of spacers for this task, and as a consequence this positioning had to be checked with a ruler, with an estimated accuracy of ±1mm.

Although not unreasonably large, these errors were exacerbated by the small size of the test propulsor, and add to the cumulative effects of the errors listed below.

2) Flow Pitch Incidence Errors

The use of the three-hole Cobra probe in these experiments makes no allowance for the presence of radial velocities. Although computational results (see Section 7.2.6) suggest that radial velocities around the propulsor are very small in comparison to axial velocity, this is none-the-less a source of error, with the dynamic pressure due to radial velocity being recorded as an augmentation of axial and tangential velocity by the probe.

3) Turbulence Errors

As shown by Blake [8], when measuring time-averaged flow pressures using a pressure probe, the effect of flow turbulence is to increase the value of pressure recorded by each of the pressure taps. For the test propulsor the principal sources of turbulence were the mesh screens used to generate the onset shear flow, the turbulence associated with the shaft and duct supports (Figure 7.2), and the velocity fluctuations associated with the development of circumferential variations of velocity within the blade passages.

However, in obtaining the flow velocities from the recorded pressures (equations 7.11..7.15), only the difference in pressure between the pressure taps is used. Thus, assuming the turbulence errors recorded by each hole to be near-identical, once might reasonably assume that this source of error is small.

4) Probe-Wall Interaction

To avoid any risk of damage, the probe was brought no closer than 5mm to the shaft or duct, whilst the probe supports prevented the probe being brought closer than about 80mm to the tunnel wall. As a consequence any errors associated with streamline deflection due to probe-wall interaction should be negligible.

5) Influence of Probe Supports

Whilst the probe was supported towards the top end of its stem (i.e. well downstream of and well above the probe tip), the flow disturbance caused by the probe support nevertheless represents a source of error in the measurement of the flow velocities, and, moreover, one that is difficult to quantify. Suffice it to say that every effort was taken to minimise the interference effects associated with the presence of the probe supports.

6) Flow Disturbance Caused by the Probe

The fundamental principal behind the use of the Cobra probe for flow velocity measurement is that it disturbs the flow field in which it is placed; if there were no flow disturbance then for cases of zero yaw (i.e. the "null" condition) the pressure recorded by the centre and side holes would be identical, and it would therefore be impossible to decompose the measured pressures into static and dynamic components.

However, the size of the probe tip (Figure 7.19) ensures that any associated flow disturbances are negligible compared to those caused by the action of the propulsor, whilst the probe stem is sufficiently far downstream to have negligible effect on the recorded pressures.

7.5 Physical Features of the Test Rig Affecting Propulsor Performance

In addition to the sources of error outlined in Section 7.4 which are directly associated with the use of the Cobra probe for velocity measurement, there are a

number of features of the test rig itself that limit the extent to which the test propulsor represents the idealised model input to the blade design method. These include:-

1) **The Aerodynamic Blockage of the Test Propulsor Assembly**

Due to time constraints, the axisymmetric velocity profile input to the blade design method was based upon measurements taken within the tunnel working section before the test propulsor assembly was installed (see Section 7.2.2). Thus, the blading, as manufactured, took no account of the modifications to the velocity profile caused by the presence of the test rig. In particular, the aerodynamic blockage of the assembly (Figure 7.6) is quite large and might be expected to result in a measured velocity gradient greater than that specified for the blade design.

2) **Flow Interference Caused by the Shaft and Duct Supports**

Although the downstream shaft support was deliberately positioned sufficiently far downstream (0.5m) of the blading to minimise any flow disturbance, the duct support, the upstream shaft support and the upstream bearing housing inevitably cause the onset flow field to deviate from axisymmetry.

Whilst these problems were minimised by fitting a nose cone (2:1 ellipsoid) to the end of the upstream shaft bearing housing, and fitting a foam fairing (not shown in Figure 7.2) to the upstream shaft support, these interference effects still represent a source of error that it is difficult to quantify.

3) **Tunnel Wall Interference**

The close proximity of the tunnel walls to the test propulsor must, to some extent, modify the test propulsor flow field. In particular, the presence of the tunnel wall might be expected to increase the velocity in the region of the bypass flow, whilst reducing the flow velocity in the core flow, causing a corresponding reduction in propulsor mass flow. This type of interference was not modelled by the blade design method (which allows free flow across the wall boundary), resulting in yet another source of error that it is difficult to quantify.

4) **Non-Axisymmetry of Onset Flow**

As stated in Section 7.2.2, the propulsor onset flow deviated from axisymmetry (Figure 7.4). As a consequence it was necessary to base the blade design on the circumferentially-averaged onset flow. Although this undoubtedly results

in a difference between the computational predictions and the experimentally-measured velocities, practical full-scale ducted propulsors rarely (if ever) encounter axisymmetric flow, and thus the significance of this error must be regarded as a test of the applicability of the blade design method to practical propulsors.

7.6 Discussion of the Experimental Results

7.6.1 Axial Velocity Measurements on the Computational "Far Upstream" Boundary

The results of axial velocity measurements on the "far upstream" boundary of the blade design method (two duct lengths upstream of the duct leading edge) are shown in Figure 7.24.

Although similar in overall form, the axial velocities recorded by the Cobra probe with the propulsor operating (Curve D) differ quite substantially (by around 20%) from those input to the blade design method (Curve A). It was thought worthwhile to investigate these differences in some depth, and as a consequence, two additional traverses were conducted as follows.

Firstly, the Cobra probe traverse was repeated with the propulsor idle (i.e. with zero shaft speed), these results being represented in Figure 7.24 by Curve C. Then, another traverse was conducted, again with the propulsor idle, but this time using the pitot-static probe (Figure 7.3) that had been used to determined the input velocity profile for the blade design method (Section 7.2.2). The results of this latter traverse are represented by Curve B in Figure 7.24.

It can be seen that these two latter traverses show successive reductions in axial velocity and correspond much more closely to the specified velocity profile (Curve A) than that does the profile measured with the propulsor operating (Curve D).

As a result, the author attributes the differences between the axial velocity profile input to the blade design method and that measured by the Cobra probe with the propulsor running to the following cumulative sources of error:-

(a) The velocity induced by the propulsor

Although the flow velocity induced by the action of propulsor decreases with distance upstream of the propulsor, the difference between Curves C and D would seem to imply that it remains significant at the computational upstream boundary, where it should ideally be zero. This could have been avoided by taking the computational boundary even further upstream.

(b) Differing Accuracy of the Pitot Probes Used

The pitot-Static probe used in determining the input to the blade design method was less accurate than the Cobra probe. In particular, the physical size of the pitot-static probe is much greater than that of the Cobra probe, and as such it would be expected to be less accurate than the Cobra probe due to the correspondingly greater disturbance it imparts on the flow. In addition, due to the spacing between its static and total pressure taps (see Section 7.2.6), the pitot-static probe might be regarded as less accurate at measuring local flow velocities than the Cobra probe whose pressure tappings are located close together on a compact probe tip.

This source of error is represented in Figure 7.24 by the difference between B and C. Had the Cobra probe been available at the time the blading was designed, this problem could have been avoided by using this probe, rather than the pitot-static probe, to measure the upstream velocity profile.

(c) The Aerodynamic Blockage of the Test Propulsor Assembly

For the reasons stated in Section 7.5, the velocity profile input to the blade design method was based on measurements taken before the test propulsor was installed in the working section, and as such took no account of the increase in flow velocity caused by the aerodynamic blockage of this assembly.

Had the velocity profile for the blade design method been determined after the ducted propulsor had been installed in the wind tunnel, this source of error could have been avoided.

(d) Non-Axisymmetric Onset Flow

As outlined in Section 7.2.2, the axial velocity profile input to the blade design method represents merely an axisymmetric approximation to the true "far upstream" velocity profile, and therefore one might expect some difference between the specified velocity profile and that actually achieved. Given the

practical difficulties in generating a truly axisymmetric velocity profile using mesh screens it is difficult to see how this source of error could have been avoided.

This factor, together with that outlined in (c) above, is represented by the differences between Curves A and B in Figure 7.24.

It will be noted that of all these sources of error, all bar that given in (d) could be avoided if a new set of blading were designed using the recommendations detailed in (a)..(c) above. Indeed, if a new blade design were to be produced, there would be the potential for reducing the differences between the measured and specified velocity profiles to within 5%. This would be a great improvement over the present results, and would be likely to improve the correlation between the computational and experimental results outlined below.

7.6.2 Axial Velocity Measurements Away from the Computational Far Upstream Boundary

The axial velocity measurements conducted away from the computational "far upstream" boundary are shown in Figure 7.25(a)..(i), generally comparing quite well in overall form with the computational predictions.

At larger radii and in the bypass flow the differences between the computation predictions and the experimental readings remain large (at around 20%) downstream of the "far upstream" boundary. However, at lower radii the computational predictions become increasingly more accurate as the flow approaches the propulsor, with Figure 7.25(b) showing near parity between the predicted and measured velocity profile at lower radii.

Whilst to some extent this improved correlation at lower radii can be attributed to viscous effects associated with the shaft boundary layer, and wall-interference effects (Section 7.5), both of which tend to reduce the velocity in the core flow region, such a trend might also have been expected due to the action of the blading dominating the behaviour of the fluid in the vicinity of the propulsor.

The velocity measurements conducted downstream of the blading within the duct (Figure 7.25(f)) also compare much better with the computational predictions, particularly at around tip radius where the two curves are almost identical. Towards the hub the differences between the measured velocities and the computational

predictions increases to around 12%, although this difference can, in part, be attributed to the presence of the shaft boundary layer and the blade root radius. Additionally, the sharp drop-off in axial velocity measurements at the blade tip would seem to be due to the blade tip clearance (which results in only partial energisation of the flow immediately adjacent to the duct), and also the presence of the duct boundary layer.

Downstream of the duct (Figures 7.25(g)..(i)) the presence of the duct wake is clearly reflected in the measured values by a sharp velocity gradient at roughly the same radius as the computational prediction. Although one would not expect the measurements to yield a true discontinuity in velocity across this wake due to flow viscosity, the effects of blade tip clearance must undoubtedly reduce the resolution of the duct wake still further.

As the flow proceeds downstream from the duct trailing edge it can be seen that the duct wake, as measured, broadens out, again due to viscous action. As a consequence, the core flow predictions of the computational method show excellent agreement (i.e. to within 3%) with the measured values far downstream of the propulsor (Figure 7.25(i)), although the differences within the bypass flow remain large.

7.6.3 Tangential Velocity Measurements Upstream of the Duct

The results of tangential velocity measurements conducted upstream of the duct leading edge are shown in Figure 7.26.

Bearing in mind the accuracy of the probe alignment (Section 7.4) and manometer readings, it can be seen that away from the shaft the measured tangential velocities are effectively zero, in keeping with the assumptions of the blade design method.

However, close to the shaft the tangential velocities rise sharply due to the skewed shaft boundary layer (which has both tangential and axial components of velocity), which is not modelled by the blade design method. Even had the upstream portion of the shaft been shrouded within a static housing (as is usually the case with practical marine propulsors), little could be done to prevent the growth of such a boundary layer within the blade passages. Thus, the extent to which the swirl induced by the shaft affects propulsor performance must be regarded as a measure of the applicability of the blade design method to practical marine propulsors.

7.6.4 Measured Flow Angles Downstream of the Blading

The flow angles recorded within the core flow at a position 8mm (0.067L) upstream of the duct trailing edge are shown in Figure 7.28.

Although the computationally-predicted flow angles become increasingly inaccurate towards the hub, this would seem to be due to the blade root radius (Figure 7.18) and presence of the shaft boundary layer. Likewise, the differences between the computational and experimental values of flow angle close to the duct can be attributed to the effects of blade tip clearance, and also the presence of the duct boundary layer.

Overall the flow angle measurements compare very well with the predictions of the blade design method. In many ways this would have been expected, for once shaft speed has been fixed, it is the blade geometry rather than the propulsor onset flow that determines these flow angles (the Kutta condition ensures that there are no significant velocities normal to the blade camberline at the blade trailing edge, resulting in this strong interdependence between blade shape and flow angle).

It will be noted that the difference between the predicted and measured flow angles remains almost constant over the majority of the core flow at approximately 1.5°. This would seem to imply that these differences are due to the effects of probe misalignment (discussed in Section 7.4) rather than any inadequacies of the blade design method.

7.6.5 Tangential Velocity Measurements Downstream of the Blading

The results of tangential velocity measurements (expressed in terms of $\overline{rV_\theta}$) downstream of the blading are shown in Figure 7.27(a)..(d).

Figure 7.27(a) shows the results of the traverse conducted within the duct, just upstream of the duct trailing edge. As with the axial velocity measurements the sharp reduction in $\overline{rV_\theta}$ at the tip is probably due to duct boundary layer and blade tip clearance, whilst the sharp rise in $\overline{rV_\theta}$ close to the hub would seem to be associated with the skewed shaft boundary layer mentioned in Section 7.6.3.

Measurements downstream of the duct (Figures 7.27(b)..(d)) clearly show the presence of the duct wake. Once again, the results show this wake to broaden as it passes downstream of the propulsor.

Overall, it can be seen that the measured values of $\overline{rV_\theta}$ within the core flow straddle the computational predictions. Towards the hub the measured values of $\overline{rV_\theta}$ are generally lower than the computational predictions, whilst at larger core flow radii the measured values exceed the design method predictions; at the mid-point of the core flow the computational and experimental values of $\overline{rV_\theta}$ are almost identical.

As the propulsor efflux passes downstream, there seems to be little change in the radial distribution of $\overline{rV_\theta}$ within the core flow, except immediately adjacent to the shaft and the duct wake. Indeed, the measured values of $\overline{rV_\theta}$ in the core flow do not differ from the computational predictions by more than 20%, and, over the majority of this region than more than 8%. It is felt that this represents quite good agreement when the following factors are taken into account:-

1) The axial velocity profile specified as input to the blade design method differs quite substantially from that actually achieved by with the test propulsor (see Section 7.6.1).

2) The effects of tunnel wall interference and the shaft boundary layer (see Sections 7.5 and 7.6.2) further affect the performance of the test propulsor.

3) Due to the large difference between axial velocity and tangential velocity around the propulsor, the tangential velocities determined using the Cobra probe are very sensitive both to slight misalignments of the probe (Section 7.4) and small errors in the manometer readings. The significance of this source of error is highlighted by the error bands shown in Figures 7.27(a)..(d) which allow for an effective probe misalignment of ±1.5°.

   Given an estimated misalignment in excess of 1.0° (Section 7.6.4), probe misalignment is undoubtedly responsible for some of the difference between the computational and experimental values of $\overline{rV_\theta}$ within the core flow, and would also seem to be the cause of the non-zero values of $\overline{rV_\theta}$ in the bypass flow.

In particular, 1) and 2) above result in the design method overestimating axial velocity close to the hub, and underestimating axial velocity close to the duct (Figure 7.25(f)). Given that the flow angles downstream of the blading are largely fixed by the blade geometry (see Section 7.6.4), the result of these experimental errors can

only be that the computational method overestimates the values of $\overline{rV_\theta}$ close to the hub and underestimates those close to the duct. Thus, the manner in which the measured values of core flow $\overline{rV_\theta}$ straddle the computational predictions (Figure 7.27(a)) would seem to be more attributable to experimental error (i.e. 1) and 2) above) than any limitations of the blade design method.

In closing, the importance of these tangential velocity measurements cannot be over-stressed. Firstly, $\overline{rV_\theta}$ is one of the principal inputs to the blade design method, and is therefore one of the principal quantities upon which the accuracy of the blade design method must be assessed. Additionally the radial distribution of $\overline{rV_\theta}$ downstream of the blading can be related to the shaft torque through momentum theory, and as such might be regarded as a key indicator of propulsor performance.

7.6.6 Shaft Power Measurements

The results of the shaft power measurements are presented in Tables 7.2 and 7.3.

As can be seen, the power absorbed by the blading as measured is 7% less than that predicted by the blade design method, which it is felt represents very good agreement if the sources of error outlined in Sections 7.4, 7.5 and 7.6.1 are considered.

7.6.7 Mass Flow Calculation

By integrating the measured axial velocity profile shown in Figure 7.25(f) an estimate of mass flow rate was obtained for the test propulsor, as shown in Table 7.1.

If the results presented in Table 7.1 are taken at face value it would seem that the ducted propulsor design method is capable of estimating propulsor mass flow to a very reasonable degree of accuracy (i.e. within 6%). Furthermore, if the mass flow results are considered in conjunction with the shaft power results in Section 7.6.6, it might be concluded that the design method gives very good estimates of overall propulsor performance.

It will be noted that even though the velocities measured far upstream of the propulsor were generally greater than the computational predictions (Section 7.6.1), the experimentally determined value of mass flow is some 6% lower than that predicted by the computational method. This over-estimation of propulsor mass flow by the blade design method (where one might reasonably expect an under-estimation) could well be due to the wall-interference effects outlined in Section 7.5, which

fortunately tend to compensate for the higher than expected measured axial velocities upstream of the propulsor.

7.6.8 Attempts at Flow Visualisation

In addition to the above experimental readings, it had also been hoped to conduct flow visualisation tests by injecting smoke from a smoke generator into the propulsor flow field. Some limited preliminary tests were conducted with the propulsor operating under design conditions, with smoke traces upstream of the duct seeming to mirror the streamline patterns shown in Figure 7.11 rather well. However, the limited output from the smoke generator and the presence of flow turbulence prevented any meaningful observations of flow downstream of the blading from being made. Unfortunately, the smoke generator (which was rather antiquated!) soon proved unserviceable, and could not be used in the preparation of results for this thesis.

Further attempts at flow visualisation were made using tufts (strands of wool or cotton) suspended from a probe. The problem encountered here was that tufts of sufficient size to be recorded on film were of such stiffness as not to respond well to the propulsor flow field, and no useful results were obtained.

7.7 Concluding Comments

The net effect of the errors outlined in Section 7.6.1 was that the test propulsor blading was designed for different flow conditions to those actually encountered. The additional sources of error highlighted in Sections 7.4 and 7.5 further limit the validity of the experimental results. As a consequence, it is difficult to draw any definite conclusions from the experimental work, although it would seem that the differences between the computational and experimental results are more due to errors associated with the test procedure than any limitations of the ducted propulsor design method.

Whilst the axial velocity measurements differ quite substantially (by around 20%) from the predictions of the design method away from the propulsor, this would seem to be due to the sources of error outlined in Section 7.6.1, together with wall interference and viscous effects. Closer to the propulsor these differences are much smaller, and in overall form the measured velocity profiles agree very well with the computational predictions.

As discussed in Section 7.6.4, the flow angles downstream of the blading are primarily determined by blade geometry and shaft speed, being relatively insensitive to the local axial velocity. Consequently, the measured flow angles downstream of the blading agree very well with the predictions of the blade design method, except immediately adjacent to the duct and hub where some differences would have been expected.

For the reasons discussed in Section 7.6.5, the tangential velocity measurements downstream of the blading were strongly affected by the errors outlined in Section 7.6.1. Additionally, the tangential velocity measurements were found to be quite sensitive to errors associated with the probe alignment and manometer readings, and as a result are only considered to be accurate to within 7% (this accuracy is based on an effective probe misalignment of 1.5° at 20° yaw). Given these two sources of error, and also that the tangential velocity measurements downstream of the blading generally lie within the error bands associated with probe misalignment (see Figure 7.27), it is concluded that the blade design method yields very reasonable estimates of tangential velocity within the propulsor flow field.

As regards overall propulsor performance, the computationally-determined values of shaft power (less transmission losses) and mass flow rate differ by only 7% from the measured values. Under the circumstances it is felt that this represents very good agreement.

Summarising, it is felt that the experimental results show the ducted propulsor design method to yield at least reasonable estimates of the design point propulsor flow field, and good estimates of overall propulsor performance

However, one of the key recommendations of this thesis (see Chapter 8) is that the experiments should be re-run with new blades designed in accordance with the suggestions of Section 7.6.1. The resulting improvements in accuracy would enable a far more detailed assessment of the blade design method to be made, at minimal extra cost in terms of time, effort and expense.

In closing, it should be noted that the experiments conducted in this Chapter were rather limited in scope. In particular, the measurements were conducted for a single blade row propulsor of uniform blade loading displaying little sign of slipstream contraction. It should be readily apparent that a far more extensive series of tests

would be required before the design method could be applied to the design of full scale propulsors with confidence.

References

1) Denton,J.D. "An Improved Time Marching Method for Turbomachinery Flow Calculations", p514, Trans. ASME, J. Eng. Power, Vol.105, No.3, 1983

2) El-Gamal,H.A. "Laminar Flow Along a Corner with Boundary Layer Suction", Ph.D. Thesis, Department of Mechanical Engineering, University College London, 1976

3) NAG Fortran Library Manual Mk.14, Vol. 3, Numerical Algorithms Group Ltd., 1990

4) O'Brien,T.P. "The Design of Marine Screw Propellers", Hutchinson Scientific and Technical, London 1962

5) Marscher,W.D. "Structural Analysis: Fatigue Life Assessment", Radial Turbine Lecture Series, von Karman Institute, April 6-10, 1992

6) Ryder,G.H., Bennett,M.D. "Mechanics of Machines", Second Edition, p299, Macmillan Education Ltd., 1990

7) Chue,S.H. "Pressure Probes for Fluid Measurement", Prog. Aerospace Sci., pp147-223, Vol.16, No.2, Pergamon Press, 1975

8) Goldstein,R.J. (Editor) "Fluid Mechanics Measurements", pp61-97, Springer-Verlag, Berlin, 1983

9) Rajaratnam,N., Muralidhar,D. "Yaw Probe Used as Preston Tube", Aeronaut. J. 72, 1059-60, 1968

	Propulsor Mass Flow† (kg/s)
Prediction of Blade Design Method	0.911
Calculated from Axial Velocity Measurements	0.858

† Based on an air density of 1.225 kg/m3

Table 7.1: Comparison of Computational and Experimental Values of Propulsor Mass Flow Rate

	DC Motor Current (Amps)	DC Motor Voltage (Volts)	Power (Watts)
Test Propulsor Running at Design Point	5.1	83.3	424.83
Shaft Running Under Design Conditions with Duct and Blading Removed	2.65	80.0	212.0

Table 7.2: Shaft Power Measurements for the Test Propulsor

	Power Absorbed by Blading (Watts)
Test Propulsor Running at Design Point	212.83
Prediction of Blade Design Method	228.96

Table 7.3: Comparison of Shaft Power Measurements with the Prediction of the Blade Design Method

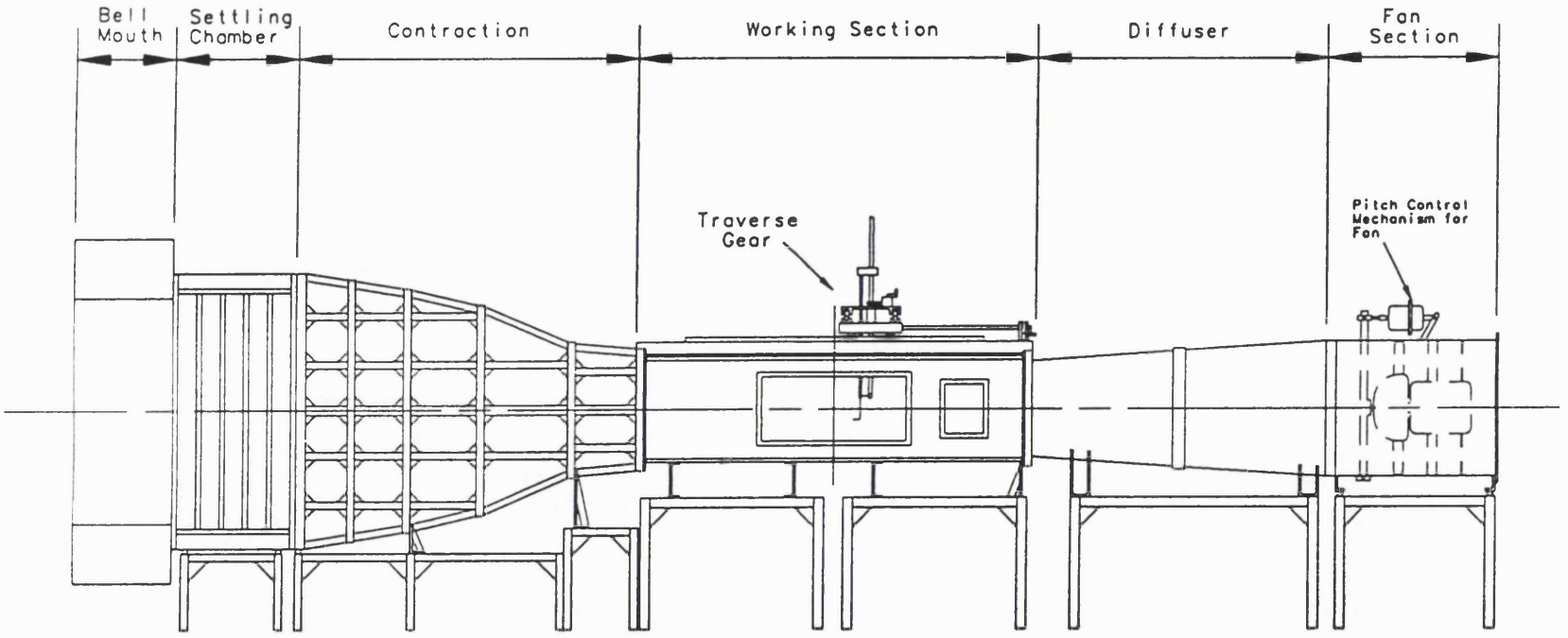

Figure 7.1: View of the Low Speed Wind Tunnel with the Modified Working Section (Based on a Drawing Presented by El-Gamal [2])

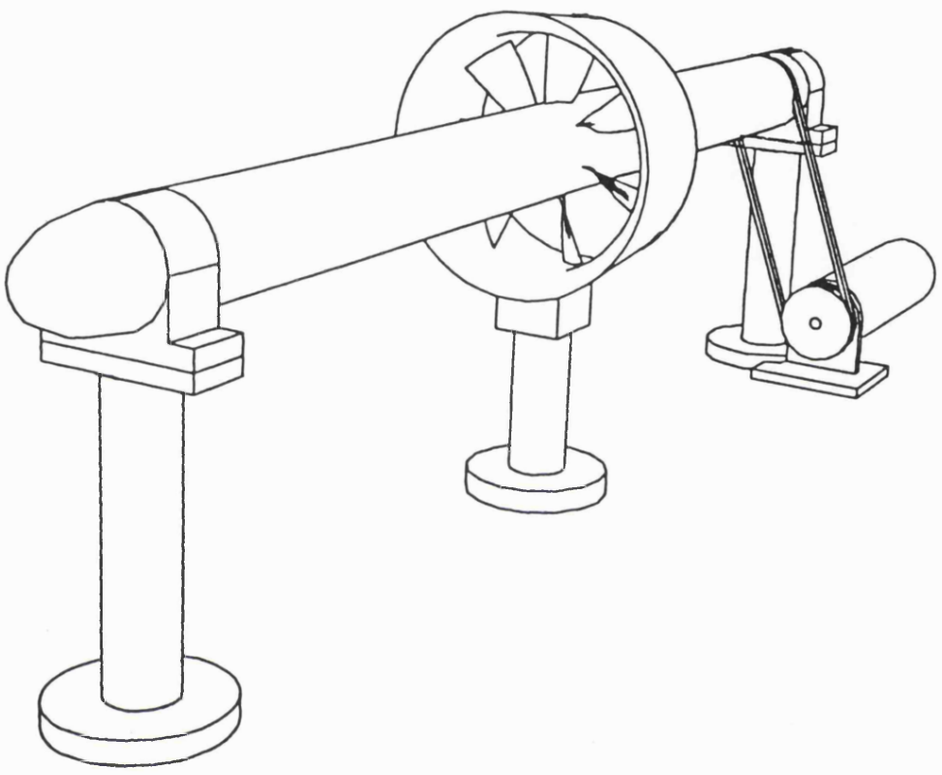

Figure 7.2: A Solid Model of the Test Propulsor as Mounted in the Tunnel Working Section

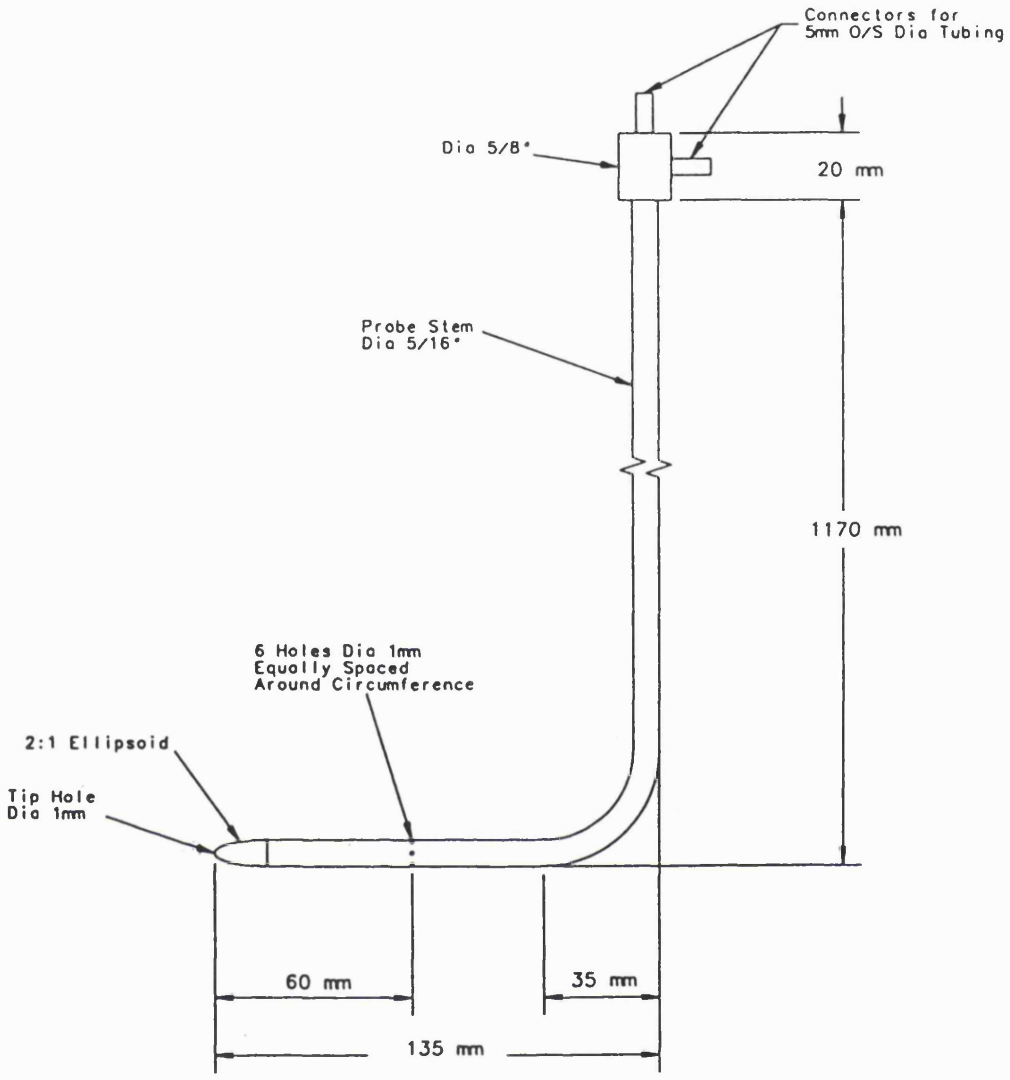

Figure 7.3: The Pitot-Static Probe Used for the Initial Velocity Profile Measurements

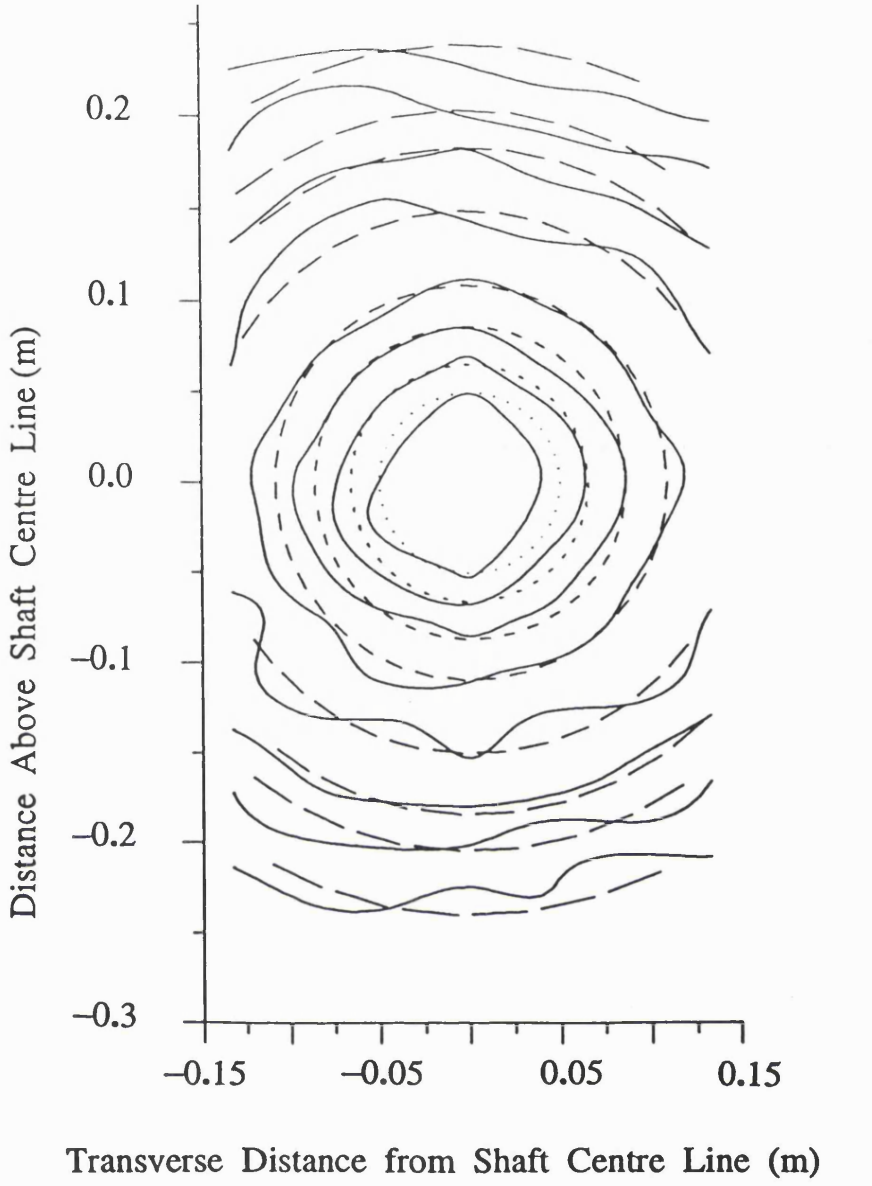

Figure 7.4: Comparison of the Measured Velocity Field with that Input into the Blade Design Method

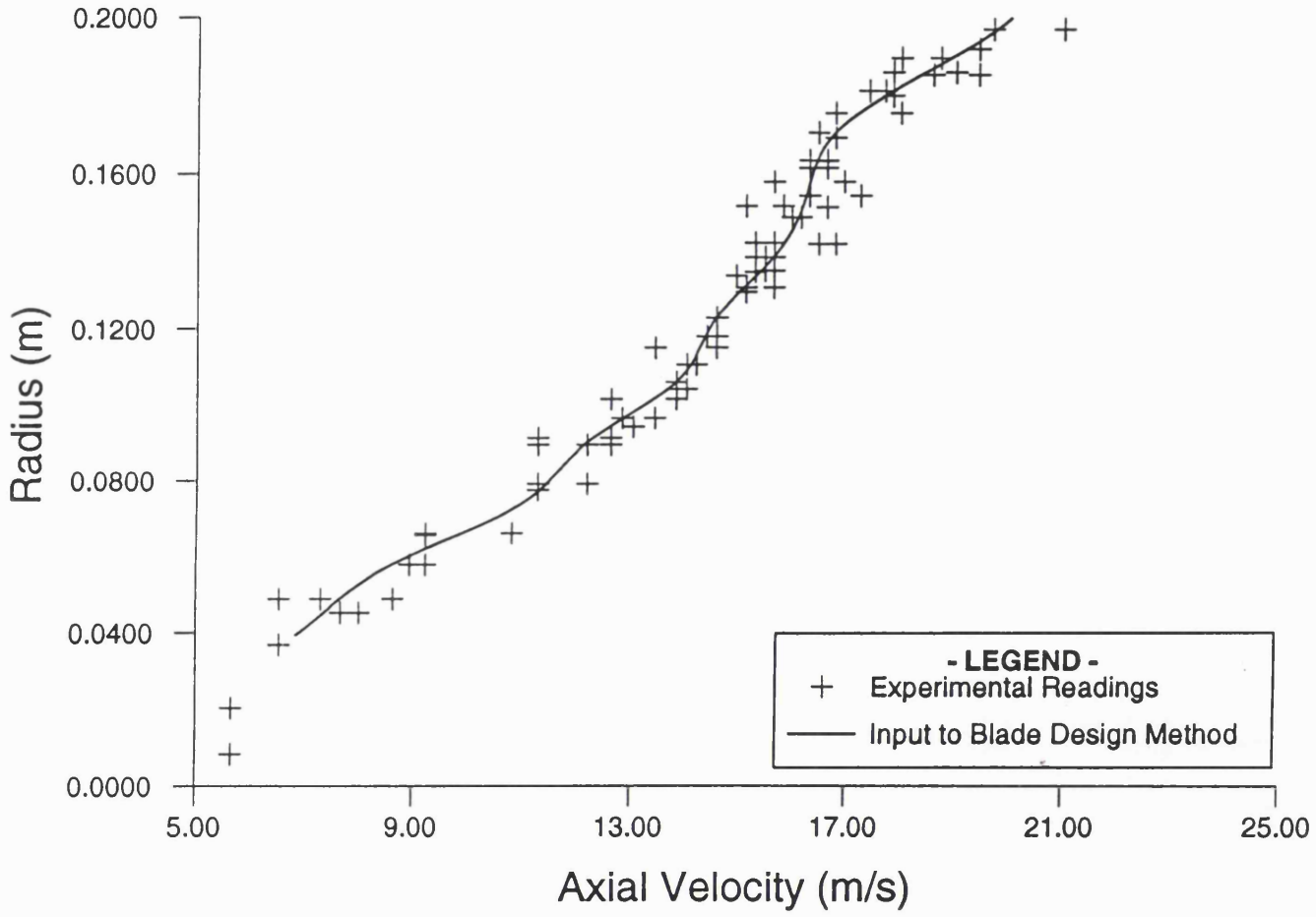

Figure 7.5: The Final "Far Upstream" Velocity Profile as Input into the Blade Design Method

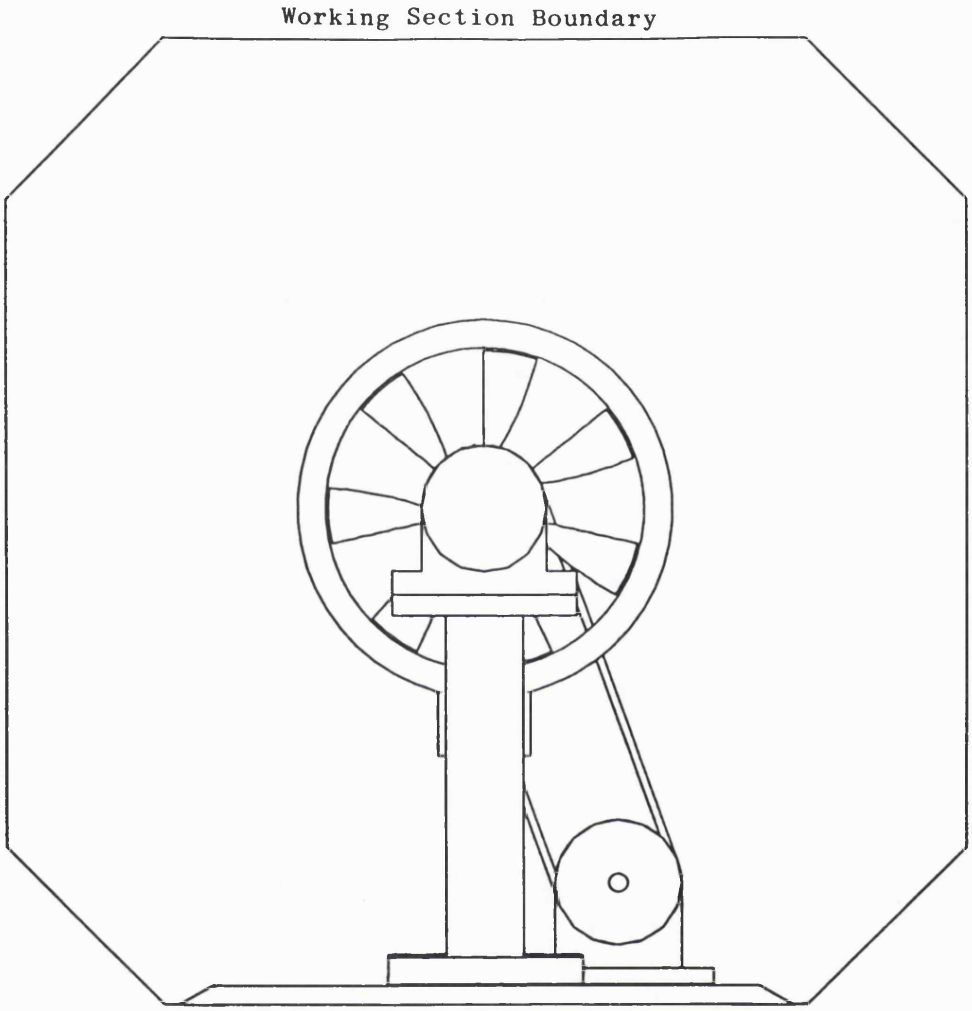

Figure 7.6: End View (to Scale) of the Test Propulsor Mounted in the Tunnel Working Section

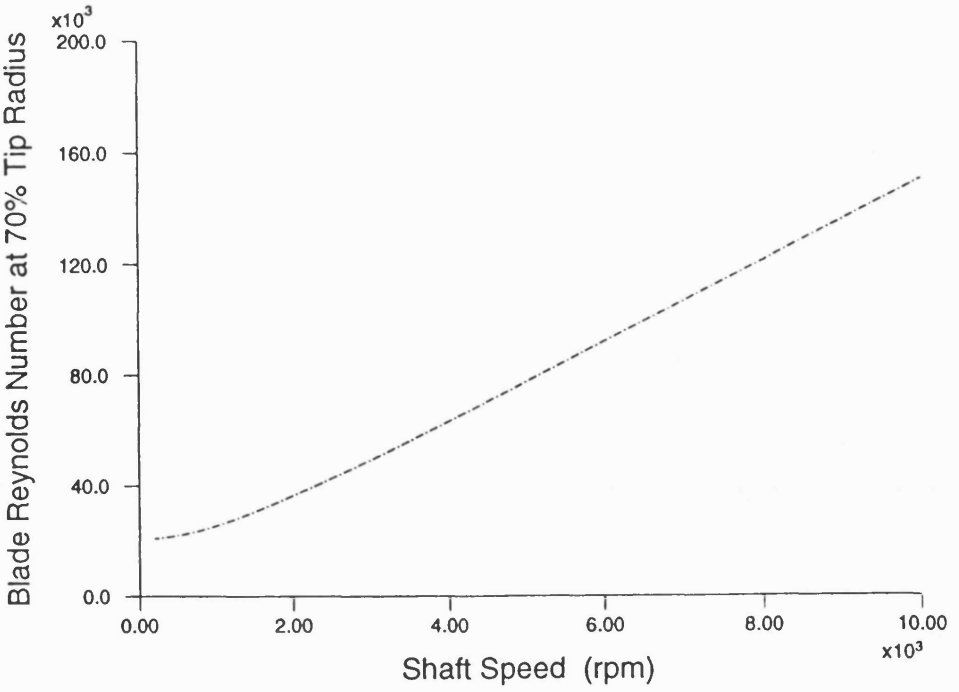

Figure 7.7: Blade Reynolds Number (Estimated) versus Shaft Speed for the Test Propulsor

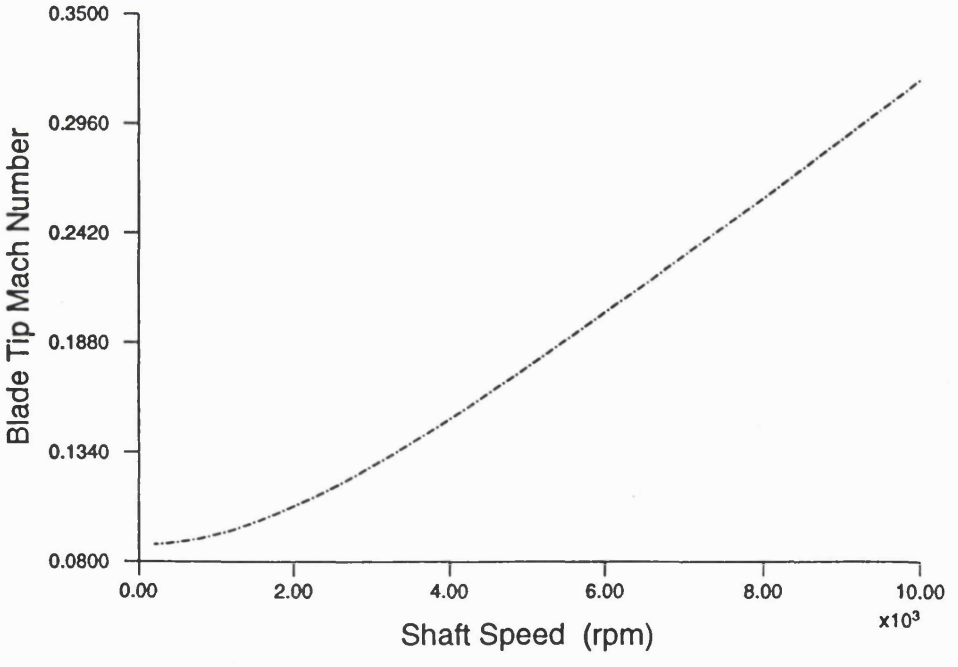

Figure 7.8: Blade Mach Number (Estimated) versus Shaft Speed for the Test Propulsor

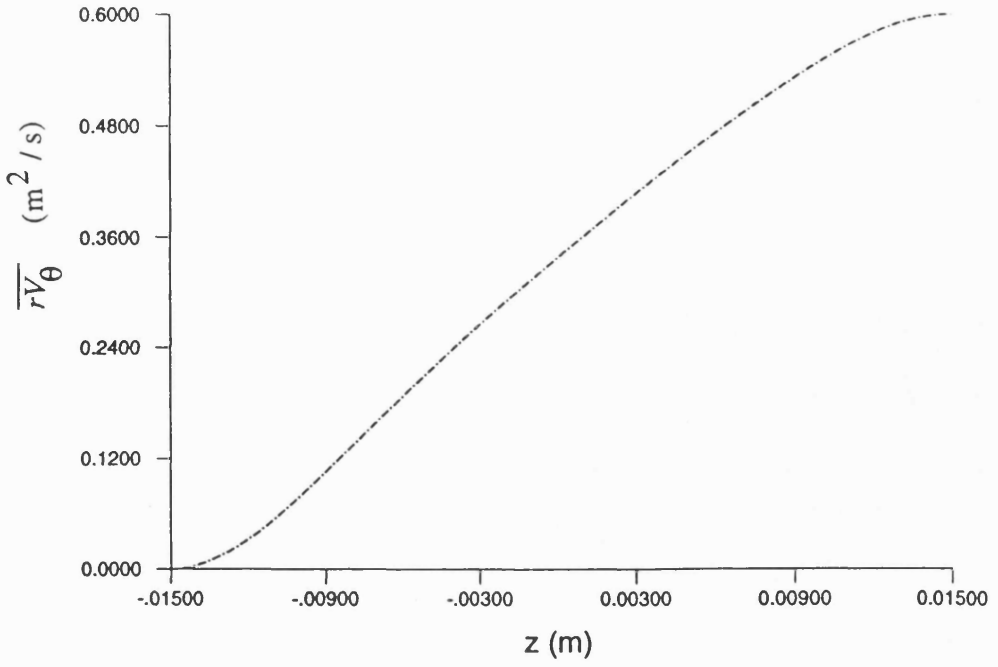

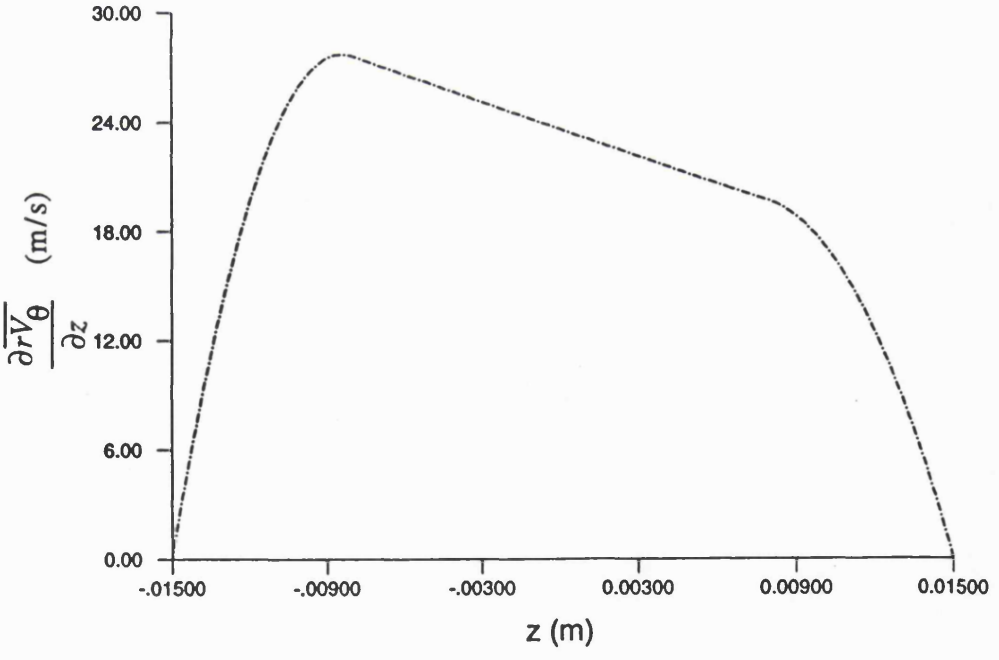

Figure 7.9: The Specified Blade Circulation Distribution (in Terms of $\overline{rV_\theta}$) for the Test Propulsor

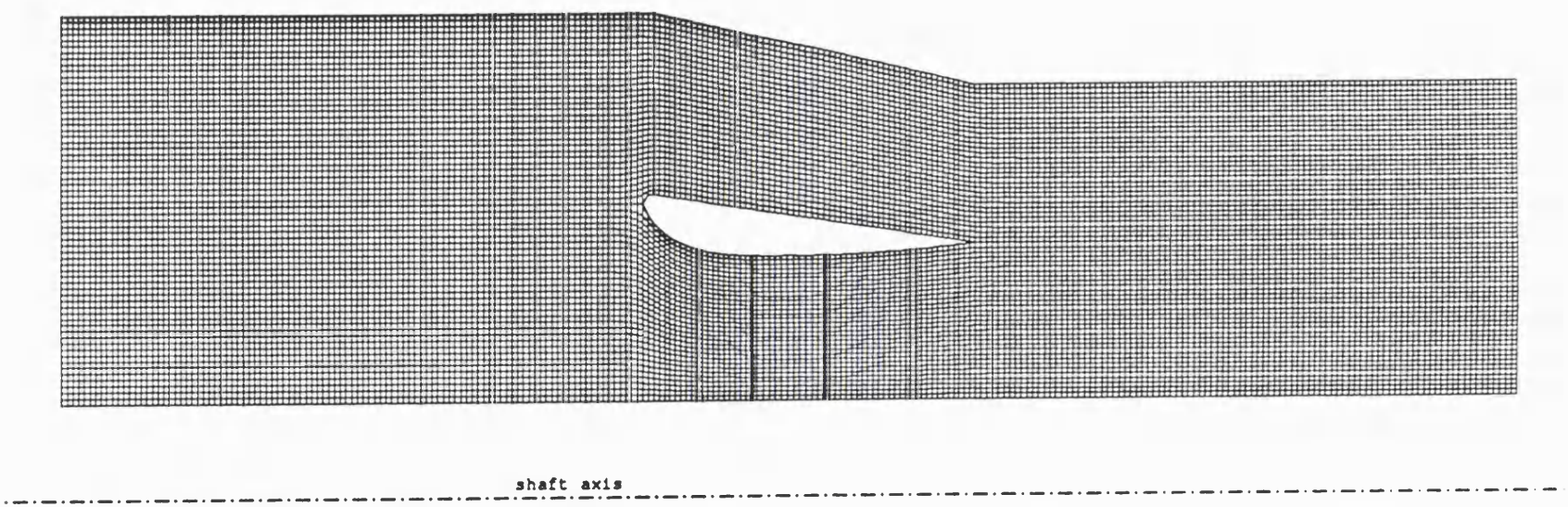

Figure 7.10: The Meridional Mesh Used in the Preliminary Design of the Test Propulsor Blading

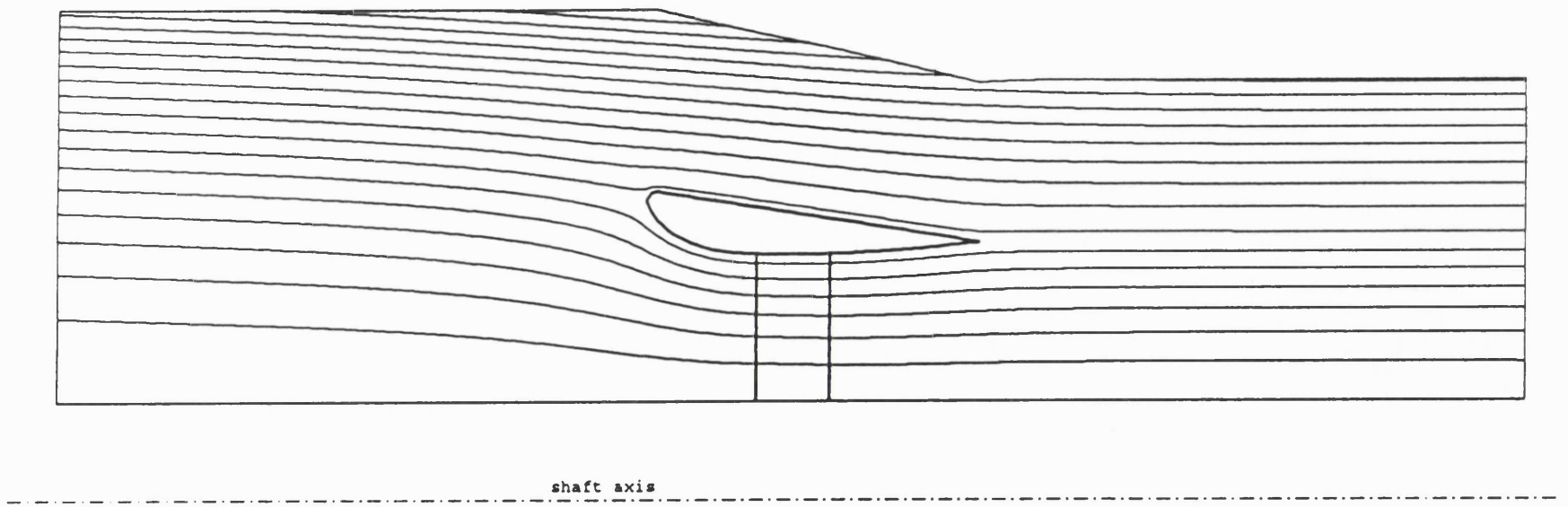

Figure 7.11: Mean Streamline Patterns for the Test Propulsor as Predicted by the Fully Three-Dimensional Run

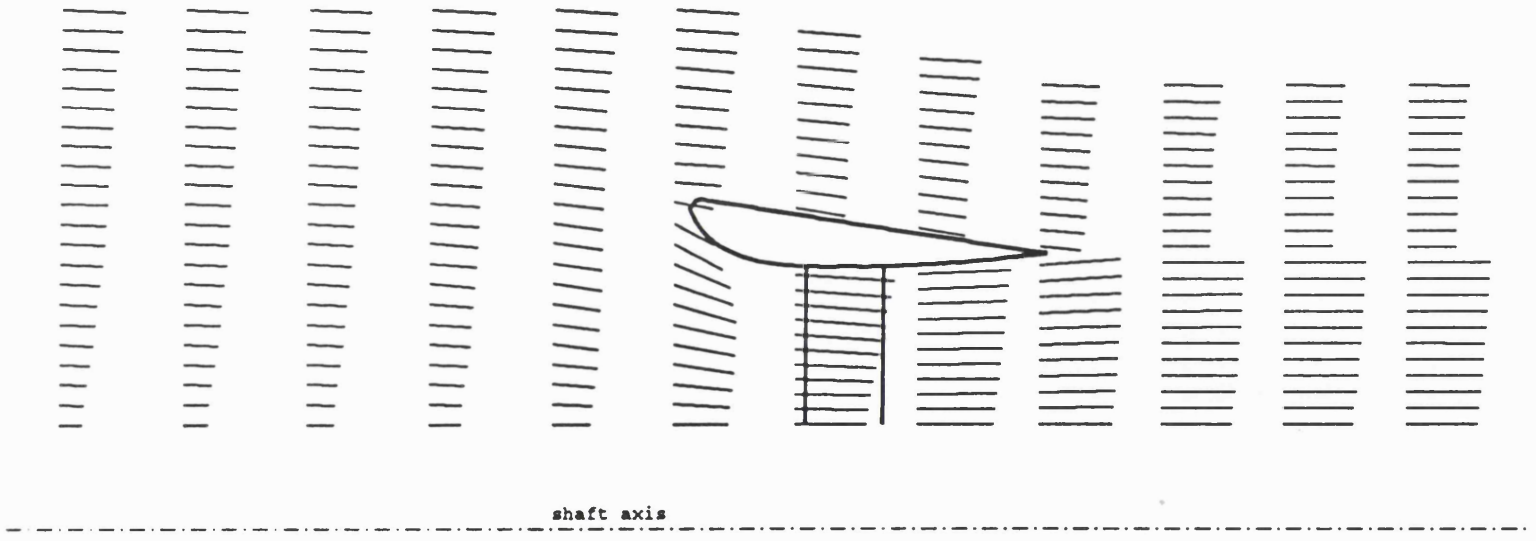

Figure 7.12: Mean Velocity Vectors for the Test Propulsor as Predicted by the Fully Three-Dimensional Run

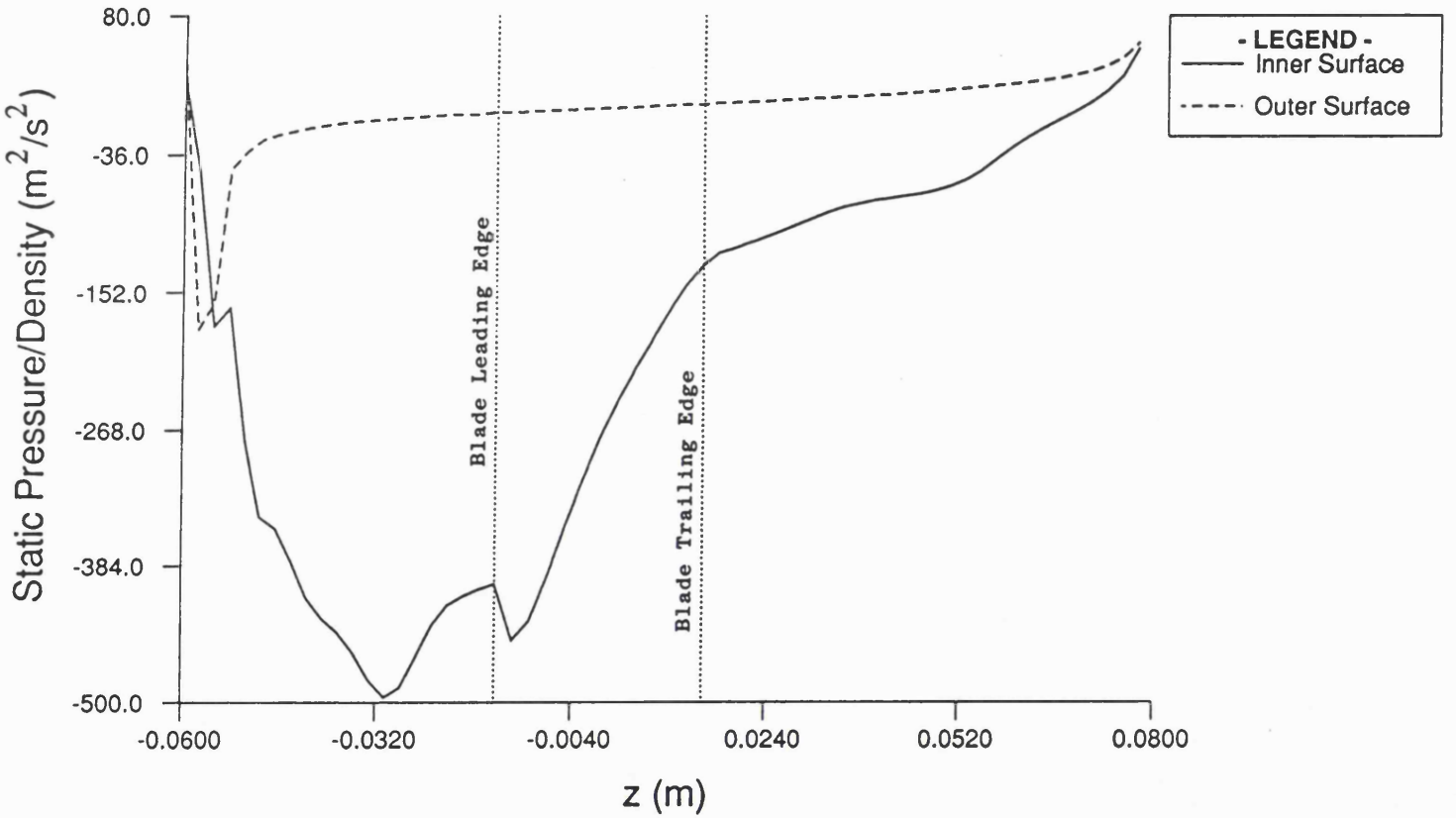

Figure 7.13: Duct Pressure Distribution (Based On Mean Flow Quantities) for the Test Propulsor as Predicted by the Fully Three-Dimensional Run

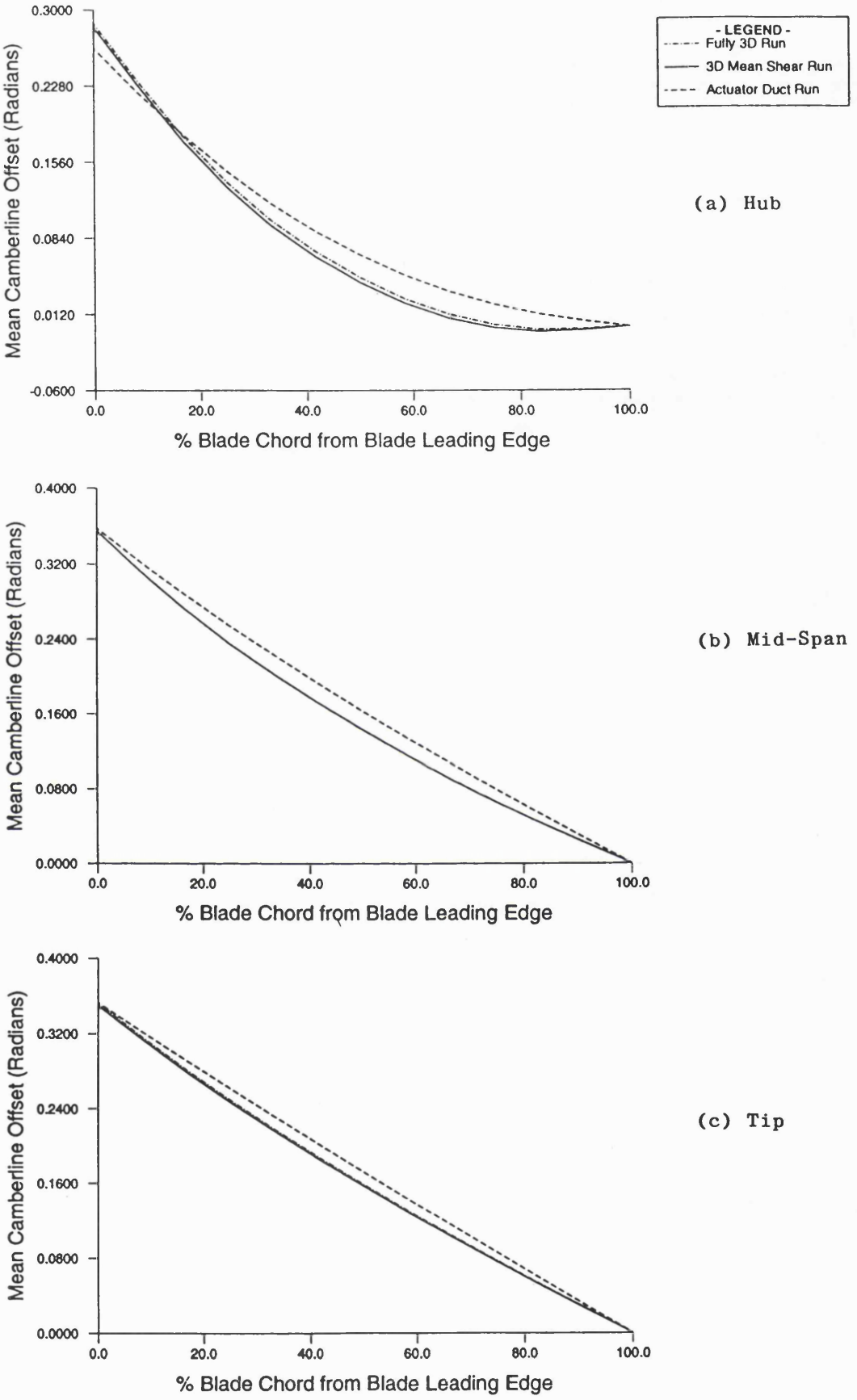

Figure 7.14: Blade Shapes for the Test Propulsor as Predicted by the Ducted Propulsor Design Method

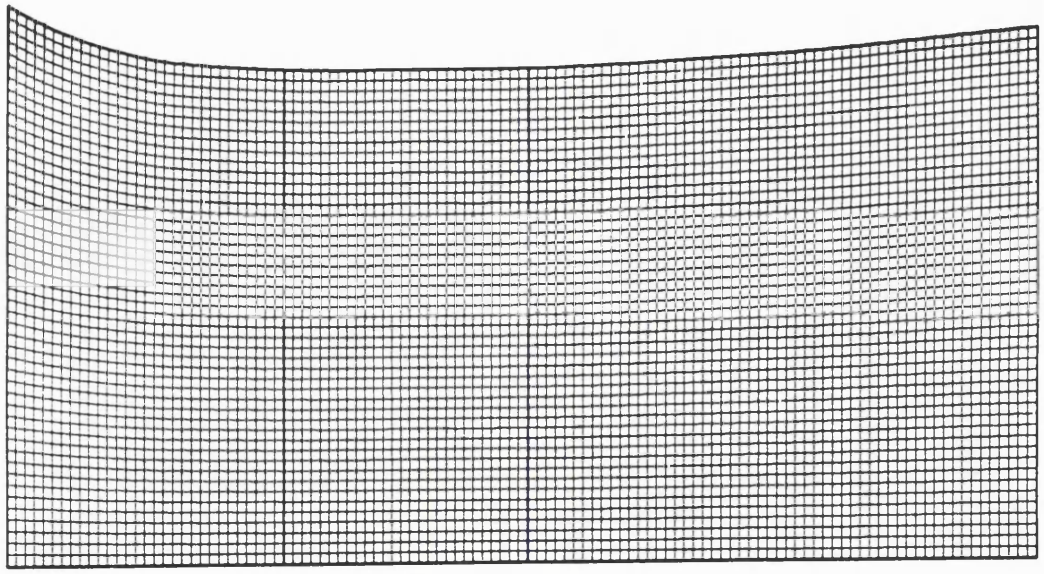

Figure 7.15: The Meridional Mesh Used for the Final Blade Design Run

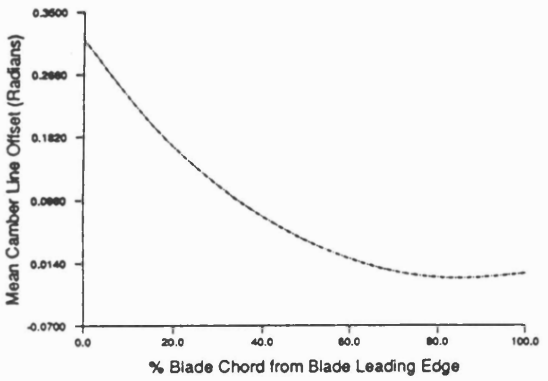

(a) Hub

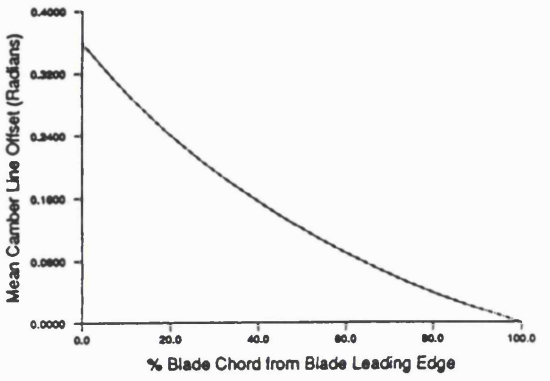

(b) 1/4 Span from Hub

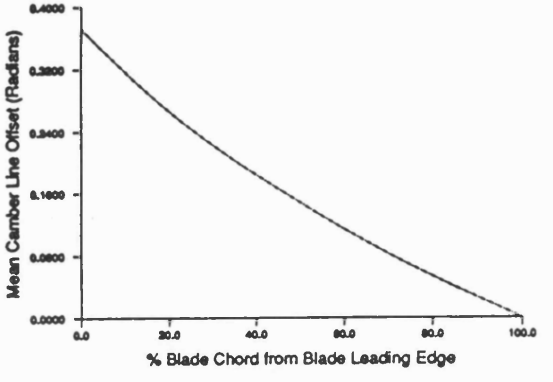

(c) Mid-Span

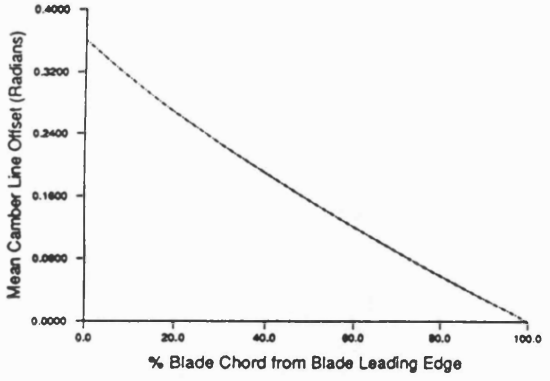

(d) 3/4 Span from Hub

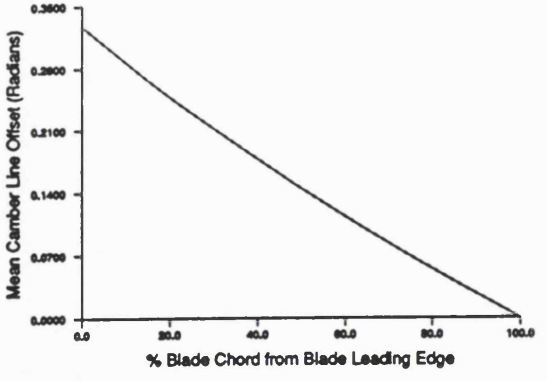

(e) Tip

Figure 7.16:
The Final Blade Shapes Used in the Manufacture of the Test Propulsor Blading (Plots Along Quasi-Streamlines)

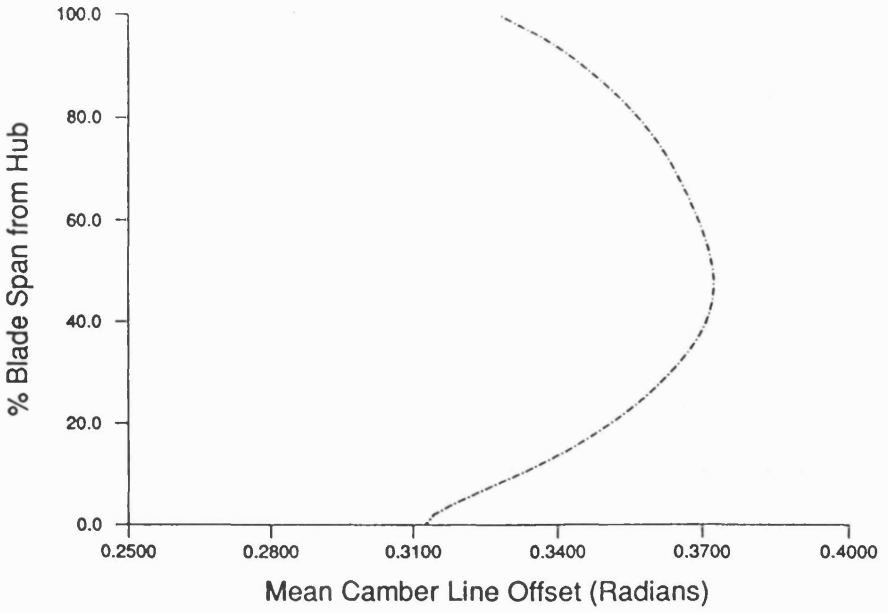

(a) Blade Leading Edge

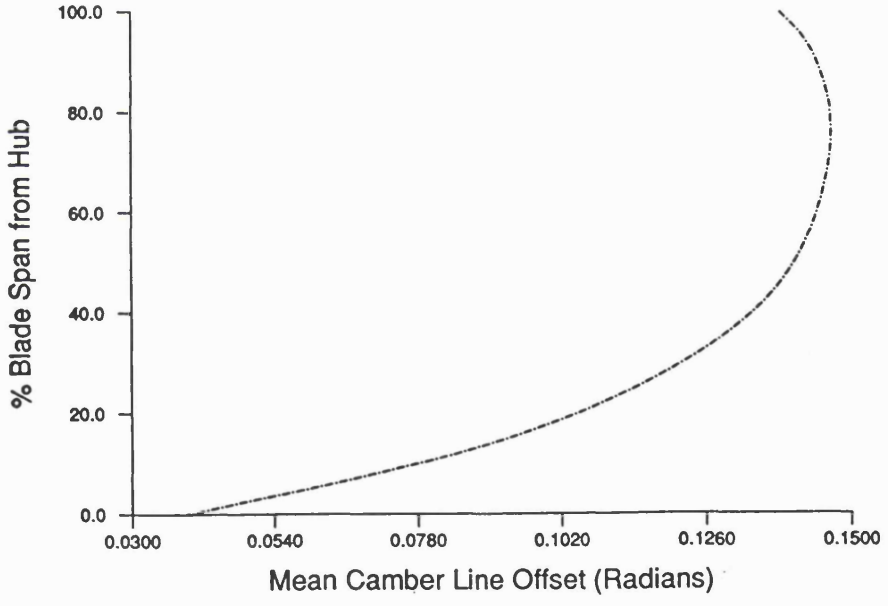

(b) Blade Mid-Chord

Figure 7.17: The Final Blade Shapes Used in the Manufacture of the Test Propulsor Blading (Plots Along Quasi-Orthogonals)

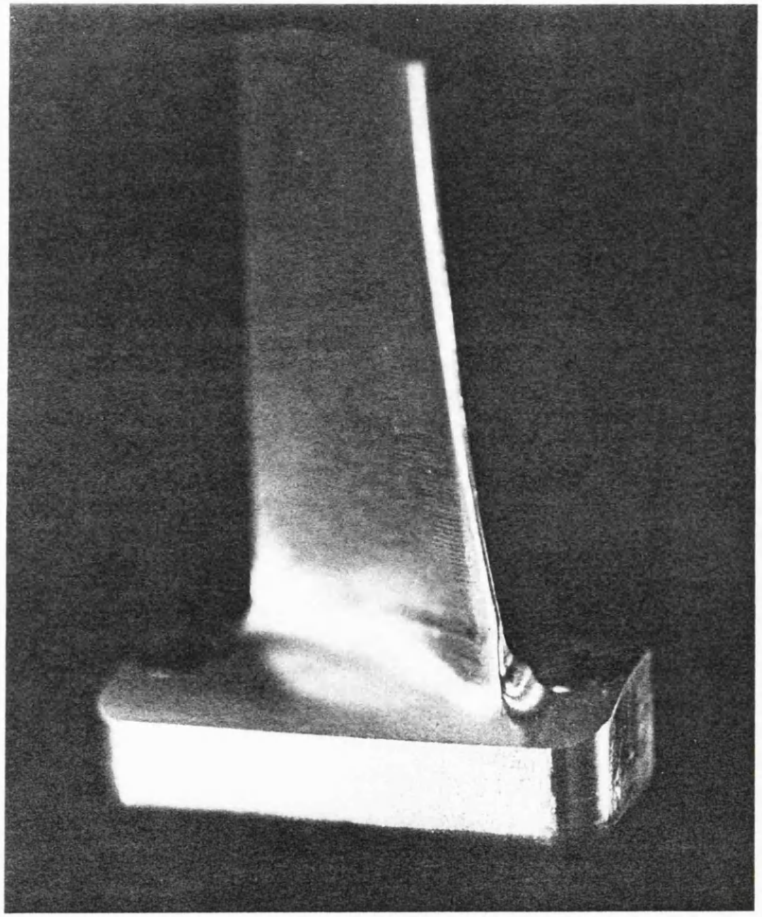

(a) Oblique View from Upstream

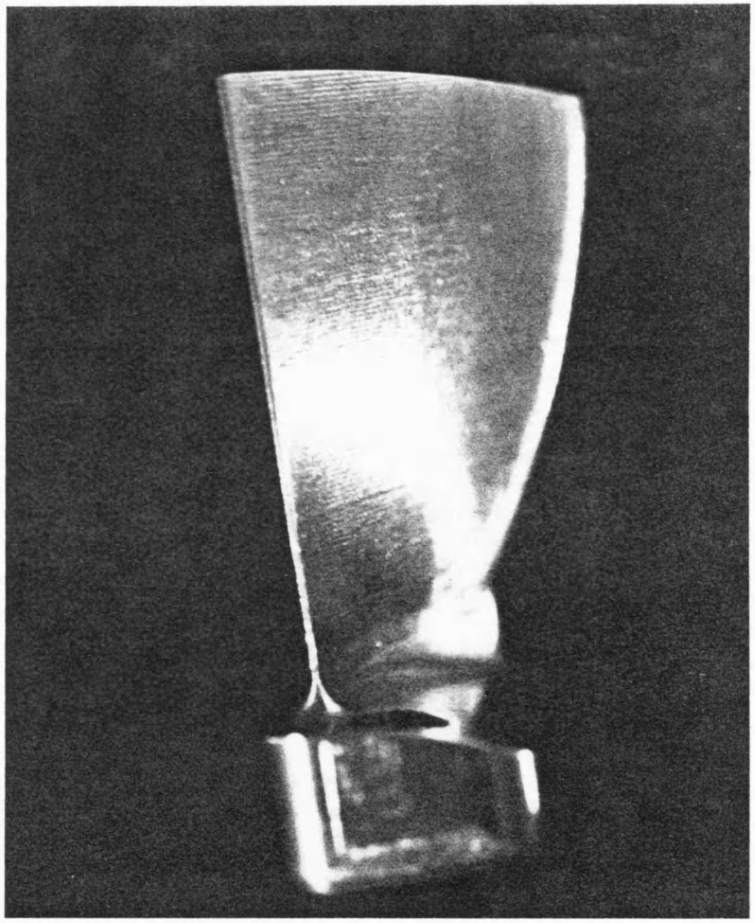

(b) Axial View from Downstream

Figure 7.18: Photographs of a Test Propulsor Blade Prior to Installation On the Shaft

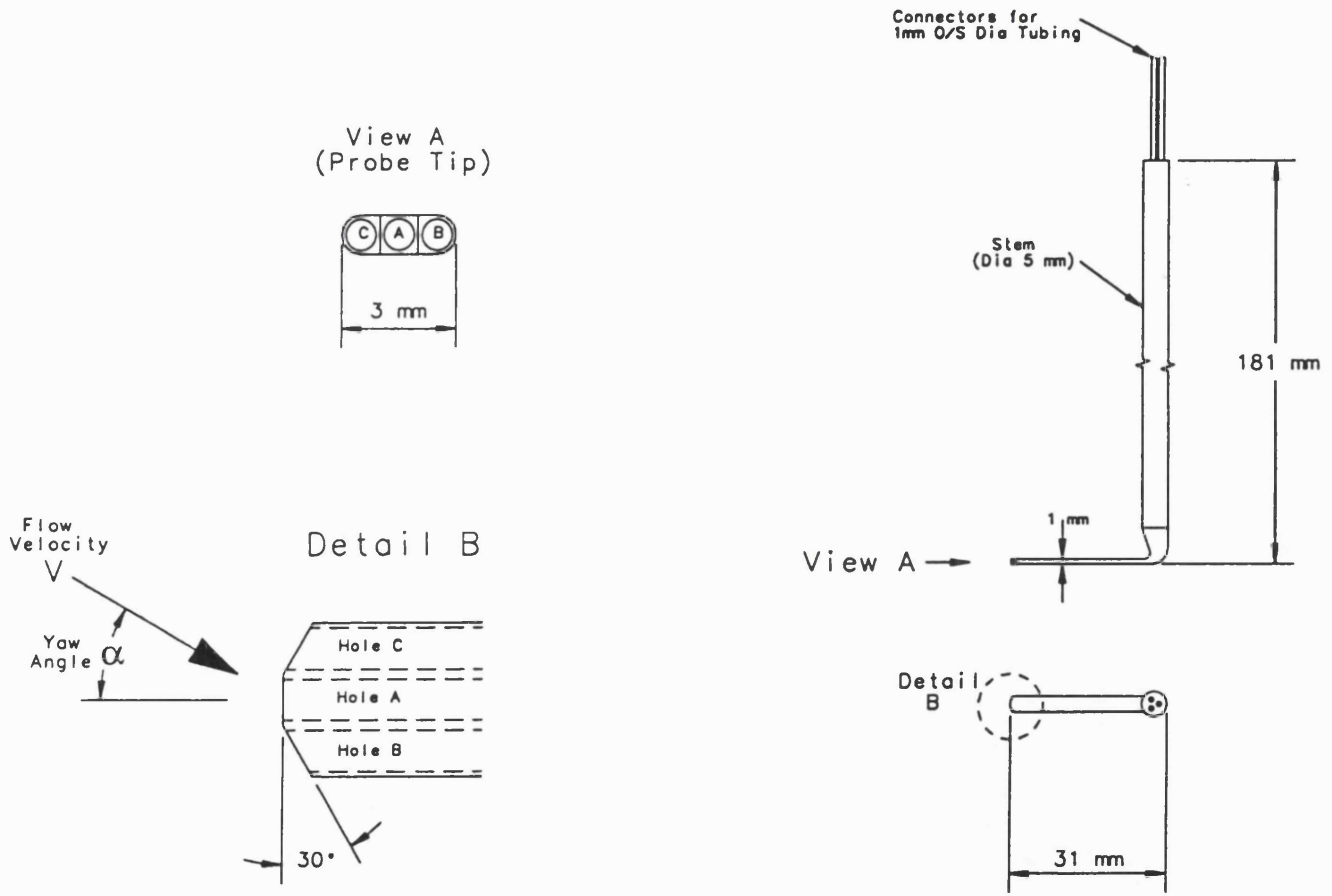

Figure 7.19: The Three Hole Cobra Probe Used for the Propulsor Flow Field Measurements

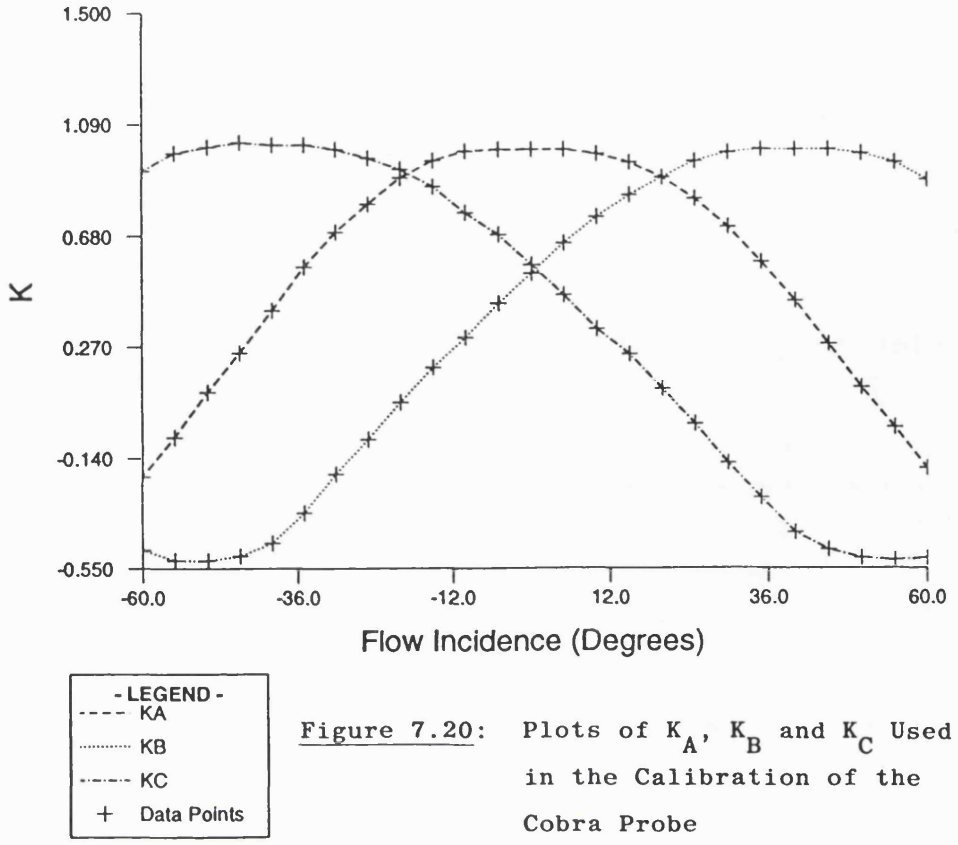

Figure 7.20: Plots of K_A, K_B and K_C Used in the Calibration of the Cobra Probe

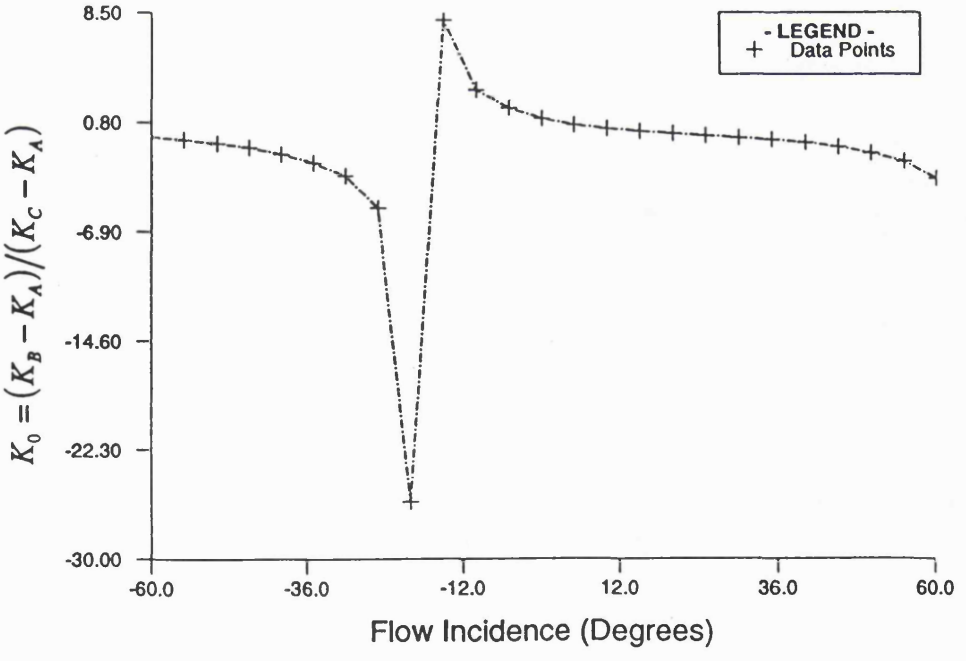

Figure 7.21: The Plot of K_0 versus Flow Incidence Determined During the Probe Calibration Process

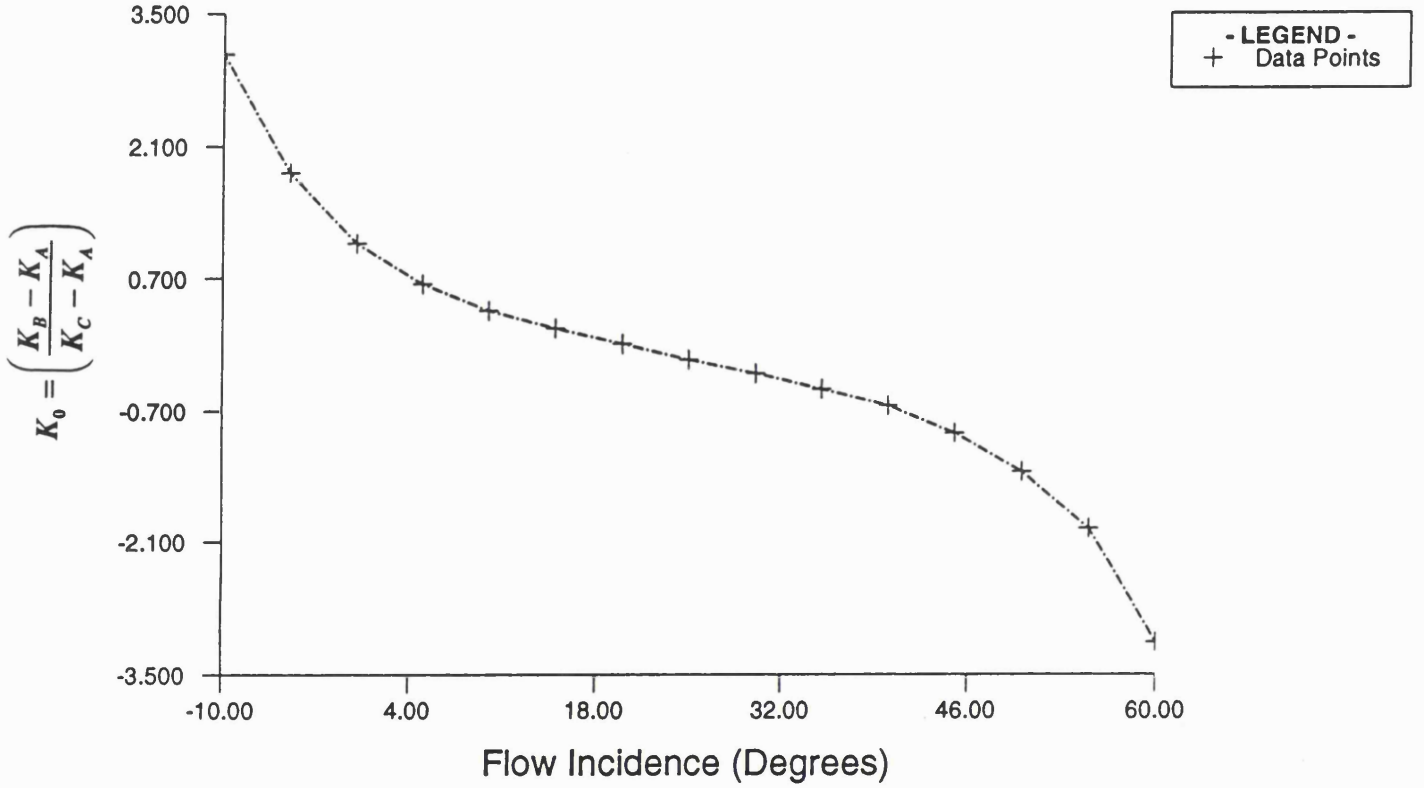

Figure 7.22: The Restricted Range of K_0 Values Used to Determine the Propulsor Flow Field Velocities

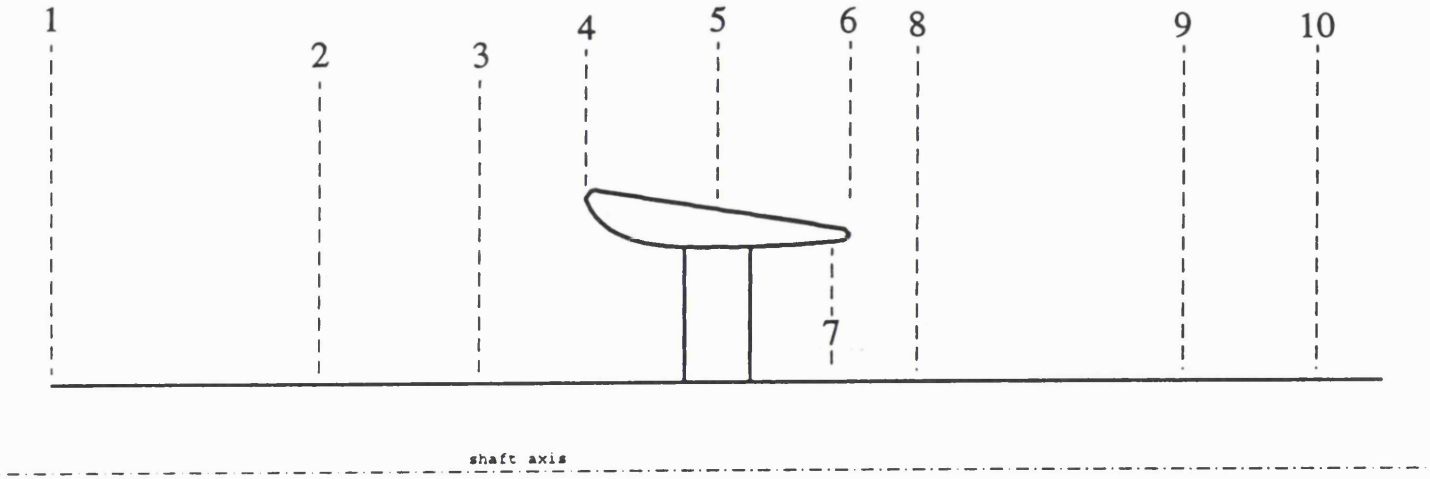

Key

1	Computational "Far Upstream Boundary" (2L Upstream of Duct Leading Edge)	6	Duct Trailing Edge
2	120mm (1L) Upstream of Duct Leading Edge	7	8mm (0.067L) Upstream of Duct Trailing Edge
3	48mm (0.4L) Upstream of Duct Leading Edge	8	30.5mm (0.254L) Downstream of Duct Trailing Edge
4	Duct Leading Edge	9	150.5mm (1.254L) Downstream of Duct Trailing Edge
5	Duct Mid-Chord	10	210.5mm (1.754L) Downstream of Duct Trailing Edge

Figure 7.23: Measurement Stations for the Test Propulsor Flow Field

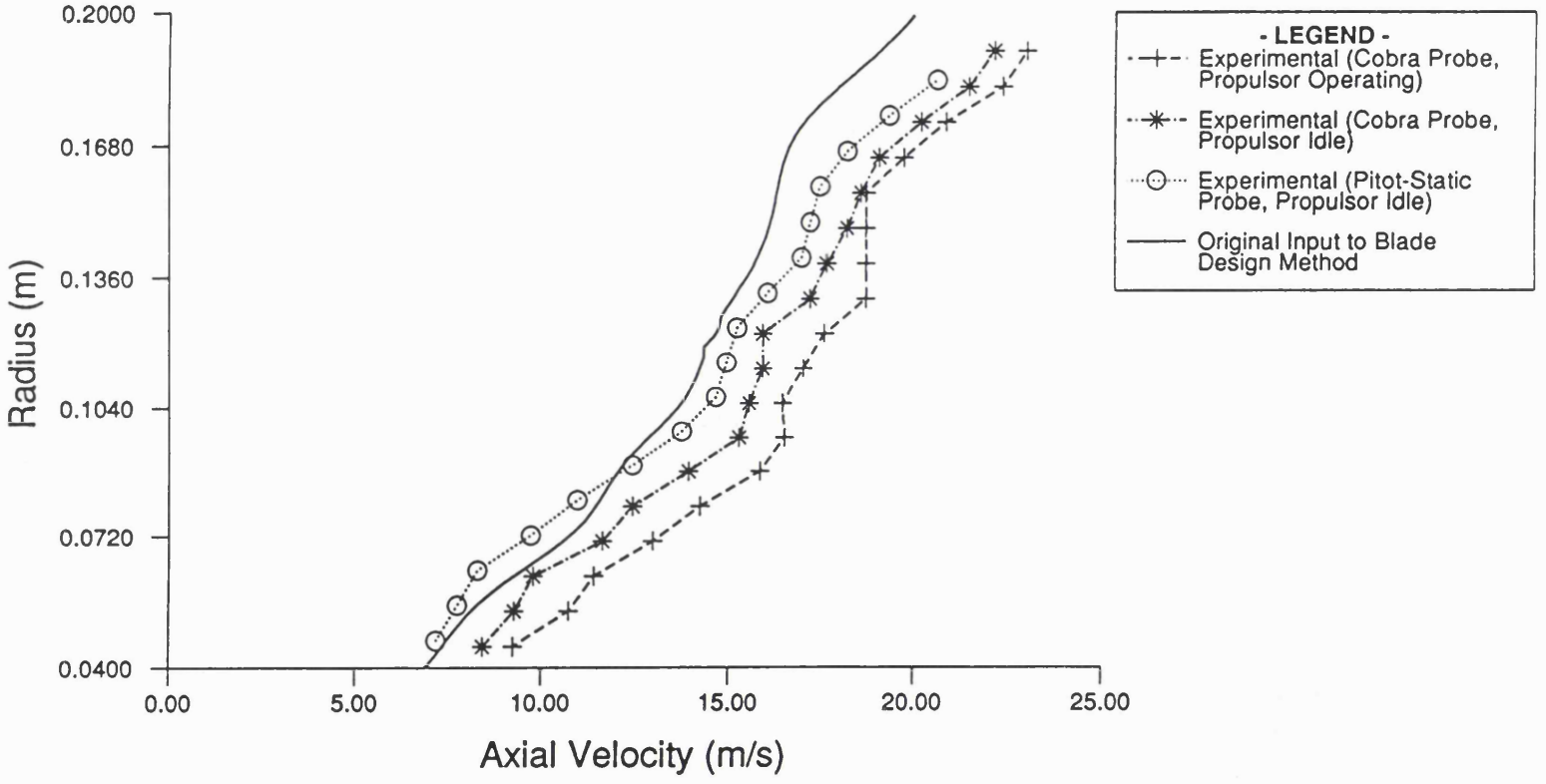

Figure 7.24: Comparison of the Axial Velocity Mesurements on the Computational "Far Upstream" Boundary (240mm (2L) Upstream of the Duct Leading Edge) with the Velocity Profile Specified as Input to the Blade Design Method

Figure 7.25: Comparison of the Axial Velocity Measurements Around the Propulsor with the Predictions of the Blade Design Method

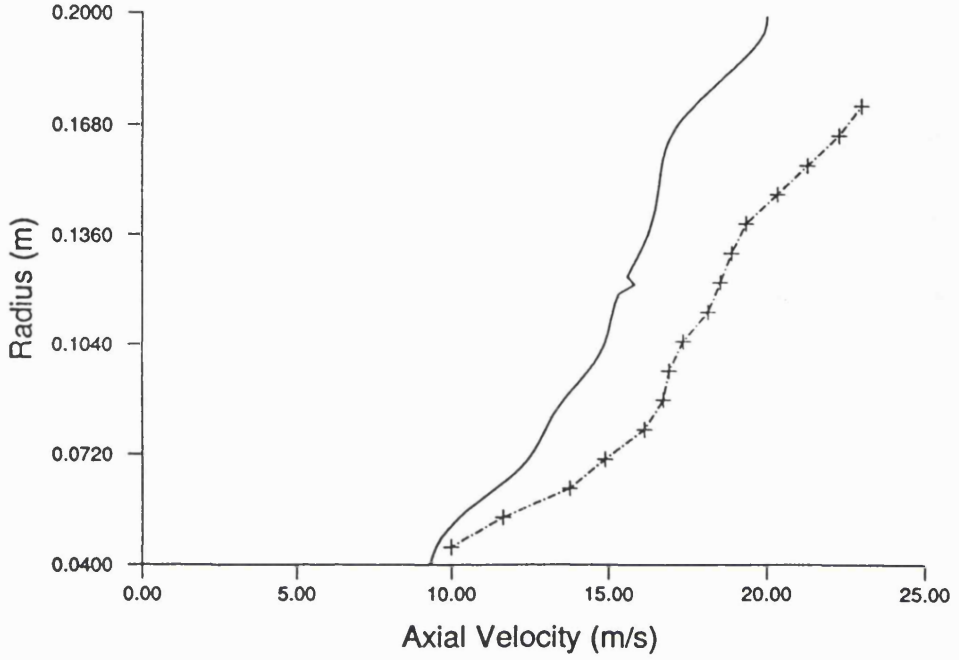

(a) 120mm (L) Upstream of Duct Leading Edge

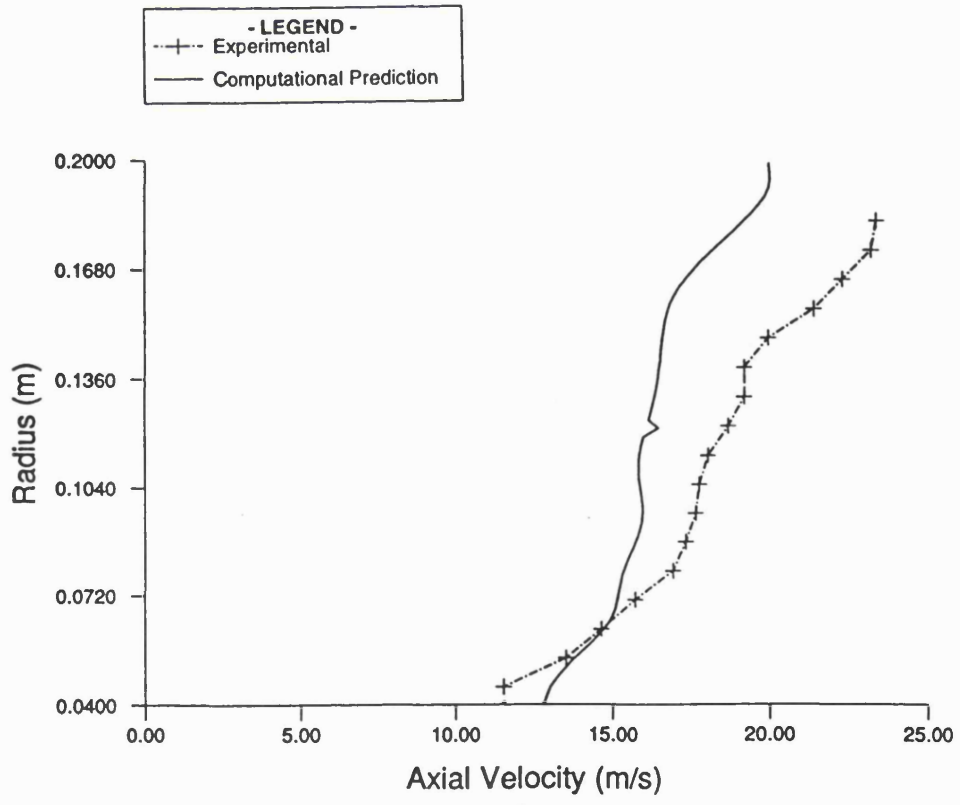

(b) 48mm (0.4L) Upstream of Duct Leading Edge

Figure 7.25 (Continued)

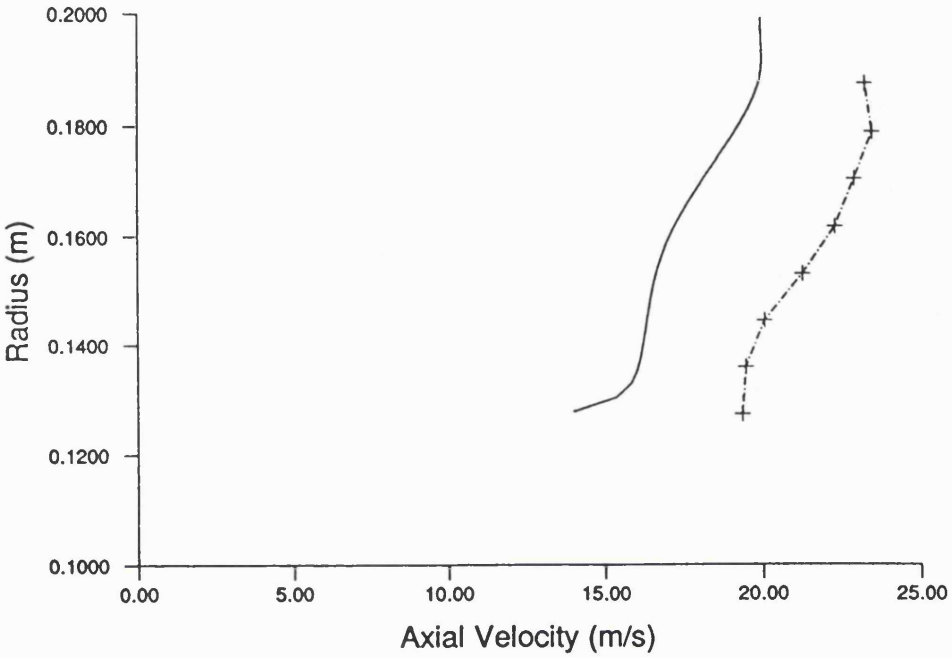

(c) Duct Leading Edge (Bypass Flow Measurements Only)

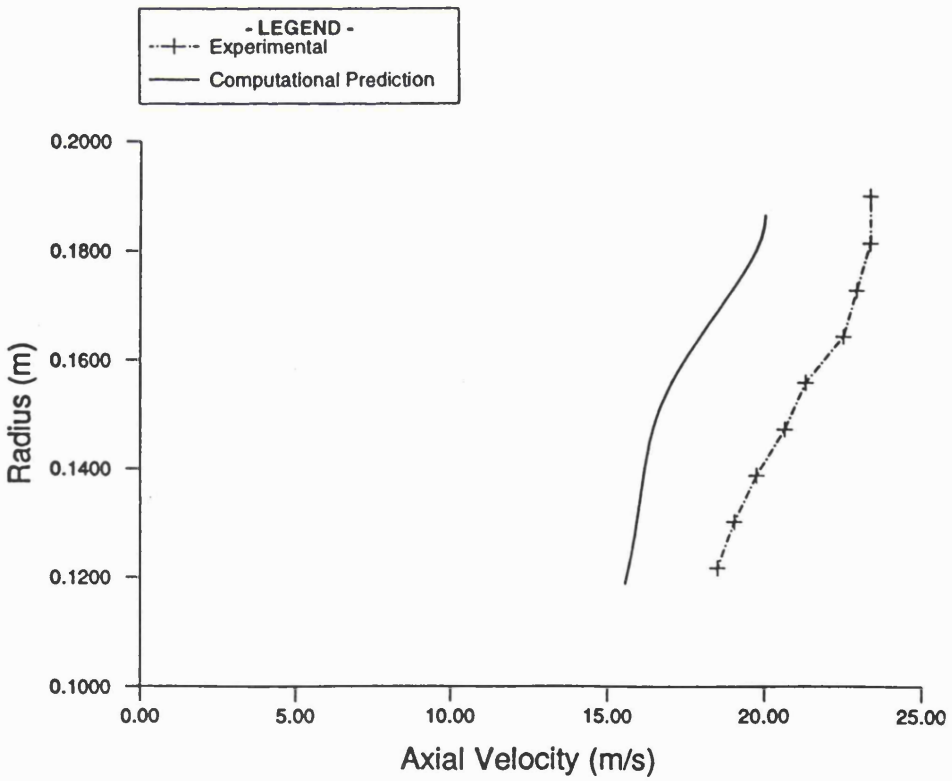

(d) Duct Mid-Chord (Bypass Flow Measurements Only)

Figure 7.25 (Continued)

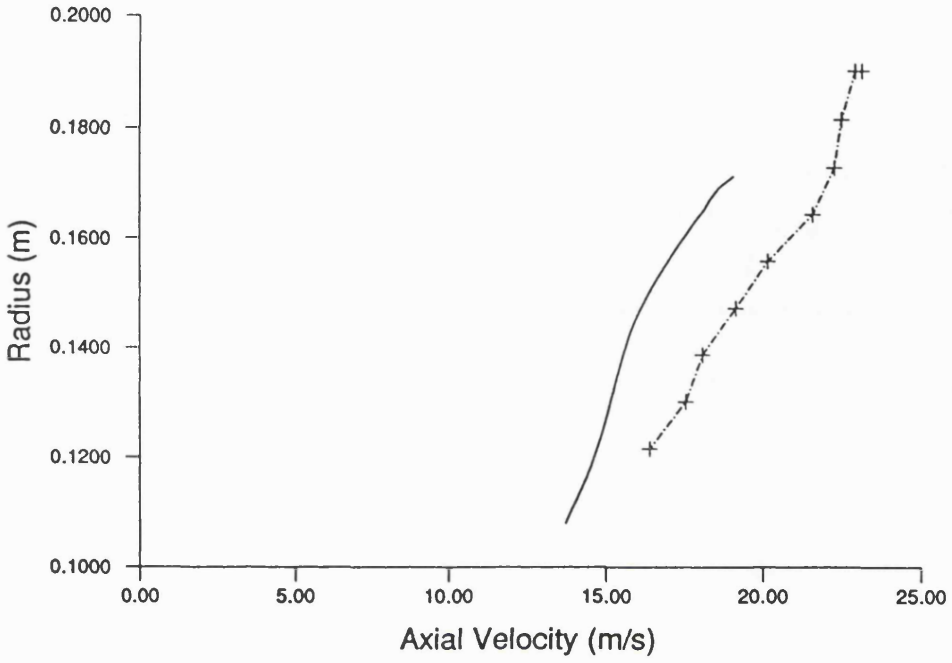

(e) Duct Trailing Edge (Bypass Flow Measurements Only)

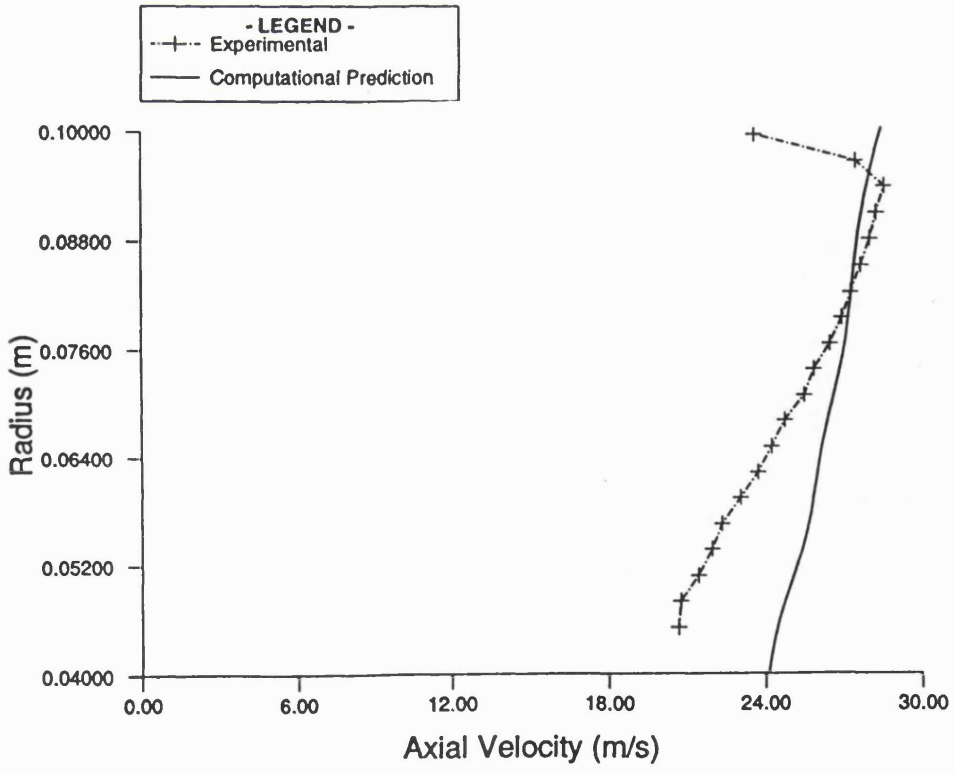

(f) 8mm (0.067L) Upstream of Duct Trailing Edge
(Core Flow Measurements Only)

Figure 7.25 (Continued)

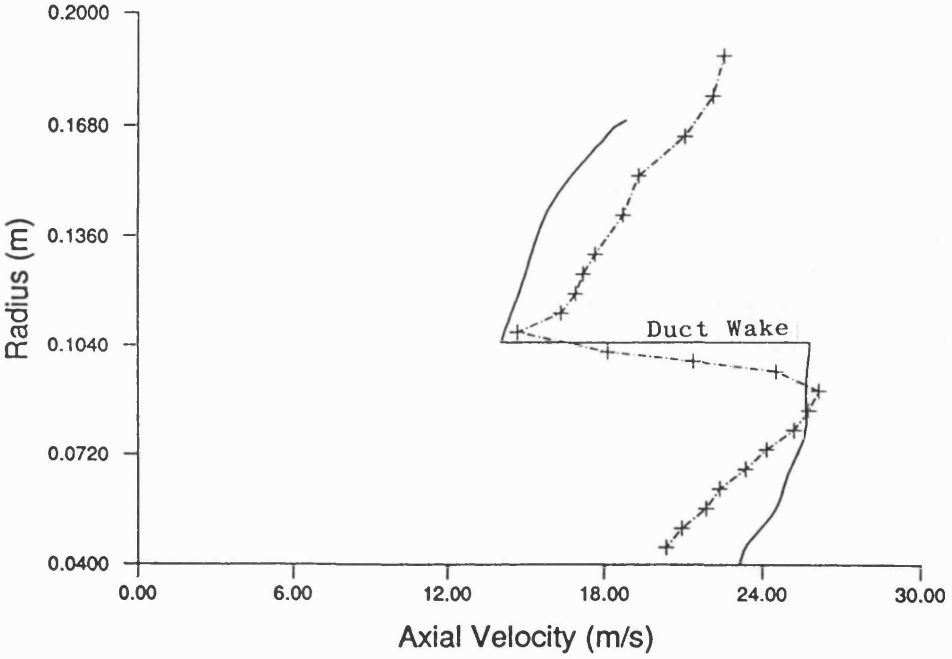

(g) 30.5mm (0.254L) Downstream of Duct Trailing Edge

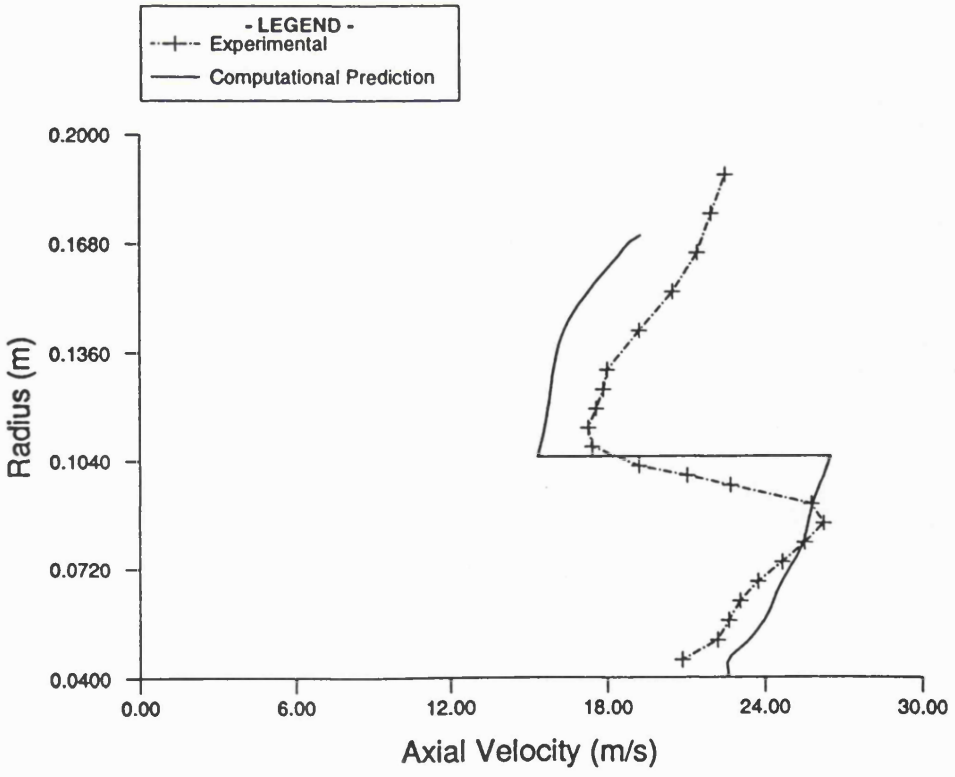

(h) 150.5mm (1.254L) Downstream of Duct Trailing Edge

Figure 7.25 (Continued)

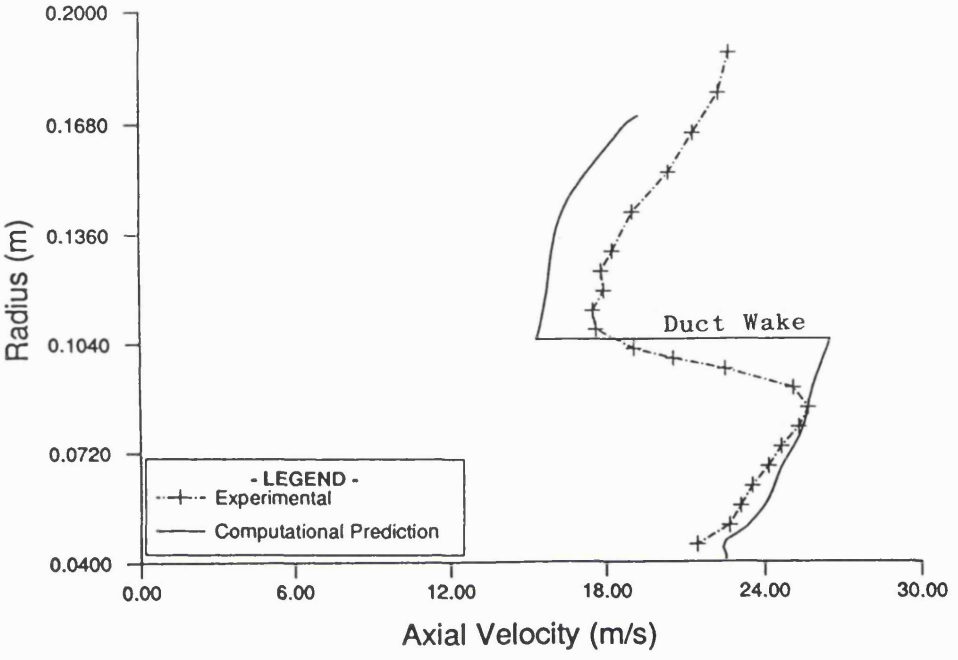

(i) 210.5mm (1.754L) Downstream of Duct Trailing Edge

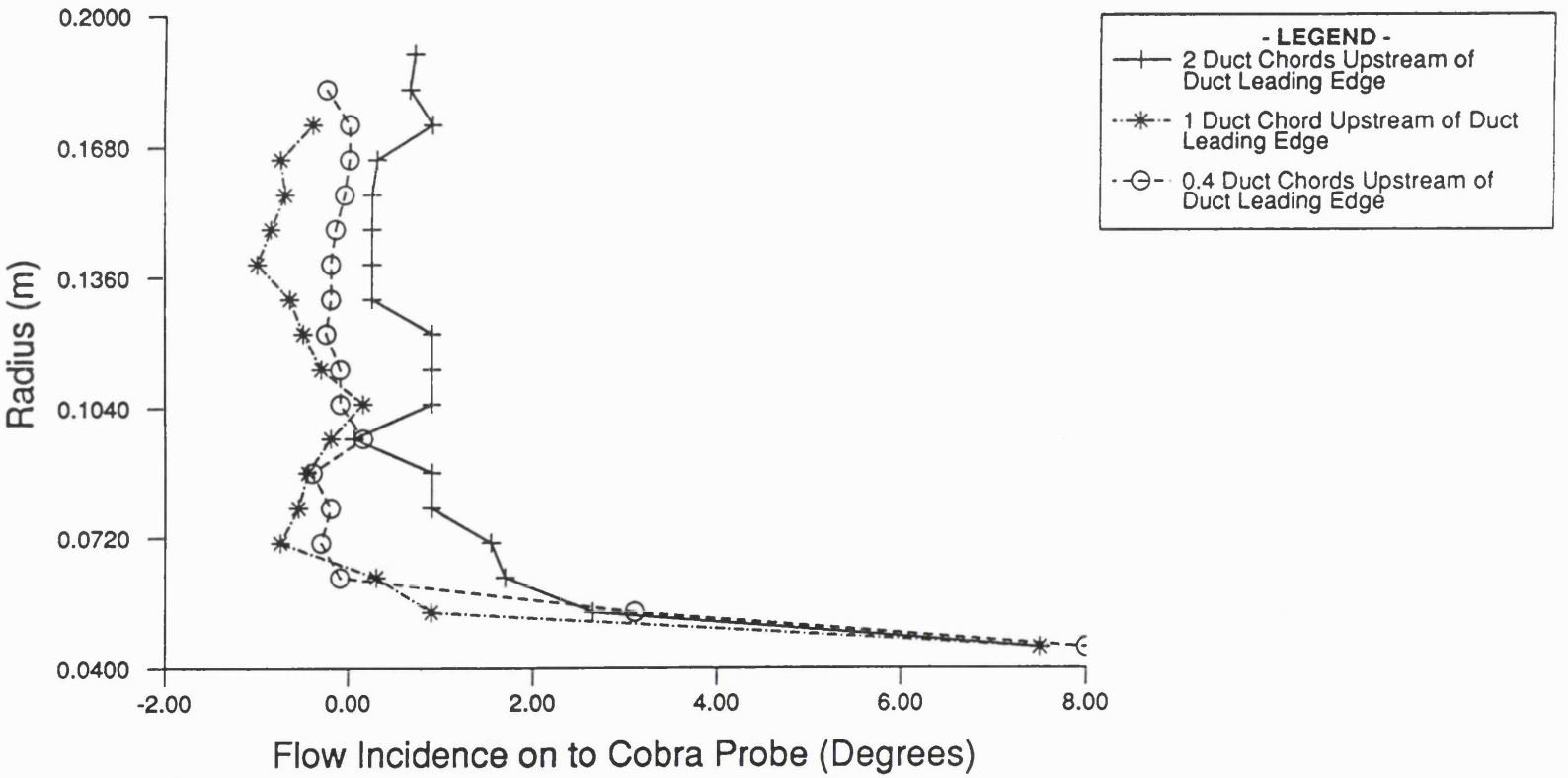

Figure 7.26: Measured Values of Swirl Velocity (Expressed in Terms of Flow Incidence onto the Probe) at Various Stations Upstream of the Test Propulsor

Figure 7.27: Comparison of the Mean Swirl ($\overline{rV_\theta}$) Measurements Downstream of the Blading with the Predictions of the Blade Design Method

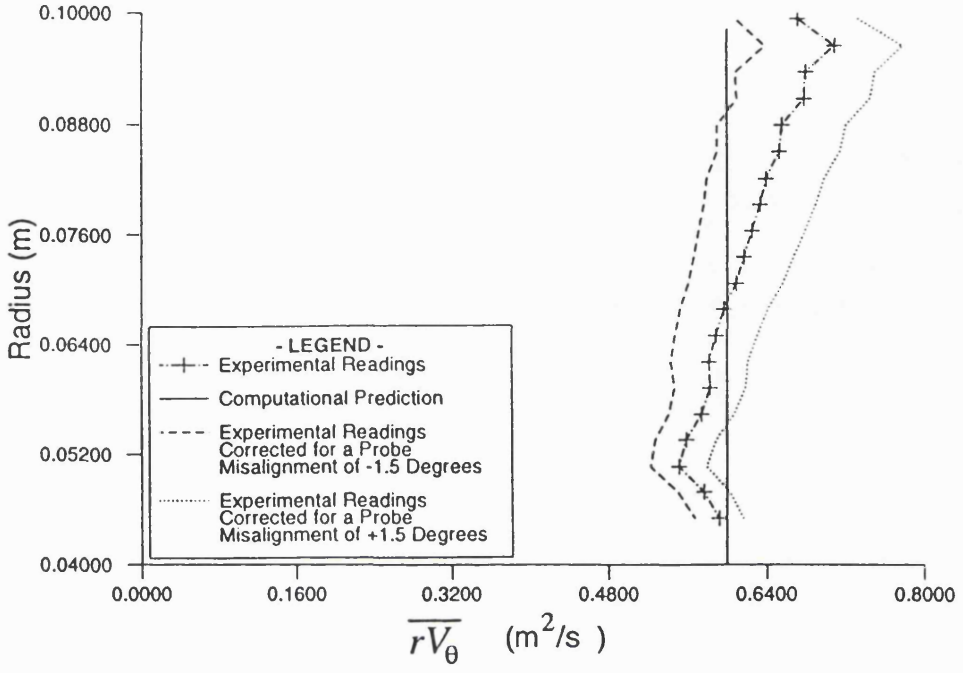

(a) 8mm (0.067L) Upstream of Duct Trailing Edge (Core Flow Measurements Only)

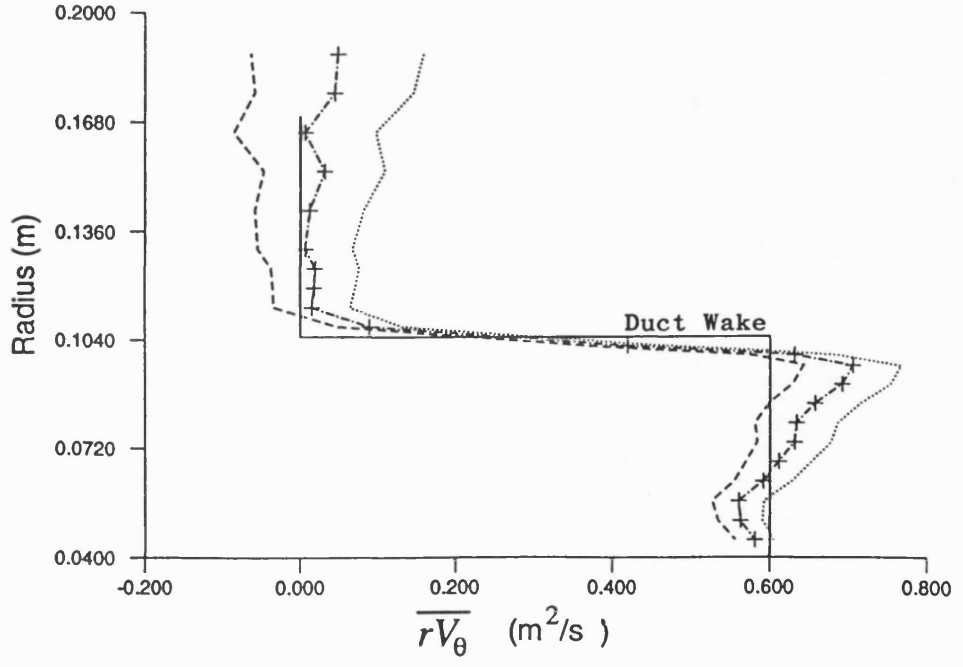

(b) 30.5mm (0.254L) Downstream of Duct Trailing Edge

Figure 7.27 (Continued)

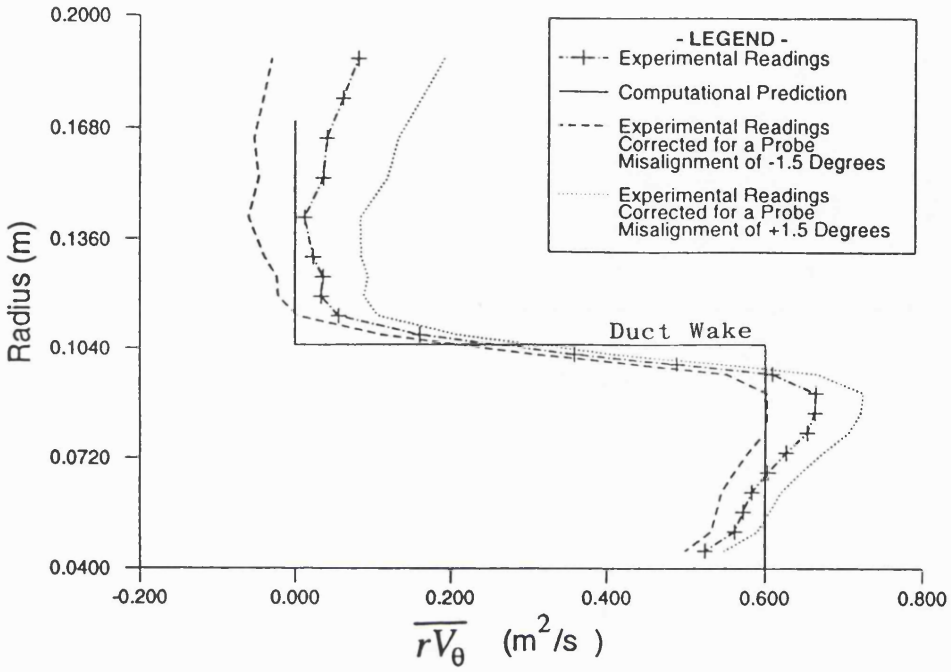

(c) 150.5mm (1.254L) Downstream of Duct Trailing Edge

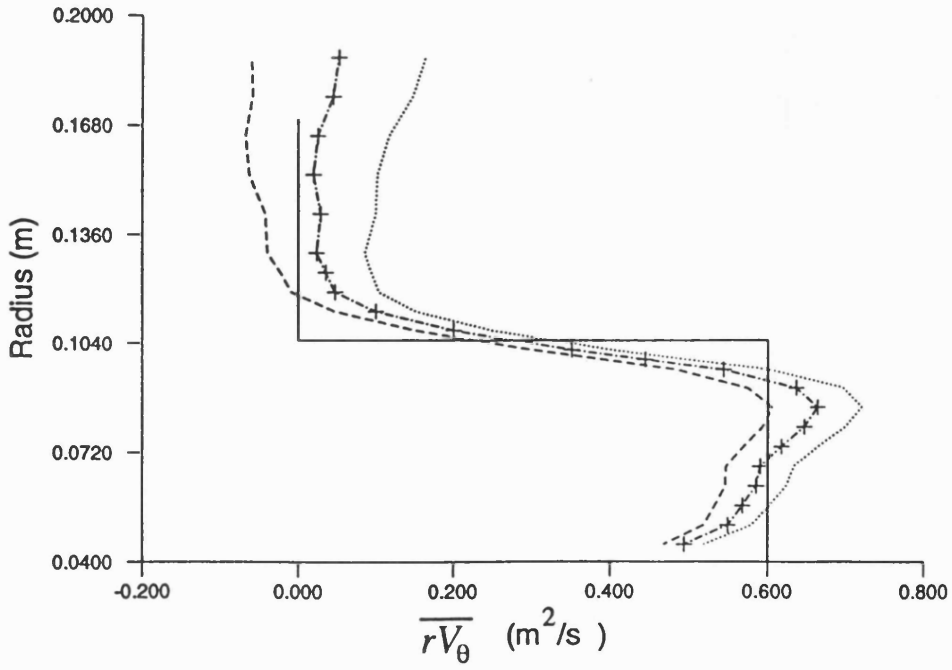

(d) 210.5mm (1.754L) Downstream of Duct Trailing Edge

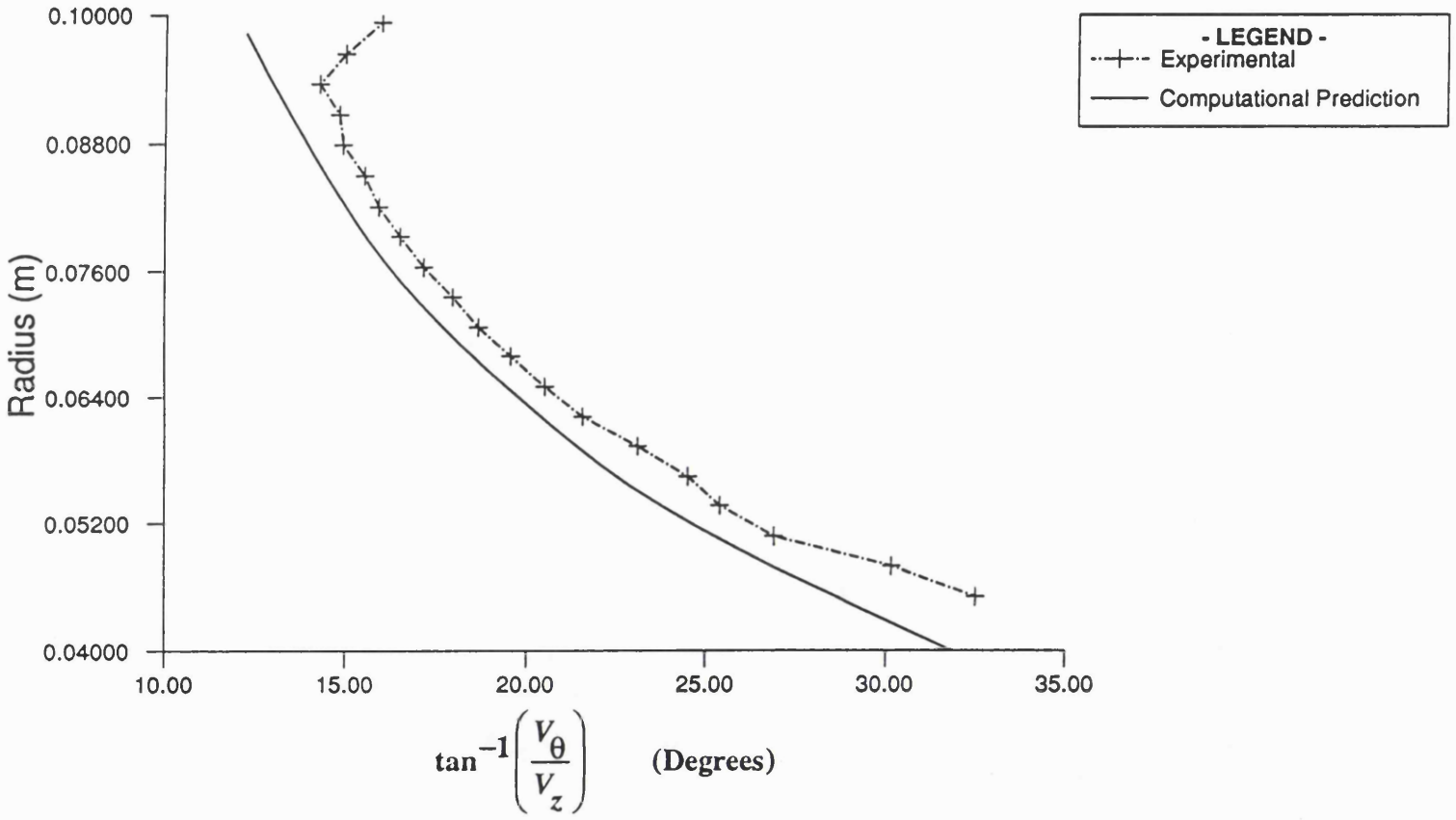

Figure 7.28: Comparison of the Experimentally-Determined Flow Angles with the Computational Predictions 8mm (0.067L) Upstream of the Duct Trailing Edge

CHAPTER 8: SUGGESTED AREAS FOR FUTURE RESEARCH

The research work outlined in this thesis highlighted several possible avenues of future research. These include:-

1) The Development of a Fully Three-Dimensional Analysis Method for Ducted Propulsors Operating in Shear Flow

Whilst the inverse design method outlined in this thesis enables the design point performance of a ducted propulsor to be predicted, there is a pressing need for a similarly capable three-dimensional analysis program to enable the off-design performance of synthesised designs to be predicted. Unlike the methods given in Section 2.3, such a method should ideally have the capability to model sheared onset flow (preferably non-axisymmetric), slipstream contraction and the presence of a second blade row simultaneously.

This requirement could be met by extending an existing turbomachine analysis method to the case of ducted propulsor flows. Although the ducted propulsor analysis problem is arguably much more complicated than that for the internal flow turbomachine, the turbomachine analysis methods reviewed by McNally and Sockol [1] and Zangeneh [2] are generally more sophisticated than those currently employed in the field of ducted propulsor design.

Particularly promising candidate methods are the finite volume method of Denton [3] and the Dawes' Navier-Stokes solver [4]. Both these methods have already found widespread application in the field of turbomachine design. At present these approaches are applicable only to flow between endwalls of infinite extent and assume the far upstream velocity field to be axisymmetric. Furthermore, the associated program codes were written for compressible flow problems, and it is believed that there may be difficulty in achieving computational convergence for marine propulsors where the flow is incompressible. Considerable effort would have to be directed at extending these two methods to ducted propulsor analysis, particularly as regards determining propulsor mass flow and dealing with the duct wake. However, if successful the resulting analysis methods would offer substantial advantages over those presented in Chapter 2. The extension of Dawes' method to ducted

propulsors is particularly exciting, as for the first time it would be possible to conduct a detailed viscous analysis of propulsor performance.

Alternatively, a Clebsch-based analysis program based on the inverse design method presented in Chapters 4 and 5 could be developed. Here, blade shape rather than $\overline{rV_\theta}$ would be fixed as an input to the method, with $\overline{rV_\theta}$ on the blade rather than blade shape being determined as output. Some limited development work conducted by the author suggested that whilst convergence of the actuator duct analysis problem could be achieved, numerical problems associated with evaluating the potential function Φ prevented any three-dimensional solutions from being obtained. Time-constraints have prevented investigation of this problem, although it has been suggested that its cause is non-zero incidence of the blades. Research into solving these difficulties could prove very worthwhile, as the modifications required to convert the inverse design code into an analysis code are minimal.

In any event, it is possible to envisage a sophisticated ducted propulsor inverse design/analysis package which would not only be highly marketable, but also offer the prospect of considerable improvements in propulsor performance.

2) The Development of a Fully Three-Dimensional Inverse Design Method for Open Propellers

Although the state of the art of blade design methods for conventional marine propellers (as reviewed by Kerwin [5]) is much further advanced than that for ducted propulsor blading, it is felt that the ducted propulsor design method outlined in this thesis could readily be extended to the design of these devices.

Indeed, in many respects the open propeller problem is much simpler than that for the ducted propulsor, since there is no duct geometry to consider, and, at least for the case of zero tip loading, there is no jump in velocity across the tip streamline.

The resulting method would offer a number of advantages over existing propeller lifting surface design techniques such as those presented by Greeley and Kerwin [6], and Brockett [7]. These methods often make assumptions regarding propeller loading, hub geometry, slipstream contraction and the

influence of shear flow, and furthermore, at present, do not include a second blade row.

Using the techniques outlined in Section 5.10, a twin blade row propeller design code could be developed for the design of tandem propellers, contra-rotating propellers, and propeller/vane wheel combinations, all of which have come to prominence in recent years as a means of improving propulsive efficiencies ([8], [9]).

3) Further Investigations into Numerical Problems Associated With the Ducted Propulsor Inverse Design Method

As stated in Sections 5.12 and 5.13, a number of difficulties were encountered in obtaining computational convergence of the ducted propulsor inverse design codes under certain circumstances. Whilst considerable effort was expended investigating these problems, and practical means for their avoidance are presented, it is possible that given further work more satisfactory means of dealing with them might be obtained.

4) Further Work On the Verification of the Ducted Propulsor Inverse Design Method

For the reasons discussed in Sections 7.7 and 7.6.1, it is strongly recommended that the experiments outlined in Chapter 7 should be re-run with a new set of blading designed in accordance with the suggestions of Section 7.6.1. This should considerably improve the correlation between the experimental measurements and computational predictions, and would also enable firmer conclusions to be drawn regarding the accuracy of the ducted propulsor inverse design method.

Additionally, it was noted in Section 7.7 that the experiments conducted for this thesis were rather limited in scope, and as such even a re-run of these tests would not fully verify the design method. It is therefore proposed that a more extensive series of experiments should be conducted, both for single and twin blade row designs using either hot wire anemometry (HWA) or laser-Doppler velocimetry (LDV) techniques. These tests, involving measurements of

circumferential variations in velocity, would enable the validity of the assumptions presented in Section 4.2, together with the overall accuracy of the computational method, to be assessed in detail. To improve the accuracy of the results a wind tunnel with a larger working section should be utilised, not only to minimise wall-interference effects, but also to enable a larger test propulsor to be used. Were a cavitation tunnel to be made available the accuracy of cavitation predictions could also be appraised.

5) Comparison of the Ducted Propulsor Design Method with Existing Computational Techniques

It would be very interesting to compare design results obtained from the ducted propulsor design method with comparable results obtained using the analysis methods outlined in Section 2.2, and the blade design methods outlined in Sections 2.3.3 and 2.3.4. Not only would this provide at least an approximate means of verifying the computational procedure, but it would also enable the significance of the various assumptions inherent in these methods (such as those associated with slipstream contraction and sheared onset flow) to be assessed.

6) Modification of the Ducted Propulsor Design Method to Deal with Static ("Bollard Pull") Design Conditions

Ducted propulsors for certain towing vessels such as tugs may be designed for a static ("bollard pull") condition where the vessel is stationary in the water with the propulsor generating some specified thrust. Under these conditions the velocity profile far upstream of the propulsor tends to zero, with the flow velocity at the blading being purely a result of the action of the blading (Figure 8.1).

Under these conditions the ducted propulsor design method as presented in this thesis is no longer applicable, since specifying zero velocity on the far upstream boundary results in zero mass flow and numerical failure.

However, it is envisaged that the design method could be extended to deal with such circumstances by replacing the Dirichlet condition for stream function on

the far upstream boundary (which at present is based on a specified axisymmetric velocity profile) by an appropriate von Neuman condition. In particular, the condition

$$\frac{\partial \overline{V}_z}{\partial z} = 0 \qquad 8.1$$

would seem ideal, at least for the simplified case of a cylindrical hub, as it allows for the velocity induced by the propulsor on the far upstream boundary (which, whilst small, is none-the-less non-zero), yet also implies the absence of axial variations in flow velocity far upstream, as one would expect.

By similar arguments, for more general cases where a non-cylindrical hub is employed a far upstream condition of

$$\frac{\partial \psi}{\partial \xi} = 0 \qquad 8.2$$

is suggested. Whilst this condition is mesh dependent, one generally defines the quasi-streamlines to align approximately with the flow far upstream, and so this is not considered to be too great a problem.

It should be noted, however, that equations 8.1 and 8.2 represent von Neuman boundary conditions; when combined with the von Neuman conditions for stream function on the $r = \infty$ and far downstream boundaries it could well be that problems are encountered in achieving numerical convergence.

For propulsor design under static conditions there are also problems associated with the very steep flow incidence one would expect at the duct leading edge (Figure 8.1). The principal area of concern is the location of the $r = \infty$ boundary which would have to be located some considerable distance away from the propulsor for the stream function boundary condition given in Section 5.3.1(e) to be valid. As a consequence, special attention would have to be paid to meshing the bypass region to ensure that a computationally efficient mesh is adopted.

Allied to this steep duct incidence, it is conceivable that reverse flow could occur in the bypass flow region, in which case the marching routines for H and τ would have to be modified.

For certain towing applications (e.g. tugs) astern performance is a prime consideration in design and thus ducts with well-rounded trailing edges (Figure 8.1) are often adopted (e.g. Nozzle No. 37, Figure 2.1). In the absence of a well-defined separation point at the duct trailing edge, it would be necessary to specify a point of flow separation at the duct trailing edge. As noted by Falcao de Campos [10], the arbitrary specification of such a stagnation point can have a significant effect on the accuracy of propulsor performance predictions, particularly as regards the duct pressure distribution.

Additionally, it is not practical to extrapolate the trailing edge of a well-rounded duct to a point in the manner described in Section 4.2. Consequently, due to the relatively poor flow resolution that could be achieved close to the trailing edge of a well-rounded duct using a computational mesh, it is likely that difficulties would be encountered in achieving convergence of propulsor mass flow by application of the Kutta condition at the duct trailing edge. The only obvious solution to this problem would be to specify both the point of flow separation from the duct and also the duct wake trajectory for a few mesh points downstream. Propulsor mass flow could then be determined from the application of the Kutta condition at some point on the duct wake.

Under "bollard pull" conditions it is quite likely that high blade loadings would be encountered. Thus, not only could the three-dimensional shear effects discussed in Chapter 6 become significant for these cases, necessitating the use of fully three-dimensional runs (Section 5.11.1), but also cavitation (which one generally tries to avoid at the design point) may occur, raising doubt over the accuracy of the blade design method.

Summarising, it can be seen from the above that considerable work would be required if the ducted propulsor design method presented in this thesis were to be applied to the design of ducted propulsors under "bollard pull" conditions. However, given that propulsors for towing vessels are often designed to achieve a specified "bollard pull", there may well prove to be demand for such a design method.

Finally, it should also be noted that the problems associated with well-rounded duct trailing edges, as outlined above, would be encountered even if the blading were to be designed for a free-running condition (i.e. with onset flow). It is therefore felt that further research into the application of the design method to cases where such ducts are employed is warranted.

7) An Inverse Design Method for Ducted Propulsors Based on a Specified Blade Loading Distribution

The inverse design method as presented in Chapters 4 and 5 determines propulsor blade shapes from a specified blade circulation distribution (expressed in terms of $\overline{rV_\theta}$). As the flow velocities at the blading are not known in advance it is difficult to obtain the required shaft torque in a single design run. Whilst this problem can be overcome by adding an extra tier to the iterative procedure (as suggested in Section 5.8), perhaps a more computationally efficient approach is to modify the method to design for a specified distribution of blade pressure loading $\left(p^+ - p^-\right)$ rather than for a given blade circulation distribution.

With such an approach the blade $\overline{rV_\theta}$ distribution would be updated each blade iteration, being marched downstream from an initial condition (e.g. $\overline{rV_\theta} = 0$) at the blade leading edge using equation A5.2:-

$$\mathbf{W}_{bl} \cdot \nabla \overline{rV_\theta} = -\frac{N_b\left(p^+ - p^-\right)}{2\pi\rho}$$

Having obtained the updated blade $\overline{rV_\theta}$ distribution in this way, the computational procedure is then identical to that for the circulation-based approach outlined in this thesis. As a consequence this pressure loading-based method could be developed from the existing method with a minimum of modifications.

Not only would the resulting method enable shaft torque to be specified as an input to the design process, but it would also enable the zero incidence and blade Kutta conditions to be satisfied by merely setting $\left(p^+ - p^-\right) = 0$ at the

blade leading and trailing edges. Furthermore, cavitation performance could be assessed in advance from estimates of static pressure at the blading.

It should noted, however, that equation 5.2 is based on an assumption of zero jump in rothalpy across the blade (Appendix V), and as such would not, strictly-speaking, be valid for fully three-dimensional runs. None-the-less, this modified inverse design method is very promising, and, bearing in mind the insignificance of three-dimensional shear effects highlighted in Chapter 7, this latter limitation is not too great a cause for concern.

8) Development of a Family of Generic Ducted Propulsor Designs

Due to the commercial and military applications of ducted propulsors it proved very difficult to obtain detailed ducted propulsor design and performance data during the course of the work outlined in this thesis. This lack of data severely hampered attempts to verify the ducted propulsor inverse design method presented in this thesis.

Were authors to publish computational and experimental results for a standard series of ducted propulsors designs, then these problems might be avoided in the future. Such a family of generic designs might consist of say four or five propulsors typical of tug, trawler, submarine and large merchant ship applications. In the long term such standardisation of data would greatly reduce the time, effort and expense involved in verifying computational methods and developing new experimental techniques.

References

1) McNally,W.D., Sockol,P.M. "Review - Computational Methods for Internal Flows with Emphasis On Turbomachinery", Trans. ASME Journal of Fluids Engineering, p6, Vol.107, March 1985

2) Zangeneh,M. "Numerical Methods for Inviscid and Viscous Flow Analysis", Radial Turbine Lecture Series, von Karman Institute, April 6-10, 1992

3) Denton,J.D. "An Improved Time Marching Method for Turbomachinery Flow Calculations", Trans. ASME, J. Eng. Power, p514, Vol.105, No.3, 1983

4) Dawes,W.N. "Application of Full Navier-Stokes Solvers to Turbomachinery Flow Problems", Lecture Series 2: Numerical Techniques for Viscous Flow Calculations in Turbomachinery Blading, von Karman Institute, 1986

5) Kerwin,J.E. "Marine Propellers", Ann. Rev. Fluid Mech., Vol.18, pp367-403, 1986

6) Greeley,D.S., Kerwin,J.E. "Numerical Methods for Propeller Design and Analysis in Steady Flow", Trans. SNAME, Vol. 90, pp415-53, 1982

7) Brockett,T.E. "Lifting Surface Hydrodynamics for Design of Rotating Blades", Proc. SNAME Propellers '81 Symposium, Virginia Beach, Va., pp357-78, 1981

8) Glover,E.J. "Propulsive Devices for Improved Propulsive Efficiency", Trans. IMarE, Vol.99, Paper 31, 1987

9) Blaurock,J. "An Appraisal of Unconventional Aftbody Configurations and Propulsion Devices", Marine Technology (SNAME), Vol.27, No.6, November 1990

10) Falcao de Campos,J.A.C., "On the Calculation of Ducted Propeller Performance in Axisymmetric Flows", Technical Report 696, Netherlands Ship Model Basin, Wageningen, The Netherlands, 1983

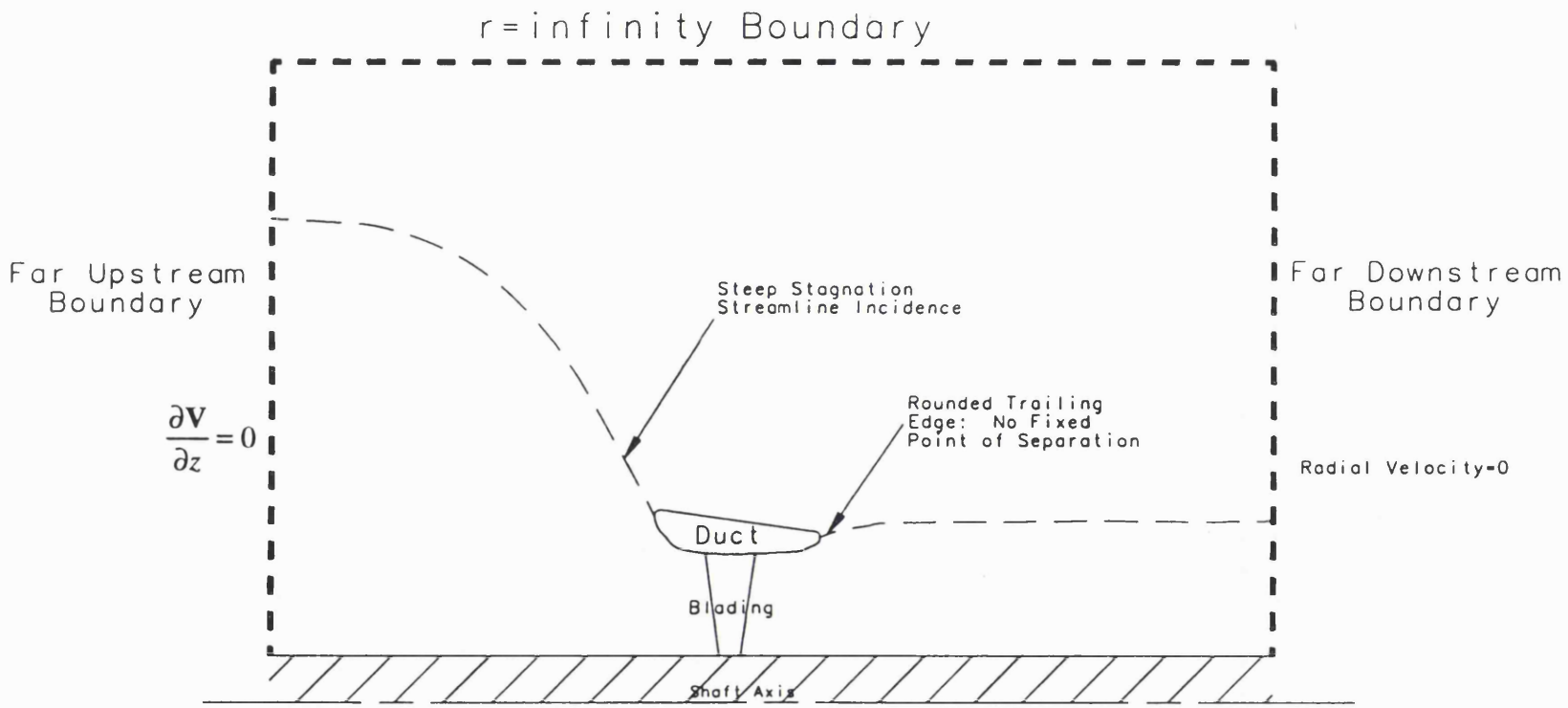

$$\frac{\partial \mathbf{V}}{\partial z} = 0$$

Figure 8.1: Ducted Propulsor Flowfield for a Tug Under "Bollard Pull" Conditions

CHAPTER 9: CONCLUDING COMMENTS

The author would like to make the following closing comments regarding the work presented in this thesis:-

1) The inverse design method presented in this thesis provides a fast and efficient means of designing ducted propulsor blading, and yet leaves considerable control of the design in the hands of the designer. The main limitations of the method would appear to associated with the assumption of inviscid flow, which takes no account of the hub, duct and blade boundary layers. Although the effects of blade cavitation are also neglected, this is considered to be less of a limitation, for ducted propulsors are generally designed to avoid this type of flow phenomenon.

   It is felt that the approach could readily be extended to the design of other marine propulsion devices such as open propellers, contra-rotating propellers, water jets, and propeller-vane wheel combinations.

2) The computational results presented in this thesis seem to indicate that the development of circumferential variations of shear vorticity within the blade passages may be neglected during the design of blading for practical ducted propulsors. As a result, the three-dimensional mean shear simplification of the ducted propulsor design method yields blade shape and performance estimates comparable to the much more complicated and time-consuming fully three-dimensional approach.

   However, the results also suggest that the development of circumferential variations of velocity within the blade passages of practical ducted propulsor designs is quite significant. Consequently the actuator duct simplification of the ducted propulsor design method, whilst both fast and robust, yields results that are, to some extent, inferior to either of the three-dimensional approaches.

   It should be stressed that these conclusions are based on free-running design conditions only, where relatively light blade loadings are usually adopted in order to maximise propulsive efficiency, and (for military applications) minimise acoustic signature.

Some words of caution are therefore warranted for cases where higher blade loadings may be used, such as the static pull design condition considered in Chapter 8. Here blade loadings may be such that three-dimensional shear phenomena are significant, in which case use of the fully three-dimensional approach would be desirable. However, in such instances blade cavitation, which is not accounted for in the design method, may well be a problem, casting the validity of the results into doubt.

3) Although the experimental work outlined in Chapter 7 goes some way towards verifying the computational design method presented in this thesis, these tests were limited in both scope and accuracy. It is felt that further verification work (such as that suggested in Chapter 8) will be required before true confidence can be placed in the predictions of this ducted propulsor design method.

4) It must be stressed that the ducted propulsor design method outlined in this thesis produces performance data and required blade shapes for a single design point. However, as with other design methods (Section 2.3), the method cannot assess the suitability of the synthesised design at the design point, and no estimate of off-design performance can be obtained without the use of a separate analysis method.

The final decision regarding the suitability of a given design must therefore be made by the designer based on numerous conflicting requirements such as off-design performance, acoustic signature, cavitation performance and efficiency.

Appendices

APPENDIX I: PROPERTIES OF THE DISCRETE FOURIER TRANSFORM

Definition of the Discrete Fourier Transform

There are several alternative definitions ([1], [2], [3]) of the discrete Fourier Transform (DFT). However, the form adopted in this thesis is

$$X^n = \frac{1}{N}\sum_{k=1}^{N} x(k)e^{-i2\pi kn/N} \quad : \; -N/2 \le n \le N/2-1 \qquad \text{A1.1}$$

with the form of the Inverse Discrete Fourier Transform (IDFT) being

$$x(k) = \sum_{n=-N/2}^{N/2-1} X^n e^{i2\pi kn/N} \qquad \text{A1.2}$$

where n and k are integers, and $x(k)$ is a function of period N defined over the range $-N/2 \le k \le N/2-1$. It will be noted that equations A1.1 and A1.2 are identical to those used by Zangeneh [3].

Periodic Nature of the DFT

From equation A1.1 it follows that

$$X^{n+N} = \frac{1}{N}\sum_{k=1}^{N} x(k)e^{i2\pi kn/N}e^{-i2\pi k}$$

Since $e^{-i2\pi k} = 1$ for all values of the integer k, it can therefore be seen that

$$X^{n+N} = X^n \qquad \text{A1.3}$$

i.e. the DFT of a function of period N is also of period N.

Frequency Domain Convolution Theorem

Consider some function $c(k)$ of period N which is the product of two functions $x(k)$ and $y(k)$, also of period N, viz

$$c(k) = x(k)\, y(k)$$

Representing x(k), y(k) and c(k) by IDFTs, it can be seen that

$$\sum_{n=-N/2}^{N/2-1} C^n e^{i2\pi kn/N} = \sum_{p=-N/2}^{N/2-1} X^p e^{i2\pi kp/N} \sum_{q=-N/2}^{N/2-1} Y^q e^{i2\pi kq/N}$$

Further defining $m=(p+q)$ yields

$$\sum_{n=-N/2}^{N/2-1} C^n e^{i2\pi kn/N} = \sum_{p=-N/2}^{N/2-1} X^p e^{i2\pi kp/N} \sum_{m=-N/2+p}^{N/2-1+p} Y^{m-p} e^{i2\pi k(m-p)/N}$$

However, as both Y^{m-p} and $e^{i2\pi k(m-p)/N}$ are functions of period N, it follows that

$$\sum_{m=-N/2+p}^{N/2-1+p} Y^{m-p} e^{i2\pi k(m-p)/N} = \sum_{m=-N/2}^{N/2-1} Y^{m-P} e^{i2\pi k(m-p)/N}$$

Therefore

$$\sum_{n=-N/2}^{N/2-1} C^n e^{i2\pi kn/N} = \sum_{p=-N/2}^{N/2-1} X^p e^{i2\pi kp/N} \sum_{m=-N/2}^{N/2-1} Y^{m-P} e^{i2\pi k(m-p)/N}$$

or

$$\sum_{n=-N/2}^{N/2-1} C^n e^{i2\pi kn/N} = \sum_{m=-N/2}^{N/2-1} \sum_{p=-N/2}^{N/2-1} X^p Y^{m-P} e^{i2\pi km/N}$$

Noting that the n^{th} component of the LHS must correspond to the m^{th} component of the RHS for equality (i.e. $n=m$), it follows that

$$C^n = \sum_{p=-N/2}^{N/2-1} X^p Y^{n-p}$$

Thus, noting from equation A1.3 that

$$Y^{n-p} = Y^{n-p+N} = Y^{n-p-N}$$

it follows that

$$C^n = \sum_{p=-N/2}^{N/2-1} X^p Y^q \qquad \text{A1.4}$$

$$\text{where q} = \begin{cases} (n-p+N) : & (n-p) < -N/2 \\ (n-p-N) : & (n-p) > N/2-1 \\ (n-p) \quad : & -N/2 \le (n-p) \le N/2-1 \end{cases}$$

Equation A1.4 is a form of the Frequency Convolution Theorem given by Brigham [1] and Cooley et al [2].

References

1) Brigham, Oran E., "The Fast Fourier Transform and Its Applications", Prentice-Hall International, 1988

2) Cooley,J.W., Lewis,P.A.W., Welch,P.D. "The Finite Fourier Transform", p77, IEEE Transactions on Audio and Electroacoustics, Vol. AU-17, No.2, June 1969

3) Zangeneh,M. "A Compressible Three-Dimensional Design Method for Radial and Mixed Flow Turbomachinery Blades", pp599-624, International Journal of Numerical Methods in Fluids", Vol.13, 1991

APPENDIX II: FOURIER REPRESENTATION OF THE PERIODIC DELTA FUNCTION $\delta_p(\alpha)$ AND THE SAWTOOTH FUNCTION $S(\alpha)$

As given by Stroud [1], a function f(t) of period s, defined over the interval $0 < t < s$ may be represented by the Fourier series

$$f(t) = \sum_{n=-N/2}^{N/2-1} F^n \, e^{i2\pi nt/s} \qquad \text{A2.1}$$

where

$$F^n = \frac{1}{s}\int_0^s f(t)\, e^{-i2\pi nt/s}\, dt \qquad \text{A2.2}$$

provided that:-

1) $f(t)$ is single-valued;
2) $f(t)$ is continuous or has a finite number of finite discontinuities;
3) $f(t)$ and $\frac{df}{dt}$ are piecewise continuous.

This Fourier representation can be applied to both the periodic Delta Function and the Sawtooth function used in Chapter 4 as follows:-

1) Periodic Delta Function $\delta_p(\alpha)$

This function, shown in Figure A2.1 has the following properties:-

(a) $\delta_p(\alpha) = 0 \quad : \alpha \neq ms, \quad m = \ldots, -2, -1, 0, 1, 2, \ldots$

(b) As $\alpha \to ms$, $\delta_p(\alpha) \to \infty \quad : m = \ldots, -2, -1, 0, 1, 2, \ldots$

(c) $\int_0^s \delta_p(\alpha)\, d\alpha = 1$

(d) $\varepsilon \xrightarrow{\lim} 0 \int_{0+\varepsilon}^{s+\varepsilon} F(\alpha)\, \delta_p(\alpha)\, d\alpha = s\, F(\alpha = s)$

Therefore, defining δ^n to be the n^{th} Fourier coefficient of $\delta_p(\alpha)$, it can be seen from equation A2.2 that

$$\begin{aligned}\delta^n &= \frac{1}{s}\int_0^s \delta_p(\alpha)\, e^{-i2\pi n\alpha/s} d\alpha \\ &= \frac{1}{s}\left(s\, e^0\right) \\ &= 1\end{aligned}$$

and therefore from equation A2.1 that

$$\delta_p(\alpha) = \sum_{n=-N/2}^{N/2-1} e^{i2\pi n\alpha/s} \qquad \text{A2.3}$$

It will be noted that this delta function is related to the periodic Dirac Delta Function, $\delta_{DIRAC}(\alpha)$, given by Lighthill [2] by

$$\delta_p(\alpha) = s\,\delta_{DIRAC}(\alpha) \qquad \text{A2.4}$$

2) Sawtooth Function S(α)

This Function (Figure A2.2) has the following properties:-

(a) A slope of minus unity for $\alpha \neq ms$: $m = \ldots, -2, -1, 0, 1, 2, \ldots$

(b) A jump of s at $\alpha = ms$: $m = \ldots, -2, -1, 0, 1, 2, \ldots$

(c) $\int_0^s S(\alpha)\, d\alpha = 0$

Defining S^n to be the n^{th} Fourier coefficient of $S(\alpha)$, it can be seen from equation A2.2 that

$$\begin{aligned}S^n &= \frac{1}{s}\int_0^s S(\alpha)\, e^{-i2\pi n\alpha/s} d\alpha \\ &= \frac{1}{s}\int_0^s \left(\frac{s}{2} - \alpha\right) e^{-i2\pi n\alpha/s} d\alpha \\ &= \frac{-is}{2\pi n} \quad : n \neq 0\end{aligned}$$

with

$$S^n = 0 \quad : n = 0$$

Therefore from equation A2.1 it follows that

$$S(\alpha) = \sum_{\substack{n=-N/2 \\ n\neq 0}}^{N/2-1} \left(\frac{-is}{2\pi n}\right) e^{i2\pi n\alpha/s} \qquad \text{A2.5}$$

Furthermore, differentiating this expression with respect to α gives

$$S'(\alpha) = \sum_{\substack{n=-N/2 \\ n\neq 0}}^{N/2-1} e^{i2\pi n\alpha/s} \qquad \text{A2.6}$$

from which it follows that

$$S'(\alpha) = \delta_p(\alpha) - 1 \qquad \text{A2.7}$$

It will be noted that equations A2.3, A2.5 and A2.7 are the expressions given by Hawthorne et al [3].

Now, applying equations A2.3, A2.5 and A2.6 to the case of the blade inverse design problem (see Chapter 4) where s is the angular spacing of the blades (i.e. $s = 2\pi/N_b$) yields

$$S(\alpha) = \sum_{\substack{n=-N/2 \\ n\neq 0}}^{N/2-1} \left(\frac{-i}{nN_b}\right) e^{iN_b n\alpha} \qquad \text{A2.8}$$

$$S'(\alpha) = \sum_{\substack{n=-N/2 \\ n\neq 0}}^{N/2-1} e^{iN_b n\alpha} \qquad \text{A2.9}$$

$$\delta_p(\alpha) = \sum_{n=-N/2}^{N/2-1} e^{inN_b\alpha} \qquad \text{A2.10}$$

as used by Zangeneh [4].

References

1) Stroud,K.A. "Fourier Series and Harmonic Analysis", Stanley Thornes (Publishers) Ltd., Cheltenham, 1984

2) Lighthill,M.J. "An Introduction to Fourier Analysis and Generalised Functions", Cambridge University Press, Cambridge, 1967

3) Hawthorne,W.R., Wang,C., Tan,C.S., McCune,J.E. "Theory of Blade Design for Large Deflections: Part I - Two-Dimensional Cascade", ASME Journal of Engineering for Gas Turbines and Power, Vol.106, April 1984

4) Zangeneh,M. "A Compressible Three-Dimensional Design Method for Radial and Mixed Flow Turbomachinery Blades", pp599-624, International Journal of Numerical Methods in Fluids", Vol.13, 1991

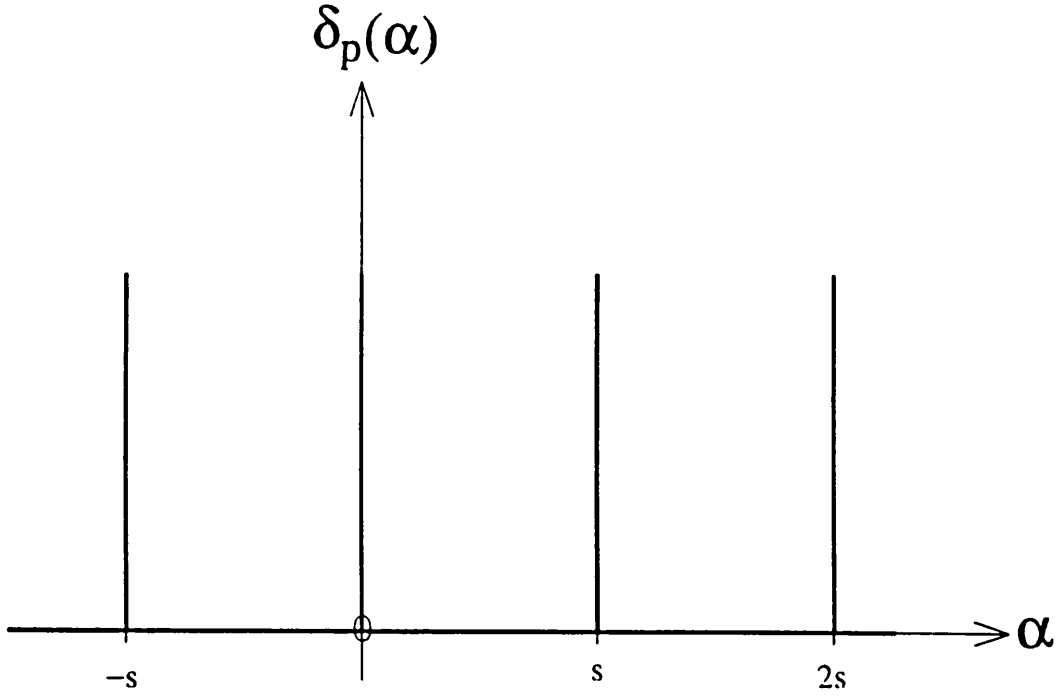

Figure A2.1: The Periodic Delta Function $\delta_p(\alpha)$

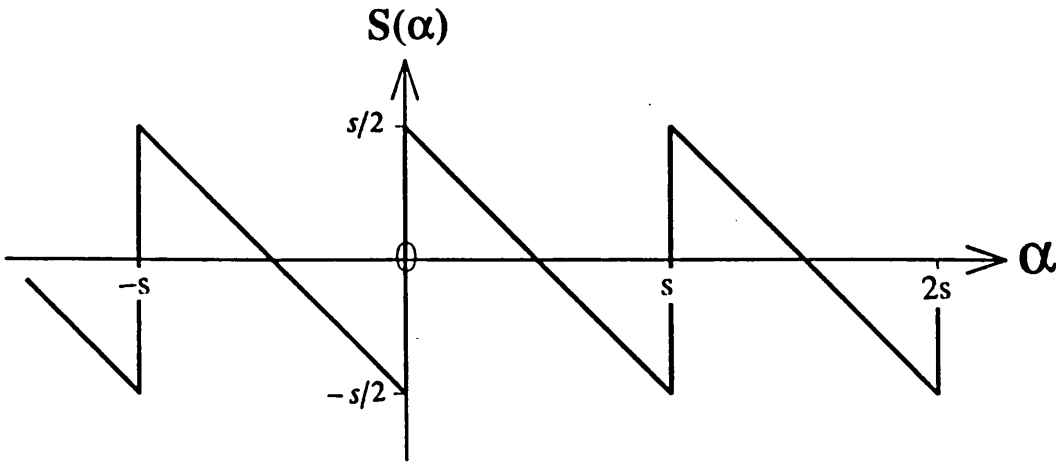

Figure A2.2: The Sawtooth Function $S(\alpha)$

APPENDIX III: SECOND ORDER ACCURATE FINITE DIFFERENCE EXPRESSIONS

Consider a function $F(\xi,\eta)$ known at discrete points (i,j) on a two-dimensional square mesh, where the two sets of mesh lines are defined by

$$\xi = si = \text{Constant}$$

and

$$\eta = sj = \text{Constant}$$

respectively, where i and j are integers and s is a constant. Using the techniques outlined by Smith [1], the derivatives of F with respect to ξ and η may be written in terms of the following second order accurate Finite Difference expressions:-

Central Difference Expressions

$$\frac{\partial F}{\partial \xi} = \frac{F(i+1,j)-F(i-1,j)}{2s} \qquad \text{A3.1}$$

$$\frac{\partial F}{\partial \eta} = \frac{F(i,j+1)-F(i,j-1)}{2s} \qquad \text{A3.2}$$

$$\frac{\partial^2 F}{\partial \xi^2} = \frac{F(i+1,j)-2F(i,j)+F(i-1,j)}{s^2} \qquad \text{A3.3}$$

$$\frac{\partial^2 F}{\partial \eta^2} = \frac{F(i,j+1)-2F(i,j)+F(i,j-1)}{s^2} \qquad \text{A3.4}$$

$$\frac{\partial^2 F}{\partial \xi \partial \eta} = \frac{F(i+1,j+1)-F(i-1,j+1)-F(i+1,j-1)+F(i-1,j-1)}{4s^2} \qquad \text{A3.5}$$

Forward Difference Expressions

$$\frac{\partial F}{\partial \xi} = \frac{-3F(i,j)+4F(i+1,j)-F(i+2,j)}{2s} \qquad \text{A3.6}$$

$$\frac{\partial F}{\partial \eta} = \frac{-3F(i,j)+4Fi,j+1)-F(i,j+2)}{2s} \qquad \text{A3.7}$$

$$\frac{\partial^2 F}{\partial \xi^2} = \frac{2F(i,j)-5F(i+1,j)+4F(i+2,j)-F(i+3,j)}{s^2} \qquad \text{A3.8}$$

$$\frac{\partial^2 F}{\partial \eta^2} = \frac{2F(i,j)-5F(i,j+1)+4F(i,j+2)-F(i,j+3)}{s^2} \qquad \text{A3.9}$$

Backward Difference Expressions

$$\frac{\partial F}{\partial \xi} = \frac{3F(i,j)-4F(i-1,j)+F(i-2,j)}{2s} \qquad \text{A3.10}$$

$$\frac{\partial F}{\partial \eta} = \frac{3F(i,j)-4F(i,j-1)+F(i,j-2)}{2s} \qquad \text{A3.11}$$

$$\frac{\partial^2 F}{\partial \xi^2} = \frac{2F(i,j)-5F(i-1,j)+4F(i-2,j)-F(i-3,j)}{s^2} \qquad \text{A3.12}$$

$$\frac{\partial^2 F}{\partial \eta^2} = \frac{2F(i,j)-5F(i,j-1)+4F(i,j-2)-F(i,j-3)}{s^2} \qquad \text{A3.13}$$

These expressions were employed in the finite difference discretisation of the ducted propulsor design method (Appendix VI).

References

1) Smith,G.D. "Numerical Solution of Partial Differential Equations: Finite Difference Methods", Third Edition, Oxford Applied Mathematics and Computing Science Series, Oxford University Press, 1985

APPENDIX IV: SOME USEFUL VECTOR RELATIONSHIPS

The following expressions, as presented by Acheson [1], were of considerable use in the formulation of the ducted propulsor design method (Chapters 4 and 5):-

Vector Identities

$$\nabla(fg) = f\nabla g + g\nabla f \qquad \text{A4.1}$$

$$\nabla\cdot(f\mathbf{F}) = f\nabla\cdot\mathbf{F} + \mathbf{F}\cdot\nabla f \qquad \text{A4.2}$$

$$\nabla\times(f\mathbf{F}) = f\nabla\times\mathbf{F} - \mathbf{F}\times\nabla f \qquad \text{A4.3}$$

$$\nabla\cdot(\mathbf{F}\times\mathbf{G}) = \mathbf{G}\cdot\nabla\times\mathbf{F} - \mathbf{F}\cdot\nabla\times\mathbf{G} \qquad \text{A4.4}$$

$$\nabla\cdot(\nabla f) = \nabla^2 f \qquad \text{A4.5}$$

$$\nabla\times(\nabla f) = 0 \qquad \text{A4.6}$$

$$\nabla\cdot(\nabla\times\mathbf{F}) = 0 \qquad \text{A4.7}$$

$$\nabla\times(\nabla\times\mathbf{F}) = \nabla(\nabla\cdot\mathbf{F}) - \nabla^2\mathbf{F} \qquad \text{A4.8}$$

$$\mathbf{F}\times(\mathbf{G}\times\mathbf{H}) = (\mathbf{F}\cdot\mathbf{H})\mathbf{G} - (\mathbf{F}\cdot\mathbf{G})\mathbf{H} \quad \text{Triple Vector Product} \qquad \text{A4.9}$$

$$\left.\begin{aligned}\mathbf{F}\cdot(\mathbf{G}\times\mathbf{H}) &= \mathbf{H}\cdot(\mathbf{F}\times\mathbf{G}) = \mathbf{G}\cdot(\mathbf{H}\times\mathbf{F}) \qquad \text{A4.10}\\ \mathbf{F}\cdot(\mathbf{G}\times\mathbf{H}) &= -\mathbf{G}\cdot(\mathbf{F}\times\mathbf{H}) \qquad \text{A4.11}\\ \mathbf{F}\cdot(\mathbf{G}\times\mathbf{H}) &= -\mathbf{F}\cdot(\mathbf{H}\times\mathbf{G}) \qquad \text{A4.12}\end{aligned}\right\} \quad \text{Triple Scalar Product}$$

Formulae for Div, Grad and Curl in Cylindrical Polar Co-ordinates

$$\nabla f = \frac{\partial f}{\partial r}\hat{\mathbf{e}}_r + \frac{1}{r}\frac{\partial f}{\partial\theta}\hat{\mathbf{e}}_\theta + \frac{\partial f}{\partial z}\hat{\mathbf{e}}_z \qquad \text{A4.13}$$

$$\nabla\cdot\mathbf{F} = \frac{1}{r}\frac{\partial(rF_r)}{\partial r} + \frac{1}{r}\frac{\partial F_\theta}{\partial\theta} + \frac{\partial F_z}{\partial z} \qquad \text{A4.14}$$

$$\nabla\times\mathbf{F} = \frac{1}{r}\begin{vmatrix}\hat{\mathbf{e}}_r & r\hat{\mathbf{e}}_\theta & \hat{\mathbf{e}}_z\\ \dfrac{\partial}{\partial r} & \dfrac{\partial}{\partial\theta} & \dfrac{\partial}{\partial z}\\ F_r & rF_\theta & F_z\end{vmatrix} \qquad \text{A4.15}$$

$$= \frac{1}{r}\left(\frac{\partial F_z}{\partial\theta} - \frac{\partial rF_\theta}{\partial z}\right)\hat{\mathbf{e}}_r + \left(\frac{\partial F_r}{\partial z} - \frac{\partial F_z}{\partial r}\right)\hat{\mathbf{e}}_\theta + \frac{1}{r}\left(\frac{\partial rF_\theta}{\partial r} - \frac{\partial F_r}{\partial\theta}\right)\hat{\mathbf{e}}_z$$

$$\nabla^2 F = \frac{1}{r}\frac{\partial}{\partial r}\left(r\frac{\partial F}{\partial r}\right) + \frac{1}{r^2}\frac{\partial^2 F}{\partial \theta^2} + \frac{\partial^2 F}{\partial z^2} \qquad \text{A4.16}$$

References

1) Acheson,D.J. "Elementary Fluid Dynamics", p348, Oxford Applied Mathematics and Computing Science Series, Oxford University Press, 1990

APPENDIX V: DETERMINATION OF BLADE PRESSURE AND VELOCITY JUMPS

Blade Pressure Jump

From equation 4.8, the force the rotating blade exerts on the fluid may be written

$$f_{bl} = -\rho\left(\mathbf{W}_{bl}\cdot\nabla\overline{rV_\theta}\right)\delta_p(\alpha)\nabla\alpha \qquad \text{A5.1}$$

Resolving this body force in the tangential direction and integrating over one blade pitch

$$\int_0^{\frac{2\pi}{N_b}} f_{bl}\cdot\hat{\mathbf{e}}_\theta\, d\theta = -\int_0^{2\pi/N_b}\rho\left(\mathbf{W}_{bl}\cdot\nabla\overline{rV_\theta}\right)\delta_p(\alpha)\, d\theta$$

$$= -\frac{2\pi\rho}{N_b}\left(\mathbf{W}_{bl}\cdot\nabla\overline{rV_\theta}\right)$$

i.e. blade force per unit meridional area $= -\dfrac{2\pi\rho}{N_b}\,\mathbf{W}_{bl}\cdot\nabla\overline{rV}_\theta$

However, blade force per unit meridional area = $(p^+ - p^-)$, where superscript + refers to the pressure side of the blade and - the suction side. Therefore an expression for the pressure jump on the blade is

$$\left(p^+ - p^-\right) = -\frac{2\pi\rho}{N_b}\,\mathbf{W}_{bl}\cdot\nabla\overline{rV_\theta} \qquad \text{A5.2}$$

which is similar to the expression given by Hawthorne and Tan [1] for a stationary turbomachine blade in inviscid, incompressible, irrotational flow. The right hand side of this equation can be evaluated using the output from the inverse design method outlined in Chapters 4 and 5.

Blade Velocity Jump

Applying the Bernoulli Streamline Theorem on the pressure and suction surfaces of the blade respectively, and neglecting the jump in rothalpy on the blade (which cannot be expressed in closed form):-

$$\frac{p^+}{\rho} = H_{bl} - \frac{\mathbf{W}^+ \cdot \mathbf{W}^+}{2} + \frac{\omega^2 r^2}{2}$$
$$\frac{p^-}{\rho} = H_{bl} - \frac{\mathbf{W}^- \cdot \mathbf{W}^-}{2} + \frac{\omega^2 r^2}{2}$$

From this it can be seen that

$$\frac{\mathbf{W}^-.\mathbf{W}^-}{2} - \frac{\mathbf{W}^+.\mathbf{W}^+}{2} = \frac{p^+ - p^-}{\rho} \qquad \text{A5.3}$$

However,

$$\frac{\mathbf{W}^- \cdot \mathbf{W}^-}{2} - \frac{\mathbf{W}^+ \cdot \mathbf{W}^+}{2} = \frac{(\mathbf{W}^- + \mathbf{W}^+)}{2} \cdot (\mathbf{W}^- - \mathbf{W}^+)$$
$$= \mathbf{W}_{bl} \cdot (\mathbf{W}^- - \mathbf{W}^+)$$

Thus, equation A5.3 becomes

$$\mathbf{W}_{bl} \cdot (\mathbf{W}^- - \mathbf{W}^+) = \frac{p^+ - p^-}{\rho}$$

Now, as $\frac{\mathbf{W}_{bl} \cdot \mathbf{W}_{bl}}{|\mathbf{W}_{bl}|^2} = 1$, this equation may be rewritten

$$\mathbf{W}_{bl} \cdot (\mathbf{W}^- - \mathbf{W}^+) = \left(\frac{p^+ - p^-}{\rho}\right) \frac{\mathbf{W}_{bl} \cdot \mathbf{W}_{bl}}{|\mathbf{W}_{bl}|^2}$$

from which it can be seen that for some value of the constant K

$$(\mathbf{W}^- - \mathbf{W}^+) = \left(\frac{p^+ - p^-}{\rho}\right) \frac{\mathbf{W}_{bl}}{|\mathbf{W}_{bl}|^2} + K\hat{\mathbf{n}}_{wbl}$$

where $\hat{\mathbf{n}}_{wbl}$ is the normal to $\mathbf{W}_{bl}$.

Again neglecting the jump in H on the blade, it can be shown from the Bernoulli streamline Theorem that there can be no jump in pressure on the blade if there is no corresponding jump in velocity. It therefore follows that K=0, giving

$$(\mathbf{W}^- - \mathbf{W}^+) = \left(\frac{p^+ - p^-}{\rho}\right)\frac{\mathbf{W}_{bl}}{|\mathbf{W}_{bl}|^2}$$

Taking the modulus of each side, the equation for the jump in relative velocity on the blade becomes

$$|\mathbf{W}^- - \mathbf{W}^+| = \frac{|p^+ - p^-|}{\rho|\mathbf{W}_{bl}|} \qquad \text{A5.4}$$

which again is similar to the expression given by Hawthorne and Tan [1] for a stationary turbomachine blade in inviscid, incompressible, irrotational flow.

Substituting equation A5.2 into this gives the final expression

$$|\mathbf{W}^+ - \mathbf{W}^-| = \frac{2\pi}{N_b|\mathbf{W}_{bl}|}\,|\mathbf{W}_{bl} \cdot \nabla\overline{rV_\theta}| \qquad \text{A5.5}$$

for the jump in relative velocity on the rotating blading.

References

1) Hawthorne,W.R., Tan,C.S. "Design of Turbomachinery Blading in 3D Flow by the Circulation Method: A Progress Report", International Conference On Inverse Design In Engineering Sciences (ICIDES), 1987

APPENDIX VI: EQUATION DISCRETISATION

Defining G(i,j) be the value of any function G at the intersection of the i^{th} quasi-orthogonal of the solution mesh with the j^{th} quasi-streamline, and using the finite difference expressions given in Appendix III, enables the discretised forms of equations 5.20...5.26 (Section 5.2) to be written as follows:-

Stream Function ψ (Equation 5.24)

This equation is elliptic in nature and was therefore discretised using the second order accurate central difference formulae given in Appendix III, becoming

$$\left.\begin{aligned}
&C_{m1}\psi(i,j)\\
&+\left(C_{m2}+C_{mb21}B_t(1/B_t)_\xi+C_{mb22}B_t(1/B_t)_\eta\right)\psi(i+1,j)\\
&+\left(C_{m3}-C_{mb21}B_t(1/B_t)_\xi-C_{mb22}B_t(1/B_t)_\eta\right)\psi(i-1,j)\\
&+\left(C_{m4}+C_{mb41}B_t(1/B_t)_\eta+C_{mb42}B_t(1/B_t)_\xi\right)\psi(i,j+1)\\
&+\left(C_{m5}-C_{mb41}B_t(1/B_t)_\eta-C_{mb42}B_t(1/B_t)_\xi\right)\psi(i,j-1)\\
&+C_{m6}\,\psi(i+1,j+1)\;+\;C_{m6}\,\psi(i-1,j-1)\\
&-C_{m6}\,\psi(i+1,j-1)\;-\;C_{m6}\,\psi(i-1,j+1)
\end{aligned}\right\} = R_m \qquad \text{A6.1}$$

where

$$C_{m1} = \frac{-2(\alpha+\gamma)}{s^2}$$

$$C_{m2} = \frac{\alpha}{s^2} + \frac{T+Jz_\eta/r}{2s}$$

$$C_{m3} = \frac{\alpha}{s^2} - \frac{T+Jz_\eta/r}{2s}$$

$$C_{m4} = \frac{\gamma}{s^2} + \frac{\Sigma-Jz_\xi/r}{2s}$$

$$C_{m5} = \frac{\gamma}{s^2} - \frac{\Sigma-Jz_\xi/r}{2s}$$

$$C_{m6} = \frac{-\beta}{2s^2}$$

$$C_{mb21} = \frac{\alpha}{2s}$$

$$C_{mb22} = \frac{-\beta}{2s}$$

$$C_{mb41} = \frac{\gamma}{2s}$$

$$C_{mb42} = \frac{-\beta}{2s}$$

$$R_m = -rB_t J\left(\overline{rV_{\theta_\eta}} f_\xi - \overline{rV_{\theta_\xi}} f_\eta + \sum_{p=-N/2}^{N/2-1}\left(H_\xi^p \tau_\eta^{-p} - H_\eta^p \tau_\xi^{-p}\right)\right)$$

Potential Function Φ (Equation 5.25)

This equation is also elliptic, and was discretised using a similar strategy to that used for ψ, yielding:-

$$\left.\begin{aligned}&\left(C_{p1} - \frac{n^2 N_b{}^2 J^2}{r^2}\right)\Phi^n(i,j) + C_{p2}\Phi^n(i+1,j) + C_{p3}\Phi^n(i-1,j)\\ &+ C_{p4}\Phi^n(i,j+1) + C_{p5}\Phi^n(i,j-1) + C_{p6}\Phi^n(i+1,j+1)\\ &- C_{p6}\Phi^n(i+1,j-1) + C_{p7}\Phi^n(i-1,j-1) - C_{p7}\Phi^n(i-1,j+1)\end{aligned}\right\} = R_p \qquad \text{A6.2}$$

where

$$C_{p1} = \frac{-2(\alpha+\gamma)}{s^2}$$

$$C_{p2} = \frac{\alpha}{s^2} + \frac{T - Jz_\eta/r}{2s}$$

$$C_{p3} = \frac{\alpha}{s^2} - \frac{T - Jz_\eta/r}{2s}$$

$$C_{p4} = \frac{\gamma}{s^2} + \frac{\Sigma + Jz_\xi/r}{2s}$$

$$C_{p5} = \frac{\gamma}{s^2} - \frac{\Sigma + Jz_\xi/r}{2s}$$

$$C_{p6} = \frac{-\beta}{2s^2}$$

$$C_{p7} = \frac{-\beta}{2s^2}$$

$$
\begin{aligned}
R_p = \frac{-ie^{-inN_b f}}{nN_b} & \left(\begin{array}{l} \alpha \overline{rV_{\theta_{\xi\xi}}} - 2\beta\, \overline{rV_{\theta_{\xi\eta}}} + \gamma\, \overline{rV_{\theta_{\eta\eta}}} \\ + \left(T - \frac{Jz_\eta}{r}\right) \overline{rV_{\theta_\xi}} + \left(\Sigma + \frac{Jz_\xi}{r}\right) \overline{rV_{\theta_\eta}} \end{array} \right) \\
& - e^{-inN_b f} \left(\alpha\, \overline{rV_{\theta_\xi}} f_\xi - \beta\, \overline{rV_{\theta_\xi}} f_\eta - \beta\, \overline{rV_{\theta_\eta}} f_\xi + \gamma\, \overline{rV_{\theta_\eta}} f_\eta \right) \\
& - H^n \left(\begin{array}{l} \alpha\, \tau^0_{\xi\xi} - 2\beta\, \tau^0_{\xi\xi} + \gamma\, \tau^0_{\xi\xi} \\ + \left(T - \frac{Jz_\eta}{r}\right) \tau^0_\xi + \left(\Sigma + \frac{Jz_\xi}{r}\right) \tau^0_\eta \end{array} \right) \\
& - \left(\alpha\, H^n_\xi \tau^0_\xi - \beta\, H^n_\xi \tau^0_\eta - \beta\, H^n_\eta \tau^0_\xi + \gamma\, H^n_\eta \tau^0_\eta \right) \\
& + \sum_{\substack{p=-N/2 \\ q\neq 0}}^{N/2-1} \tau^q \left(\begin{array}{l} \alpha\, H^p_{\xi\xi} - 2\beta\, H^p_{\xi\eta} + \gamma\, H^p_{\eta\eta} \\ + \left(T - \frac{Jz_\eta}{r}\right) H^p_\xi + \left(\Sigma + \frac{Jz_\xi}{r}\right) H^p_\eta \\ - \frac{J^2 N_b^2 p^2}{r^2} H^p \end{array} \right) \\
& + \sum_{\substack{p=-N/2 \\ q\neq 0}}^{N/2-1} \left(\begin{array}{l} \alpha\, H^p_\xi \tau^q_\xi - \beta\, H^p_\xi \tau^q_\eta - \beta\, H^p_\eta \tau^q_\xi + \gamma\, H^p_\eta \tau^q_\eta \\ - \frac{J^2 N_b^2 pq}{r^2} H^p \tau^q \end{array} \right)
\end{aligned}
$$

$$
q = \begin{cases} (n-p+N) : & (n-p) < -N/2 \\ (n-p-N) : & (n-p) > N/2-1 \\ (n-p) \quad : & -N/2 \le (n-p) \le N/2-1 \end{cases}
$$

and $-N/2 \le n \le N/2-1 : n \neq 0$.

Blade Wrap Angle f (Equation 5.20) and Mean Swirl $\overline{rV}_\theta$ (Equation 5.21)

These equations, being hyperbolic in nature, were discretised using the Crank-Nicholson Implicit Scheme, producing:-

$$
\begin{aligned}
& - C_A f(i,j-1) + C_B f(i,j) + C_A f(i,j+1) \\
& \qquad = \qquad \text{A6.3} \\
& \frac{J(V_{\theta bl} - \omega r)}{r} + C_A f(i-1,j-1) + C_B f(i-1,j) - C_A f(i-1,j+1)
\end{aligned}
$$

and

$$
\begin{aligned}
&- C_A\,\overline{rV}_\theta(i,j-1) + C_B\,\overline{rV}_\theta(i,j) + C_A\,\overline{rV}_\theta(i,j+1) \\
&\qquad = \\
&C_A\,\overline{rV}_\theta(i-1,j-1) + C_B\overline{rV}_\theta(i-1,j) - C_A\overline{rV}_\theta(i-1,j+1)
\end{aligned}
\qquad \text{A6.4}
$$

where

$$
C_A = C_A\,(i,j) = \frac{\left(\sqrt{\alpha}\,\mathbf{V}_{bl}.\hat{\mathbf{e}}^n_\eta\right)_{(i,j)} + \left(\sqrt{\alpha}\,\mathbf{V}_{bl}.\hat{\mathbf{e}}^n_\eta\right)_{(i-1,j)}}{2}
$$

$$
C_B = C_B\,(i,j) = \frac{\left(\sqrt{\gamma}\,\mathbf{V}_{bl}.\hat{\mathbf{e}}^n_\xi\right)_{(i,j)} + \left(\sqrt{\gamma}\,\mathbf{V}_{bl}.\hat{\mathbf{e}}^n_\xi\right)_{(i-1,j)}}{2}
$$

Each of these two equations reduces to a tridiagonal system of equations (Figure A6.1) which may be solved at each quasi-orthogonal using techniques similar to those presented by Press et al [1].

Drift Function H (Equation 5.22) and Drift Function τ (Equation 5.23)

These equations are also hyperbolic and were discretised in a similar fashion to A6.3 and A6.4 above:-

$$
\begin{aligned}
&\sum_{p=-N/2}^{N/2-1}\left(- C_2 H^p(i,j-1) + (C_1+C_3)H^p(i,j) + C_2\,H^p(i,j+1)\right) \\
&\qquad = \\
&\sum_{p=-N/2}^{N/2-1}\left(+ C_2 H^p(i-1,j-1) + (C_1-C_3)H^p(i-1,j) - C_2\,H^p(i-1,j+1)\right)
\end{aligned}
\qquad \text{A6.5}
$$

$$
\begin{aligned}
&\sum_{p=-N/2}^{N/2-1}\left(- C_2\tau^p(i,j-1) + (C_1+C_3)\tau^p(i,j) + C_2\,\tau^p(i,j+1)\right) \\
&\qquad = \\
&\qquad R_\tau \\
&+ \sum_{p=-N/2}^{N/2-1}\left(+ C_2\tau^p(i-1,j-1) + (C_1-C_3)\tau^p(i-1,j) - C_2\,\tau^p(i-1,j+1)\right)
\end{aligned}
\qquad \text{A6.6}
$$

where

$$C_1 = C_1(i,j,p,n) = \frac{\left(\frac{\sqrt{\alpha}\,\mathbf{W}^q \cdot \hat{\mathbf{e}}_\xi^n}{J}\right)_{(i,j)} + \left(\frac{\sqrt{\alpha}\,\mathbf{W}^q \cdot \hat{\mathbf{e}}_\xi^n}{J}\right)_{(i-1,j)}}{2}$$

$$C_2 = C_2(i,j,p,n) = \frac{\left(\frac{\sqrt{\gamma}\,\mathbf{W}^q \cdot \hat{\mathbf{e}}_\eta^n}{J}\right)_{(i,j)} + \left(\frac{\sqrt{\gamma}\,\mathbf{W}^q \cdot \hat{\mathbf{e}}_\eta^n}{J}\right)_{(i-1,j)}}{8}$$

$$C_3 = C_3(i,j,p,n) = \frac{iN_b}{4}\left(\left(\frac{pW_\theta^q}{r}\right)_{(i,j)} + \left(\frac{pW_\theta^q}{r}\right)_{(i-1,j)}\right)$$

$$R_\tau = \begin{cases} 1 & : n = 0 \\ 0 & : n \neq 0 \end{cases}$$

$-N/2 \leq n \leq N/2-1$

$$q = \begin{cases} (n-p+N) : & (n-p) < -N/2 \\ (n-p-N) : & (n-p) > N/2-1 \\ (n-p) \quad : & -N/2 \leq (n-p) \leq N/2-1 \end{cases}$$

These equations reduce to a system of block tridiagonal equations at each quasi-orthogonal, with complex sub-matrices of size N×N, as shown in Figure A6.2 (see also Anderson et al [2], and Fletcher [3]).

Duct Kutta Condition (Equation 5.26)

This equation was discretised using second order accurate forward and backward difference expressions for $\psi_{\eta b}$ and $\psi_{\eta c}$ respectively, giving

$$\psi(i,j) = \frac{\left(\frac{4r^2J^2\left(2\omega\,\overline{rV}_{\theta c} - \overline{V}_{\theta c}^2\right)}{\gamma} - T_1\right)}{T_2} \qquad \text{A6.7}$$

where

$$T_1 = +16\psi^2(i,j-1) - 8\psi(i,j-1)\,\psi(i,j-2) + \psi^2(i,j-2) - 16\psi^2(i,j+1) + 8\psi(i,j+1)\,\psi(i,j+2) - \psi^2(i,j+2)$$

$$T_2 = +6\psi(i,j-2) - 24\psi(i,j-1) + 24\psi(i,j+1) - 6\psi(i,j+2)$$

References

1) Press,W.H., Flannery,B.P., Teukolsky,S.A., Vetterling,W.T. "Numerical Recipes - The Art of Scientific Computing (FORTRAN Version)", p40, Cambridge University Press, 1989

2) Anderson,A., Tannehill,J.C., Pletcher,R.H. "Computational Fluid Mechanics and Heat Transfer", p551, Series in Computational Methods in Mechanics and Thermal Sciences, McGraw Hill, 1984

3) Fletcher,C.A.J. "Computational Techniques for Fluid Dynamics: Volume I - Fundamental and General Techniques", p188, Second Edition, Springer Series in Computational Physics, Springer-Verlag, Berlin, 1991

$$\begin{pmatrix} b_1 & c_1 & & & & & & & \\ a_2 & b_2 & c_2 & & & & & & \\ & a_3 & b_3 & c_3 & & & & & \\ & & \cdot & \cdot & \cdot & & & & \\ & & & \cdot & \cdot & \cdot & & & \\ & & & & a_{m-2} & b_{m-2} & c_{m-2} & & \\ & & & & & a_{m-1} & b_{m-1} & c_{m-1} & \\ & & & & & & a_m & b_m & \end{pmatrix} \begin{pmatrix} u_1 \\ u_2 \\ u_3 \\ \cdot \\ \cdot \\ u_{m-2} \\ u_{m-1} \\ u_m \end{pmatrix} = \begin{pmatrix} r_1 \\ r_2 \\ r_3 \\ \cdot \\ \cdot \\ r_{m-2} \\ r_{m-1} \\ r_m \end{pmatrix}$$

Matrix of Coefficients

Right Hand Side Vector

Figure A6.1: The Matrix Representation of a Tridiagonal System of Equations

$$\begin{pmatrix} \mathbf{B}_1 & \mathbf{C}_1 & & & & & & & \\ \mathbf{A}_2 & \mathbf{B}_2 & \mathbf{C}_2 & & & & & & \\ & \mathbf{A}_3 & \mathbf{B}_3 & \mathbf{C}_3 & & & & & \\ & & \cdot & \cdot & \cdot & & & & \\ & & & \cdot & \cdot & \cdot & & & \\ & & & & \mathbf{A}_{m-2} & \mathbf{B}_{m-2} & \mathbf{C}_{m-2} & & \\ & & & & & \mathbf{A}_{m-1} & \mathbf{B}_{m-1} & \mathbf{C}_{m-1} & \\ & & & & & & \mathbf{A}_m & \mathbf{B}_m & \end{pmatrix} \begin{pmatrix} \mathbf{U}_1 \\ \mathbf{U}_2 \\ \mathbf{U}_3 \\ \cdot \\ \cdot \\ \mathbf{U}_{m-2} \\ \mathbf{U}_{m-1} \\ \mathbf{U}_m \end{pmatrix} = \begin{pmatrix} \mathbf{R}_1 \\ \mathbf{R}_2 \\ \mathbf{R}_3 \\ \cdot \\ \cdot \\ \mathbf{R}_{m-2} \\ \mathbf{R}_{m-1} \\ \mathbf{R}_m \end{pmatrix}$$

NB

1) $\mathbf{A}_j$, $\mathbf{B}_j$, $\mathbf{C}_j$: $1 < j < m$ are all square submatrices of known coefficients

2) $\mathbf{U}_j$: $1 < j < m$ are all column vectors containing the unknown quantity.

3) $\mathbf{R}_j$: $1 < j < m$ are all column vectors containing the right hand sides of the equations.

Figure A6.2: The Matrix Representation of a Block Tridiagonal System of Equations

APPENDIX VII: FORCING THE NORMAL DERIVATIVE OF ROTHALPY TO ZERO AT THE ENDWALLS

As stated in Section 5.13, it was generally found necessary to force the normal derivative of rothalpy at the endwalls to zero
i.e. satisfy

$$\nabla H \cdot \hat{\mathbf{e}}_\eta^n = 0 \qquad \text{A7.1}$$

in order to achieve satisfactory convergence for fully three-dimensional runs of the ducted propulsor inverse design programs.

This was achieved by imposing

$$\nabla H^m \cdot \hat{\mathbf{e}}_\eta^n = 0 \quad : -N/2 \le m \le N/2-1 \qquad \text{A7.2}$$

along the hub quasi-streamline, the duct upper and lower surfaces, and the duct wake. The technique used was similar to that employed by Borges [1] to force the normal derivative of blade wrap angle to zero at the endwalls and involves linearly extrapolating the value of $\nabla H^m \cdot \hat{\mathbf{e}}_\eta^n$ from an unmodified value typically 4 or 5 mesh points away from the endwall down to zero at the endwall for $N/2 \le m \le N/2-1$. This results in the equation

$$\nabla H^m \cdot \hat{\mathbf{e}}_\eta^n = \left(\nabla H^m \cdot \hat{\mathbf{e}}_\eta^n\right)_X \quad : -N/2 \le m \le N/2-1 \qquad \text{A7.3}$$

where $\left(\nabla H^m \cdot \hat{\mathbf{e}}_\eta^n\right)_X$ is the required value of $\nabla H^m \cdot \hat{\mathbf{e}}_\eta^n$ obtained from linear extrapolation. Expanding equation A7.3 and applying the co-ordinate transform techniques outlined in Section 5.1 gives

$$H_\eta^m - \left(\frac{\beta}{\gamma}\right) H_\xi^m = \frac{J}{\sqrt{\gamma}}\left(\nabla H^m \cdot \hat{\mathbf{e}}_\eta^n\right)_X \quad : -N/2 \le m \le N/2-1 \qquad \text{A7.4}$$

This equation is discretised using second order accurate finite difference expressions (see Appendix III). In the region of the hub endwall a central difference discretisation of H_ξ^m together with a backward difference discretisation of H_η^m are used, whilst at

the tip endwall a forward difference discretisation of H_{η}^{m} is used. In each instance boundary conditions of $H_{\xi\xi}^{m} = 0$ are applied on the far upstream and far downstream boundaries, and for the case of a ducted propulsor, the duct leading edge.

The discretised form of A7.4 so obtained enables each Fourier harmonic of rothalpy (including the mean component) to be individually marched one quasi-streamline at a time towards the endwalls by solving a tridiagonal system of equations (see Appendix VI) on each quasi-streamline. The initial condition for this procedure is the rothalpy distribution on a quasi-streamline typically four or five mesh points from the relevant endwall. The result is a rothalpy distribution which has only been modified close to the endwalls, and which satisfies equation A7.1 at the endwalls, as required

References

1) Borges,J. "Three Dimensional Inverse Design of Turbomachinery", Ph.D. Thesis, Cambridge University Engineering Department, Cambridge, 1986

APPENDIX VIII: THE RELATIONSHIP BETWEEN $\overline{rV_\theta}$ AND BLADE CIRCULATION

Consider an element of a turbomachine blade taken at constant radius r, where δr is the span of the element and ω is the shaft angular speed (Figure A8.1).

Define two points A and B to lie at the leading edge and trailing edge of the element respectively, with a third point P lying at some arbitrary point on the blade. Let $\overline{V_{\theta le}}$, $\overline{V_{\theta te}}$ and $\overline{V_\theta}$ be the circumferential mean tangential velocities at points A, B and P respectively.

If the circumferential mean axial velocity, $\overline{V_z}$, is assumed to be invariant along the section chord, and if the circumferential variations in shear vorticity are neglected, then circulation theory [1] enables the lift force on section AP to be written

$$\delta L_{AP} = \rho \Gamma_{AP} \overline{V_z} \qquad \text{A8.1}$$

where Γ_{AP} is the circulation between the leading edge and point P. It will be noted that this lift force acts parallel to the induced velocity $\left(\overline{V_\theta} - \overline{V_{\theta le}}\right)$ and therefore lies in the tangential direction.

The corresponding elemental torque on section AP is therefore

$$\delta Q_{AP} = \rho r \Gamma_{AP} \overline{V_z} \qquad \text{A8.2}$$

However, as the mass flow over the blade element may be written

$$\dot{m} = 2\pi\rho r \overline{V_z}\, \delta r / N_b \qquad \text{A8.3}$$

the one-dimensional Euler turbine equation [2] enables the elemental torque per blade to be written

$$\delta Q_{AP} = \frac{2\pi\rho r^2 \overline{V_z}\left(\overline{V_\theta} - \overline{V_{\theta le}}\right)}{N_b}\, \delta r \qquad \text{A8.4}$$

Comparing equations 8.2 and 8.4 it follows that the circulation along constant radius between the blade leading edge and any point P(r,z) on the blade may be written

$$\Gamma(r,z)=\frac{2\pi}{N_b}\left(\overline{rV_\theta}-\overline{rV_{\theta\,le}}\right) \qquad \text{A8.5}$$

Furthermore that the circulation around the entire blade section may be written

$$\Gamma(r)=\frac{2\pi}{N_b}\left(\overline{rV_{\theta\,te}}-\overline{rV_{\theta\,le}}\right) \qquad \text{A8.6}$$

which is similar to the expressions given by Hawthorne and Tan [3], and Dang and Wang [4].

These last two equations represent the fundamental relationship between blade circulation and mean swirl $\overline{rV_\theta}$. They enable blade circulation to be specified in terms of $\overline{rV_\theta}$, as was the case with the inverse design method presented in this thesis.

References

1) Abbott,I.H., Von Doenhoff,A.E. "Theory of Wing Sections", p45, Dover Publications Inc., New York, 1959

2) Dixon,S.L. "Fluid Mechanics, Thermodynamics of Turbomachinery", p30, Third Edition, Pergamon Press, 1978

3) Hawthorne,W.R., Tan,C.S. "Design of Turbomachinery Blading in 3D Flow by the Circulation Method: A Progress Report", International Conference On Inverse Design In Engineering Sciences (ICIDES), 1987

4) Dang,T.Q., Wang,T. "Design of Multi-Stage Turbomachinery Blading by the Circulation Method: Actuator Duct Limit", ASME Paper 92-GT-286, 1992

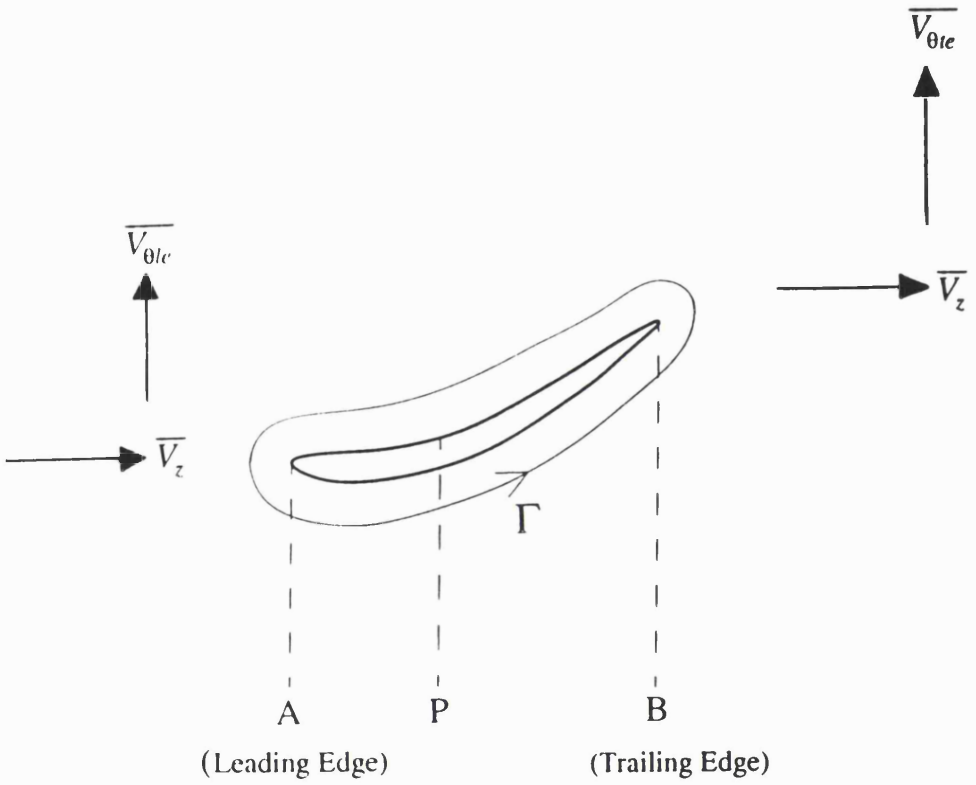

Figure A8.1: Circulation About a Blade Section at Constant Radius

APPENDIX IX: DUCT PROFILES AND BLADE THICKNESS DISTRIBUTIONS

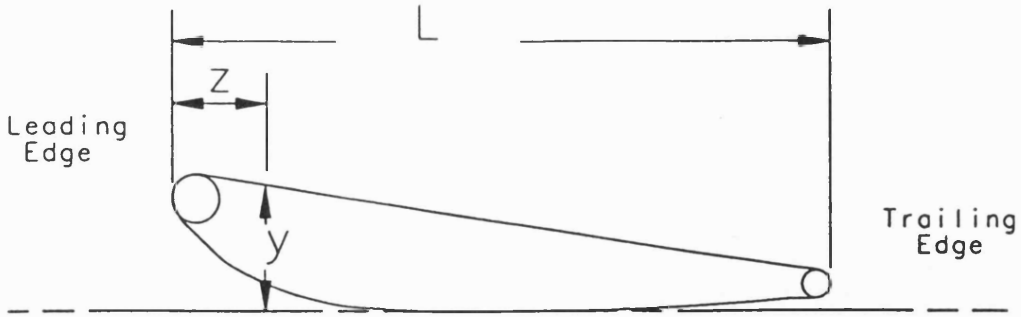

Percent z/L	Lower Surface y/L	Upper Surface y/L
0.0	0.1825	0.1825
1.25	0.1466	0.2072
2.5	0.1280	0.2107
5.0	0.1037	0.2080
7.5	0.0800	
10.	0.0634	
15.	0.0387	
20.	0.0217	
25.	0.0100	
30.	0.0048	
40.	0.0000	Straight Line
50.	0.0000	
60.	0.0000	
70.	0.0029	
80.	0.0082	
90.	0.0145	
95.	0.0186	
100.	0.0236	0.0607

Radius of any point on duct relative to shaft axis = y + D/2 + c

Where: D = maximum blade tip diameter
c = blade tip clearance

Duct leading edge fillet diameter = 5.57% L
Duct trailing edge fillet diameter = 3.78% L

L/D = 0.5 gives an NSMB No.19A Duct

Figure A9.1: A Duct Profile for a Merchant Ship Propulsor

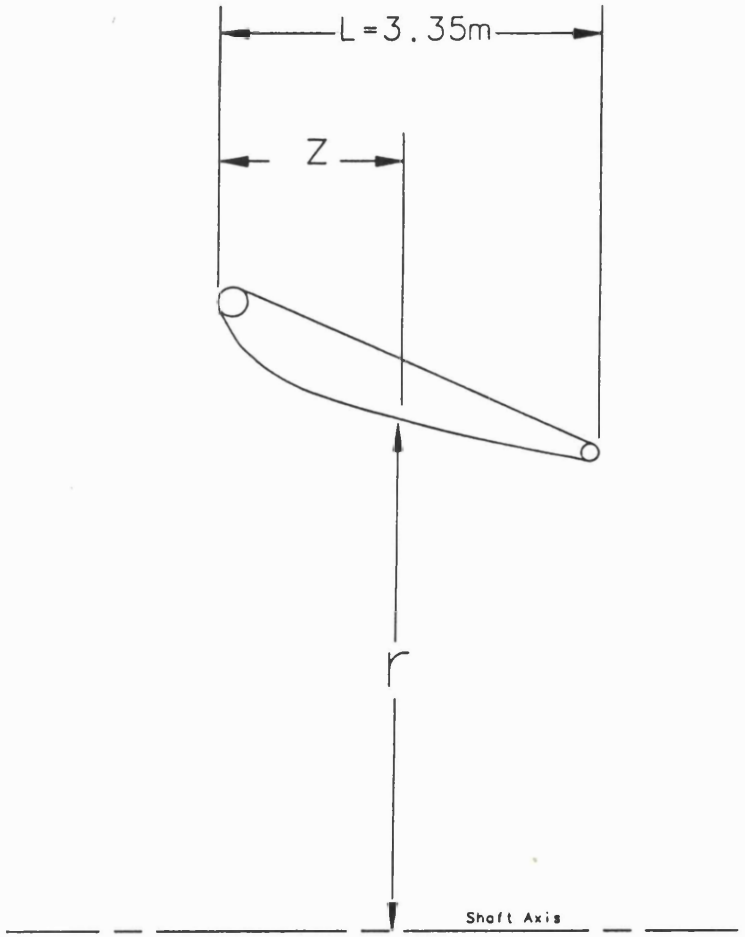

z (m)	Lower Surface r (m)	Upper Surface r (m)
0.0	3.391	3.391
0.042	3.260	3.463
0.084	3.186	3.463
0.168	3.083	3.432
0.251	2.981	3.396
0.335	2.903	3.361
0.502	2.775	3.290
0.670	2.673	3.219
0.837	2.589	3.149
1.005	2.527	3.078
1.340	2.421	2.936
1.675	2.331	2.794
2.010	2.241	2.652
2.345	2.161	2.511
2.680	2.089	2.369
3.015	2.021	2.227
3.182	1.990	2.156
3.350	1.961	2.086

Figure A9.2: A Duct Geometry for a Submarine Propulsor

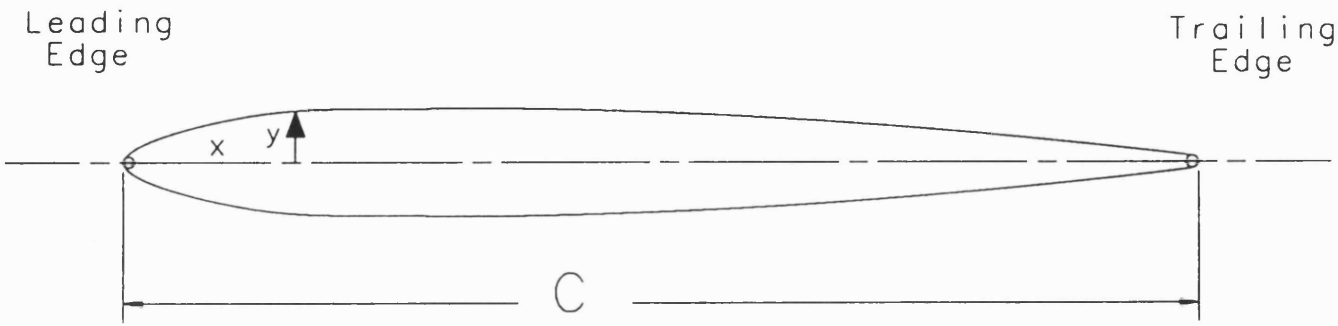

$x<0.3$: $y/C = A(0.154920(x/C)^{1/2} - 0.061004(x/C) - 0.283666(x/C)^{2} + 0.332527(x/C)^{3})$

$x>=0.3$: $y/C = A(0.040318 + 0.066147(x/C) - 0.118248(x/C)^{2} + 0.017783(x/C)^{3})$

Where: A is an arbitrary constant
C is blade chord
Maximum y=0.05AC
Leading Edge Radius = 0.06AC
Trailing Edge Radius = 0.03AC

A = 1.0 gives a NACA C4 thickness distribution

Figure A9.3: A Blade Thickness Distribution

APPENDIX X: HELMHOLTZ DECOMPOSITION AND THE CLEBSCH REPRESENTATION OF VORTICITY

For the reasons outlined in Section 3.4, it was the Clebsch Representation of velocity and vorticity (see Section 4.3) that was adopted for the work presented in this thesis, as it was felt that this approach was the best means of developing a fully three-dimensional ducted propulsor design method with a minimum of assumptions. This appendix now gives further details of the Clebsch approach. However, it is interesting to consider first the more traditional approach of modelling flow fields using Helmholtz decomposition.

Helmholtz Decomposition

With this approach [1] the velocity is expressed as the sum of an irrotational vector and a solenoidal vector, viz.

$$\mathbf{V} = \nabla\Phi + \nabla\times\Psi \qquad \text{A10.1}$$

where Φ is a scalar potential and Ψ is a solenoidal vector potential. The first term on the right hand side of this equation represents the irrotational component of the velocity field, whilst the second term accounts for the rotational component.

Noting [1] that Ψ is solenoidal (i.e. $\nabla\cdot\Psi=0$) it can then be seen that the corresponding flow vorticity is

$$\Omega = \nabla\times\mathbf{V} = \nabla(\nabla\cdot\Psi) - \nabla^2\Psi$$

or

$$\Omega = -\nabla^2\Psi \qquad \text{A10.2}$$

Additionally applying the condition of continuity ($\nabla\cdot\mathbf{V}=0$) to equation A10.1 gives

$$\nabla^2\Phi = 0 \qquad \text{A10.3}$$

The Helmholtz decomposition of velocity is very useful for certain cases, such as plane two-dimensional flow, where Ψ becomes the stream function which is constant along streamlines.

The Clebsch Formulation

Here the velocity is decomposed in the form

$$\mathbf{V} = \nabla\Phi + \lambda\nabla\mu \qquad \text{A10.4}$$

where Φ is a scalar potential, and λ and μ are scalar functions. The first term on the right hand side of this equation represents the irrotational component of the velocity field and is identical to the corresponding term in the Helmholtz decomposition. Although the second term on the right hand side represents the rotational component of the velocity field, it is formulated differently to the corresponding term in the Helmholtz decomposition, and thus accounts for the difference between the Clebsch and Helmholtz decomposition of velocity.

Now, using equation A10.4 the vorticity may be written

$$\begin{aligned}\boldsymbol{\Omega} = \nabla\times\mathbf{V} &= \nabla\times\nabla\Phi + \nabla\times(\lambda\nabla\mu)\\ &= \lambda\nabla\times\nabla\mu + \nabla\lambda\times\nabla\mu\end{aligned}$$

i.e. $$\boldsymbol{\Omega} = \nabla\lambda\times\nabla\mu \qquad \text{A10.5}$$

From this it can be seen that the Clebsch representation satisfies the solenoidal condition on vorticity (i.e. $\nabla\cdot\boldsymbol{\Omega} = 0$) as required. It should be noted that there are generally an infinite number of combinations of λ and μ that satisfy equations A10.4 and A10.5 at a given point in the flow field. However, for the Clebsch representation to be valid throughout the flow domain it is necessary for λ and μ to be chosen so as to be fully compatible with the equations of motion of the fluid, in which case λ and μ tend to correspond to quantities of physical significance such as rothalpy, drift function and blade shape (see Section 4.4).

To interpret the significance of the Clebsch scalars λ and μ equation A10.5 can be used to show that

$$\nabla\lambda\cdot\boldsymbol{\Omega} = \nabla\lambda\cdot(\nabla\lambda\times\nabla\mu) = 0$$

and

$$\nabla\mu\cdot\boldsymbol{\Omega} = \nabla\mu\cdot(\nabla\lambda\times\nabla\mu) = 0$$

As $\nabla\lambda$ is normal to the surfaces λ=constant, and $\nabla\mu$ is normal to the surfaces μ =constant, it can then be seen that the vortex lines lie in both the surfaces λ=constant

and μ=constant. In other words, the vortex lines of the flow always lie along the intersection of the surfaces λ=constant and μ=constant (Figure A10.1).

References

1) Panton,R.L. "Incompressible Flow", p.350, John Wiley & Sons Inc., New York, 1984

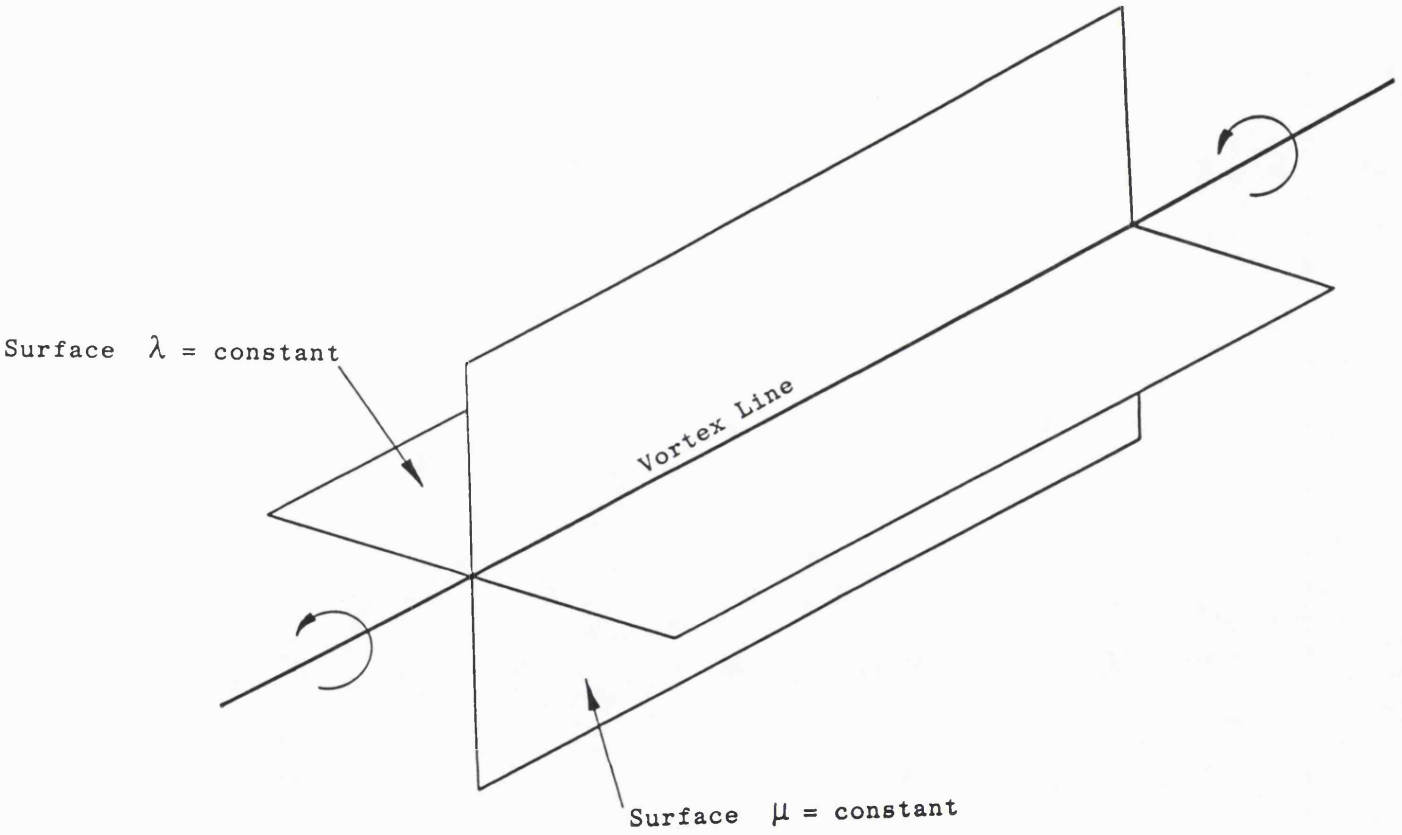

Figure A10.1: The Physical Significance of the Clebsch Scalars λ and μ